National Technical University, Athens

Faculty of Civil Engineering

# Soil–structure interaction under strong seismic moment: *Material* and *geometric* nonlinearity

Marios E. Apostolou

Civil Engineer, MSc.

A thesis submitted for the
Degree of Doctor of Philosophy

November 2011

Εθνικό Μετσόβιο Πολυτεχνείο

Σχολή Πολιτικών Μηχανικών

# Μή γραμμική αλληλεπίδραση εδάφους–κατασκευής υπό ισχυρή σεισμική ροπή

Μάριος Ε. Αποστόλου

Πολιτικός Μηχανικός MSc.

Νοέμβριος 2011

# ΠΡΟΛΟΓΟΣ

Η διεθνής έρευνα στην σεισμική αλληλεπίδραση εδάφους-κατασκευής τις τελευταίες δεκαετίες έχει ως επί το πλείστον βασισθεί σε δύο θεμελιώδεις παραδοχές: (α) γραμμική (ή ισοδύναμη-γραμμική), ιξωδο-ελαστική εδαφική συμπεριφορά και (β) πλήρη επαφή του θεμελίου με το υποστηρίζον έδαφος. Ωστόσο, σε συστήματα υψίκορμων κατασκευών με επιφανειακή θεμελίωση, ακόμα και υπό καθεστώς μέτριας σεισμικής εξαίτησης, η αναπτυσσόμενη ροπή στο θεμέλιο (λόγω της αδράνειας της ανωδομής) ενδέχεται να οδηγήσει σε εξάντληση της αντοχής της διεπιφάνειας (και κατά συνέπεια σε αποκόλληση του θεμελίου). Επιπλέον, η ανάληψη της αδρανειακής ροπής του θεμελίου από το έδαφος έχει ως αποτέλεσμα την ανάπτυξη σημαντικών πλαστικών ζωνών στο εδαφικό υλικό πλησίον της θεμελίωσης. Από τα παραπάνω αναδεικνύεται η αναγκαιότητα ενδελεχούς αντιμετώπισης των μη-γραμμικών φαινομένων που σχετίζονται με την δυναμική συμπεριφορά συστημάτων επιφανειακού θεμελίου-εδάφους.

Στην παρούσα διατριβή μελετάται η σεισμική απόκριση επιφανειακών θεμελίων με θεώρηση των μη-γραμμικών φαινομένων που απορρέουν αφ'ενός μεν από την αποκόλληση του θεμελίου από το έδαφος και αφετέρου δε από την πλαστική συμπεριφορά του εδαφικού υλικού στην περιοχή της θεμελίωσης. Θεμελιώδης προϋπόθεση για την γένεση των δύο ανωτέρω μορφών μη-γραμμικής συμπεριφοράς είναι η ανάπτυξη από την ανωδομή μεγάλων λικνιστικών ταλαντώσεων. Προς τον σκοπό αυτόν η έρευνα εστιάζεται στην ανάλυση υψίκορμων (*slender*) συστημάτων με επιφανειακή θεμελίωση όπου η κύρια μορφή αδρανειακής ταλάντωσης είναι η λικνιστική. Εν κατακλείδι, η μελέτη του προβλήματος επιμερίζεται στις κατωτέρω βασικές ενότητες:

- ✓ *Δυναμική απλών συστημάτων λικνισμού.*
- ✓ *Μη γραμμικές καμπύλες δύναμης–μετακίνησης για επιφανειακά θεμέλια.*
- ✓ *Φέρουσα ικανότητα επιφανειακών θεμελίων λόγω μεγάλης σεισμικής ροπής.*
- ✓ *Ελατηριωτό προσομοίωμα για την ανάλυση της λικνιστικής απόκρισης υπό καθεστώς μεγάλων δομητικών και εδαφικών μετακινήσεων.*

***Δυναμική απλών λικνιστικών συστημάτων:*** Ως εισαγωγή στην ανάλυση της λικνιστικής συμπεριφοράς υψίκορμων κατασκευών έχει μελετηθεί η δυναμική μερικών τυπικών συστημάτων υψίκορμων κατασκευών:

- ✓ Άκαμπτη κατασκευή σε ανένδοτη θεμελίωση (πλήρης αποκόλληση του θεμελίου).
- ✓ Μονοβάθμιος ιξωδο-ελαστικός ταλαντωτής σε ανένδοτη θεμελίωση (πλήρης αποκόλληση του θεμελίου).
- ✓ Μονοβάθμιος ελαστικός ταλαντωτής σε ενδόσιμη (ελαστική ή ελαστοπλαστική) θεμελίωση χωρίς αποκόλληση του θεμελίου.

Η μελέτη των ανωτέρω συστημάτων περιλαμβάνει σε πρώτο στάδιο την κατά *Lagrange* κατάστρωση των εξισώσεων κινήσεως. Σε όλες τις περιπτώσεις έχουν συμπεριληφθεί στις εξισώσεις οι μη-γραμμικοί όροι ώστε να είναι εφικτή η μελέτη της απόκρισης σε επίπεδα μεγάλων δομητικών μετακινήσεων, ακόμα και κοντά στα όρια της ανατροπής. Η αριθμητική επίλυση των εξισώσεων πραγματοποιήθηκε με βήμα-προς-βήμα εν-χρόνω ολοκλήρωση, μέσω της μεθόδου άμεσης διατύπωσης (*explicit algorithm*). Ως διέγερση στην βάση χρησιμοποιήθηκαν πραγματικές καταγραφές σεισμικών επεισοδίων αλλά και εξιδανικευμένοι παλμοί της εδαφικής κίνησης (κυρίως τριγωνομετρικοί παλμοί ενός κύκλου και παλμοί τύπου *Ricker*). Στην μέχρι τώρα μελέτη των ανωτέρω συστημάτων πραγματοποιήθηκε πλήθος

παραμετρικών αναλύσεων και εξήχθησαν κανονικοποιημένα διαγράμματα του πλάτους ταλάντωσης (γωνία λικνισμού θ, καμπτική παραμόρφωση u) ως προς τις ιδιότητες της ανωδομής (γεωμετρία, ιδιοπερίοδος), την ενδοσιμότητα του εδάφους καθώς και την ένταση και τα χαρακτηριστικά της σεισμικής διέγερσης. Ειδικότερα για τον λικνισμό άκαμπτης κατασκευής σε ανένδοτη θεμελίωση (η πιο απλή περίπτωση λικνιστικού συστήματος) διαφάνηκε ότι για επαρκώς μεγάλες κατασκευές η απόκριση είναι προβλέψιμη. Στην περίπτωση μάλιστα εξιδανικευμένων παλμικών διεγέρσεων το πλάτος της γωνίας προέκυψε υπό κανονικοποιημένη μορφή μέσω απλών εμπειρικών διαγραμμάτων. Από το σύνολο των αποτελεσμάτων προέκυψε ότι το πλάτος της γωνίας λικνισμού είναι ανάλογο του υψίκορμου (slenderness) της κατασκευής, της έντασης και κυρίως της δεσπόζουσας περιόδου της σεισμικής διέγερσης. Οι συνθήκες κατά τις οποίες τα υψηλά επίπεδα λικνισμού οδηγούν τελικώς σε ανατροπή μελετήθηκαν διεξοδικά στην μέχρι τώρα έρευνα. Ειδικότερα, υπολογίσθηκε παραμετρικά η ελάχιστη απαιτούμενη σεισμική επιτάχυνση για ανατροπή ως προς την γεωμετρία του συστήματος και την περίοδο της διέγερσης.

***Ανάλυση της σεισμικής απόκρισης του συστήματος εδάφους-θεμελίου με πεπερασμένα στοιχεία:*** Σε αυτήν την ενότητα η ανάλυση της σεισμικής απόκρισης του συστήματος ευωδούται με την αριθμητική μέθοδο των πεπερασμένων στοιχείων. Προς τον σκοπόν αυτόν χρησιμοποιείται ο γενικής χρήσεως κώδικας πεπερασμένων στοιχείων *ABAQUS* (διαθέσιμος στο ΕΜΠ). Η προσομοίωση του θεμελίου και του εδάφους πραγματοποιείται με τετραπλευρικά στοιχεία επίπεδης παραμόρφωσης ενώ η ανωδομή περιγράφεται απλοποιητικά με στοιχεία δοκού. Η αποκόλληση του θεμελίου από το έδαφος επιτυγχάνεται με χρήση ειδικών στοιχείων κενού (*gap elements*) μέσω ενός εξελιγμένου αλγόριθμού επαφής διαθέσιμου στο *ABAQUS* που επιτρέπει την ρεαλιστική προσομοίωση της λικνιστικής συμπεριφοράς ακόμα και κοντά στα όρια της ανατροπής. Η ολοκλήρωση των εξισώσεων κινήσεως γίνεται εν-χρόνω (βήμα προς βήμα) μέσω επαναληπτικής διαδικασίας σύγκλισης (*implicit algorithm*). Στις μέχρι τώρα

αναλύσεις η συμπεριφορά του εδαφικού υλικού θεωρήθηκε είτε ιξωδο-ελαστική ή ελαστοπλαστική σύμφωνα με το κριτήριο αστοχίας *Mohr-Coulomb*.

***Φέρουσα ικανότητα επιφανειακών θεμελίων λόγω μεγάλης σεισμικής ροπής:*** Η προκαταρκτική διερεύνηση της σεισμικής συμπεριφοράς των επιφανειακών θεμελίων κοντά στην αστοχία κατέδειξε ότι η οριακή ροπή ανατροπής επηρεάζεται αφενός μεν από την αποκόλληση του θεμελίου σε περιπτώσεις σχετικώς μεγάλων συντελεστών ασφαλείας έναντι κατακόρυφου φορτίου (FS > 2), αφετέρου δε από τις αναπτυσσόμενες πλαστικοποιήσεις στο έδαφος θεμελίωσης για κατακόρυφα φορτία κοντά στο μέγιστο επιτρεπόμενο (1 < FS < 2). Απόρροια της αλληλεπίδρασης της γεωμετρικής και "*υλικών*" μη-γραμμικότητας του συστήματος είναι η μεγιστοποίηση της οριακής ροπής ανατροπής για κατακόρυφο στατικό φορτίο κοντά στο ήμισυ του μέγιστου επιτρεπομένου.

***Ελατηριωτό προσομοίωμα για την ανάλυση της λικνιστικής απόκρισης υπό καθεστώς μεγάλων δομητικών και εδαφικών μετακινήσεων:*** Στην ενότητα αυτήν αναπτύχθηκε απλοποιητική μεθοδολογία για τον αναλυτικό υπολογισμό των καταστατικών σχέσεων δύναμης-μετακίνησης στο σύστημα θεμελίου-εδάφους μέσω του ελατηριωτού προσομοιώματος (*beam-on-Winkler-foundation*). Αντίθετα με την έως τώρα διαθέσιμη στην βιβλιογραφία προσεγγιστική επίλυση του προβλήματος που περιορίζει το εύρος εφαρμογής της σε πολύ μικρές μετακινήσεις της ανωδομής, στην παρούσα μελέτη λαμβάνεται υπ' όψιν η αναπτυσσόμενη -γεωμετρικής φύσεως- μη-γραμμικότητα του προβλήματος (*p-δ effects*) που λαμβάνει χώρα σε μεγάλες γωνίες λικνισμού λόγω της αποκόλλησης του θεμελίου. Η ανωτέρα θεώρηση επιτρέπει την ρεαλιστική βαθμονόμηση της δυσκαμψίας του συστήματος εδάφους-θεμελίου από την περιοχή των μικρών παραμορφώσεων έως κοντά στην ανατροπή.

# Acknowledgements

The work described in this thesis has been made possible through support and financial assistance provided to me during the course of the study.

Most of this work was part of two joint research programs in which NTUA participated: (a) a project funded by the European Commission with the acronym 'QUAKER' (2003-2006) on '*Fault-rupture and strong shaking effects on the safety of composite foundations and pipeline systems*', and (b) a project titled 'X-SOILS' (2003-2007) on the '*Foundation on class X soils under strong seismic excitation*' funded by the Greek General Secretariat for Research and Technology.

I am also indebted to many people for their interest and assistance during this course of work.

First of all, I would like to express my deep gratitude and appreciation to my supervisor, Professor George Gazetas, who gave me invaluable guidance and was always accessible with friendly support and enthusiasm throughout my graduate studies in NTUA.

Many thanks to Nikos Gerolymos, and Ioannis Anastasopoulos, Lecturer and Doctor at NTUA respectively for their fruitful comments on my thesis and cooperation throughout these years.

I also thank my father and my mother whose lifetimes have been devoted to my education. This thesis is dedicated to them.

# Contents

***Chapter 4 (60pp)***

**Finite element analysis of the uplifting response**



***Chapter 5 (36pp)***

**Foundation capacity and permanent displacements under earthquake loading**

# Notation

| | |
|---|---|
| $g$ | acceleration of gravity |
| $m$ | structural mass |
| $N = mg$ | vertical (gravitational) load of the foundation |
| $Q$ | horizontal load of the foundation |
| $M$ | overturning moment of the foundation |
| $B$ | width of a strip or rectangular footing |
| $b$ | half-width of a strip or rectangular footing |
| $\beta$ | half-width of the effective footing |
| $R = \sqrt{b^2 + {z_c}^2}$ | half-diagonal of a rigid block |
| $J_o$ | moment of inertia about a corner point |
| $J_b$ | moment of inertia about the footing bottom mid-point |
| $p = \sqrt{mgR/J_o}$ | size or frequency parameter |
| $r = \left(1 - \frac{3}{2}\sin^2\theta_c\right)^2$ | impact coefficient of restitution |
| $\mathrm{sgn}(\bullet)$ | signum function of $(\ )$ |
| $t_i$ | time of impact |
| $\mathcal{A} = a_g / a_c$ | 'dynamic' amplification of the overturning acceleration |
| $a_c = b/h$ | 'static' overturning acceleration |

| | |
|---|---|
| $PGA$ | peak ground acceleration |
| $\theta$ | angle of rocking rotation |
| $\Theta = \theta \,/\, \theta_c$ | dimensionless rocking rotation |
| $\theta_{\max}$ | amplitude of rocking rotation |
| $\theta_c = \arctan\left(b/h\right)$ | critical rocking angle of overturning |
| $\theta_{uplift}$ | critical rocking angle of incipient uplift |
| $\phi = \dot{\theta}$ | angular velocity of rocking |
| $u_b$ | horizontal displacement of the footing |
| $w_b$ | vertical displacement of the footing |
| $\tau = p\,t$ | stretched time |
| $\Psi$ | phase shift |
| $\omega_E$ | excitation frequency |
| $\Omega = \omega_E \,/\, p$ | frequency ratio |
| $E$ | Young modulus of soil |
| $s_u$ | undrained shear strength of soil |
| $N_u$ | ultimate vertical load of the foundation (under static conditions) |
| $FS_v = N_u \,/\, N$ | safety factor of the foundation against vertical loading |
| $\chi = \left(FS_v\right)^{-1}$ | inverse of the safety factor against vertical loading *or simpler* vertical load factor |
| $M_u$ | ultimate moment of the foundation |
| $\theta_u$ | angle of rocking rotation at $M = M_u$ |

# *Chapter 1*:

# Introduction

## 1.1 DESCRIPTION of the PROBLEM

Research on seismic soil-structure interaction (SSI) over the last decades has mostly relied on the assumption of linear (or at most equivalent-linear) elastic soil behaviour and fully bonded contact between footing and soil. Seismic design of structure-foundation systems has followed a somewhat parallel path: the still prevailing 'capacity design' philosophy allows substantial plastic deformation in the superstructure but requires that no significant plastification should be developed below ground level. With respect to shallow foundations this assumption implies that:

- foundation elements (e.g. piles, footings, caissons) must remain structurally elastic (or nearly elastic)
- bearing capacity soil failure mechanisms must not be mobilised
- sliding at the soil-foundation interface must not take place, while the amount of foundation uplift must be restricted to about half of the fully-bonded contact area.

However, seismic accelerograms recorded in the last twenty years, especially after the Northridge 1994 and Kobe 1995 earthquakes, have revealed that very substantial ground and spectral acceleration levels can be experienced in the near-fault zones. Seismic loads transmitted onto shallow foundations in such cases will most probably induce significant nonlinear inelastic action in the soil and soil–foundation interface. Three possible types of foundation-soil nonlinearity as sketched in Fig. 1.1 emerge:

- sliding at the soil-structure interface

- uplifting of the foundation from the supporting soil
- bearing capacity type of soil failure

Observations of shallow foundations in recent earthquakes confirm the above argument. The most spectacular examples of strongly nonlinear foundation response which led to bearing capacity and uplifting failures of buildings took place in the city of Adapazari during the Kocaeli 1999 earthquake (Gazetas *et al.*, 2003). But such phenomena are not limited to buildings: the Rion-Antirrion cable-stayed bridge is mentioned as an example of a contemporary monumental bridge, the shallow foundations of which, despite their colossal 90 m diameter had to be designed allowing for strong nonlinear response. Hence, sliding, uplifting and partial mobilisation of soil bearing capacity are expected to occur in order to resist the prescribed high levels of seismic excitation (Pecker & Teyssandier, 1998; Gazetas, 2001). Offshore platforms are also a type of structures where nonlinear mechanisms are likely to develop on the soil-foundation system as a result of (a) the large overturning moments of the environmental loads, and (b) the usually poor subsoil conditions. Under such circumstances conventional foundation design is inadequate and inefficient, and more rigorous analytical methods are most often employed.

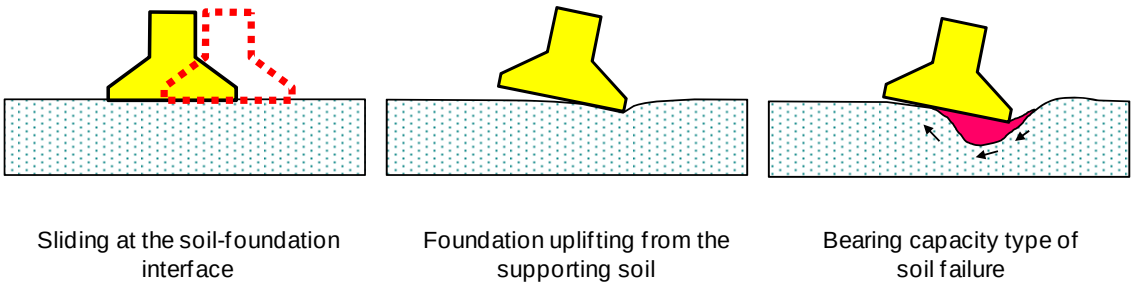


**Figure 1.1** 'Plastic hinges approach' at soil-foundation interface (Gazetas and Apostolou, 2004).

Finally, for seismically retrofitting structures designed with the small acceleration levels of the past, the necessity to explicitly consider the occurrence of one or more of the above-mentioned nonlinearities is often unavoidable. The 1997 *NEHRP Guidelines for the Seismic Rehabilitation of*

*Buildings* (FEMA, 1997) first acknowledge that the ductility demands on structures could be reduced when allowing the ultimate moment capacity of the foundation to be mobilised, particularly for shear walls. A typical example of concrete frame with a slender shear wall for a retrofitted multi-storey building is portrayed in Fig. 1.2.

Under such an alternative approach, the task of the geotechnical seismic design lies with the adoption of a foundation configuration, capable of exploiting the benefits of the nonlinear, softening response under severe ground shaking, without 'facilitating' excessive permanent displacements to develop.

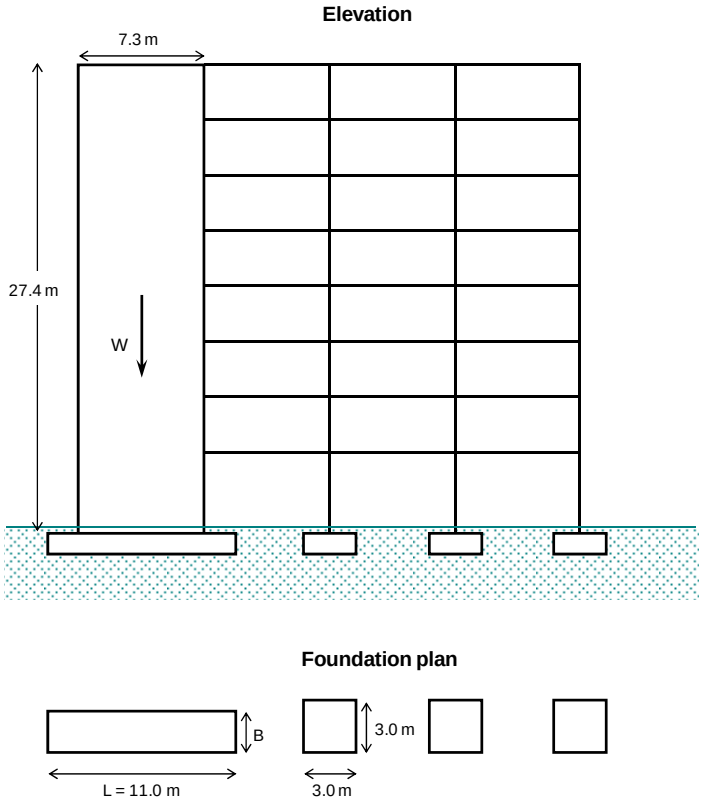


**Figure 1.2** Typical example of concrete frame with shear wall for a 8-storey building (after NEHRP, 1997).

## 1.2 OBJECTIVES of the STUDY

The study is focused on the nonlinear effects associated with the response of a shallow foundation subjected to large overturning moment. Slender structural systems are more vulnerable to develop

high levels of foundation moment even during a moderate seismic shaking and evidently rocking component of motion is predominant. In the domain of large displacements, nonlinear features of such a soil-foundation system may be summarised in:

- separation of a footing undergoing rocking oscillations from the supporting soil ('uplifting'), and
- mobilisation of bearing capacity type failure surface mechanisms under large cyclic overturning moments ('soil failure').

These fundamental nonlinear effects associated with foundation rocking arise from:

- the negligible tensile capacity of the soil-foundation interface during swaying-rocking motion, which results in uplifting of the foundation as well as in inadvertently, creating second order $(P-\delta)$ effects (geometrical nonlinearity – *type A*),
- the plastification of the supporting soil, especially in the vicinity of the corner points of the foundation stemming from the concentration of high vertical stresses and amplified by the cyclic response of the superstructure (material nonlinearity – *type B*).

Within this framework the main objectives of the study can be summarised as follows:

(a) To gain insight on the profoundly nonlinear dynamics of rocking on rigid soil. In light of this it is of great importance to distinguish uplifting from overturning which are identical under static consideration.

(b) To identify the key parameters affecting the rocking response of a structure on compliant supporting medium. In case of inelastic soil medium to study the interplay of the two predescribed sources of nonlinear actions.

(c) To estimate levels of fail-safe response under severe ground excitation.

(d) To establish design criteria for shallow foundations to withstand strong shaking with minor permanent displacements.

Three elementary slender systems with a strip footing subjected to rocking vibrations can be employed to distinguish linear from nonlinear SSI either due to type A or B mechanisms, as illustrated in Fig.1.3:

(a) *Rocking without uplift on elastic soil.* Tensile capacity along the interface is considered large enough to prevent uplifting. When overturning moment is imposed to the footing, coupled swaying-rocking motion initiates due to soil compliance. Foundation is then rotating around a point which lies along the central vertical axis of the interface (*pole of rotation*). For a very slender structure, this pole is fixed on the interface midpoint. The linear response of the system may be obtained through conventional SSI studies available in literature.

(b) *Rocking on rigid soil.* In this case soil-foundation interface has no tensile capacity. Consequently, under large overturning moment, the footing can rotate only around its corner points (poles of rotation). Once rocking initiates, subsequent uplifting occurs. In slender systems sliding is prevented. A geometrically-induced, profoundly non linear response emerges (type A).

(c) *Rocking without uplift on inelastic soil.* Tensile capacity along the interface is considered large enough to prevent uplifting. In this way non linear response is attributed exclusively to inelastic soil behaviour (type B). Compared to the linear system, the pole of rotation now shifts towards the unloading edge.

It is worthy of note that a strip footing on elastic soil with a tensionless contact interface is also an example of pure geometric nonlinear SSI. In this case though, nonlinear rocking response is 'cushioned' by the deformability of supporting soil. As a result, rocking without uplift occurs at low levels of the overturning moment whereas at higher levels, the footing uplifts partially from the

supporting soil. Accordingly, rocking response is bounded by the limiting cases of (a) and (b). Nevertheless, this system will also be examined in detail as it simplifies (for a lightly-loaded footing) the actual problem of nonlinear SSI in which both geometric and material nonlinearities develop.

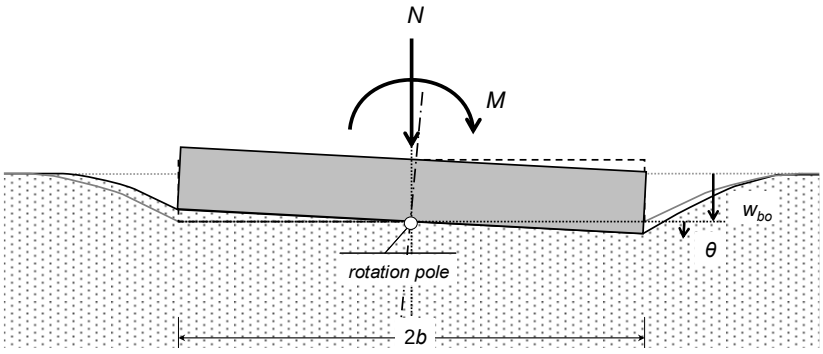


**(a) rocking on elastic soil**

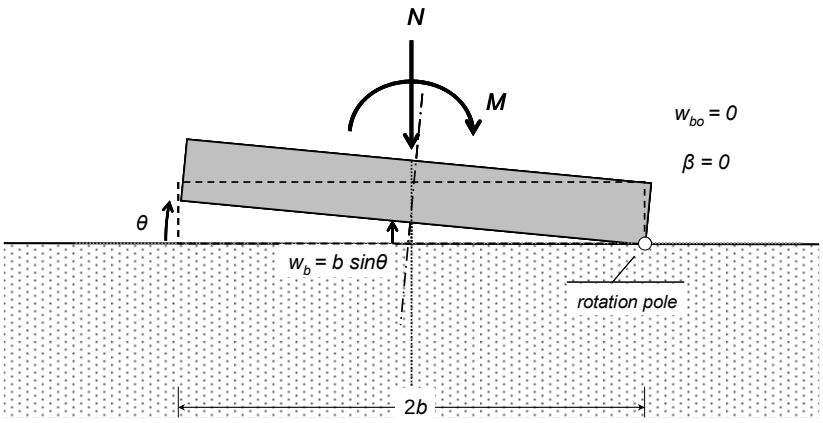


**(b) rocking and uplift on rigid soil**

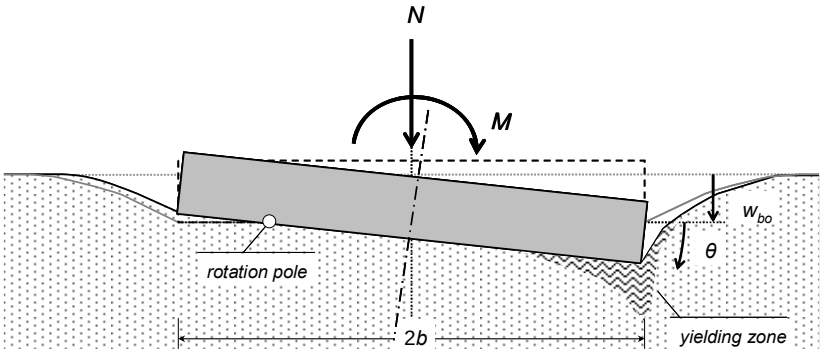


**(c) rocking on inelastic soil**

**Figure 1.3** Large displacement analysis of rocking behaviour for a slender structural system; Simplified states of response.

## 1.3 OUTLINE of the STUDY

An overview of the fundamental analytical tools to address the SSI effects in a rigorous or simplified linear formulation is presented in Chapter 2. The most widespread techniques available in the literature to assess nonlinear phenomena related to inelastic soil behaviour or large structural displacements are also discussed in the same chapter.

An introduction to study the geometrically nonlinear SSI is attempted in Chapter 3. To this extent, rocking behaviour of a rigid, block-type or one-storey structure supported on a rigid, horizontally oscillating base is examined. In the case of a one-storey structure the flexibility of the pier is also considered. The profound nonlinear aspects of the dynamic rocking response are highlighted under (a) free vibration, (b) harmonic shaking, (c) earthquake shaking.

In Chapter 4 the compliance of the supporting soil is implemented in the analysis of the rocking response of shallow foundations. To this end, a series of sophisticated nonlinear finite element analyses is performed with soil medium described with (a) visco-elastic and (b) inelastic material. In the latter, nonlinear soil behaviour is described with advanced plasticity models. Hence, nonlinear behaviour of soil is approached by: (a) the elastic–perfectly plastic model determined by the elastic parameters $E$, $\nu$ and the Mohr-Coulomb failure criterion described with the strength parameters $c$, $\phi$ and, (b) the von Mises failure criterion combined with an isotropic and kinematic hardening model in the post-yielding domain. The latter is most suitable for the analysis of the dynamic behaviour of cohesive soils under undrained conditions. Monotonic response is calculated with static 'push-over' analysis to extract backbone load-displacement curves. Moreover, time-domain analysis using simple pulses or earthquake records as bedrock excitation is carried out to elucidate the nonlinear features of the dynamic response of the soil-foundation system.

In Chapter 5, the afore-discussed nonlinear finite element analysis is focused on the limiting case that the capacity of the foundation is reached. Interaction curves are produced under static conditions and compared to the existing solutions of the literature. The analysis is extended in the time-domain by

using both pulse-type time histories and earthquake records. Permanent cumulative displacements are also calculated in light of a fundamental sensitivity study.

The limitations of conventional Winkler-based modelling under strong overturning moments are highlighted in Chapter 6. To overcome these drawbacks, a macroscopic modelling of the soil–foundation system is developed, capable of representing the large-displacement domain of the response. Analytical equations for the monotonic load-displacement relationship are extracted incorporating both geometric and material nonlinearities. Such analytical backbone curves may be implemented in dynamic SSI analysis through the concept of nonlinear macro-element to represent the near-field soil-foundation system.

The conditions under which uplifting leads to large angles of rotation and eventually to overturning are investigated in Chapter 7 through rigorous, large displacement approach. The structure is resting on the surface of either a rigid base or a linearly elastic continuum. Directivity–affected near-fault ground motions, idealised as Ricker wavelets or trigonometric pulses, are used as excitation. A profoundly nonlinear rocking behaviour is revealed for both rigid and elastic soil conditions. This geometrically nonlinear response is further amplified by unfavourable sequences of long–duration pulses in the excitation.

*Chapter 2*:

# Overview of linear and nonlinear soil–structure interaction methods for shallow foundations

## 2.1 INTRODUCTION

Shallow mat foundations are generally chosen for buildings and bridges on stiff and strong soils. Under certain circumstances however, surface foundation may be the most suitable solution even when soft or poor soil conditions are encountered. As an example, for critical offshore facilities deep foundation is often an impracticable method. Moreover in many regions around the world with soft soils and high water table (e.g. Adapazari, Turkey) shallow mat foundations may be the only economically feasible solution.

A schematic of soil-structure interaction problem for a spread footing is depicted in Fig. 2.1. During earthquake shaking, soil deforms under the influence of the arriving 'incident' seismic waves and 'carries' dynamically with it the foundation and the supported structure. In turn, the induced motion of the superstructure generates inertia forces which result in dynamic forces and moments at the foundation that are subsequently transmitted into the supporting soil. Thus, superstructure-induced deformations develop in the soil while additional waves emanate from the soil–foundation interface. In response, foundation and superstructure undergo further dynamic displacements, which generate further inertial forces and so on (Gazetas and Mylonakis, 1998).

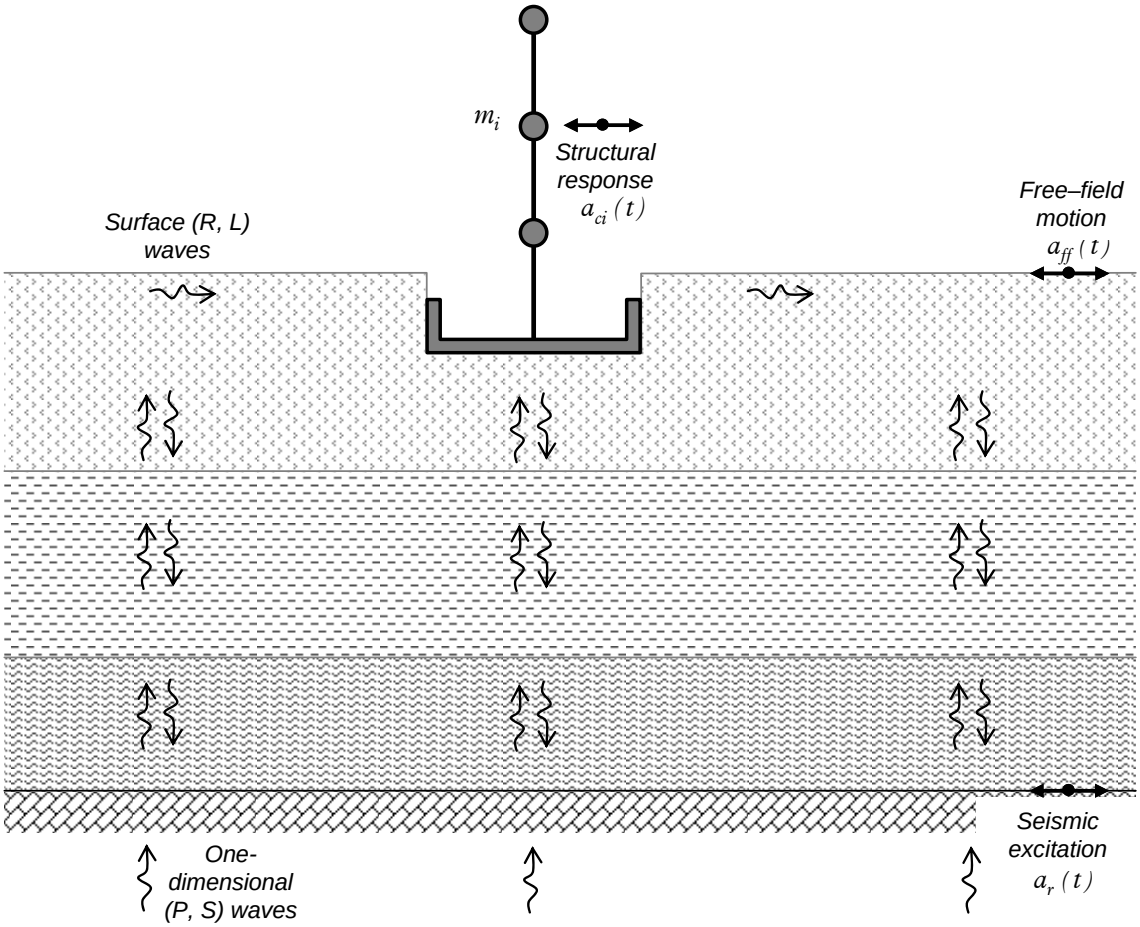


**Figure 2.1** Schematic of the soil-structure interaction problem in a horizontally–layered soil profile.

## 2.2 LINEAR SOIL–STRUCTURE INTERACTION

The phenomena of seismic SSI described in the preceding occur simultaneously. Within the limits of a linear procedure however, it is convenient (both conceptually and computationally) to obtain the response of the soil–foundation–structure system as a superposition of the two interaction effects:

(a) '*Kinematic interaction*', (KI) referring to the distress of the structure as the incident seismic waves are reflected and scattered by the foundation which in turn develops curvatures and bending moments due to its different rigidity with respect to the surrounding soil (Fig. 2.2a),

(b) '*Inertial interaction*', (II) referring to the oscillation of the superstructure generated by the motion induced at the foundation level which in turn imposes additional dynamic loading to the foundation and the surrounding soil (Fig. 2.2b).

Before proceeding to the analysis of SSI, a site response analysis must be preceded to calculate the free-field motion which will be applied as input for the KI analysis. This task requires that the *design motion* be known at a specific ('control') point, usually taken at the rock-outcrop surface.

For a linear soil–foundation–structure system the mathematical validity of this multistep approach emerges from the so-called *superposition theorem* (Whitman, 1972; Kausel and Roesset, 1974; Gazetas and Mylonakis, 1998) which states that the equation of motion for the overall system in its matrix formulation,

$$[M]\cdot\{\ddot{u}\}+[K]\cdot\{u\}=-[M]\cdot\{I\}a_r \qquad [2.1]$$

can be decoupled in the two following differential equations:

$$[M_{so}]\cdot\{\ddot{u}_{kin}\}+[K]\cdot\{u_{kin}\}=-[M_{so}]\cdot\{I\}a_r \qquad [2.2a]$$

$$[M_{st}]\cdot\{\ddot{u}_{iner}\}+[K]\cdot\{u_{iner}\}=-[M_{st}]\cdot\left(\{\ddot{u}_{kin}\}+\{I\}a_r\right) \qquad [2.2b]$$

where: $\{u\}$ is the relative displacement vector of points in the soil or the structure with respect to the top of the 'rock', $\{u_{kin}\}$ and $\{u_{iner}\}$ are respectively the kinematic and the inertial relative displacements, $\{I\}$ is the unit vector, $[K]$ is the stiffness matrix of the system, $[M]$ is the mass matrix of the system, $[M_{so}]$ is the mass matrix assuming that only the soil and the foundation have mass (i.e. the mass of the superstructure is made zero), and $[M_{st}]$ is the mass matrix assuming that there is mass only in the superstructure (i.e. the mass of foundation and soil are made zero). By definition it is $[M]=[M_{so}]+[M_{st}]$ and $\{u\}=\{u_{kin}\}+\{u_{iner}\}$.

For computational convenience, analysis of the inertial interaction described with Eq. 2.2b is further subdivided into two consecutive independent analysis steps, as follows (Kausel and Roesset, 1974):

(b1) Computation of the dynamic foundation impedances (*springs* and *dashpots*) associated with the swaying and rocking motion of the foundation (for shallow foundations cross-swaying-rocking terms are usually neglected) as shown in Fig. 2.2b1; and

(b2) Analysis of the dynamic response of the superstructure supported on the springs and dashpots of step (b1), subjected to the kinematic *foundation input motion* of step (a) (Fig. 2.2b2).

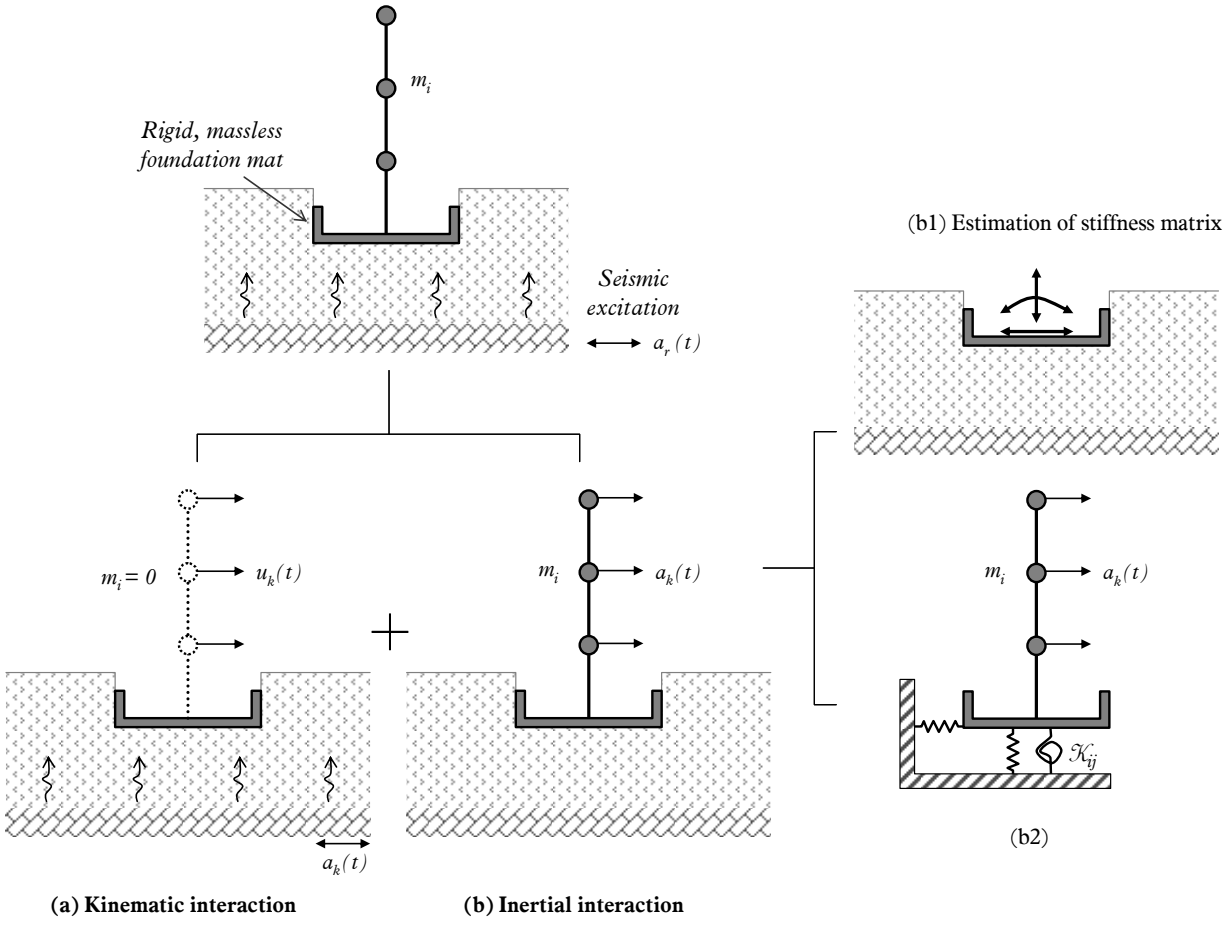


**Figure 2.2** The geometry of SSI problem; decomposition into kinematic and inertial response (Kausel *et al.*, 1976).

Given that the analysis in each individual step is performed rigorously, the superposition theorem provides the exact solution of the linear problem. In addition, it can be a reasonable approximation in cases of moderately–nonlinear soil behaviour (Gazetas and Mylonakis, 1998).

The conventional approach to foundation design is based on such a linear, frequency-domain SSI analysis, to derive dynamic forces and moments transmitted onto the foundation along with considerations for inelastic structural response (e.g. by reducing the moments in columns through the behaviour 'ductility' factor $q$). Factors of safety against sliding and exceedance of ultimate capacity, are introduced in the design, in a way similar to the traditional static design. The foundations are then designed in such a way that these transmitted horizontal forces and overturning moments, increased by 'overstrength' factors, would not induce sliding or bearing capacity failure.

The relative importance of the kinematic and inertial effects on the structural response depends on the foundation characteristics and the nature of the incoming wave field (Pecker and Pender, 2000). In particular, for structural systems with a surface or an embedded at a shallow depth foundation, the kinematic effect on the structural response is often small and could be neglected.

An important step in terms of inertial interaction analysis is the determination of the dynamic impedance of an 'associated' rigid but massless foundation subjected to harmonic loading of frequency, $\omega$. This is defined as the ratio between the steady-state force (moment) and the resulting displacement (rotation) at the base of the foundation. Since dynamic force and displacement are generally out of phase, any dynamic displacement can be resolved into two components: one in phase and one $90^0$ out of phase with the imposed harmonic load. Impedances may therefore be written in complex notation:

$$\mathcal{K} = K_1 + iK_2 \qquad [2.3]$$

in which, $K_1$ and $K_2$ are the *dynamic impedance functions*.

In his seminal work (1936), Reissner motivated by Lamb's earlier studies on the *dynamic Boussinesq problem* (1904) demonstrated theoretically that a vertically loaded circular foundation vibrating on a halfspace could be represented with 1-dof visco-elastic oscillator. By comparing his analytical results from the halfspace theory with those from the lumped-mass system he showed that the equivalent lumped parameters should be frequency dependent. In this way he established the *displacement functions*, $f_1(\omega)$ and $f_2(\omega)$, to express the vertical displacement $u_v$ by:

$$u_v = \frac{P_0 \exp(i\omega t)}{GR}(f_1 + i f_2) \qquad [2.4]$$

in which, $P_0$ is the amplitude of the total force applied to the circular contact area, $G$ is the shear modulus of the halfspace, and $R$ is the radius of the circular contact area. According to Reissner's findings, the dynamic impedance components of Eq. 2.3 are functions of the vibrational frequency $\omega$ as well. In addition, soil visco-elastic parameters $(G,\ \nu,\ \text{and}\ \rho)$ should also be included in these components. Hsieh (1962) showed that in analogy with the 1-dof oscillator, the real part in Eq. 2.3 represents the stiffness and inertia of the supporting soil whereas the imaginary part describes the absorption of energy within the soil medium through radiation damping. By a reorganisation of dynamical equilibrium equation of the lumped system and in combination with Reissner's equation (Eq. 2.4) the complex dynamic impedance of steady-state vibration can be written:

$$\mathcal{K} = K - m\omega^2 + i\omega C \qquad [2.5a]$$

in which, $K = GR\dfrac{f_1}{f_1^2 + f_2^2}$ and $C = -\dfrac{GR}{\omega}\dfrac{f_2}{f_1^2 + f_2^2}$ [2.5b]

The parameters $K$ and $C$ in Eq. 2.5b are the familiar spring and damping terms respectively, of the equivalent lumped system, both functions of the frequency of vibration. Lysmer (1965) uncovered that when multiplying the displacement function $f = f_1 + i f_2$ by a factor $4/(1-\nu)$, a new displacement function $F = F_1 + i F_2$ is obtained which is essentially independent of $\nu$. By adopting

the *dimensionless frequency factor* , $a_0 = \frac{\omega b}{V_S}$, he was able to derive charts of $F_1$ and $F_2$ as functions solely determined by $a_0$. This discovery allowed Lysmer to provide values for the lumped parameters $K$ and $C$. By introducing a *modified dimensionless mass ratio,* $B_z = \frac{1-\nu}{4}\frac{m}{\rho R^3}$, for the vertical vibration of the rigid circular footing, and based on Reissner's expression for the displacement amplitude, $A_z$, Lysmer developed normalised response curves through the magnification factor $M = \frac{4GR}{(1-\nu)Q_0}A_z$ for several values of $B_z$. After studying the variations of spring and dashpot factors with frequency $(a_0)$, as obtained from the elastic halfspace theory, he further noted that constant values of these quantities could be used. Hence, he chose the spring constant equal to the static value $\left[k_v = 4GR/(1-\nu)\right]$ and fitted the damping term for the range $(0 < a_0 < 1)$ to be $c_v = 3.4R^2\sqrt{G\rho}/(1-\nu)$. According to this engineering approximation (often called 'Lysmer's Analog'), the steady-state response of the footing can be computed through the equation of motion of the equivalent lumped system:

$$m\ddot{u}_v + \frac{3.4R^2\sqrt{G\rho}}{1-\nu}\dot{u}_v + \frac{4GR}{1-\nu}u_v = Q \qquad [2.6]$$

Richart and Whitman (1967) extended Lysmer's Analog by demonstrating that all modes of vibration can be studied by means of visco-elastic lumped systems having properly selected frequency-independent parameters. A remarkable agreement is revealed from the comparison between the exact halfspace and the approximated 1-dof response, as illustrated in the charts of Fig. 2.3 for the different modes of vibration.

An alternative way of Eq. 2.5a is derived by separating the static from the dynamic component and expressing stiffness and damping terms as a function of $a_0$ :

$$\mathcal{K} = K \cdot \left\{ k(a_0) + i \cdot a_0 \cdot c(a_0) \right\} \qquad [2.7]$$

in which, $K$ is the static stiffness, irrelative to the vibration frequency, $k(a_0)$ and $c(a_0)$ are respectively, dynamic stiffness and radiation dashpot coefficients, both frequency dependent.

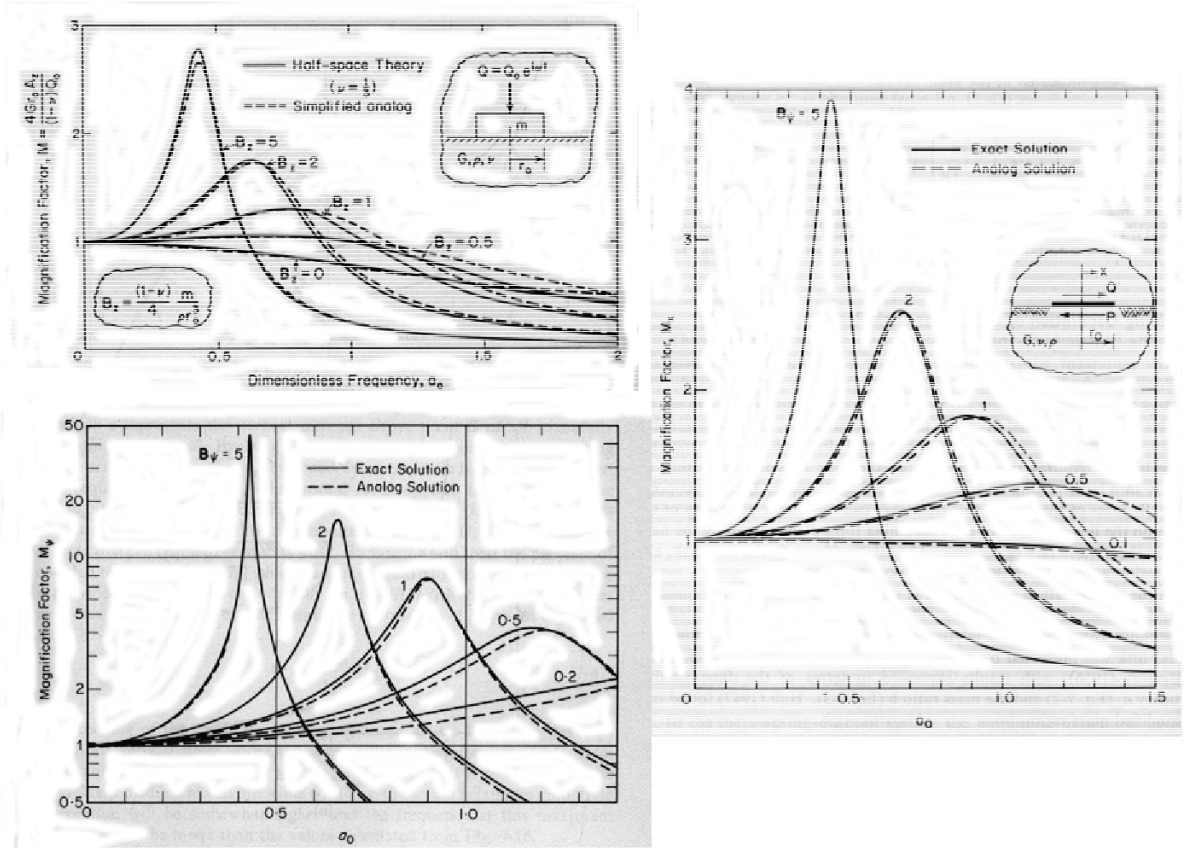


**Figure 2.3** Comparison between the exact halfspace and the analog 1-dof dynamic response of a rigid circular footing, for the different modes of vibration (after Richart *et al.*, 1970).

Dynamic impedance functions ('springs' and 'dashpots') may be obtained with various computational methods which can be grouped into four categories: (a) *analytical and semi-analytical* methods that can handle multi-layered soil deposits and rectangular surface foundations (e.g. Gazetas and Roesset, 1976), (b) *dynamic finite element* methods that can treat any type of soil profile or foundation geometry (even three- dimensional) provided that powerful computational resources are available, (c) *combined analytical–numerical* methods which take advantage of the other two methods (e.g. the *boundary element method*), and (d) *approximate techniques* that simplify the physics of the problem and can

provide engineering solutions to some very complicated situations (among others Meek and Veletsos, 1973; Wolf, 1985, 1988). There is a variety of ready-to-use solutions for dynamic impedance functions available in the literature covering a wide range of idealised soil profiles and foundation geometries. For example, dynamic spring and dashpot coefficients for arbitrarily shaped and strip footings on homogeneous halfspace can be obtained in the form of algebraic formulas and charts illustrated in Table 2.1 and Fig. 2.4 respectively.

**Table 2.1** Dynamic stiffnesses and dashpot coefficients for arbitrarily shaped foundations on the surface of a homogeneous halfspace (Gazetas, 1991).

| Mode of vibration | Dynamic stiffnesses $\mathcal{K}^* = K \cdot k(a_0)$ | | | *Radiation dashpot coefficient $C$ (General shapes)* |
|---|---|---|---|---|
| | Static stiffness $K$ | | Dynamic stiffness coefficient $k$ (General shape; $0 \le a_0 \le 2$)$^+$ | |
| | General shape (foundation-soil contact surface is of area $A_b = x4l^2$ and has a circumscribed rectangle $2l$ by $2b$; $l > b$) | Strip $(2l \to \infty)$ | | |
| Vertical, z | $K_v = \frac{2Gl}{1-\nu}\left[0.73 + 1.54x^{0.75}\right]$ | $K_v^* = \frac{K_v}{2l} \cong \frac{0.73G}{1-\nu}$ | $k_v = k_v\left(\frac{l}{b}, \nu, a_0\right)$ is plotted in Graph a | $C_v = \left(\rho V_{La} A_b\right) \cdot \tilde{c}_v$ $\tilde{c}_v = \tilde{c}_v\left(\frac{l}{b}, \nu; a_0\right)$ is plotted in Graph c |
| Swaying, y (lateral) | $K_{h,y} = \left[\frac{2Gl}{2-\nu}\left(2 + 2.5x^{0.85}\right)\right]$ | $K_{h,y}^* = \frac{K_{h,y}}{2l} = \frac{2G}{2-\nu}$ | $k_{h,y} = k_{h,y}\left(\frac{l}{b}, a_0\right)$ is plotted in Graph b | $C_{h,y} = \left(\rho V_{La} A_b\right) \cdot \tilde{c}_{h,y}$ $\tilde{c}_{h,y} = \tilde{c}_{h,y}\left(\frac{l}{b}; a_0\right)$ is plotted in Graph d |
| Swaying, x (longitudinal) | $K_{h,x} = K_{h,y} - \frac{0.2}{0.75-\nu} Gl\left[\left(1 - \frac{b}{l}\right)\right]$ | – | $k_{h,x} \cong 1$ | $C_{h,x} \cong \rho V_S A_b$ |
| Rocking, around x | $K_{rx} = \frac{G}{(1-\nu)} \mathcal{J}_{bx}^{0.75} \left(\frac{l}{b}\right)^{0.25} \left(2.4 + 0.5\frac{b}{l}\right)$ | $K_{rx}^* = \frac{K_{rx}}{2l} = \frac{\pi G b^2}{2(1-\nu)}$ | $k_{rx} = 1 - 0.20a_0$ | $C_{rx} = \left(\rho V_{La} \mathcal{J}_{bx}\right) \cdot \tilde{c}_{rx}$ $\tilde{c}_{rx} = \tilde{c}_{rx}\left(\frac{l}{b}; a_0\right)$ is plotted in Graphs e and f |
| Rocking, around y | $K_{ry} = \frac{G}{(1-\nu)} \mathcal{J}_{by}^{0.75} \left[3\left(\frac{l}{b}\right)^{0.15}\right]$ | – | $\begin{cases} k_{ry} \cong 1 - 0.30a_0, \\ \nu < 0.45 \end{cases}$ $\begin{cases} k_{ry} \cong 1 - 0.25a_0\left(\frac{l}{b}\right)^{0.3}, \\ \nu \cong 0.50 \end{cases}$ | $C_{ry} = \left(\rho V_{La} \mathcal{J}_{by}\right) \cdot \tilde{c}_{ry}$ $\tilde{c}_{ry} = \tilde{c}_{ry}\left(\frac{l}{b}; a_0\right)$ is plotted in Graph g |

* for the strip footing case is equivalent to a rectangular with $l/b = 20$

\+ $a_0 = \omega b / V_S$

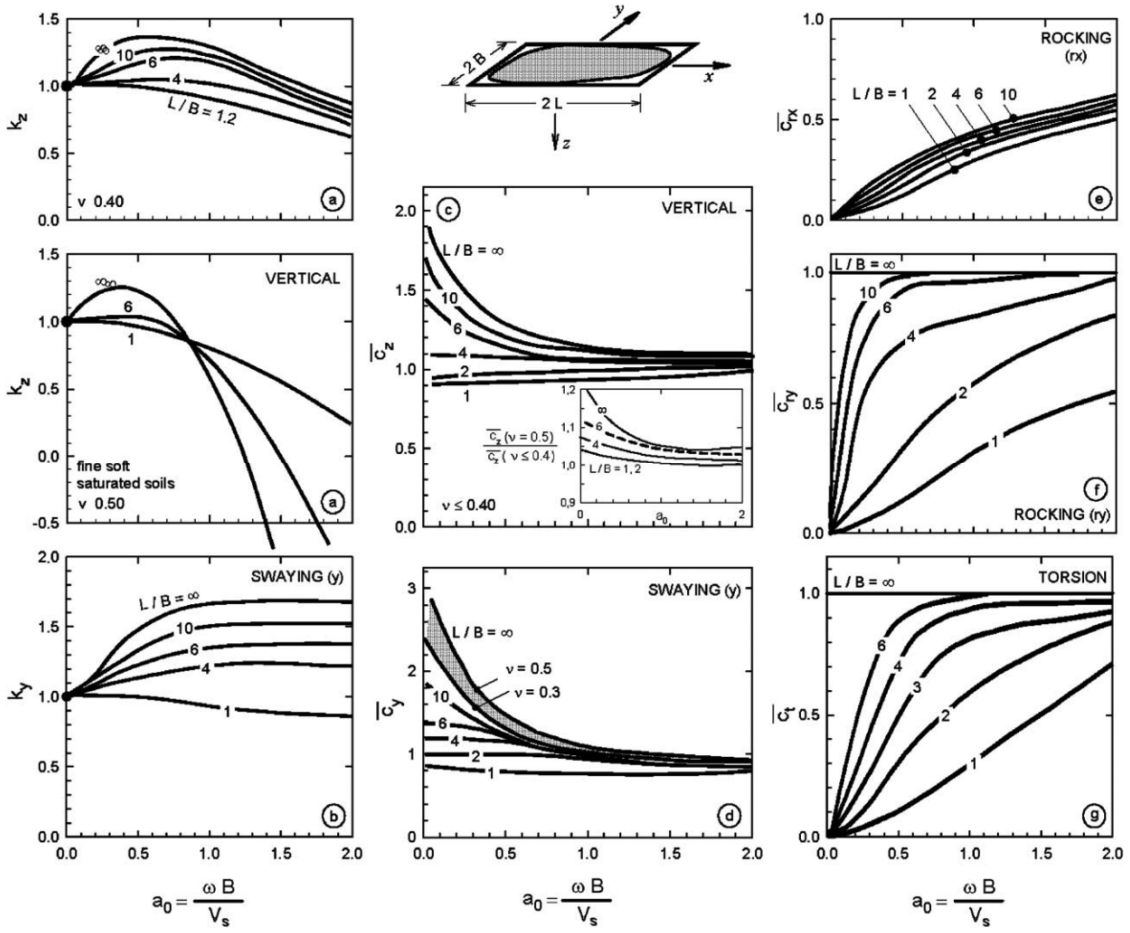


**Figure 2.4** Graphs accompanying Table 2.1 for the dynamic stiffness and radiation dashpot coefficients (Gazetas, 1991; reprinted in Mylonakis *et al.*, 2006).

For the type of structural systems examined in this study (e.g. shear walls and bridge piers) the dimensionless frequency factor ranges over values less than 0.5. As derived from the graphs of Fig. 2.4, for such low levels of $a_0$, the response is marginally affected by the dynamic stiffnesses coefficients ($k_a \cong 1$, $a = h, v, r$). Static stiffnesses coefficients such those presented in Table 2.1 may be adequate to represent the stiffness of the elastic supporting medium. In addition, rocking vibration (and consequently the overall response of a slender structure) in the lateral (weak) direction is practically undamped as $c_r \cong 0$. Significant damping is predicted for the translational modes of response when $a_0 < 0.5$, and particularly for strip footings.

### 2.2.1 Simplified procedures

As described above, within the limits of a linear formulation, the SSI effects can be considered as a superposition of the kinematic and the inertial components. For simplicity, in case of a shallow foundation the kinematic component can be neglected without loss of accuracy. The effect of the inertial soil-structure interaction on the dynamic response of the structure may be summarised in an increase in the natural period and a change (usually an increase) of the effective damping of the fixed-base system. The increase in the natural period, $T_0 = 2\pi\sqrt{m/k}$ , of the fixed-base system is attributed to soil flexibility under swaying and rocking motion and can be quantified according to Dunkerley's rule (Dunkerley, 1894; Jeffcott, 1918):

$$\tilde{T} = \sqrt{T_0^2 + T_h^2 + T_m^2} \qquad [2.8]$$

in which, $T_h = 2\pi\sqrt{m/K_h}$ and $T_m = 2\pi\sqrt{J_{cb}/K_m}$ are respectively the natural period in the *swaying* and *rocking* mode whereas $K_h$ and $K_m$ are the static stiffnesses of the foundation in these modes. The mass moment of inertia $J_{cb}$ is calculated with reference to the midpoint of the foundation baseline. In addition the change of the effective damping can be evaluated approximately, through the following expression:

$$\tilde{\xi} = \xi_i + \frac{\xi_0}{\left(\tilde{T}/T_0\right)^3} \qquad [2.9a]$$

in which, $\xi_0$ is the effective damping ratio of the fixed-based system and $\xi_i$ is the damping ratio of the foundation associated to radiation damping within soil medium (frequency dependent). Wolf (1985) proposed an alternative way for evaluating effective damping directly from $\xi_h$, $\xi_m$, namely the foundation damping components in the swaying and rocking mode respectively:

$$\tilde{\xi} = \frac{T_0^2\,\xi_0 + T_h^2\,\xi_h + T_m^2\,\xi_m}{\tilde{T}^2} \qquad [2.9b]$$

A 1-dof, fixed-base system with equivalent lumped parameters from Eqs 2.8 and 2.9 can be utilised instead of the actual coupled system to assess the effects of SSI through a simplified response spectrum analysis. In so doing, response spectra of the equivalent fixed-base system in terms of the normalised shear force are computed for different values of the *relative flexibility parameter*, $\phi_0 = h/V_s\,T_0$, in the graphs of Fig. 2.5 (dotted lines), as derived by Veletsos and Meek (1974). In the same graphs the shear force of the 3-dof, compliant-base system is also plotted for comparison (solid lines).

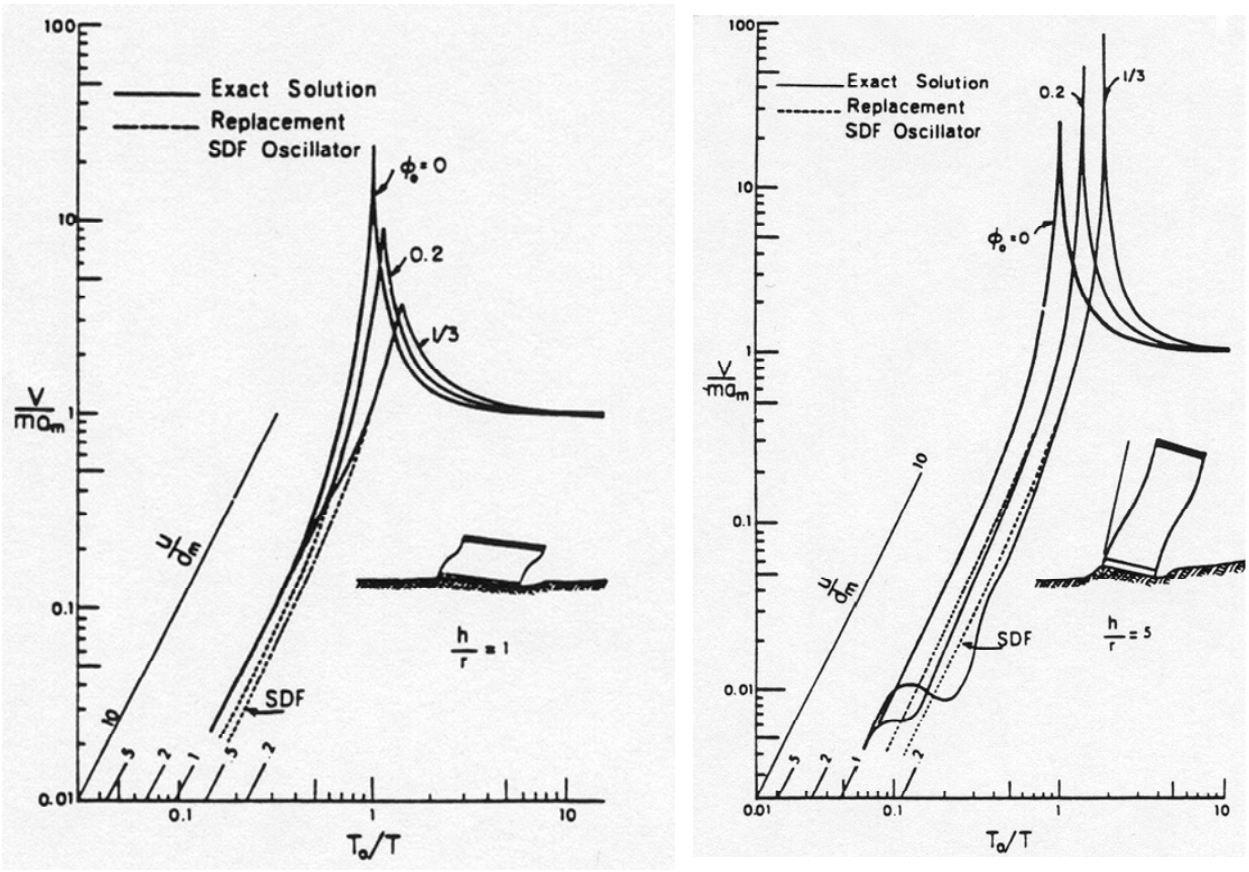


**Figure 2.5** Response spectra of the normalised shear force computed with the illustrated structural system on compliant soil (solid lines) and the equivalent 1-dof fixed-base system (Veletsos and Meek, 1974, reprinted in FEMA 369 document, 2000).

The structural model proposed by Veletsos and Meek (1974) to address the SSI effects, comprises two masses at the deck and the foundation mat. When the foundation is relatively small compared to the

mass of the superstructure, a one-storey structure with a mass $m$ at height $h$ and mass moment of inertia $J_{cb} = J_{cm} + mh^2$ can be employed. In this case Eq. 2.8 becomes:

$$T = 2\pi \sqrt{\frac{m}{k} + \frac{J_{cm} + mh^2}{K_m} + \frac{m}{K_h}} \qquad [2.10a]$$

and for a concentrated mass $m_c$ at point C ($J_{cm} = 0$):

$$T = 2\pi \sqrt{\frac{m}{k} + \frac{mh^2}{K_m} + \frac{m}{K_h}} \qquad [2.10b]$$

This simplified, one-storey coupled system as illustrated in Fig. 2.6, will be employed in this study to examine the nonlinear features of SSI.

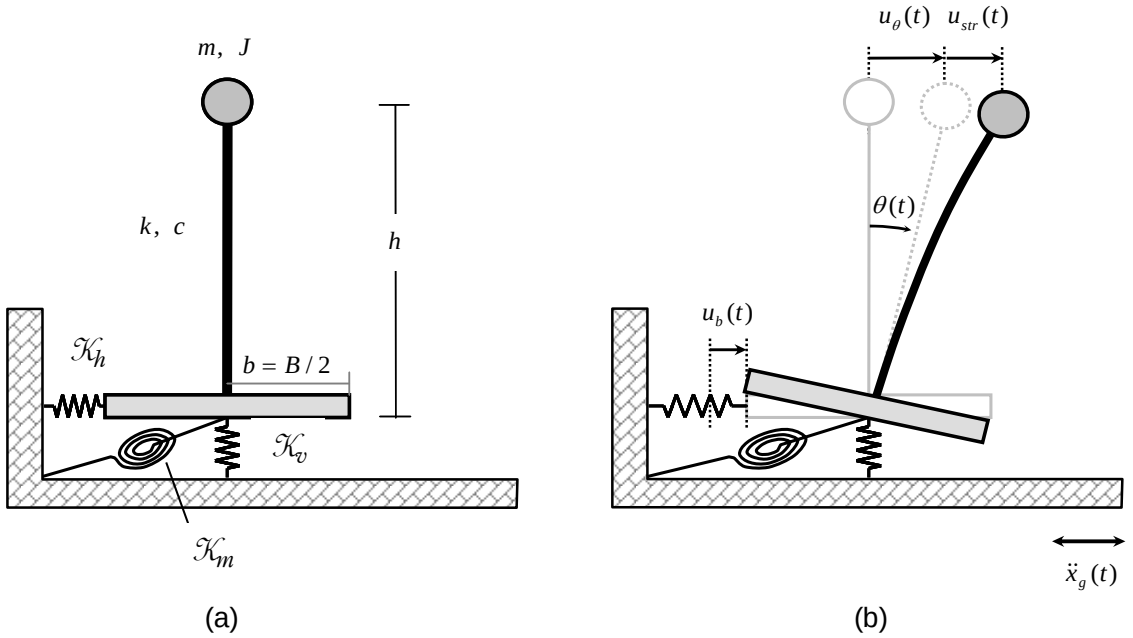


**Figure 2.6** Kinematics of the simplified one-storey coupled system; (a) at rest, (b) displaced due to a base acceleration $\ddot{x}_g(t)$.

### *Interplay of structural and soil compliance*

Quite often, swaying vibration is not a key parameter in inertial interaction due to the large lateral stiffness of the soil–foundation system especially for embedded foundations. Soil compliance in the

rocking mode however, may affect significantly the dynamic response. This is more evident in slender systems imposing large overturning moments to the foundation. In addition, for slender but quite flexible structures, inertia loading results to flexural vibrations of the superstructure with marginal rocking motion. Consequently, it is of great importance to predict the predominant mode of response when designing for slender structural systems. An interesting way to outline the interplay between structural and soil flexibility on the dynamic response is through the pattern of a bridge pier. It is a typical example of highway bridge piers constructed in Greece, however the pile-foundation which is usually adopted in design practice has been substituted by a rectangular spread footing of 9 m in width. A vertical load of 1000 t representing the deck mass is applied at 11 m above the ground surface (slenderness ratio $11/4.5 = 2.44$). As depicted in Fig. 2.6, the total horizontal displacement of the lumped mass is the sum of the horizontal components of the three vibration modes: the horizontal and rocking oscillation of the footing (swaying and rocking respectively), and the relative displacement of the mass centre to the pier base, due to flexural deformations of the pier (story drift):

$$u = u_b + u_\theta + u_{str} \qquad [2.11]$$

Within the context of a linear SSI approach, the rotation pole is constantly located at the footing midpoint, hence $u_\theta = h\theta$. A quantitative estimate of the participation of rocking on the overall response of the bridge pier can be given by the following period ratio as derived by Dunkerley's formula:

$$\frac{T_m}{T} = \left( \sqrt{1 + \frac{K_m}{h^2 k} + \frac{K_m}{h^2 K_h}} \right)^{-1} \qquad [2.12]$$

The rocking period ratio of the employed bridge pier is calculated with Eq. 2.12 and presented in Table 2.2 for different types of the pier cross section. Accordingly, the period in each independent mode of response can also be calculated with Eq. 2.8. Both soft and stiff soil conditions are considered (soil Young modulus of 20 MPa and 100 MPa respectively) to elucidate the effect of the flexural

rigidity on the fundamental natural period of the structure. While the diameter of $d_p = 2$ m seems to be a lower bound in the design practice of bridge piers, for the sake of analysis even lower values $d_p$ are implemented. Moreover, the rocking period ratio is plotted in the graphs of Fig 2.7 as a function of the slenderness for three different pier sections: (a) a cyclic section of diameter $d_p = 2$ m, (b) a cyclic section of diameter $d_p = 3$ m, and (c) a rectangular section of width $d_p = 1$ m in the longitudinal direction, and $d_p = 2b$ in the transverse (rocking) direction.

**Table 2.2** The period of the structural system calculated for two different soil conditions.

| Pier section | $d_p$ (m) | $T_m$ (sec) | $T_h$ (sec) | $T_o$ (sec) | T (sec) |
|---|---|---|---|---|---|
| | | $E_{soil}$ = 20 MPa | | | |
| Cyclic | 1 | 1.17 | 0.47 | 3.46 | 3.68 |
| Cyclic | 1.5 | 1.17 | 0.47 | 1.53 | 1.98 |
| Cyclic | 2 | 1.17 | 0.47 | 0.86 | 1.53 |
| Cyclic | 3 | 1.17 | 0.47 | 0.38 | 1.32 |
| Rectangular | 10 | 1.17 | 0.47 | 0.10 | 1.26 |
| | | $E_{soil}$ = 100 MPa | | | |
| Cyclic | 1 | 0.51 | 0.21 | 3.46 | 3.50 |
| Cyclic | 1.5 | 0.51 | 0.21 | 1.53 | 1.63 |
| Cyclic | 2 | 0.51 | 0.21 | 0.86 | 1.02 |
| Cyclic | 3 | 0.51 | 0.21 | 0.38 | 0.67 |
| Rectangular | 10 | 0.51 | 0.21 | 0.10 | 0.56 |

In the limiting case of $d_p = 1$ m the flexural mode apparently accompanied with large displacement demands, dominates the response. On the other hand, in the structural system with a rectangular pier section, rocking is the predominant mode of response even for relatively low values of slenderness ratio and regardless soil conditions. Similar behaviour is expected for the stiff cyclic pier section of $d_p = 3$ m with an exception of a very slender structure on stiff soil. A more complicated response is revealed for the 2 m width pier due to its increased flexibility. Hence, depending on its slenderness and soil deformability, the structural system can respond either as a rocking or as a flexural oscillator.

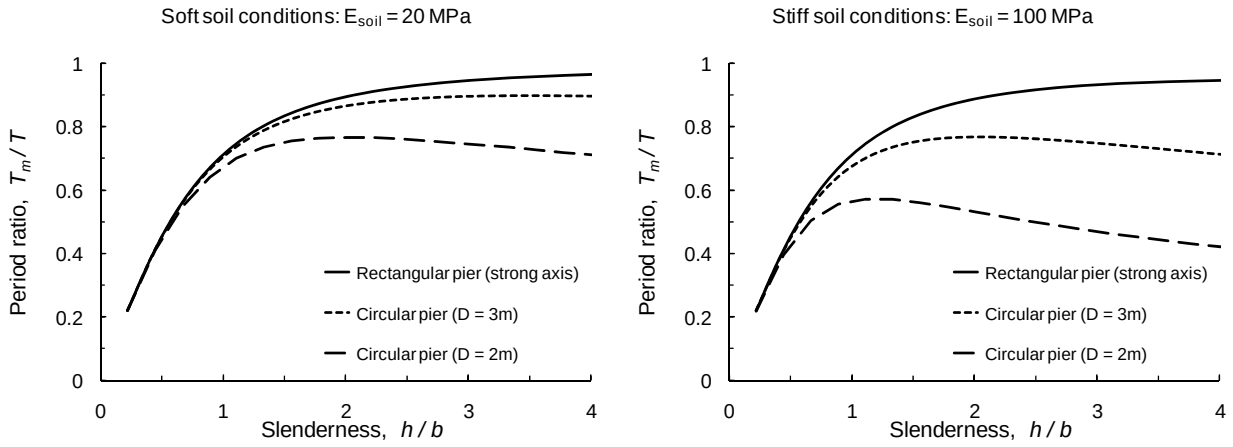


**Figure 2.7** The ratio of the rocking period to the effective period of the system as a function of the slenderness of the structure.

## 2.3 NONLINEAR LINEAR SOIL–STRUCTURE INTERACTION

Decomposition of the SSI problem into the afore-described tasks (site response analysis, kinematic interaction, inertial interaction) is a convenient tool for calculating the dynamic response of the structural system. Nevertheless, it does not necessarily entail that these steps must be performed separately. The advent of powerful computational machines nowadays, makes feasible a one-step numerical analysis of SSI (e.g. through the finite element method). Such a rigorous, time-domain analysis however, should also incorporate complex three- dimensional geometry, a detailed representation of soil profile, and most importantly sophisticated nonlinear algorithms to describe inelastic soil behaviour (*material nonlinearity*). The latter together with nonlinearities arising from large structural displacements (*geometrical nonlinearities*) comprise the nonlinear SSI effects.

### 2.3.1 Material nonlinearity

Soil response under large deformations is generally nonlinear, hysteretic and irreversible. Such a nonlinear behaviour is more pronounced in the *near field* (i.e. the soil medium in the vicinity of the structural foundation) where considerable concentration of stresses transmitted by the structural

system may take place. On the other hand, a *far field* domain may also be determined at a sufficient distance from the foundation where inelastic soil action is only governed by the seismic waves propagation (Pecker and Pender, 2000). Nonlinear, inelastic behaviour of soil and the structural elements is usually addressed in the SSI literature as *material nonlinearities*.

In early SSI studies only a little work had been done to incorporate soil nonlinearities. In the pioneering work of Idriss and Seed (1968) nonlinear soil behaviour was approached by the *equivalent linear method* (ELM). According to this iterative procedure, soil visco-elastic characteristics (i.e. shear stiffness and damping ratio) are modified after each iteration of a linear, wave propagation analysis until they reach values which are consistent with the calculated strains. The equivalent linear method is a valid engineering approximation for calculating moderately nonlinear soil response induced by the propagating seismic waves in the free field. It does not however address the need for predicting inelastic soil strains developed in the near field primarily due to foundation vibration. These additional plastic strains may be very significant in particular for slender structural systems which can generate large overturning moments even under moderate ground shaking.

Considerable attention has been given since the late 1960's to the development of constitutive models to describe nonlinear soil characteristics. Among the numerous soil models developed, elasto- (visco)-plastic models appear to be most promising. It may be argued that plastic models based on isotropic plastic hardening rules are adequate for situations in which only loading (and moderately unloading) occurs, however it is unlikely that such restrictions can be met at every point in general boundary value problems. In order to account for hysteretic effects, more elaborate plastic models based on a combination of isotropic (Hill, 1950) and kinematic (Prager, 1959) plastic hardening rules have been proposed. An important theoretical development in plasticity has been made simultaneously by Mroz, 1967 and Iwan, 1967. They showed how continuous yielding could be represented by a set of nested yield surfaces in stress space. The notion, in combination with kinematic and isotropic hardening/softening plastic rules, can give rise to a material representation of considerable power and flexibility. The concept has been adopted and enlarged by Prevost (1977, 1978 and 1985) and Mroz

(1980). Both theories suffer inherent limitations namely storage requirements for the multi-surface theory, *a priori* selection of an evolution law and arbitrariness in the mapping rule for the bounding surface theory.

### 2.3.2 Geometric nonlinearity

In terms of a rigorous SSI analysis procedure geometric nonlinearity can be generated either at the structural centre of mass when undergoing a large lateral movement $\left(P-\delta \text{ effect}\right)$ or at the soil-foundation interface. Geometrically nonlinear behaviour of the foundation may arise when a large horizontal force (sliding) or overturning moment (uplift) is applied. The latter case is associated with loss of contact (partial or total) between the structural foundation and the supporting soil because of the inability of soil to sustain tensile stress. Uplift onset results to a soil-foundation interface of transient geometry and imposes the moment-rotation relationship to a softening behaviour even under elastic soil conditions.

For structure with a shallow foundation on a horizontally vibrating soil two states of response can be distinguished: (a) the *full-contact* phase and (b) the *uplifting* phase. In the former case the structure whether remains at rest (rigid superstructure) or exhibits flexural oscillations (deformable superstructure). The transition from the full-contact to the uplifting case is determined by an uplifting criterion. For rigid soil conditions uplifting occurs when the overturning moment reaches the ultimate moment capacity of the foundation.

The important effects of foundation uplift on the dynamic response of structures have been demonstrated in early analytical and experimental studies of the simplified 'rigid soil' model (Meek, 1975; Huckelbridge and Clough, 1978; Chopra and Yim, 1985). It has been found that uplifting modifies the dynamics of the structure in a way qualitatively similar with the sliding isolation which cuts-off accelerations larger than a critical value. Later studies incorporated soil compliance and material nonlinearities to extract similar conclusions for the uplifting response (Yim and Chopra,

1984; Crémer *et al.*, 2002; Gazetas and Apostolou, 2004; Gajan and Kutter, 2008; Anastasopoulos *et al.*, 2008). But while sliding systems survive strong seismic forces with (large) permanent displacements, for an uplifting structure the 'penalty' to pay is large rotations (permanent for soils of poor strength) and occasional overturning.

### 2.3.3 Recent developments in nonlinear SSI

Nonlinear numerical modelling of the entire soil-foundation-structure system through realistic representation of the exact geometry and sophisticated tools for inelastic soil behaviour has nowadays become a challenging task given the computational resources and capabilities available nowadays. However such a sophisticated numerical analysis (e.g. with the finite element method) requires also extensive discretisation of soil medium, which may not be feasible to perform in common geotechnical design practice.

An engineering approximation to efficiently evaluate the nonlinear effects of inertial interaction in the domain of large displacements can be obtained if the supporting medium is substructured into two subdomains (Pecker and Pender, 2000): (a) a *far field* domain which extends a sufficient distance from the foundation, in which soil nonlinearities only governed by the propagation of seismic waves, and (b) a *near field* domain, in the vicinity of foundation where both geometrical and material nonlinearities associated to SSI are important. The exact boundary between these two domains does not need to be precisely determined. The far field domain is approached by linear or equivalent linear impedance function in which only radiation damping (viscous type) is implemented. On the other hand, a *macroscopic* approach is adopted for the near field domain which is represented with a nonlinear *macro-element* of six degrees of freedom in the general case (three translational and three rotational). Damping now arises from inelastic soil behaviour underneath the foundation and obeys Masing's law. A schematic of the macroscopic modelling is illustrated in Fig. 2.8.

A dynamic macro-element based on this macroscopic consideration was developed by Cremer *et al.*, 2001 for shallow foundation on cohesive soil. Later studies on macro-element modelling have been presented by Gajan and Kutter, 2009; Chatzigogos *et al.*, 2009; Figini *et al.*, 2011. A detailed review of the available macro-element models in literature will be presented in Chapter 5.

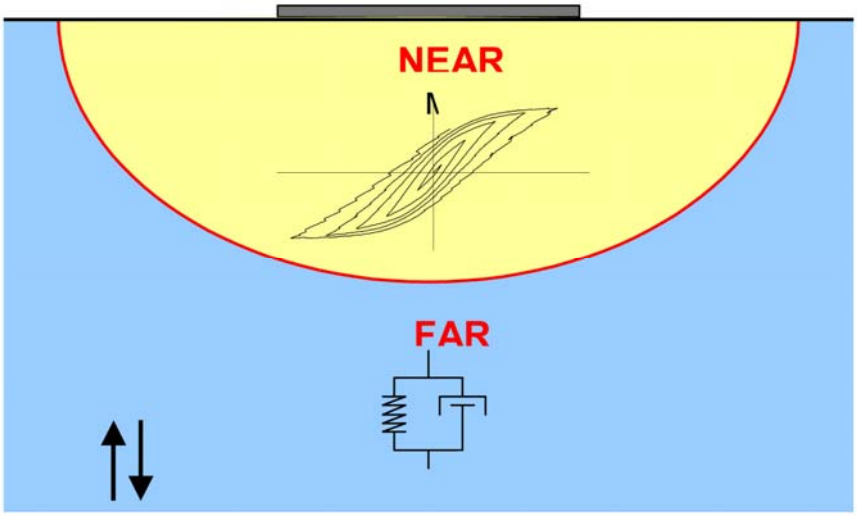


**Figure 2.8** Conceptual subdomains for dynamic soil-structure analyses (Pecker and Pender, 2000).

## 2.4 SEISMIC CODE PROVISIONS

According to almost every seismic building code, the structural response and consequently the foundation loads are computed considering fixed base conditions at the support and therefore neglecting soil-structure interaction. Inherent to this approach is the belief that the effect of SSI is always towards reducing seismic loads (Pecker and Pender, 2000). Admittedly, the increase in the damping ratio due to SSI explicitly reduces the seismic forces developed to the superstructure and the foundation. However, the most important effect of SSI which is the increase in the natural period of the structural system does not necessarily lead towards smaller spectral accelerations. Examples of detrimental effect of the increased natural period in cases of unusually soft soil profiles have been recently demonstrated in literature (e.g. Gazetas and Mylonakis, 1998).

The ambiguous role of SSI has been recognised in some modern codes. According to Eurocode 8 (prEN 1998-5:1999) provisions, 'the effects of dynamic soil-structure interaction shall be taken into account in the case of: (a) structures where $P-\delta$ effects play a significant role; (b) structures with massive or deep seated foundations; (c) slender tall structures; (d) structures supported on very soft soils, with average shear velocity less than 100 m/s'.

Although not widely used in practice, engineering guidelines exist in the United States for simple characterisation of SSI effects.

One set of guidelines is intended for use with force-based characterisation of seismic design, as is commonly used for new building construction. These procedures were introduced by the *Applied Technology Council* document (ATC-3-06, 1978, 1984) and an updated version has recently been published in the *NEHRP Recommended Provisions for Seismic Regulations for New Buildings and Other Structures* (BSSC, 2004). According to these procedures the fixed-base building period and damping ratio are modified to account for the effects of foundation compliance. The derived *flexible-base* vibration properties are used with the site design response spectrum to obtain the base shear for seismic design. The foundation-soil characterisation inherent to these procedures consists of foundation springs for translational and rotational degrees of freedom that depend on a strain-compatible soil shear modulus. The soil behaviour is modelled as visco-elastic with no limiting shear stress.

The second set of guidelines is intended for use with nonlinear static methods for structural performance assessment, as commonly used for building retrofit design (ATC-40, 1994; BSSC, 1997). In this approach, the structural performance is characterised by a nonlinear static pushover curve. The shape of the pushover curve, as well as the distribution of member shears and moments, can be sensitive to foundation modelling. Accordingly, the afore mentioned documents provide recommendations for modelling the soil-foundation system as elastic-perfectly-plastic elements positioned at each footing. The elastic portion is based on the real part of well-known impedance

functions for foundation lateral translation, vertical translation, and rocking. The plastic portion of the foundation springs is based on limiting soil pressures associated with bearing capacity failure (in the vertical direction) and sliding/passive failure (in the lateral direction). It has to be made clear however, that these procedures are intended for relatively simply calculations of base shear or pushover curves, and are not immediately amenable for use in the relatively sophisticated nonlinear response history analyses that are becoming increasingly common for major projects. In addition, while the afore-discussed procedures implicitly account for soil nonlinearity through the use of an equivalent-linear shear modulus, such springs inadequately represent the nonlinear response of foundations, which may include relatively complex gapping and energy-dissipation mechanisms. Accordingly, there is a recognised need in common geotechnical practice for the development of relatively sophisticated engineering tools for characterising the nonlinear, time-dependent behaviour of the foundation-soil interface.

*Chapter 3:*

# Dynamics of rocking structures on rigid soil; an introduction to geometric nonlinearity

## 3.1 INTRODUCTION

The most vivid illustration of geometrically nonlinear rocking behaviour stems from the paradigm of a slender structure on rigid (undeformable) soil. For the analysis purposes of such a system two different states of response can be distinguished: (a) the *full-contact* phase and (b) the *uplift* phase. In the full-contact (linear) phase the structure remains at a relative rest (rigid body) or undergoes flexural oscillations (deformable body). On the other hand, in the uplifting (nonlinear) phase solely rocking with total uplift may take place with the edges of the foundation being alternately the pivot points. Uplifting and correspondingly geometrically nonlinear behaviour is initiated when the overturning moment reaches the gravitational moment which is equivalent to the ultimate moment capacity of the foundation. From this point on the moment-rotation relationship follows a declining branch due to the gradually amplifying $P-\delta$ effects. This reduction of the foundation moment is totally reversible though, when the direction of rotation changes. Rocking vibration on rigid soil is damped as a part of the mechanical energy dissipates during each impact. Consequently, after transient motion has expired, the rocking body eventually settles back at its initial position due to gravity. Clearly, the only likely failure mode of such a structural system is overturning about a corner point. The more slender the structure the more vulnerable to toppling is. While nonlinear dynamic features of rocking on rigid soil are investigated in depth in this Chapter, overturning response will be discussed separately in Chapter 7.

Two simplified structural systems on rigid soil undergoing rocking motion are involved in this Chapter:

- a rigid *block-type* structure, and
- a rigid or flexible *one-storey* structure with a foundation mat

The driving equations of motion of both systems are extracted using a large-displacement approach. To this end, in the case of a flexible oscillator a Lagrange formulation is adopted. The dynamic response is then calculated by a direct (explicit) integration of the equations of motion during each time increment. A fundamental parametric study of the uplifting response is presented next, in terms of the flexural and rocking displacements.

## 3.2 ROCKING of a RIGID STRUCTURE

### 3.2.1 Statement of the problem – Equations of motion

Consider a rigid rectangular block simply supported on rigid soil which is subjected to horizontal shaking. The coefficient of friction is adequately large so that sliding is prevented. For small levels of the ground acceleration $a_g = a_g(t)$ (in units of $g$) the moment of the inertia force with reference to the foundation midpoint ($ma_g h$) does not exceed the restoring, gravitational moment ($mgb$). In this way, the block remains attached to, and follows the oscillation of the ground. As soon as the ultimate moment $mgb$ is reached, uplifting initiates setting the block on rocking motion. The system configuration together with the acting forces and moments are illustrated in Fig. 3.1.

George Housner (1963) first investigated in depth the rocking behaviour of block-type structures on rigid soil subjected to earthquake shaking. Using an energy approach he uncovered the role of the excitation frequency and of the block size on the overturning potential. Ishiyama (1982) determined the possible modes of response for a rigid body on rigid floor and established transition criteria from

one to another. Makris and his co-workers (1998, 1999) focused on the transient rocking response of rigid blocks under near-source ground shaking idealised as trigonometric pulses, and derived the acceleration amplitude needed for overturning.

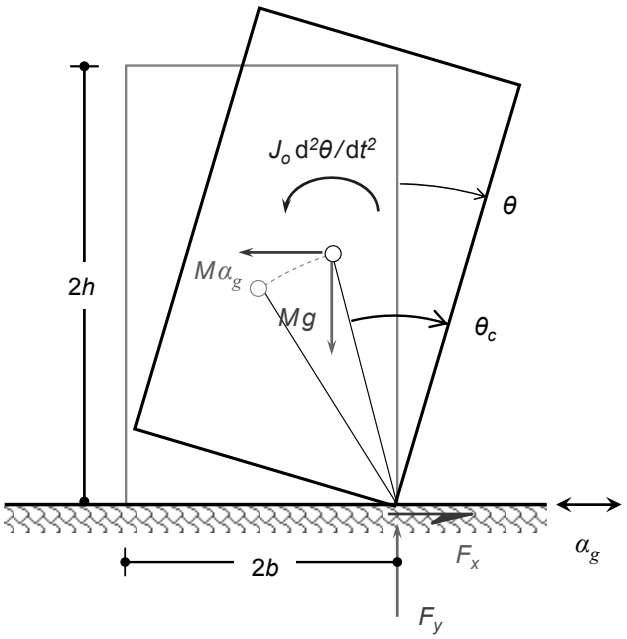


**Figure 3.1** The rocking block on a rigid oscillating base: configuration of the system and acting forces and moments.

Under pseudo-static conditions, once uplifting is initiated about the corner point, the body will unavoidably overturn. In other words, the critical acceleration for uplifting is identical to the minimum required to *statically* overturn the block. It is given by the so called *West formula* (Milne and Omori, 1893); in units of $g$:

$$a_{over,st} \equiv a_c = \frac{b}{h} \qquad [3.1]$$

On the contrary, under dynamic base excitation reaching $a_c$ simply initiates rocking motion. In this case $a_c$ is the maximum acceleration that can be developed at the mass centre of the block. The moment of the foundation is therefore bounded by $a_c$ to an ultimate value of $ma_ch = Nb$ where $N = mg$ is the central, vertical (gravitational) load. This peak value is reached instantaneously as soon as uplift initiates $(\theta = 0)$ and from then on the moment is gradually decreasing due to $P-\delta$ effects.

Finally, the moment reduces to zero at a rotational angle of $\theta = \theta_c$ where $\tan\theta_c = b/h$ is the aspect ratio (or the half width/half height ratio). The moment-rotation response of the foundation from the uplift onset to overturning is portrayed in Fig. 3.2.

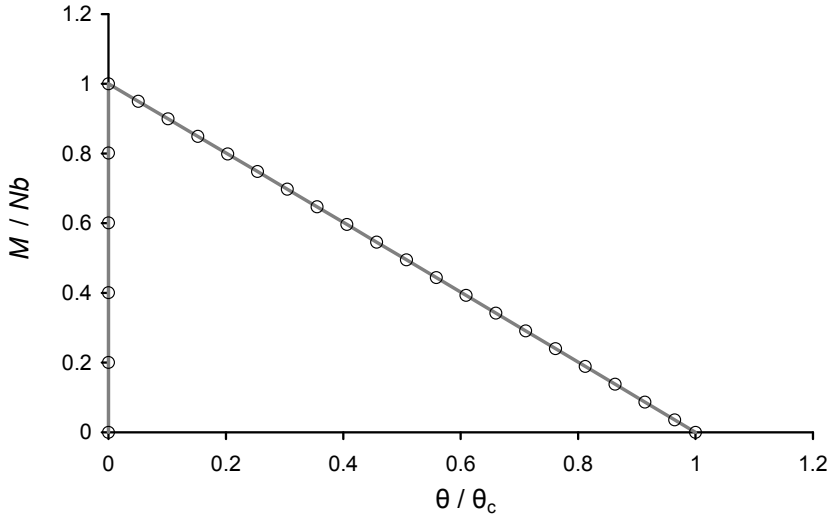


**Figure 3.2** Moment–rotation relationship of the rocking block.

The dynamic response is determined by the rocking equation of motion:

$$\ddot{\theta}(t) = -p^2 \left\{ \sin\left[\theta_c \,\mathrm{sgn}\,\theta(t) - \theta(t)\right] + a_g(t) \cos\left[\theta_c \,\mathrm{sgn}\,\theta(t) - \theta(t)\right] \right\} \qquad [3.2]$$

where: $\theta(t) < 0$ (or $> 0$) denotes the angle of rotation about O (or, respectively, about O'); $\theta_c = \arctan(b/h)$ is the angle shown in Fig. 3.1; and $p = \sqrt{mgR/J_o}$ is a characteristic *frequency parameter* of the block; $R$ is half the diagonal of the block. The frequency parameter is a measure of the block size in a sense that large values of $p$ correspond to relatively small structures and vice versa. For a solid rectangular block the moment of inertia about its pivot point is $J_o = (4/3)\,mR^2$ and therefore $p = \sqrt{3g/4R}$. The vertical component of base acceleration is neglected, as its effect has been found to be negligible on rocking. It is clear that whether the block will safely undergo rocking or eventually overturn depends on its size and slenderness as well as on the nature and intensity of ground shaking. The conditions for dynamic overturning of a rigid block are discussed in detail in

Chapter 7. The effects of the vertical acceleration of the base on the overturning response will be also discussed in that chapter.

When a rigid body is rocking back and forth about its pivot points, it impacts the ground and loses a part of its kinetic energy, even after a purely elastic impact. Its angular velocity right after the impact (at time $t_i^+$) is a fraction of that just prior to impact (at time $t_i^-$):

$$\dot{\theta}^2(t_i^+) = r\,\dot{\theta}^2(t_i^-) \qquad [3.3]$$

where $r$ is known in the literature as *the coefficient of restitution.* An upper bound of $r$ can be obtained by applying conservation of the angular momentum with respect to the pivot point (Housner, 1963; Makris & Black, 2001):

$$r = \left(1 - \frac{2mR^2}{J_o}\sin^2\theta_c\right)^2 \qquad [3.4a]$$

or for a rectangular block,

$$r = \left(1 - \frac{3}{2}\sin^2\theta_c\right)^2 \qquad [3.4b]$$

From this relationship it is shown that the coefficient of restitution is dependent only upon the slenderness of the structure. For example, for a five-story building with an angle $\theta_c = 0.4$ rad it is $r = 0.60$. In general lines slender bodies tend to preserve their angular velocity after impact whereas others with a lower mass centre undergo a more 'dissipative' impact. In the limiting case where $\theta_c \to 0.95\,\text{rad}\,(54^0)$, the coefficient of restitution reduces down to zero even under elastic impact condition. A sophisticated impact model has been recently presented based on Dirac-delta type forces (Prieto *et al.*, 2004). It results into a smooth (exponential) reduction of the velocity during impact, however such an in-depth analysis of impact mechanism is beyond the scope of this study.

Typical theoretical values of $r$ are presented in Table 3.1.

**Table 3.1** Dynamic parameters for typical rocking systems.

| Rocking system | Slenderness angle, $\theta_c$: degrees | Half-diagonal, $h$: m | Frequency parameter, $p$: rad/sec | Max. coefficient of restitution, $r_{max}$ |
|---|---|---|---|---|
| Precarious rocks | 20 - 30 | 0.5 – 1 | 3 – 4 | 0.4 – 0.7 |
| Tombstones | 9 | 0.6 | 3.4 | 0.93 |
| Electrical transformers | 22 | 2.5 | 1.7 | 0.62 |
| Five-story building | 25 - 30 | 8 - 10 | 0.8 – 1 | 0.4 – 0.55 |

These values have been calculated with Eq. 3.4 considering elastic impact conditions. In reality, some additional energy is lost, dependent on the nature of the materials at the impact surface. Experimental values of $r$ have been recently presented by Uematsu *et al.* (2000) from shaking table tests as shown in Table 3.2. In the same table, measured values of the static and kinematic coefficient of friction are also presented (Ishiyama *et al.*, 1982 and Uematsu *et al.*, 2000). In the analytical study of this chapter though, it is presumed that the static coefficient of friction is large enough to prevent sliding.

**Table 3.2** Experimental values of $r$ from shake-table tests (Ishiyama *et al.*, 1982 and Uematsu *et al.*, 2000).

| Base Surface | Specimen | Static coefficient of friction | Kinematic coefficient of friction | Coefficient of restitution |
|---|---|---|---|---|
| Concrete casing | wood (oak) | 0.29 | 0.44 | 0.52 |
| | wood (fir) | 0.30 | 0.11 | 0.49 |
| Carpet | wood (oak) | 0.35 | 0.45 | 0.49 |
| | wood (fir) | 0.45 | 0.35 | 0.49 |
| Vinyl resin | hard rubber | 0.96 | 0.47 | 0.86 |
| | plastic | 0.74 | 0.35 | 0.83 |
| | wood | 0.81 | 0.49 | 0.59 |
| Granite | hard rubber | 0.81 | 0.68 | 0.86 |
| | plastic | 0.44 | 0.54 | 0.90 |
| | wood | 0.35 | 0.40 | 0.53 |

The rocking response of a rigid block can be obtained at any time increment through numerical integration of Eqs. 3.2 and 3.3. For slender blocks subjected to harmonic excitation however, Eq. 3.2 can be reduced to the following piecewise linearised and dimensionless form:

$$\ddot{\Theta} - \Theta = -\mathcal{A}\cos(\Omega\tau + \Psi) - \operatorname{sgn}\Theta \qquad [3.5]$$

in which $\Theta = \theta / \theta_c$, $\mathcal{A} = a_g / a_c$, $\Omega = \omega_E / p$, $\tau = p\,t$, and $\Psi$ are respectively the dimensionless rotation, 'dynamic' amplification of the overturning acceleration, dimensionless frequency, time and phase shift. The double-dot superscript denotes differentiation with respect to 'stretched' time $\tau$. The closed-form solution of Eq. 3.5 has been derived by Spanos and Koh (1984):

$$\Theta^{+}(\tau) = \alpha^{+}\sinh\tau + \beta^{+}\cosh\tau + 1 + \gamma\cos(\Omega\tau + \Psi) \qquad \theta > 0 \qquad [3.6a]$$

$$\Theta^{-}(\tau) = \alpha^{-}\sinh\tau + \beta^{-}\cosh\tau - 1 + \gamma\cos(\Omega\tau + \Psi) \qquad \theta < 0 \qquad [3.6b]$$

where $\alpha^{+}$, $\alpha^{-}$, $\beta^{+}$, $\beta^{-}$ are integration constants and $\gamma = -\mathcal{A}/\left(1+\Omega^2\right)$.

Although Eq. 3.2 has been extracted from the dynamic (moment) equilibrium of a rectangular structure, it is also applicable to a rigid structure of any geometry. In this case, the half-diagonal $R$ refers to the distance of the mass centre to the pivot point. Also, $b$ and $h$ are respectively, the horizontal and vertical projection of the half-diagonal.

An interesting case of a rocking vibrator is a rigid one-storey structure with his mass concentrated at height $h$ (Apostolou and Gazetas, 2004). Neglecting the rotary inertia about the mass centre, the frequency parameter and the coefficient of restitution are respectively:

$$p = \sqrt{\frac{mgR}{mR^2}} = \sqrt{\frac{g}{R}} \qquad [3.7a]$$

$$r = \left(1 - \frac{2mR^2}{mR^2}\sin^2\theta_c\right)^2 = \left(1 - 2\sin^2\theta_c\right)^2 \qquad [3.7b]$$

Notably, in terms of the rocking response this single-d-o-f system is equivalent to a rectangular block of the same slenderness when $R_{sdof} = (4/3)R_{block}$ and $r_{c,sdof} = r_{c,block}$ (inelastic impact).

### 3.2.2 Free rocking vibrations

Unlike the simple pendulum case, the free-vibration response of a rocking structure (inverted pendulum) is nonlinear even at small amplitudes of rotation. The nonlinearities of the inverted pendulum are more pronounced as the rocking amplitude increases. Considering small displacements and slender structures the governing equation of motion (Eq. 3.5) reduces as follows $(\mathcal{A} = 0)$:

$$\ddot{\theta} - p^2\theta = -p^2 \operatorname{sgn}\theta\,\theta_c \qquad [3.9]$$

Although this simplified equation of motion is piecewise linear, the response preserves its nonlinear features. A general solution of Eq. 3.9 may be obtained as originally derived by Perry (1881):

$$\theta(t) = C_1 \cosh(pt) + C_2 \sinh(pt) + \operatorname{sgn}\theta\,\theta_c \qquad [3.10]$$

in which $C_1$ and $C_2$ are integration constants. This analytical solution of the free-vibration response may also be extracted by the general solution of the driven system (Eq. 3.6). For free vibrations induced by an initial rotation of $\theta_o$ $\left(\dot{\theta}_o = 0\right)$ the rocking rotation is

$$\theta(t) = \theta_c - (\theta_c - \theta_o)\cosh pt \qquad [3.11]$$

The latter analytical expression of rocking rotation was originally presented by Yasumi and Akao (1951) as a special case of Perry's general solution and revisited by Housner in 1963. The validity of this equation is however limited to the interval of time from the initial condition of rest to the first

impact. From this point and on integration constants $C_1$ and $C_2$ should be re-calculated after each impact taking into account the new initial conditions $\theta(t_i^+)=0$ and $\dot{\theta}(t_i^+)=\sqrt{r}\,\dot{\theta}(t_i^-)$. Time histories of the free-vibration rocking response of a slender rectangular block $\left(p=0.8 \text{ rad/sec},\ \tan\theta_c=0.2\right)$ due to initial rotation $\theta_o$ are computed with explicit integration of Eq. 3.2 and plotted in Fig. 3.3 for three levels of $\theta_o$ (solid lines): a *small* $\left(\theta_o=0.25\,\theta_c\right)$, a *moderate* $\left(\theta_o=0.5\,\theta_c\right)$, and a *strong near-failure* $\left(\theta_o=0.9\,\theta_c\right)$ level. The coefficient of restitution at each impact is calculated with Eq. 3.4 ('elastic' impact conditions are regarded). Clearly, the natural period is strongly dependent upon the amplitude of rotation in such a way that large amplitudes are associated with slow rocking at first. Then the amplitude decreases after each impact resulting in a gradually decreasing period which eventually approaches zero. In the same figure time histories calculated with the linear formulation (Eqs 3.10 and 3.11) are also plotted (dotted lines). For all levels of initial rotation, it yields that the linearised equation of motion can efficiently predict the nonlinear rocking response.

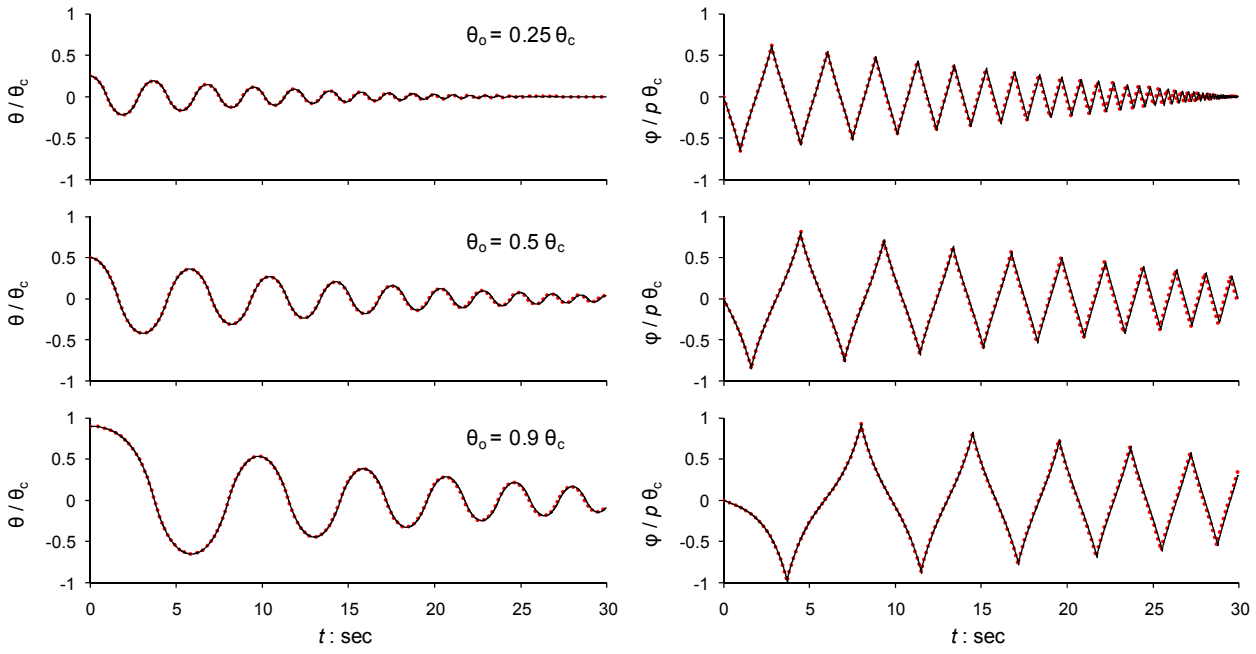


**Figure 3.3** Time histories of the normalised rocking rotation and velocity under free vibrations $\left(p=0.8 \text{ rad/sec},\ \tan\theta_c=0.2,\ r=0.889\right)$, due to initial rotation $\theta_o$: comparison of the nonlinear solution (solid lines) with the linearised solution (dotted lines) for three levels of $\theta_o$.

### *Natural period*

The required time for the block to move from the position of $\theta = \theta_o$ to $\theta = 0$ is equal to the quarter of the free-vibration period. Neglecting the energy dissipation at each impact, the period of motion during each cycle can be calculated from Eq. 3.11 as a hyperbolic function of the rocking amplitude $\theta_n$ (Yasumi and Akao, 1951; Housner, 1963):

$$T(\theta) = \frac{4\,\mathrm{acosh}\left(\dfrac{1}{1-\theta_n/\theta_c}\right)}{p} \qquad [3.12]$$

Due to the profoundly nonlinear behaviour of the inverted pendulum, for $\theta \to 0$ the free-vibration period does not approach a constant (linear) value $T_o$ but it continuously decreases and eventually reaches zero. On the other hand, for large amplitudes of rocking, the period of the rocking block increases in a way similar to the simple pendulum. In the limiting case of $\theta_n \to \theta_c$ it is derived that $T \to \infty$.

On the basis of a nonlinear formulation, the period of motion during free vibration is derived from the conservation of the total (kinetic and potential) energy at an angle $\theta$ and at $\theta_n$:

$$\frac{1}{2} J_o \dot{\theta}^2 + mgR\cos(\theta_c - \theta) = mgR\cos(\theta_c - \theta_n) \qquad [3.13]$$

which leads to

$$\dot{\theta} = \frac{\mathrm{d}\theta}{\mathrm{d}t} = p\sqrt{2\left[\cos(\theta_c - \theta_n) - \cos(\theta_c - \theta)\right]} \qquad [3.14]$$

By separating variables and integrating, we can finally express the period as a function of the rocking amplitude:

$$T(\theta_n) = \frac{2\sqrt{2}}{p} \int_0^{\theta_n} \frac{\mathrm{d}\theta}{\sqrt{\cos(\theta_c - \theta_n) - \cos(\theta_c - \theta)}} \qquad [3.15]$$

The *elliptic integral of the first kind* in Eq. 3.15 is calculated by its normal mode:

$$K(a) = \frac{\pi}{2} \sum_{m=0}^{\infty} \left[ \frac{(2m-1)!!}{(2m)!!} \right]^2 a^{2m} \qquad [3.16]$$

in which $a = a(\theta)$. The nonlinear calculation of the rocking period at the free-vibration regime is plotted in the graph of Fig. 3.4 together with the closed-form simplified solution. A perfect match between the linear and nonlinear solution is achieved, which confirms the efficiency of the linearised system in predicting the free-vibration response.

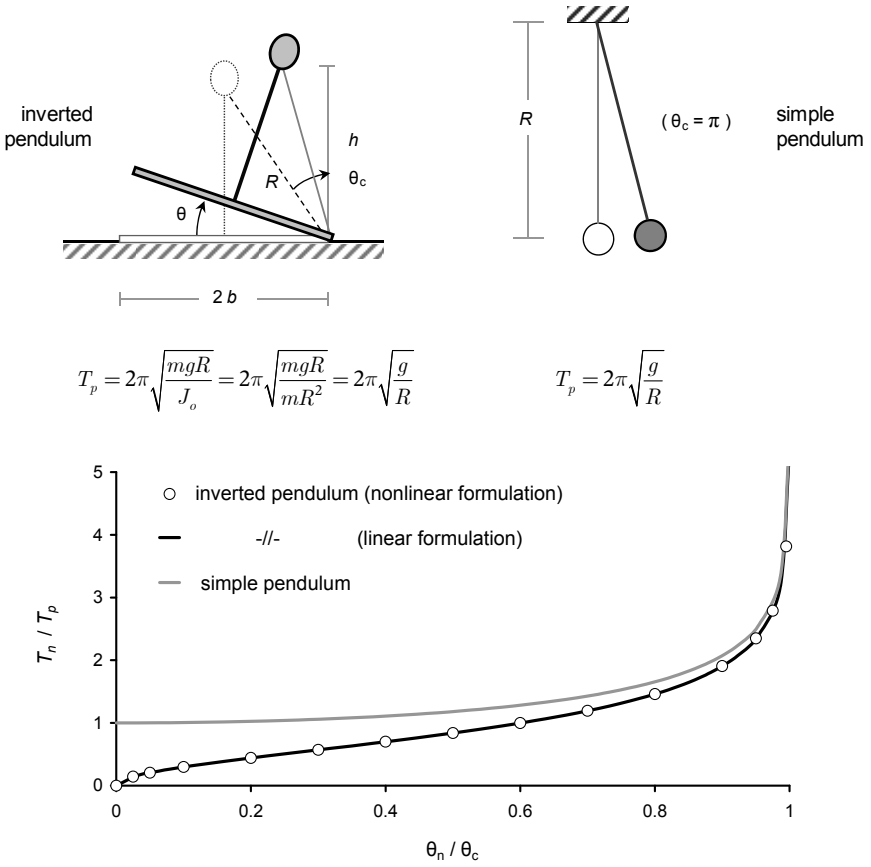


**Figure 3.4** Normalised free-vibration period of the inverted pendulum from linear and nonlinear formulation (white circles and black line respectively) and comparison to that of the simple pendulum (grey line).

### *Effective damping*

During free rocking vibrations energy dissipation of the system is associated exclusively with the energy loss at each impact. A relation between the peak rotation after the nth impact $\theta_n$ and the initial amplitude $\theta_o$ may be extracted analytically from the linear formulation (Housner, 1963):

$$\frac{\theta_n}{\theta_c} = 1 - \sqrt{1 - r^n \left[1 - \left(1 - \frac{\theta_o}{\theta_c}\right)^2\right]} \qquad [3.17]$$

In this study Housner assumed that rocking on a rigid base would be an effective means of dissipating energy. Priestley *et al.* (1978) motivated by the analytical expression for the amplitude reduction, utilised the *logarithmic decrement* of the rocking amplitude after $n$th impact to calculate an *equivalent viscous damping ratio* $\xi$ in a similar way with that of the lightly damped harmonic oscillator:

$$\xi = \frac{1}{n\pi} \ln\left(\frac{\theta_o}{\theta_n}\right) \qquad [3.18a]$$

And after substituting Eq. 3.17 into Eq. 3.18a

$$\xi = \frac{1}{n\pi} \ln\left\{\frac{\theta_o}{\theta_c} \frac{1}{1 - \sqrt{1 - r^n \left[1 - \left(1 - \theta_o / \theta_c\right)^2\right]}}\right\} \qquad [3.18b]$$

From the latter equation it is revealed that the energy dissipates more rapidly during large amplitude motion (see Fig. 3.5a). Makris and Konstantinidis (2003) suggested a simple expression to approximately obtain the equivalent viscous damping irrespective of the number of impacts or the initial rocking amplitude:

$$\xi \cong -0.34 \ln(r) \qquad [3.19]$$

According to the Federal Emergency Management Agency document *Prestandard and commentary for the seismic rehabilitation of buildings* (FEMA 356, 2000) an empirical expression for the damping ratio as a function of the coefficient of restitution is recommended:

$$\xi = 0.4\left(1-\sqrt{r}\right) \qquad [3.20]$$

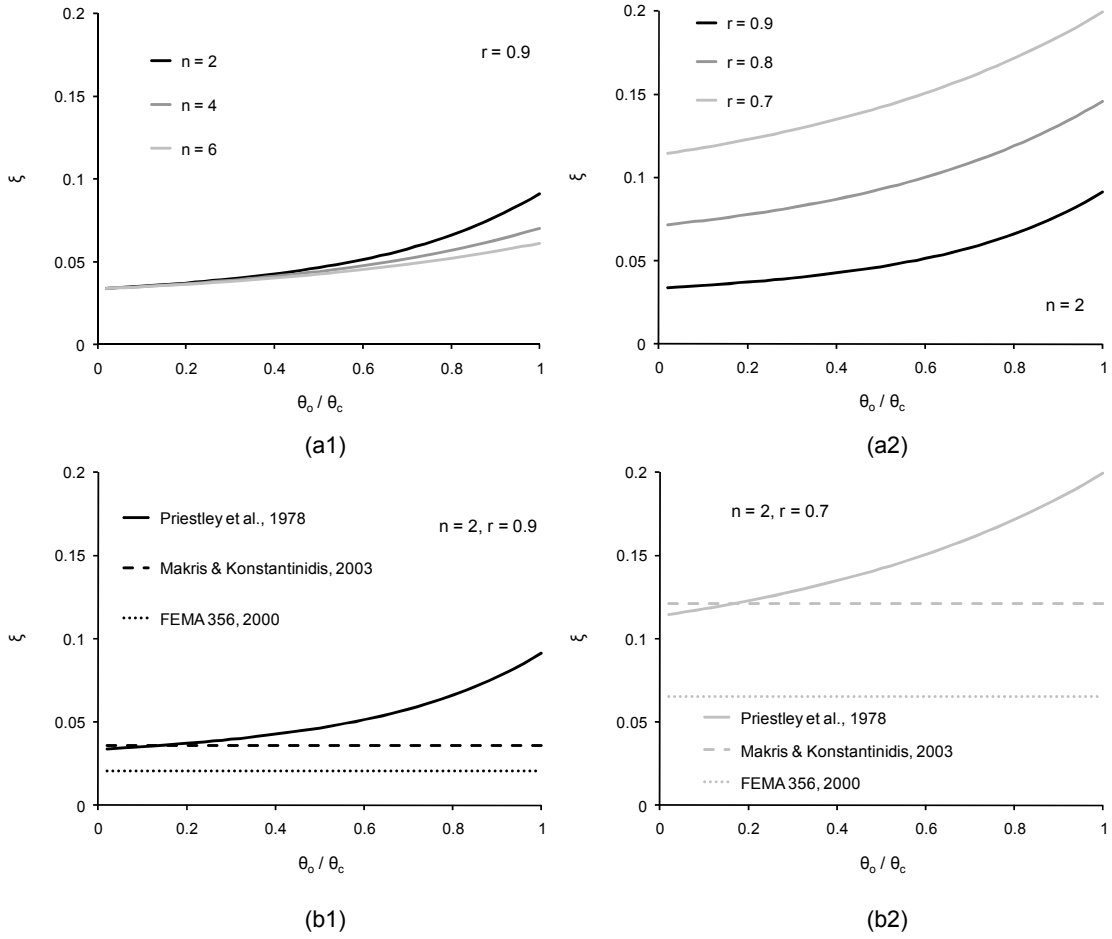


**Figure 3.5** The equivalent viscous damping ratio of the rocking block calculated from the Priestley *et al.* analogy as a function of the initial rocking amplitude for different impact numbers (a1) and for different values of the coefficient of restitution (a2). Comparison with the empirical formulae of Makris & Konstantinidis (dashed lines) and FEMA Guidelines (dotted lines) for $n = 2, \quad r = 0.9$ (b1) and for $n = 2, \quad r = 0.7$ (b2).

Makris and Konstantinidis revealed in their study that the FEMA-recommended empirical expression underestimates the damping ratio by a factor of about 2. On the other hand, their proposed formula derived values of $\xi$ in a good agreement with Priestley's results. A comparison of the afore-discussed

methods for estimating the equivalent viscous damping ratio of the rocking block is presented in the graphs of Fig. 3.5b for $n=2,\quad r=0.9$ (b1) and for $n=2,\quad r=0.7$ (b2). It is evident that for small values of ratio $\theta_o/\theta_c$, i.e. for stable rocking motion, Eq. 3.19 provides results in close agreement with Priestley's formula especially in the range of small rocking amplitudes where a linearised solution could be adopted. It is also clear that the FEMA-recommended expression leads to substantially underestimated values of $\xi$.

### *State-space formulation*

Global information concerning the nonlinear dynamics of the rocking block under free vibration can be drawn through a so-called *state-space* formulation. In particular, by letting $\phi=\dot{\theta}$, $\dot{\phi}=\ddot{\theta}$ and substituting them into the governing equation of motion the rocking angular displacement and velocity $(\theta$ and $\phi$ respectively$)$ are the independent state variables of the two-dimensional system:

$$\dot{\theta}=\phi=f(\theta,\phi) \qquad [3.21a]$$

$$\dot{\phi}=p^2\sin\left(\operatorname{sgn}\theta\theta_c-\theta\right)=g(\theta,\phi) \qquad [3.21b]$$

The solution of this dynamical system can be uniquely defined by the state vector $\mathbf{x}=\begin{pmatrix}\theta & \phi\end{pmatrix}^T$. Such a system is often called *autonomous* in a sense that time has been explicitly eliminated. For a given initial condition $(\theta_o,\phi_o)$ the total amount of the points $(\theta,\phi)$ which satisfy Eqs 3.21 comprise an *orbit* of the response in the *phase plane*. The orbits of *stable* and *unstable* solutions are portrayed in Fig. 3.6 for a rocking block of $\theta_c=0.2\,\text{rad}$ and $p=0.8\,\text{rad/sec}$. In the same graph a closed curve (*limit cycle*) separating the stable from the unstable region of the phase plane is also plotted. This *seperatrix* encloses all the stable orbits of the response whereas it is surrounded by the unbounded orbits which eventually lead to overturning. Each trajectory is characterised by a unique energy level:

$$E = \frac{1}{2} J_o \dot{\theta}^2 + mgR\cos(\theta_c - \theta) \qquad [3.22a]$$

or in normalised form:

$$\mathcal{H} = \frac{1}{2}\dot{\theta}^2 + p^2\cos(\theta_c - \theta) = \frac{E}{J_o} \qquad [3.22b]$$

which is also known as the *first integral of motion.*

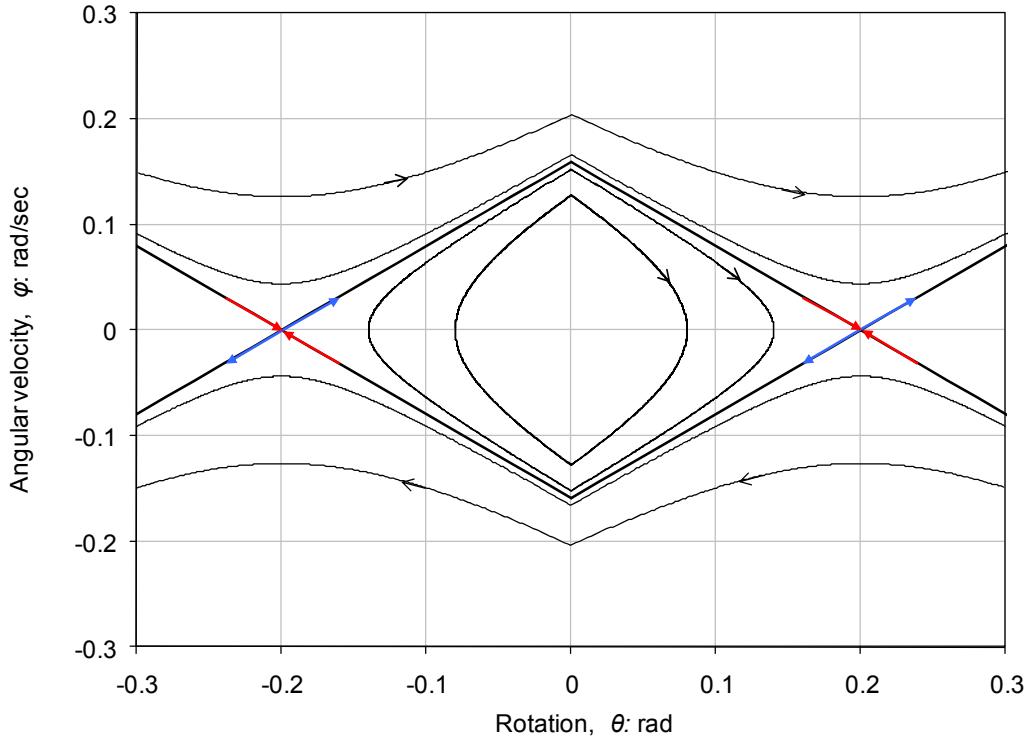


**Figure 3.6** The phase portrait of the rocking block ( $\tan\theta_c = 0.2$ and $p = 0.8\,\text{rad/sec}$ ).

The equilibrium points of the system are calculated from the condition $(\dot{\theta},\dot{\phi}) = (0,0)$ or equivalently $\left(\dot{\theta},\ \text{sgn}\,\theta\theta_c - \theta\right) = \left(0,\ k\pi\right)$. Unlike the simple pendulum case, for a rocking block on a rigid base $k = 0$. The system therefore possesses two equilibrium points:

$$(\theta_c, 0) \text{ and } (-\theta_c, 0) \qquad [3.23]$$

The former equilibrium point represents critical overturning for a clockwise rotation whereas the latter corresponds to a counter-clockwise rotation. Zero point $(0,0)$ is also an equilibrium point since for initial conditions $\theta_o = \phi_o = 0$ it is $\theta(t) = \phi(t) = 0$ at any time. It is remarked that equilibrium points defined with Eq. 3.23 are vertices of the limit cycle at its intersection with the horizontal axis. Given that the total energy of the equilibrium point is $E_e = mgR$, the first integral of motion of the limit cycle is $\mathcal{H} = p^2$. This is the lowest energy level of a trajectory required to 'escape' from the stable region. Similarly, for the simple pendulum with $\omega^2 = g/l$ it is $\mathcal{H} = \omega^2$.

***Linearisation around the equilibrium points***

For a point $\mathbf{x} = \mathbf{a} + \mathbf{v}$ close to equilibrium point $\mathbf{a}$ the nonlinear system described with Eqs 3.21 can be represented with the linear system $\dot{\mathbf{v}} = A\mathbf{v}$ where $Y = \begin{pmatrix} \theta \\ \phi \end{pmatrix}$, $\dot{Y} = \begin{pmatrix} \dot{\theta} \\ \dot{\phi} \end{pmatrix}$ and $A$ is the *Jacobian* with reference to $\mathbf{a}$:

$$A = \begin{bmatrix} \dfrac{\partial f(\mathbf{a})}{\partial \theta} & \dfrac{\partial f(\mathbf{a})}{\partial \phi} \\ \dfrac{\partial g(\mathbf{a})}{\partial \theta} & \dfrac{\partial g(\mathbf{a})}{\partial \phi} \end{bmatrix} = \begin{bmatrix} 0 & 1 \\ p^2 & 0 \end{bmatrix} \qquad [3.24]$$

The characteristic polynomial of this matrix is $p(\lambda) = \lambda^2 - p^2$ with eigenvalues $\lambda_{1,2} = \pm p$. Consequently, the equilibrium point $(\theta_c, 0)$ is a *saddle* point. For the eigenvalue $\lambda_1 = p$ the corresponding eigenvector is $\mathbf{v}_1 = (1 \quad p)^T$ whereas for the eigenvalue $\lambda_2 = -p$ it is $\mathbf{v}_2 = (1 \quad -p)^T$. In the neighbourhood of the point $(\theta_c, 0)$ the vectors $\mathbf{v}_1$ and $\mathbf{v}_2$ generate the field of the vectors $\mathbf{v} = (\theta \quad \phi)^T$ which satisfy the linearised system $\dot{\mathbf{v}} = F(\mathbf{v})$:

$$\mathbf{v} = c_1 e^{pt}\mathbf{v}_1 + c_2 e^{-pt}\mathbf{v}_2 \qquad [3.25]$$

The direction determined by the eigenvector $\mathbf{v}_1 = (1 \quad p)^T$ $\left\{\text{respectively, } \mathbf{v}_2 = \begin{pmatrix} 1 & -p \end{pmatrix}^T\right\}$ comprises the *unstable* {respectively, *stable*} *invariant manifold* of the vector field at equilibrium point $(\theta_c, 0)$. Each trajectory originating on the invariant manifold remains attached to it and departs from {respectively, approaches} the equilibrium point at a rate of $p$. These conclusions may also be applied to the equilibrium point $(-\theta_c, 0)$ as the corresponding eigenvalues and eigenvectors remain the same. Such a trajectory which is a limit cycle (for pendulum case also known as *heteroclinic orbit*), is generated by the *invariant manifolds* of the equilibrium points and represents a *critical overturning* condition. As the stable manifold is defined by the second part of Eq. 3.25 (i.e. the red vectors in the phase-portrait of Fig. 3.6), it is derived that critical overturning of a rocking structure requires a theoretically infinite long time. This is a very important conclusion for the study of overturning response as discussed in Chapter 7.

### 3.2.3 Rocking under harmonic excitation

Within the limits of the analysis of geometrically induced nonlinear rocking of shallow foundations, the present study is generally focused on the transient response, capable of representing the response under strong earthquake excitation. Nevertheless, when rocking on a rigid base in considered, steady-state response can be an efficient tool to elucidate the profoundly nonlinear features of rocking behaviour. Moreover, an earthquake record of many significant cycles could conservatively be represented with a harmonic excitation. The governing equation of rocking motion in its rigorous formulation (Eq. 3.2) is highly nonlinear and therefore, extracting a closed-form analytical solution is rather impossible even under harmonic loading. When the piecewise linear system is considered though (a reasonable simplification for slender blocks), an analytical treatment of rocking under harmonic base excitation may be feasible leading to the solution of Eq. 3.6, as developed by Spanos and Koh (1986). Initially, a comparison between the nonlinear and the linearised response is carried out to determine limits of applicability of the linear formulation. Then, nonlinear formulation of the governing equation of motion (i.e. Eq. 3.2 and Eq. 3.3) is adopted to examine in-depth the nonlinear

features of the harmonically driven rocking vibration. To this end the response is computed through numerical integration explicitly at each time increment.

***Linearised vs nonlinear response***

Time histories of the rocking response of a slender rectangular block $\left(\tan\theta_c = 0.2,\ r = 0.8\right)$ are computed first comparatively with both linear and nonlinear formulation of the equation of motion. To this end, a harmonic excitation of $a_{\max} = 1.0$ g (namely five times larger than the pseudo-static overturning acceleration, $a_{over,st} = \tan\theta_c = 0.2$ g) and $T_E = 0.4$ sec is applied at the base. Three different values of the frequency (size) parameter $p$ are implemented in the analysis: $p_1 = 0.8$ rad/sec, $p_2 = 1.6$ rad/sec, and $p_3 = 3.2$ rad/sec, representing a large, a moderately large, and a small block respectively. Linear formulation is based on the closed-form solution of Eqs 3.6a and as derived by Spanos and Koh (1984). The response is plotted in the graphs of Fig. 3.7 in terms of the normalised rotation and velocity time histories (dotted lines). Nonlinear solution of the rocking steady-state response is obtained with explicit integration of Eq. 3.2 (solid lines).

Originally, the response of the large block is computed, where an excellent agreement between piecewise linear and nonlinear response is achieved. When downsizing the block (by doubling the frequency parameter, $p$), time histories predicted by linear formulation match those of the nonlinear formulation in the beginning, however they diverge from the nonlinear ones, shortly after the first few loading cycles. Actually, it seems that linear formulation predicts a steady-state response which is dominated by a single frequency, whereas nonlinear formulation unveils an enhanced response by 'capturing' more *subharmonic* frequencies. Nevertheless, the rocking amplitude computed with both methods is still practically the same. Finally, by further decreasing the size of the block it yields that overturning is inevitable in both solutions, however according the nonlinear formulation it comes quite later than 'linear' failure.

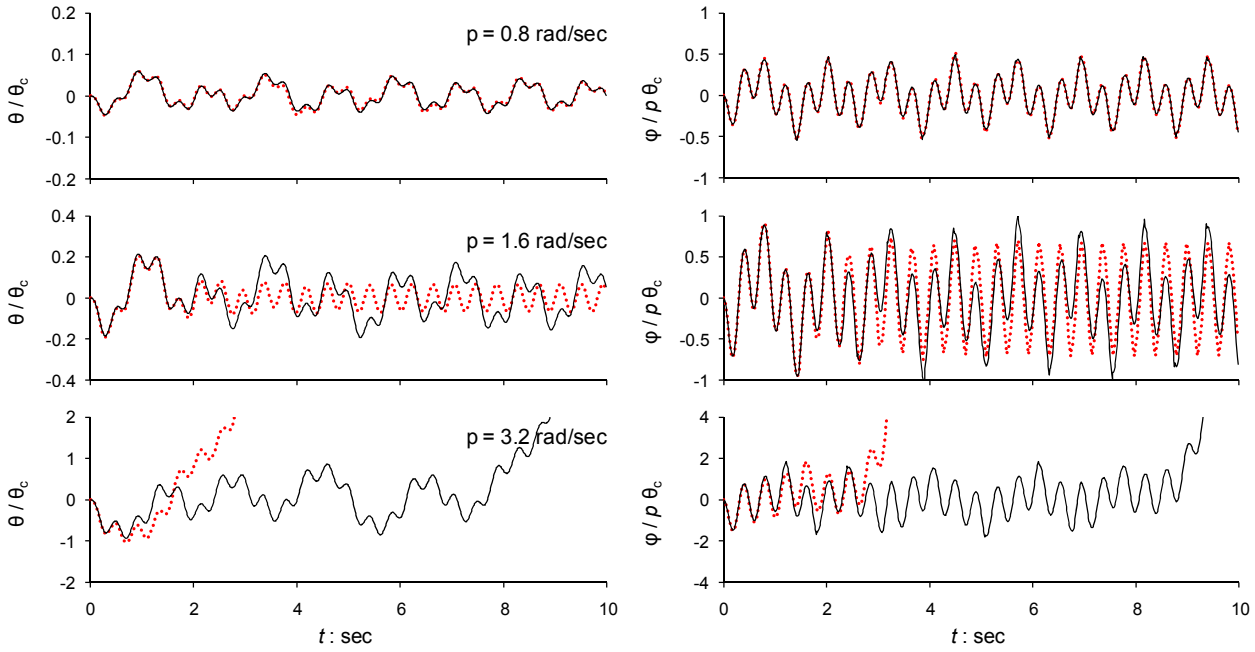


**Figure 3.7** Time histories of the normalised rocking rotation and velocity of a rigid rectangular block $(\tan\theta_c = 0.2,\ r = 0.8)$ under harmonic base excitation $(T_E = 0.4 \text{ sec},\ a_{\max} = 1.0 \text{ g})$: comparison between the nonlinear (solid lines) and the linearised solution (dotted lines) for three different values of $p$.

The analysis of rocking response is repeated next for the same parameters $\tan\theta_c = 0.2$ and $r = 0.8$. The three different values of the frequency (size) parameter $p$ implemented before ($p_1 = 0.8$ rad/sec, $p_2 = 1.6$ rad/sec, and $p_3 = 3.2$ rad/sec) are used again. The excitation period of the harmonic shaking at the base has been doubled (0.8 sec), whereas the amplitude has been reduced to half $(0.5 \text{ g})$, in such a way that the peak ground velocity $(PGV = PGA/\omega)$ remains unchanged.

Time histories of the rotation and velocity are plotted in the graphs of Fig. 3.8, computed with both linear (dotted lines) and nonlinear formulation (solid lines). By comparing the results of Figs 3.7 and 3.8 it turns out that the rotation and velocity amplitudes remain at the same levels as the peak ground velocity is kept constant. Also, an excellent agreement between piecewise linear and nonlinear response is obtained in the response of the large block $(p_1 = 0.8 \text{ rad/sec})$, as before. What is more interesting now is that for the moderately large block $(p_2 = 1.6 \text{ rad/sec})$, linear formulation manages

to predict the exact solution. Even in the 'small block' case, the rocking response and overturning computed with linear formulation is in a quite satisfactory agreement with the exact solution.

In concluding, both series of analyses presented above, reveal that rocking response of large blocks is well predicted even when a linear formulation of the equation of motion is utilised. On the other hand, steady-state analysis of a small rocking block is quite sensitive to whether a linear or nonlinear formulation is adopted. The lower threshold of what is called 'a large block' may be expressed with the frequency parameter, $p$. This distinction however between small and large blocks is affected by the excitation frequency in such a manner that a block of a certain size may be considered as small for a ground shaking of relatively short period while being regarded as large for a motion of longer period.

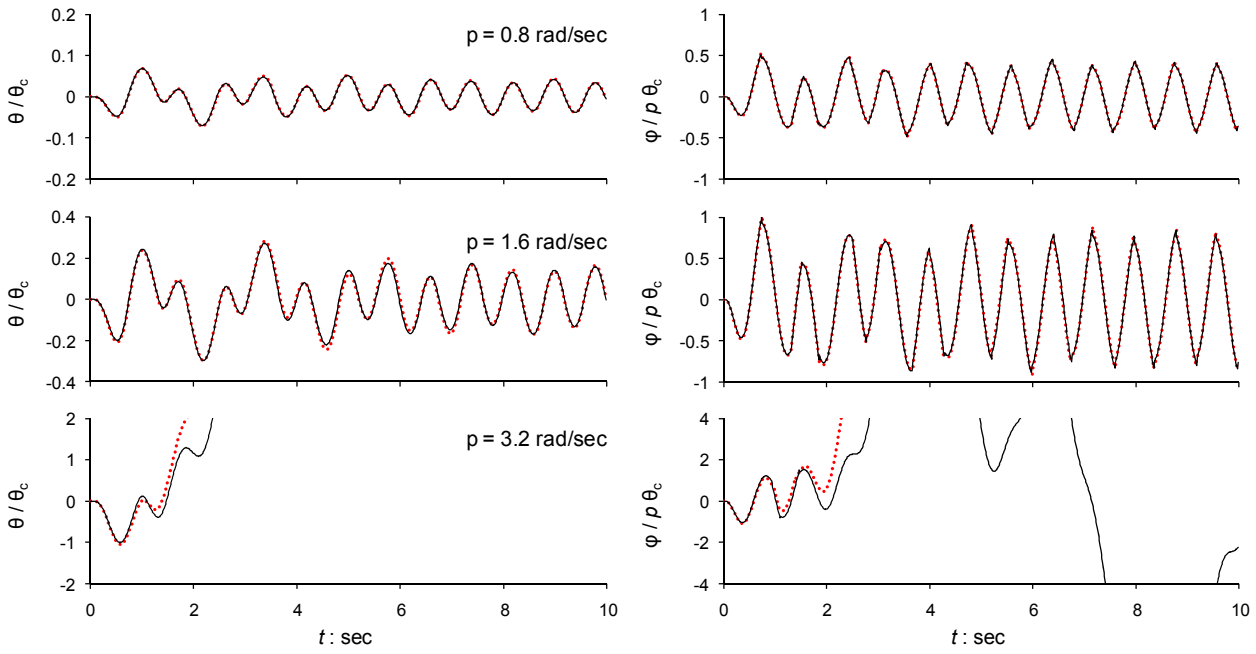


**Figure 3.8** Time histories of the normalised rocking rotation and velocity of a rigid rectangular block $(\tan\theta_c = 0.2,\ r = 0.8)$ under harmonic base excitation $(T_E = 0.8 \text{ sec},\ a_{\max} = 0.5 \text{ g})$: comparison between the nonlinear (solid lines) and the linearised solution (dotted lines) for three different values of $p$.

### *Rocking spectra*

All analyses presented above with both linear and nonlinear formulation reveal among others the sensitivity of the rocking response to the size of the block as described with the parameter $p$. It is

concluded that the smaller the block the larger the amplitude is, and eventually for blocks smaller than a limiting size overturning occurs. An interesting way of portraying the response of a rigid structure under rocking vibration is in the form of the *rotation response spectrum* or simply *rocking spectrum*, as introduced by Makris and Konstantinidis (2003). For a certain value of slenderness, the amplitude of rotation is plotted as a function of the *period parameter*, $T_p = 2\pi/p$ or simpler the frequency parameter, $p$. For a rectangular block the period parameter is $T_p = 4\pi\sqrt{R/3g} \cong 2.3\sqrt{R}$, whereas for a rigid one-storey structure it is $T_p = 2\pi\sqrt{R/g} \cong 2\sqrt{R}$. Note that the latter period is equal to the natural period of a linearised pendulum of length, $R$ (see also Fig. 3.4).

The slender block considered before $\left(\tan\theta_c = 0.2,\ r = 0.8\right)$ is revisited to compute rocking spectra under harmonic excitation with both linear and nonlinear formulation. Extending the previous analyses, a moderate and a strong ground motion is regarded ($a_{\max}$ = 0.5 g and 1.0 g respectively) whereas for the excitation period the same levels are used again ($T_E = 0.4$ sec and 0.8 sec). These values yield four sets of rocking spectra: (a) $\mathcal{A} = 2.5$, $T_E = 0.4$ sec, $PGV = 31.2$ cm/sec, (b) $\mathcal{A} = 5$, $T_E = 0.4$ sec, $PGV = 62.4$ cm/sec, (c) $\mathcal{A} = 2.5$, $T_E = 0.8$ sec, $PGV = 62.4$ cm/sec, and (d) $\mathcal{A} = 5$, $T_E = 0.8$ sec, $PGV = 124.8$ cm/sec. The computed rocking spectra with both linear and nonlinear formulation are plotted in the graphs of Fig. 3.9. The beneficial role of block size (large values of $p$ correspond to small blocks) is revealed again through all computed spectra. The detrimental effect of the excitation period is also clear as the long period motion ($T_E = 0.8$ sec - bottom spectra) results to higher rocking amplitudes and requires smaller levels of $p$ for critical overturning. A comparison of the linear to the nonlinear formulation may also be extracted from the rocking spectra of Fig. 3.9. Apart from the rocking amplitude which can readily be obtained from the spectra, the capability to efficiently predict the rocking time history with the linear formulation is also of special interest. The range of values of $p$ in which the linearised solution is in good agreement with the exact (nonlinear) in terms of time histories is also shown in Fig. 3.9 above each spectrum. It is shown that there is a

threshold value of $p$ under which, the linear formulation predicts satisfactory the rocking response. Additionally, the range of $p$ formed by this threshold value can nearly cover the whole bandwidth of safe rocking under harmonic shaking, provided the peak ground velocity is sufficiently small. Nevertheless, linear formulation can efficiently predict the rocking amplitude and critical overturning in most cases even when this threshold value of $p$ has been exceeded.

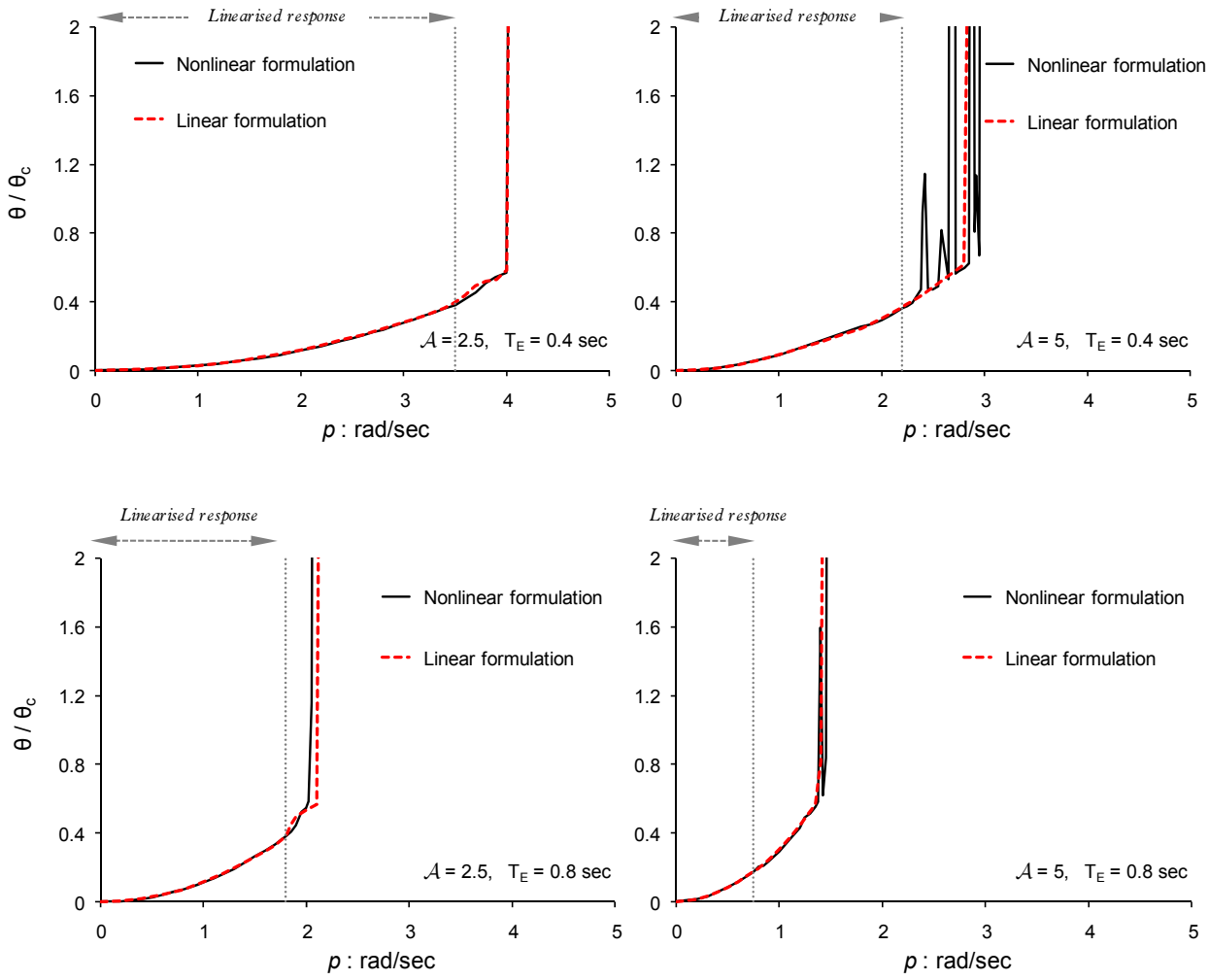


**Figure 3.9** Rocking spectra of a slender block $\left(\tan\theta_c = 0.2,\ r = 0.8\right)$, subjected to harmonic shaking at the base: (a) $PGV = 31.2$ cm/sec, (b) $PGV = 62.4$ cm/sec, (c) $PGV = 62.4$ cm/sec, (d) $PGV = 124.8$ cm/sec.

A major advantage of linear formulation over nonlinear, is that the response can be expressed through dimensionless parameters. It is therefore interesting to develop normalised diagrams of the linearised

response regarding that for relatively large bodies (including common civil engineering structures) rocking can be efficiently predicted by linear formulation. Hence, by introducing the dimensionless rotation, $\Theta = \theta / \theta_c$, frequency, $\Omega = \omega_E / p = T_p / T_E$, and amplitude (i.e. dynamic amplification), $\mathcal{A} = a_{\max} / a_c$ rocking spectra under harmonic shaking can be computed for different levels of the coefficient of restitution. In Fig. 3.10 the rocking spectra for $r = 0.97$ and $0.90$ are presented.

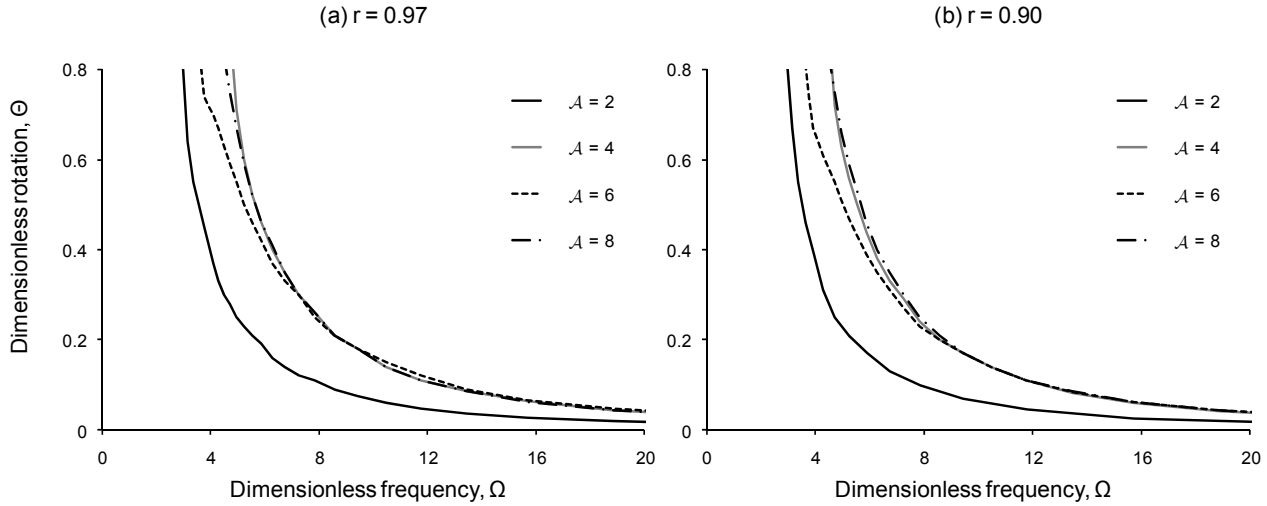


**Figure 3.10** Rocking spectra of the dimensionless rotation, $\Theta = \theta / \theta_c$ with respect to the dimensionless frequency $\Omega = \omega_E / p$ for a harmonic excitation. The response has been computed with the linear formulation of the equation of motion, for different levels of the dynamic amplification $\mathcal{A} = a_g / a_c$ and two values of the coefficient of restitution: (a) $r = 0.97$ and (b) $r = 0.90$.

### *Modes of response*

Depending on the amplitude and the frequency of the harmonic excitation, rocking of a rigid body may either be a *bounded* or *unbounded* motion. In the latter, rocking motion inevitably leads to overturning. In the former, the rigid block undergoes safe rocking vibration which can be distinguished into *periodic*, *quasi-periodic*, and *chaotic* response with a single dominant frequency, a finite number of *incommensurate* frequencies, and an infinite number of frequencies, respectively (Yim and Lin, 1991).

Rocking response of a rigid block ($\tan\theta_c = 0.2$, $p = 0.8\,\text{rad/sec}$) subjected to a harmonic base excitation of period $T_E = 0.4\,\text{sec}$ is computed next. Two levels of the peak ground acceleration are employed: (i) $a_{\max} = 0.5\,\text{g}$ and (ii) $a_{\max} = 1.0\,\text{g}$ namely 2.5 and 5 times respectively larger than the pseudo-static overturning acceleration $\left(a_{over,st} = 0.2\,\text{g}\right)$. A coefficient of restitution $r = 0.8$ is first adopted. The results are plotted in the graphs of Fig. 3.11a in terms of time histories of the rotation $\theta$ and the angular velocity $\phi$, and phase portraits $\left(\theta,\phi\right)$. Unlike pseudo-static consideration which would predict toppling, the rocking block safely undergoes rocking vibration even for a peak ground acceleration 5 times larger than $a_{over,st}$. Moreover, for $a_{\max} = 0.5\,\text{g}$ rocking is symmetric to the vertical axis and the response is periodic with a frequency equal to the excitation frequency $\left(f_E = 1/0.4\,\text{sec} = 2.5\text{hz}\right)$. After doubling the excitation amplitude $\left(a_{\max} = 1.0\,\text{g}\right)$, the motion is still symmetric to the vertical axis. Remarkably, it is now enhanced with two more frequencies which are rational multiple of the fundamental frequency, evidence of a *one-third subharmonic* response or a $\left(1,3\right)$ mode. It is recalled that a $\left(n,m\right)$ mode represents a symmetric response of $n$ impacts per cycle and $m$ frequencies.

The analysis of rocking response of the afore-discussed block is repeated next by modifying impact conditions, i.e. by setting $r = 1$. Stable rocking motion is computed again for both levels of base shaking (Fig 3.11b). In contrast to the periodic motion discussed before, rocking is not symmetric to the vertical axis and the response is not dominated by a single frequency equal to the excitation frequency. Interestingly, the dynamical system possesses a finite number of frequencies as portrayed in the phase diagram of Fig. 3.11b., none of these frequencies however, is any longer a rational multiple of the fundamental frequency. This feature of rocking vibration first unveiled by Yim and Lin (1991), is well-known in the nonlinear dynamics literature as quasi-periodic response and is considered a transition between periodic and chaotic response.

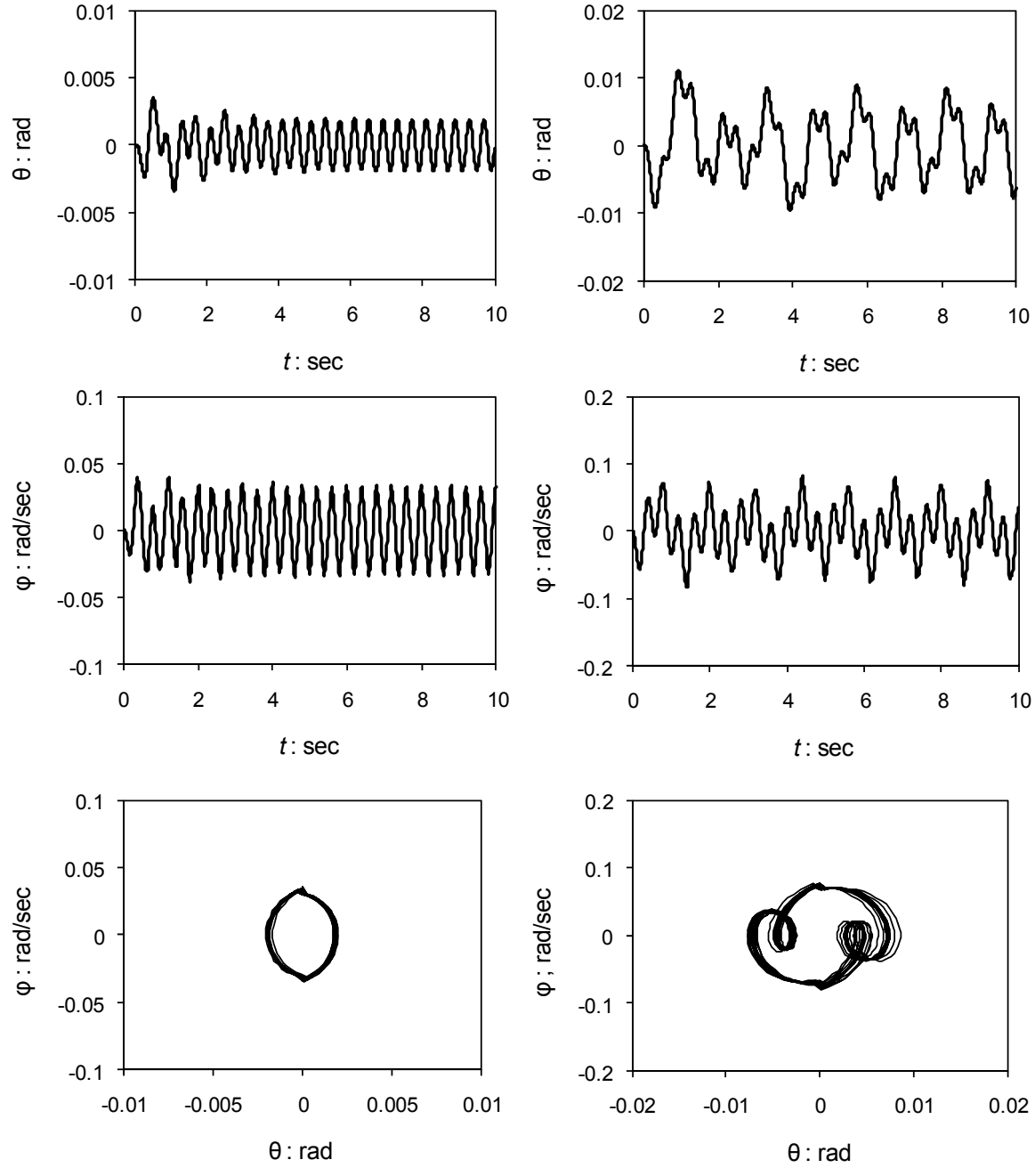


**Figure 3.11a** Periodic response of a rocking block ( $\tan\theta_c = 0.2$ and $p = 0.8\,\text{rad/sec}$ ) subjected to a medium (i) and strong (ii) harmonic base excitation of period $T_E = 0.4\,\text{sec}$. The coefficient of restitution is $r = 0.8$.

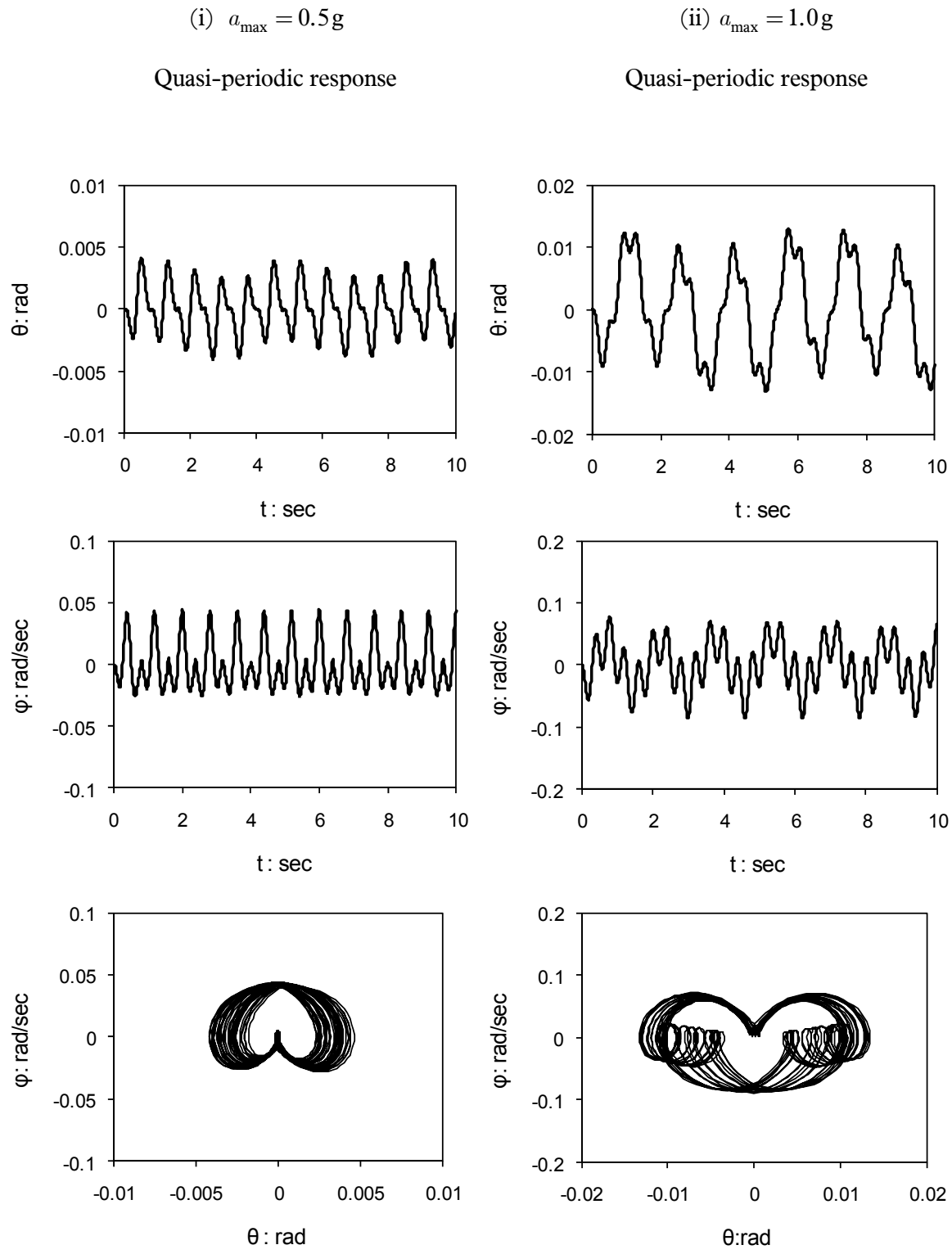


**Figure 3.11b** Quasi-periodic response of a rocking block ( $\tan\theta_c = 0.2$ and $p = 0.8\,\text{rad/sec}$ ) subjected to a medium (i) and strong (ii) harmonic base excitation of period $T_E = 0.4\,\text{sec}$. The coefficient of restitution is $r = 1.0$.

Periodic and quasi-periodic response can be readily identified by inspection of the *Poincare map* (i.e. the intersection of a periodic orbit in the state space with a section transversal to the flow). In this way, the periodic response is illustrated as a one-dot or a three-dot map, representing the harmonic [case (i)] or the one-third subharmonic response [case (ii)] respectively (Fig. 3.12a). Quasi-periodic response is depicted by a closed dotted line called *torus* (Fig. 3.12b).

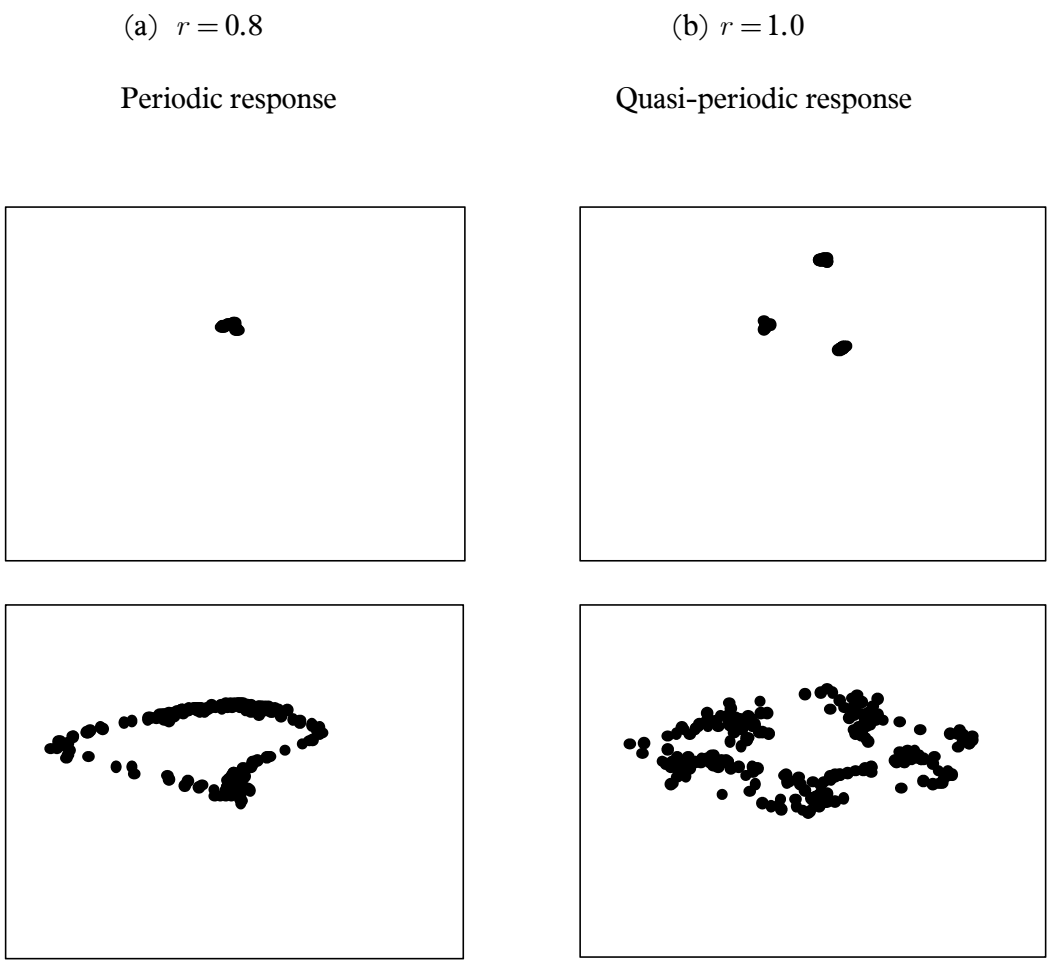


**Figure 3.12** Poincare maps of a rocking block ( $\tan\theta_c = 0.2$ and $p = 0.8\,\text{rad/sec}$ ) for the analysis presented in Fig3.11.

### 3.2.4 Rocking under earthquake excitation

Analysis of the steady-state response is a useful tool to explore the nonlinear features of rocking behaviour. Nevertheless, earthquake loading often contains only a few significant cycles. In addition,

near-fault ground motion should be represented with sine or cosine pulses of one cycle (Makris and Roussos, 1998) or more efficiently with *Ricker* pulses especially when studying rocking (Apostolou *et al.*, 2007). Many examples of these pulses have been uncovered in near-fault records of $M_S \geq 6.5$ earthquakes, such as the Imperial Valley 1979, Erzincan 1992, Northridge 1994, Kobe 1995, Kocaeli 1999, Chi-Chi 1999 (Gerolymos *et al.*, 2005). These pulses are the result of two effects: the '*forward rupture directivity*' effect and '*permanent offset*' (or '*fling*') effect (Somerville, 2003; Hisada and Bielak, 2003). Some of the most common idealised pulses to represent near-fault ground motion which will be employed in the analysis are illustrated in Fig. 3.13.

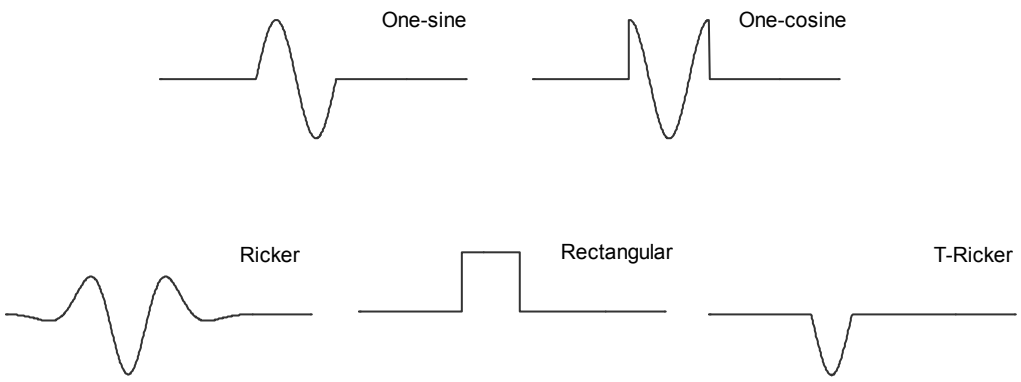


**Figure 3.13** Idealised pulses utilised to represent near-fault ground motion.

For the analysis of rocking under earthquake excitation, a slender block of $\tan\theta_c = 0.2$ and $p = 1.387\,\text{rad/sec}$ is employed. In the beginning, the rigid base is excited with a Ricker pulse of peak ground acceleration $0.4\,\text{g}$ and predominant period $0.67\,\text{sec}$ and $2 \times 0.67\ \text{sec} = 1.33\ \text{sec}$. The time histories of rocking displacement and velocity are plotted in the graphs of Fig. 3.14. In the same Figure, the trajectories of rocking motion in the normalised $\Theta - \Phi$ plane are also plotted. The response has been separated into a transient part (white circles) and a free vibration part (black solid line). The beginning and the end of the transient response occurs at the moment of the onset and expiration of base excitation respectively (large white circles). In the phase portrait the bounding cycle separating safe from overturning area is also shown.

During transient mode, the solution is obtained with the equation of rocking motion (Eq. 3.2). As in the case of harmonic shaking, the increase of the excitation period results in amplifying rocking vibration. At the moment ground excitation expires (large white circle) the response engages the free vibration mode. Hence, the response is computed with the homogeneous solution of Eq. 3.2 (nonlinear formulation) or Eq. 3.10 (the analytical solution according to linear formulation) with initial values $\theta_0$ and $\phi_0$ being computed from the last increment of the transient mode. As depicted in the predescribed study of free vibrations, larger rocking amplitudes correspond to larger vibration period and damping. Consequently, each subsequent cycle of free vibration regime becomes smaller and shorter. In the time histories portrayed in Fig.3.14 this dissipative mechanism is more pronounced for the short-period excitation (left-hand side) in which, the initial rotation $\theta_0$ is smaller. Another interesting conclusion from the phase portraits of Fig. 3.14 is that the trajectory can temporarily reach or even cross the limit cycle during transient mode without overturning to occur if the point $(\theta_0, \phi_0)$ at the moment the excitation expires is bounded by this cycle.

The sensitivity analysis of rocking response is focused next on the size parameter $p$. In this respect, the analysis with the initial parameters (Fig. 3.14, left-hand side) is repeated after doubling $p$ to $2 \times 1.387 = 2.774$ rad/sec. The results are plotted in Fig. 3.15. When compared to the analysis of a double $T_E$ (Fig. 3.14, right-hand side), the rocking displacement and velocity amplitude is still the same as the dimensionless period $\Omega = \frac{\omega_E}{p}$ has not changed. On the other hand, time seems to be running quite faster as the dimensionless time $\tau = pt$ has now become double. These conclusions can also be extracted from the comparison of the phase portraits which are identical as time has been eliminated.

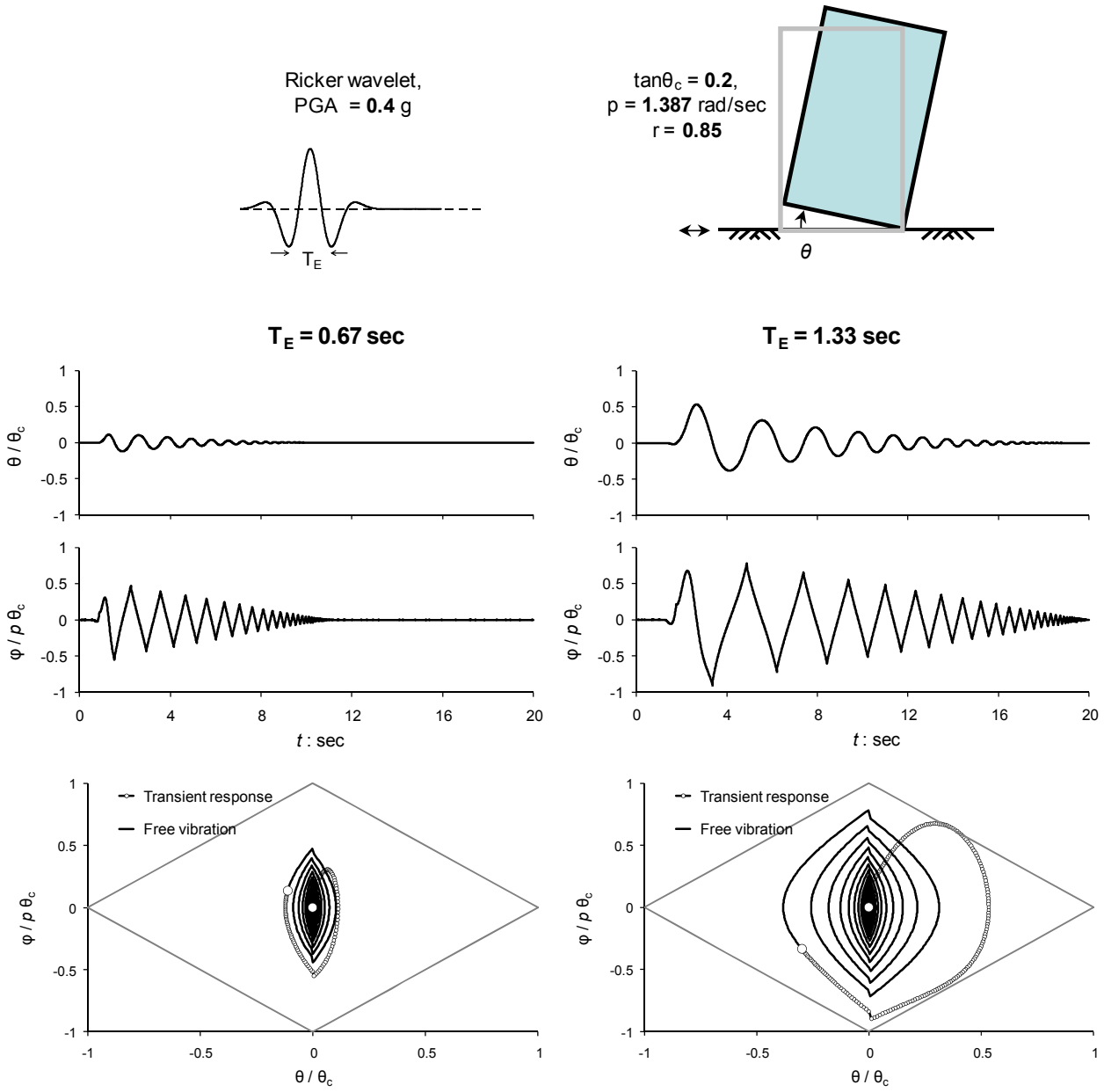


**Figure 3.14** Rocking response of a rigid structure ($\tan\theta_c = 0.2$, $p = 1.387\,\text{rad/sec}$, and $r = 0.85$) subjected to a Ricker pulse excitation at base $(PGA = 0.4\,\text{g})$ with predominant period of (a) $T_E = 0.67$ sec and (b) $2T_E = 1.33$ sec.

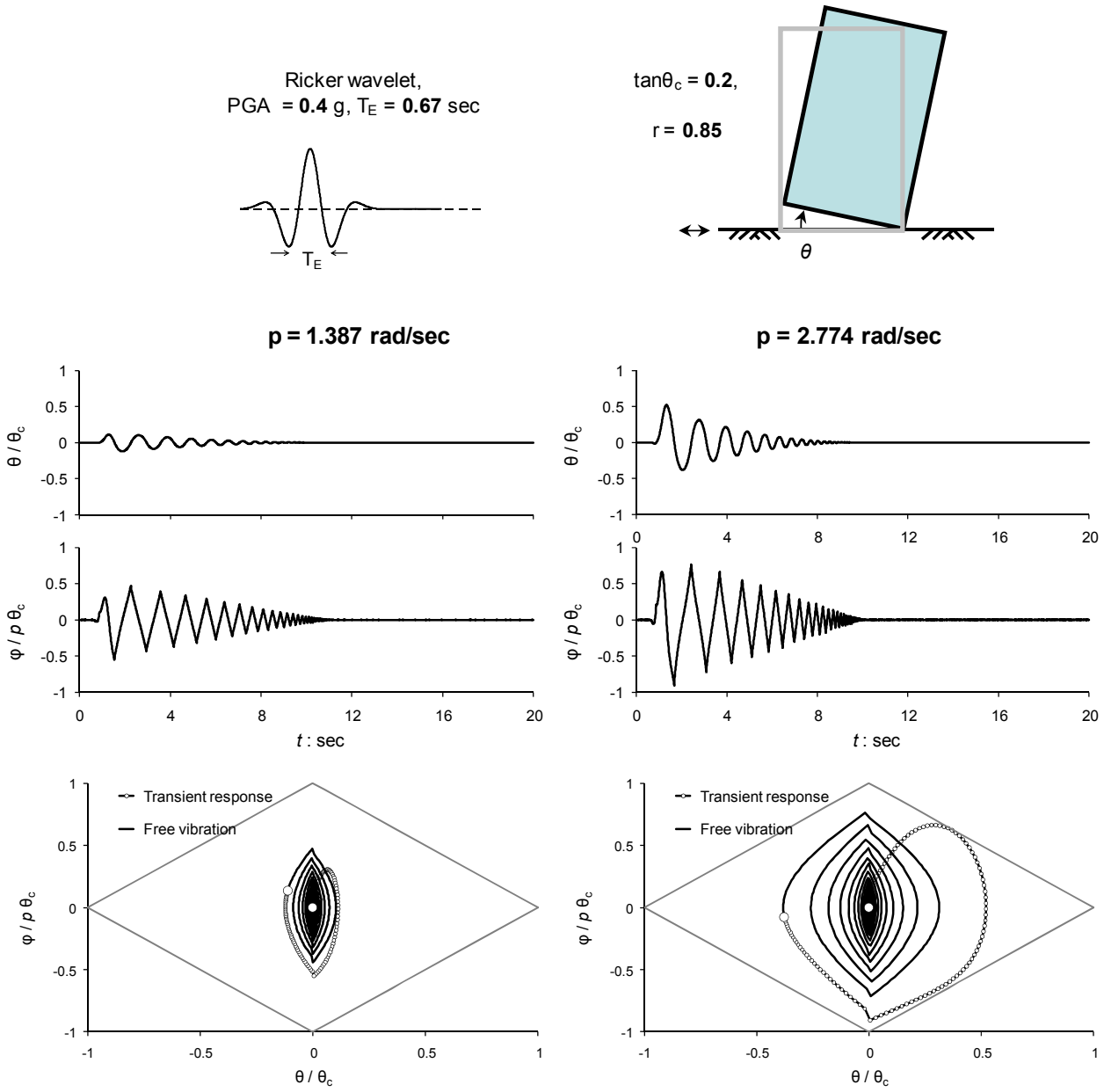


**Figure 3.15** Rocking response of a rigid structure ( $\tan\theta_c = 0.2$, and $r = 0.85$ ) of size parameter (a) $p = 1.387\,\text{rad/sec}$, and (b) $2p = 2.774\,\text{rad/sec}$. A Ricker pulse excitation of $PGA = 0.4\,\text{g}$ and $T_E = 0.67\,\text{sec}$ is applied at base.

### *Rocking spectra*

As for the steady-state response, linearised rocking spectra of the dimensionless rotation, $\Theta$ with respect to the dimensionless frequency $\Omega$ can be computed for a pulse-type excitation. Originally, a Ricker pulse is imposed as excitation for different levels of the dynamic amplification ( $\mathcal{A}$= 2, 4, 6, and

8) and two values of the coefficient of restitution ($r = 0.97$ and $0.90$). The computed spectra are plotted in Fig. 3.16.

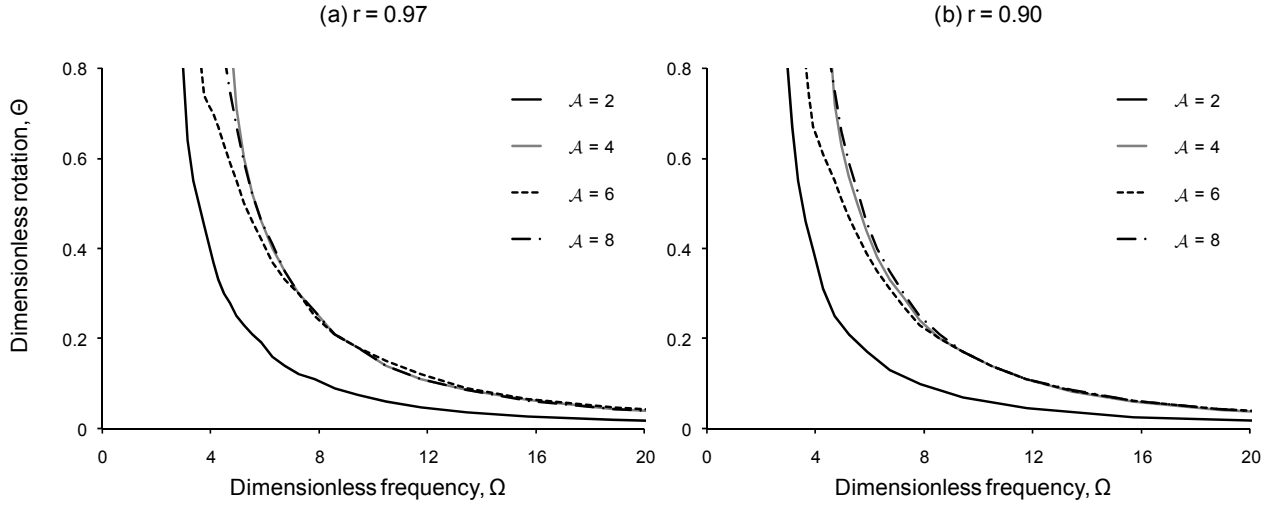


**Figure 3.16** Rocking spectra of the dimensionless rotation, $\Theta = \theta / \theta_c$ with respect to the dimensionless frequency $\Omega = \omega_{\mathrm{E}} / p$ for a Ricker pulse-type excitation. The response has been computed with the linear formulation of the equation of motion, for different levels of the dynamic amplification $\mathcal{A} = a_g / a_c$ and two values of the coefficient of restitution: (a) $r = 0.97$ and (b) $r = 0.90$.

An interesting normalisation can result when both dimensionless rotation and frequency are compacted to a single parameter, $\Pi_\Theta = \Theta\Omega^2$. In this way, $\Pi_\Theta$ can be plotted in terms of the amplification $\mathcal{A}$ or its inverse $1/\mathcal{A}$, providing a single rocking spectrum for a certain value of the coefficient of restitution. Under such a consideration, a series of analyses is performed to derive the normalised rocking spectra of the basic pulses for different levels of $r$, as portrayed in Fig. 3.13. For comparison, the rocking spectrum $\Pi_\Theta - 1/\mathcal{A}$ under harmonic excitation is also plotted in Fig. 3.13.

A measure for potential destructiveness of the basic motions utilised (or in general, of any recorded motion) can be drawn from these spectra as shown in Fig. 3.13. Hence, it can be seen that among these motions, the one-sine pulse is the most detrimental for a rocking block whereas the one-cosine is the most beneficial. The Ricker pulse results in large values of $\Pi_\Theta$ in a range of $1/\mathcal{A} = 0.15 - 0.30$.

Finally, the one-directional pulses (T-Ricker, rectangular) follow a unique exponential decay curve for all values of $r$, as in these cases, the largest rocking amplitude is observed before the first impact.

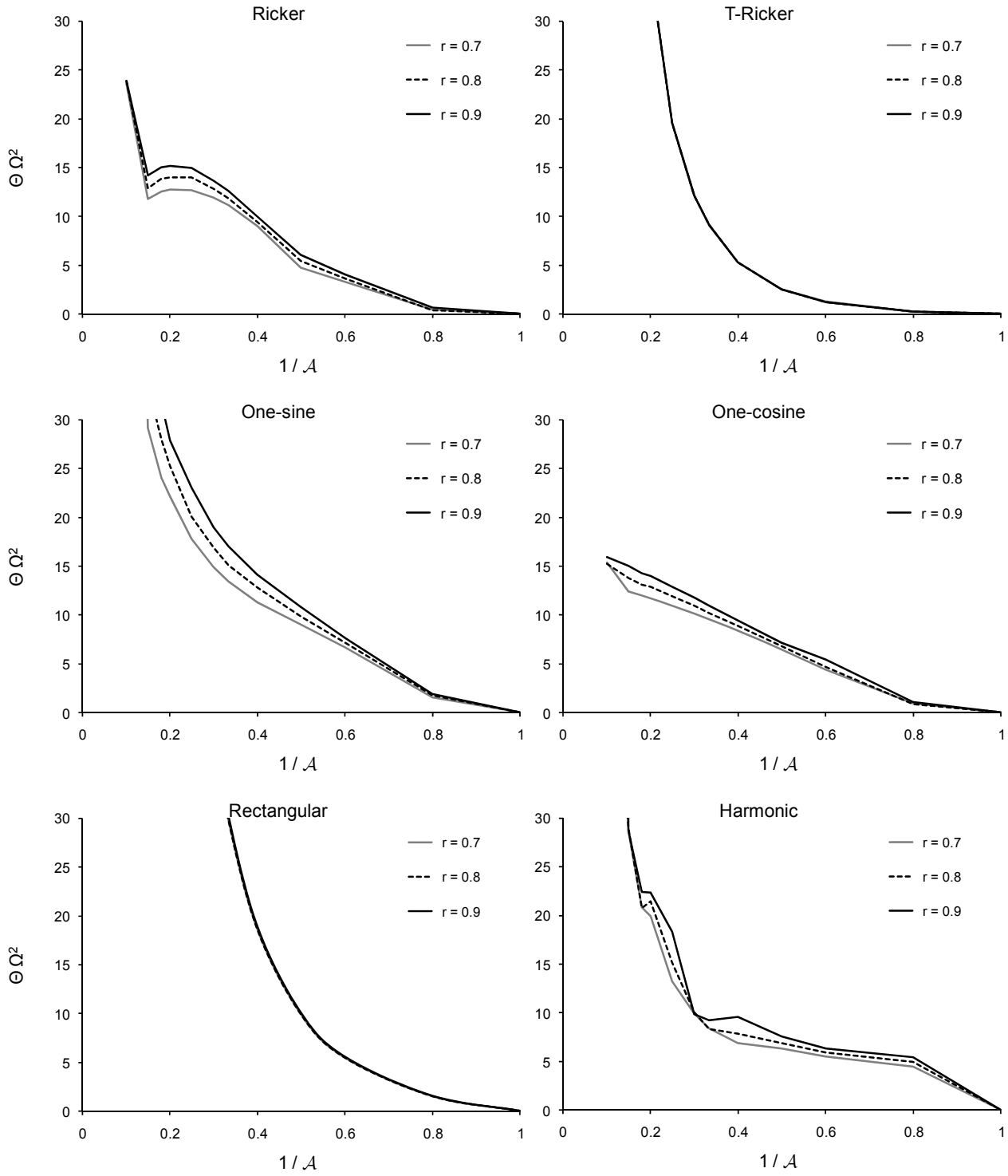


**Figure 3.17** Normalised rocking spectra of a rigid block, subjected to pulse-type shaking at the base, for three different values of the coefficient of restitution and comparison to those from harmonic shaking (bottom right).

The afore described methodology can be extended to compute rocking spectra of recorded ground motions and accordingly, to derive estimates for the potential destructiveness. Indicatively, the rocking spectra of two typical near-fault records are illustrated in Fig. 3.18.

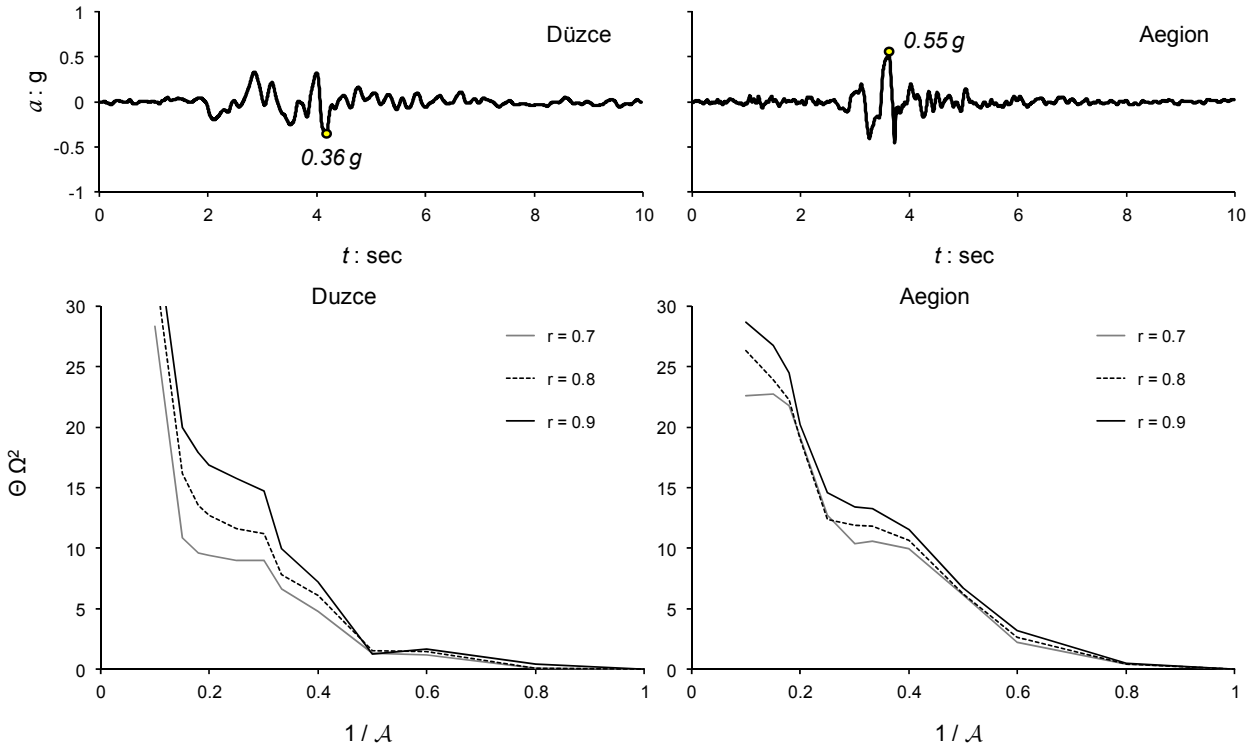


**Figure 3.18** Normalised rocking spectra of a rigid block, subjected to the earthquake records of Düzce and Aegion, for three different values of the coefficient of restitution.

### *Structural response*

After examing the rocking response of rigid rectangular blocks in terms of rocking rotation and angular velocity, we can now further study the response of rocking structures through the one-storey uplifting oscillator introduced earlier. Both the pier of the superstructure and footing are considered rigid and massless. In contrast to the block-type structure, the structural mass is now concentrated at the top of the pier. Once the system is set on rocking motion the inertial forces developed at the mass point result in section shear forces and moments along the pier. As in the study of the rigid block, the governing equation of rocking motion (Eq. 3.2) can be applied in which the size parameter $p$ is given by Eq. 3.7a. A slender one-storey oscillator of $\tan\theta_c = 0.2$ and $p = 1.387$ rad/sec is considered,

submitted to a long duration, Ricker wavelet pulse of peak ground acceleration, $PGA = 0.4$ g and excitation period, (a) $T_E = 0.67$ sec and (b) $T_E = 1.33$ sec. The results are shown in Fig. 3.19, in terms of: (a) time histories of the normalised rocking angle, structural acceleration (at the mass point), and base moment, and (b) moment-rotation curves. The time history of the rocking angle is identical to the block portrayed in Fig. 3.15, as both systems share common rocking parameters $p$ and $\theta_c$. In the beginning, the structure follows the accelerating base with its footing fixed on the ground. As soon as the ground acceleration reaches the critical acceleration, $a_c = b/h$, the rocking motion enters the uplifting regime. During this mode, the structural acceleration departs from the excitation acceleration at the base, tracking on a plateau which is defined by the critical value $a_c$. This plateau exhibits a sudden reversal and shortening during each impact. Accordingly, the time histories of the base shear force and moment track on the same path, being linear functions of $a_{cm}$ ($Q = -mga_{cm}$ and $M = -mga_{cm}h$). Eventually, due to energy loss at every impact, rocking terminates. The period of the time history of any structural quantity is determined from the duration of each cycle of rocking motion. The moment-rotation curves of the earthquake response are also plotted in Fig. 3.19 together with the monotonic curves in both directions. Throughout the response the dynamic, cyclic curve traces the static one, whereas after reversing direction of rotation it follows the beaten track.

This restoring mechanism of the uplifting response together with the bounded motion in terms of the structural quantities are two major advantages of rocking structures.

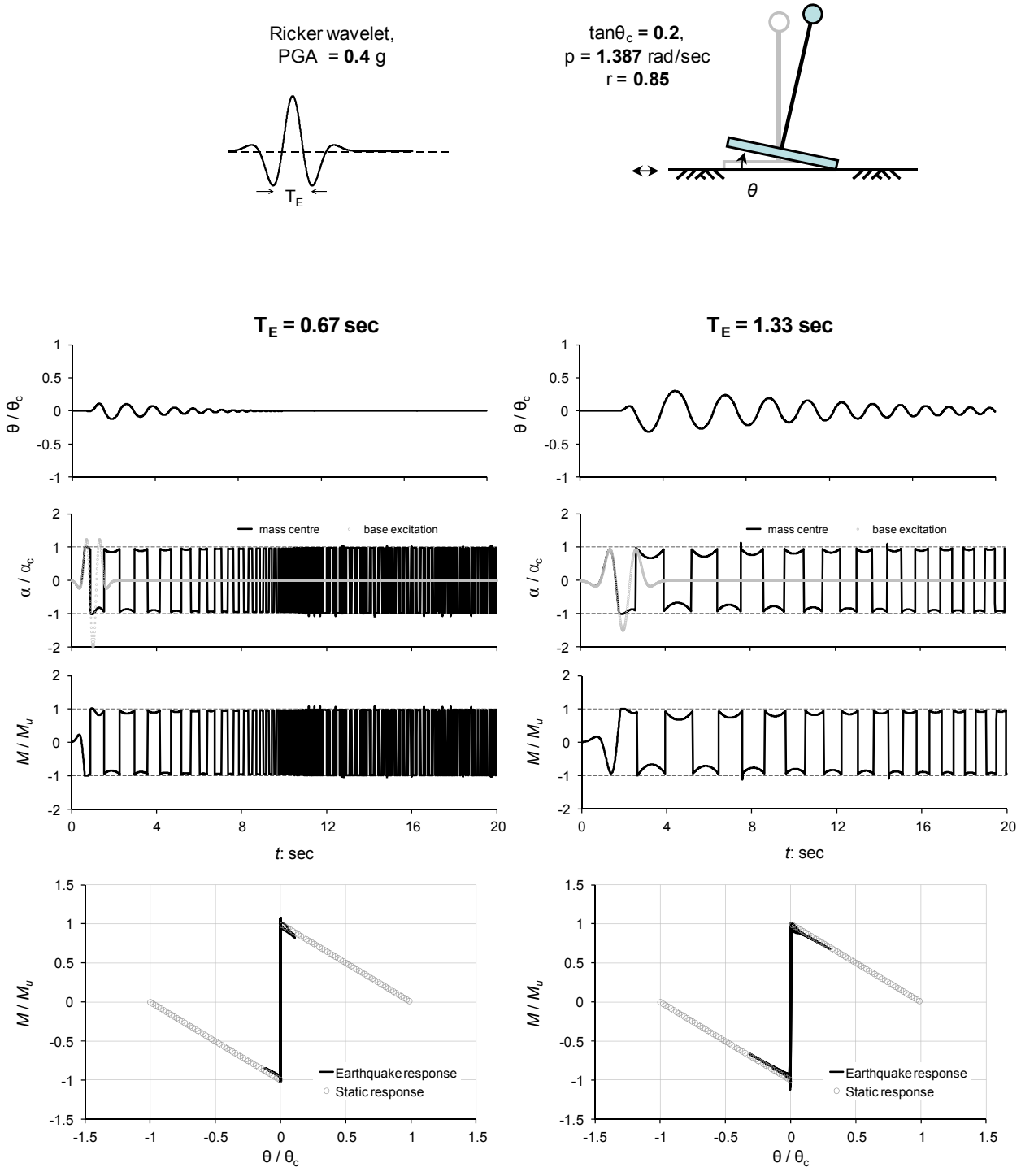


**Figure 3.19** Structural response of a rigid one-storey structure ( $\tan\theta_c = 0.2$, $p = 1.387\,\text{rad/sec}$, and $r = 0.85$ ). A long-duration Ricker wavelet is applied as a base excitation of peak ground acceleration, $PGA = 0.4\,\text{g}$ and excitation period, (a) $T_E = 0.67\,\text{sec}$ (left-hand side) and (b) $T_E = 1.33\,\text{sec}$ right-hand side.

## 3.3 ROCKING of a FLEXIBLE 1-DOF STRUCTURE

### 3.3.1 Statement of the problem, Equations of motion

In the foregoing, only rigid bodies were employed to analyse rocking response. This may be a reasonable approximation of block-type (usually small) non-structural elements. However, slender engineering structures such as high-rise buildings which are vulnerable to experience rocking with uplift may not be efficiently represented with rigid structural models. An elastic sdof oscillator with a foundation mat allowed to uplift from its rigid base is employed here as illustrated in Fig. 3.20. This model comprises a lumped mass $m$ located at a height $h$ above a rigid and massless foundation of width $2b$. The mass point is connected to the foundation with a vertical beam characterised with the visco-elastic parameters $k$ and $\xi$. The coefficient of friction at the foundation interface is considered large enough to prevent sliding of the structure.

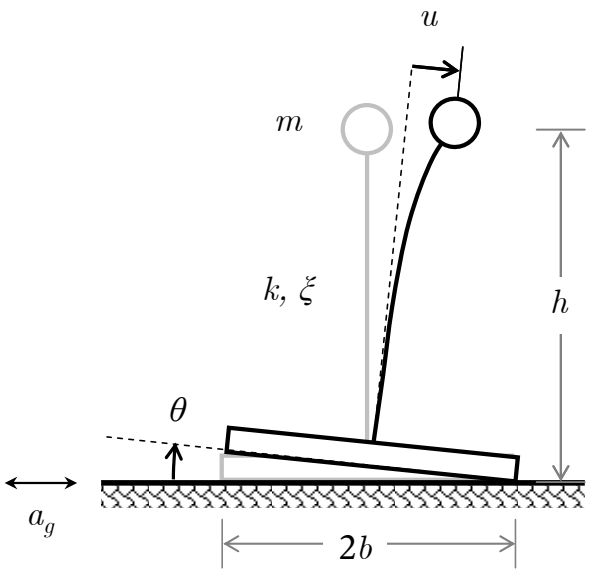


**Figure 3.20** Configuration of the sdof uplifting oscillator.

Depending on whether the foundation mat is in full contact with the supporting base or not, two different states of response can be distinguished: (a) the *full-contact* phase and (b) the *uplift* phase. In the full-contact phase the structure undergoes only flexural oscillations. During this state the system

reduces to a sdof harmonic oscillator and the dynamic response may be determined by the relative displacement of the mass centre $u$. Provided that no plastic deformations develop, the uplifting model yields to the well-known visco-elastic sdof system. However, once uplifting occurs the dynamic response is a result of coupled flexural and rocking oscillations with $u$ and $\theta$ being the independent variables. A highly nonlinear response is unveiled in this mode attributed to $P-\delta$ effects which is amplified by the flexural deformation of the superstructure.

The independent variables and the system parameters of the uplifting oscillator are summarised in Table 3.3.

**Table 3.3** Independent variables and system parameters of the uplifting oscillator.

| | | |
|---|---|---|
| $u$ | Structural (relative) displacement | Independent variables |
| $\theta$ | Rocking angle | |
| $\tan\theta_c = b/h$ | Aspect ratio | Inverted pendulum parameters |
| $p$ | Frequency (size) parameter | |
| $\omega$ | Natural frequency | Harmonic oscillator parameters |
| $\xi$ | Critical damping ratio | |

Muto *et al.* (1960) first incorporated such a structural model to investigate experimentally the effect of the structural flexibility on the uplifting response. Meek (1975) utilised the same model to derive the equations of motion and to calculate the response for a harmonic base excitation. In these pioneering articles the beneficial effects of foundation uplift on the dynamic distress of the structure were demonstrated. Substantial contribution to the analysis of the uplifting response has been also provided by subsequent researchers, mainly by Psycharis (1983, 1991), Yim and Chopra (1985), and more recently by Oliveto *et al.* (2003).

All previous analytical studies have been based on a small-displacement approach, which is not suitable for near-overturning conditions. Only Oliveto *et al.* (2003) derived equations of motion

appropriate to large rotations (but small elastic deformations of the pier). A large displacement approach is involved in this study for both rocking and flexural modes of response. In this respect, a *Lagrangian* non-linear formulation is utilised to extract the equations of motion for the one-storey structure portrayed in Fig. 3.20. To this extent the governing equation of motion can be expressed as a function of the Lagrangian $\mathcal{L}$ in the following compact form:

$$\frac{\mathrm{d}}{\mathrm{d}t}\left(\frac{\partial \mathcal{L}}{\partial \dot{q}_i}\right) - \frac{\partial \mathcal{L}}{\partial q_i} + \frac{\partial D}{\partial \dot{q}_i} = 0 \qquad [3.26]$$

where $q_i$ is the generalised variable and $D$ is the dissipation function adopted to incorporate hysteretic damping. The Lagrangian function is defined as the difference between the kinetic energy $T$ and the potential energy $V$:

$$\mathcal{L} = T - V \qquad [3.27]$$

The generalised variables of the system comprise the angle of rocking rotation $\theta\left(=q_\theta\right)$ and the relative (flexural) displacement of the mass centre $u\left(=q_u\right)$.

The kinematics of the system employed to formulate the Lagrangian equations of motion are portrayed in Fig. 3.21. The horizontal supporting base is represented with a rigid plane which can undergo horizontal and vertical vibrations relative to the inertial frame $XY$. The position of the mass point relative to the base is determined with respect to the frame $xy$ which is parallel to inertial frame and fixed to the contact point.

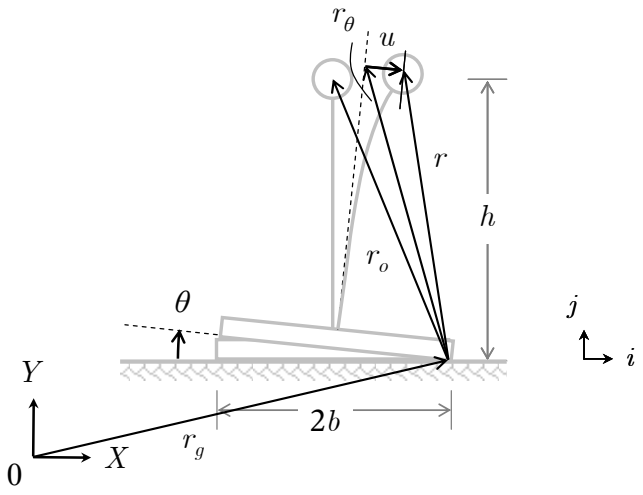


**Figure 3.21** Kinematics of the sdof uplifting oscillator.

The absolute position vector (with respect to the inertial frame) to the centre of mass is given by:

$$\vec{r}_t = \vec{r}_g + \vec{r}_\theta + \vec{u} \qquad [3.28]$$

where $\vec{r}_g = x_g\hat{i} + y_g\hat{j}$ is the position vector of the contact point with $\hat{i}$ and $\hat{j}$ being respectively the horizontal and vertical unit vectors. $\vec{r}_\theta = R\hat{r}_\theta$ is the relative position vector of the mass centre due to rocking rotation, and $\vec{u} = u\hat{s}$ is the relative position vector of the mass centre due to flexural oscillation of the superstructure. The formulation of the vectors $\vec{r}_\theta$ and $\vec{u}$ and their time derivatives with reference to the inertial frame is obtained by examming all possible directions of rocking and flexural displacement as shown in Fig. 3.22. To this end the unit vectors $\hat{r}_\theta$ and $\hat{s}$ are expressed with reference to the inertial frame:

$$\hat{r}_\theta = -\sin\left(\operatorname{sgn}\theta\,\theta_c - \theta\right)\hat{i} + \cos\left(\operatorname{sgn}\theta\,\theta_c - \theta\right)\hat{j} \qquad [3.29a]$$

and

$$\hat{s} = \cos\theta\,\hat{i} - \sin\theta\,\hat{j} \qquad [3.29b]$$

where $\operatorname{sgn}\bullet$ is the signum function.

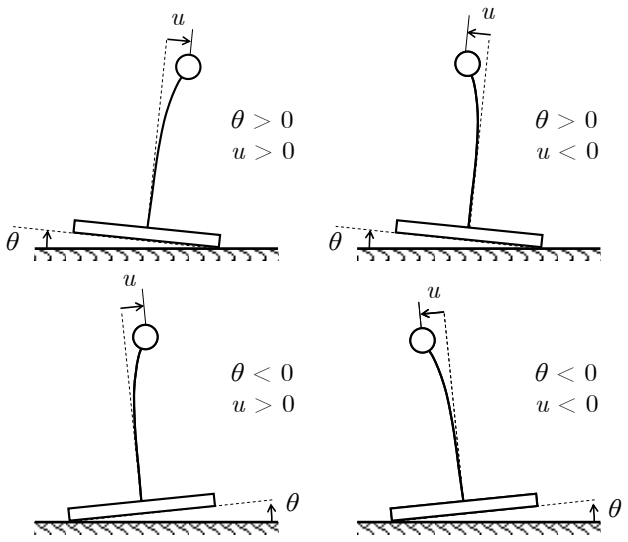


**Figure 3.22** The different modes of the uplifting response.

Finally, the following expressions are derived satisfying the above combinations:

$$\vec{u} = u\cos\theta\,\hat{i} - u\sin\theta\,\hat{j} \qquad [3.30a]$$

$$\frac{\mathrm{d}\vec{u}}{\mathrm{d}t} = \left(\dot{u}\cos\theta - u\dot{\theta}\sin\theta\right)\hat{i} - \left(\dot{u}\sin\theta + u\dot{\theta}\cos\theta\right)\hat{j} \qquad [3.30b]$$

$$\vec{r}_\theta = -R\sin\left(\operatorname{sgn}\theta\,\theta_c - \theta\right)\hat{i} + R\cos\left(\operatorname{sgn}\theta\,\theta_c - \theta\right)\hat{j} \qquad [3.30c]$$

$$\frac{\mathrm{d}\vec{r}_\theta}{\mathrm{d}t} = R\dot{\theta}\cos\left(\operatorname{sgn}\theta\,\theta_c - \theta\right)\hat{i} + R\dot{\theta}\sin\left(\operatorname{sgn}\theta\,\theta_c - \theta\right)\hat{j} \qquad [3.30d]$$

where the dot symbol indicates differentiation with respect to time. The absolute velocity vector is derived by differentiating $\vec{r}_t$ with respect to time:

$$\vec{v} = \frac{\mathrm{d}\vec{r}_t}{\mathrm{d}t} = \frac{\mathrm{d}\vec{r}_g}{\mathrm{d}t} + \frac{\mathrm{d}\vec{r}_\theta}{\mathrm{d}t} + \frac{\mathrm{d}\vec{u}}{\mathrm{d}t} \qquad [3.31]$$

where $\frac{\mathrm{d}\vec{r}_g}{\mathrm{d}t} = \dot{x}_g\hat{i} + \dot{y}_g\hat{j}$ is the velocity vector of the contact point. Also, $\frac{\mathrm{d}\vec{u}}{\mathrm{d}t}$ and $\frac{\mathrm{d}\vec{r}_\theta}{\mathrm{d}t}$ are given by Eqs 3.30b and 3.30d respectively. Finally we get:

$$\begin{aligned}\vec{v} \;=\; &\left[\dot{x}_g + R\dot{\theta}\cos\left(\operatorname{sgn}\theta\,\theta_c - \theta\right) + \dot{u}\cos\theta - u\dot{\theta}\sin\theta\right]\hat{i} \\ &+\left[\dot{y}_g + R\dot{\theta}\sin\left(\operatorname{sgn}\theta\,\theta_c - \theta\right) - \dot{u}\sin\theta - u\dot{\theta}\cos\theta\right]\hat{j}\end{aligned} \qquad [3.32]$$

and therefore:

$$\vec{v}\cdot\vec{v} \;=\; v_x^2 \;+\; v_y^2 \qquad [3.33a]$$

or

$$\begin{aligned}\vec{v}\cdot\vec{v} \;=\; &\left(\dot{x}_g + R\dot{\theta}\cos\left(\operatorname{sgn}\theta\,\theta_c - \theta\right) + \dot{u}\cos\theta - u\dot{\theta}\sin\theta\right)^2 \\ &+\left(\dot{y}_g + R\dot{\theta}\sin\left(\operatorname{sgn}\theta\,\theta_c - \theta\right) - \dot{u}\sin\theta - u\dot{\theta}\cos\theta\right)^2\end{aligned} \qquad [3.33b]$$

Eventually after some algebraic manipulations:

$$\begin{aligned}\vec{v}\cdot\vec{v} \;=\; &\dot{x}_g^2 + \dot{y}_g^2 + R^2\dot{\theta}^2 + \dot{u}^2 + u^2\dot{\theta}^2 \\ &+2\dot{x}_g R\dot{\theta}\left[\cos\theta_c\cos\theta + \operatorname{sgn}\theta\sin\theta_c\sin\theta\right] + 2\dot{y}_g R\dot{\theta}\left[-\cos\theta_c\sin\theta + \operatorname{sgn}\theta\sin\theta_c\cos\theta\right] \\ &+2\dot{x}_g\dot{u}\cos\theta - 2\dot{y}_g\dot{u}\sin\theta - 2\dot{x}_g u\dot{\theta}\sin\theta - 2\dot{y}_g u\dot{\theta}\cos\theta \\ &+2R\dot{\theta}\,\dot{u}\cos\theta_c - 2R\dot{\theta}^2\,u\operatorname{sgn}\theta\sin\theta_c\end{aligned} \qquad [3.33c]$$

The kinetic energy of the system is:

$$T \;=\; \frac{1}{2}m\,\vec{v}\cdot\vec{v} \qquad [3.34a]$$

or

$$\begin{aligned} T &= \frac{1}{2}m\dot{x}_g^2+\frac{1}{2}m\dot{y}_g^2+\frac{1}{2}mR^2\dot{\theta}^2+\frac{1}{2}m\dot{u}^2+\frac{1}{2}mu^2\dot{\theta}^2 \\ &+m\dot{x}_gR\dot{\theta}\left[\cos\theta_c\cos\theta+\operatorname{sgn}\theta\sin\theta_c\sin\theta\right]+m\dot{y}_gR\dot{\theta}\left[-\cos\theta_c\sin\theta+\operatorname{sgn}\theta\sin\theta_c\cos\theta\right] \\ &+m\dot{x}_g\dot{u}\cos\theta-m\dot{y}_g\dot{u}\sin\theta-m\dot{x}_gu\dot{\theta}\sin\theta-m\dot{y}_gu\dot{\theta}\cos\theta \\ &+mR\dot{\theta}\dot{u}\cos\theta_c-mR\dot{\theta}^2u\operatorname{sgn}\theta\sin\theta_c \end{aligned} \qquad [3.34b]$$

The potential energy of the system is

$$V=V_{gravity}+V_{flexural} \qquad [3.35]$$

in which $V_{gravity}=mg\vec{r}_t\,\hat{j}$ is the potential energy due to gravity and $V_{flexural}=\frac{1}{2}ku^2$ is the potential energy due to flexural deformations of the superstructure. However, the quantity $\vec{r}_t\,\hat{j}$ in the former is the vertical component of the position vector $r_y=y_g+R\cos\left(\operatorname{sgn}\theta\theta_c-\theta\right)-u\sin\theta$. Eventually, the potential energy of the system becomes:

$$V=mgRy_g+mgR\cos\theta_c\cos\theta+mgR\operatorname{sgn}\theta\sin\theta_c\sin\theta-mgu\sin\theta+\frac{1}{2}ku^2 \qquad [3.36]$$

By substitution of Eqs 3.34b and 3.36 to Eq. 3.28 we can formulate the Lagrangian of the system as a function of the independent variables and their time derivatives:

$$\begin{aligned} \mathcal{L} &= \frac{1}{2}m\dot{x}_g^2+\frac{1}{2}m\dot{y}_g^2+\frac{1}{2}mR^2\dot{\theta}^2+\frac{1}{2}m\dot{u}^2+\frac{1}{2}mu^2\dot{\theta}^2 \\ &+m\dot{x}_gR\dot{\theta}\left[\cos\theta_c\cos\theta+\operatorname{sgn}\theta\sin\theta_c\sin\theta\right]+m\dot{y}_gR\dot{\theta}\left[-\cos\theta_c\sin\theta+\operatorname{sgn}\theta\sin\theta_c\cos\theta\right] \\ &+m\dot{x}_g\dot{u}\cos\theta-m\dot{y}_g\dot{u}\sin\theta-m\dot{x}_gu\dot{\theta}\sin\theta-m\dot{y}_gu\dot{\theta}\cos\theta \\ &+mR\dot{\theta}\dot{u}\cos\theta_c-mR\dot{\theta}^2u\operatorname{sgn}\theta\sin\theta_c \\ &-mgRy_g-mgR\cos\theta_c\cos\theta-mgR\operatorname{sgn}\theta\sin\theta_c\sin\theta+mgu\sin\theta-\frac{1}{2}ku^2 \end{aligned} \qquad [3.37]$$

The derivatives of the Lagrangian with respect to $\theta$ and $\dot{\theta}$ are:

$$\begin{aligned}\frac{\partial \mathcal{L}}{\partial \theta} =& -m\ddot{x}_g R\dot{\theta}\cos\theta_c\sin\theta + m\ddot{x}_g R\dot{\theta}\,\mathrm{sgn}\,\theta\sin\theta_c\cos\theta - m\ddot{y}_g R\dot{\theta}\,\mathrm{sgn}\,\theta\sin\theta_c\sin\theta \\ & -m\ddot{y}_g R\dot{\theta}\cos\theta_c\cos\theta - m\ddot{x}_g\dot{u}\sin\theta - m\ddot{y}_g\dot{u}\cos\theta - m\ddot{x}_g u\dot{\theta}\cos\theta \\ & +m\ddot{y}_g u\dot{\theta}\sin\theta + mgR\cos\theta\sin\theta - mgR\,\mathrm{sgn}\,\theta\sin\theta_c\cos\theta + mgu\cos\theta\end{aligned} \quad [3.38a]$$

and

$$\begin{aligned}\frac{\partial \mathcal{L}}{\partial \dot{\theta}} =& \; mR^2\dot{\theta} + mu^2\dot{\theta} + m\dot{x}_g R\left[\cos\theta_c\cos\theta + \mathrm{sgn}\,\theta\sin\theta_c\sin\theta\right] \\ & +m\dot{y}_g R\left[-\cos\theta_c\sin\theta + \mathrm{sgn}\,\theta\sin\theta_c\cos\theta\right] - m\dot{x}_g u\sin\theta \\ & -m\dot{y}_g u\cos\theta + mR\dot{u}\cos\theta_c - 2mR\dot{\theta}\,u\,\mathrm{sgn}\,\theta\sin\theta_c\end{aligned} \quad [3.38b]$$

By differentiating Eq 3.38b with respect to time we get:

$$\begin{aligned}\frac{\mathrm{d}}{\mathrm{d}t}\left(\frac{\partial \mathcal{L}}{\partial \dot{\theta}}\right) =& \; mR^2\ddot{\theta} + mu^2\ddot{\theta} + 2mu\dot{\theta}\dot{u} \\ & +m\ddot{x}_g R\cos\theta_c\cos\theta - m\dot{x}_g R\cos\theta_c\sin\theta\dot{\theta} + m\ddot{x}_g R\,\mathrm{sgn}\,\theta\sin\theta_c\sin\theta + m\dot{x}_g R\,\mathrm{sgn}\,\theta\sin\theta_c\cos\theta\dot{\theta} \\ & -m\ddot{y}_g R\cos\theta_c\sin\theta - m\dot{y}_g R\cos\theta_c\cos\theta\dot{\theta} + m\ddot{y}_g R\,\mathrm{sgn}\,\theta\sin\theta_c\cos\theta - m\dot{y}_g R\,\mathrm{sgn}\,\theta\sin\theta_c\sin\theta\dot{\theta} \\ & -m\ddot{x}_g u\sin\theta - m\dot{x}_g\dot{u}\sin\theta - m\dot{x}_g u\dot{\theta}\cos\theta - m\ddot{y}_g u\cos\theta - m\dot{y}_g\dot{u}\cos\theta + m\dot{y}_g u\dot{\theta}\sin\theta \\ & +mR\ddot{u}\cos\theta_c - 2mR\ddot{\theta}\,u\,\mathrm{sgn}\,\theta\sin\theta_c - 2mR\dot{\theta}\,\dot{u}\,\mathrm{sgn}\,\theta\sin\theta_c\end{aligned} \quad [3.39]$$

The dissipation function is:

$$D = \frac{1}{2}c\,\dot{u}^2 \quad [3.40]$$

Its derivative with respect to $\dot{\theta}$ is:

$$\frac{\partial D}{\partial \dot{\theta}} = 0 \quad [3.41]$$

The first equation of motion is:

$$\frac{\mathrm{d}}{\mathrm{d}t}\left(\frac{\partial \mathcal{L}}{\partial \dot{\theta}}\right) - \frac{\partial \mathcal{L}}{\partial \theta} + \frac{\partial D}{\partial \dot{\theta}} = 0 \quad [3.42a]$$

and after substituting and eliminating $m$:

$$\begin{gathered}\left(R^2+u^2-2Ru\,\mathrm{sgn}\,\theta\sin\theta_c\right)\ddot{\theta}+R\cos\theta_c\ddot{u}\\+\ddot{x}_g\left[R\cos\left(\mathrm{sgn}\,\theta\,\theta_c-\theta\right)-u\sin\theta\right]+\ddot{y}_g\left[R\sin\left(\mathrm{sgn}\,\theta\,\theta_c-\theta\right)-u\cos\theta\right]\\+gR\sin\left(\mathrm{sgn}\,\theta\,\theta_c-\theta\right)-gu\cos\theta+2\dot{u}\dot{\theta}\left(u-R\,\mathrm{sgn}\,\theta\sin\theta_c\right)=0\end{gathered} \quad [3.42b]$$

Similarly, the derivatives of the Lagrangian with respect to $u$ and $\dot{u}$ are:

$$\frac{\partial\mathcal{L}}{\partial u}=m\dot{\theta}^2u-m\dot{x}_g\dot{\theta}\sin\theta-m\dot{y}_g\dot{\theta}\cos\theta-mR\dot{\theta}^2\,\mathrm{sgn}\,\theta\sin\theta_c+mg\sin\theta-ku \quad [3.43a]$$

and

$$\frac{\partial\mathcal{L}}{\partial\dot{u}}=m\dot{u}+m\dot{x}_g\cos\theta-m\dot{y}_g\sin\theta+mR\dot{\theta}\cos\theta_c \quad [3.43b]$$

By differentiating Eq 3.43b with respect to time we get:

$$\frac{\mathrm{d}}{\mathrm{d}t}\left(\frac{\partial\mathcal{L}}{\partial\dot{u}}\right)=m\ddot{u}+m\ddot{x}_g\cos\theta-m\dot{x}_g\sin\theta\dot{\theta}-m\ddot{y}_g\sin\theta-m\ddot{y}_g\cos\theta\dot{\theta}+mR\ddot{\theta}\cos\theta_c \quad [3.44]$$

The derivative of the dissipation function with respect to $\dot{u}$ is:

$$\frac{\partial D}{\partial\dot{u}}=c\dot{u} \quad [3.45]$$

The second equation of motion is:

$$\frac{\mathrm{d}}{\mathrm{d}t}\left(\frac{\partial\mathcal{L}}{\partial\dot{u}}\right)-\frac{\partial\mathcal{L}}{\partial u}+\frac{\partial D}{\partial\dot{u}}=0 \quad [3.46a]$$

and after substituting and eliminating $m$:

$$\ddot{u}+R\cos\theta_c\ddot{\theta}-g\sin\theta+\omega^2u+\ddot{x}_g\cos\theta-\ddot{y}_g\sin\theta-\dot{\theta}^2\left(u-R\,\mathrm{sgn}\,\theta\sin\theta_c\right)+2\xi\omega\dot{u}=0 \quad [3.46b]$$

Eqs 3.42b and 3.46b form the Lagrangian equations of motion for the studied system.

The structural mass has been eliminated from the governing equations of motion as in the case of a rigid rocking body or a harmonic oscillator.

In the limiting case of a infinitely rigid system $(\omega = 0)$ Eq. 3.46b yields $u = 0$. In this way Eq. 3.42b reduces to the following equation:

$$R^2\ddot{\theta} + \ddot{x}_g\left[R\cos\left(\text{sgn}\,\theta\,\theta_c - \theta\right)\right] + \ddot{y}_g\left[R\sin\left(\text{sgn}\,\theta\,\theta_c - \theta\right)\right] + gR\sin\left(\text{sgn}\,\theta\,\theta_c - \theta\right) = 0 \qquad [3.47a]$$

or

$$\ddot{\theta} + p^2\frac{\ddot{x}_g}{g}\left[\cos\left(\text{sgn}\,\theta\,\theta_c - \theta\right)\right] + p^2\frac{\ddot{y}_g}{g}\left[\sin\left(\text{sgn}\,\theta\,\theta_c - \theta\right)\right] + p^2\sin\left(\text{sgn}\,\theta\,\theta_c - \theta\right) = 0 \qquad [3.47b]$$

The latter is the well-known rocking equation of motion for a rigid structure with a lumped-mass ( $p = \sqrt{g/R}$ ) as described in Eq. 3.2.

For simplicity we neglect the vertical component of the base acceleration $\ddot{y}_g$. In this way, the following nonlinear equations of motion are derived in each state of response:

***Full-contact phase*:**

For a rocking oscillator on a rigid base, full-contact conditions entail that no rocking displacements are developed $(\theta = 0)$. In this regime Eq. 3.46b reduces to the well-known linear equation of the sdof oscillator:

$$\ddot{u} + \omega^2 u + 2\xi\omega\dot{u} = -\ddot{x}_g \qquad [3.48]$$

***Uplift phase*:**

During the uplift regime the independent variables $u$ and $\theta$ are calculated by the Lagrange formulation:

*Equation Lagrange (1)*

$$\left[R^2 + u^2 - 2Ru\,\mathrm{sgn}\,\theta\sin\theta_c\right]\ddot{\theta} + R\cos\theta_c\ddot{u} + gR\sin(\mathrm{sgn}\,\theta\theta_c - \theta) - ug\cos\theta + \mathrm{O}_1(u,\dot{u},\theta,\dot{\theta}) = -\ddot{x}_g\left[R\cos(\mathrm{sgn}\,\theta\theta_c - \theta) - u\sin\theta\right] \qquad [3.49a]$$

*Equation Lagrange (2)*

$$\ddot{u} + R\cos\theta_c\ddot{\theta} - g\sin\theta + \omega^2 u + 2\xi\omega\dot{u} - \mathrm{O}_2(u,\theta,\dot{\theta}) = -\ddot{x}_g\cos\theta \qquad [3.49b]$$

where $\mathrm{O}_1(u,\dot{u},\theta,\dot{\theta})$ and $\mathrm{O}_2(u,\theta,\dot{\theta})$ the non-linear terms $\mathrm{O}_1(u,\dot{u},\theta,\dot{\theta}) = 2\dot{u}\dot{\theta}(u - R\,\mathrm{sgn}\,\theta\sin\theta_c)$ and $\mathrm{O}_2(u,\theta,\dot{\theta}) = \dot{\theta}^2(u - R\,\mathrm{sgn}\,\theta\sin\theta_c)$. These two equations of motion can be formed in a matrix equation:

$$\begin{bmatrix} R^2 + u^2 - 2Ru\,\mathrm{sgn}\,\theta\sin\theta_c & R\cos\theta_c \\ R\cos\theta_c & 1 \end{bmatrix}\cdot\begin{bmatrix}\ddot{\theta}\\ \ddot{u}\end{bmatrix} + \begin{bmatrix}0 & 0\\ 0 & 2\xi\omega\end{bmatrix}\cdot\begin{bmatrix}\dot{\theta}\\ \dot{u}\end{bmatrix} + \begin{bmatrix}0 & -g\cos\theta\\ 0 & \omega^2\end{bmatrix}\cdot\begin{bmatrix}\theta\\ u\end{bmatrix} + \begin{bmatrix}gR\sin(\mathrm{sgn}\,\theta\theta_c - \theta)\\ -g\sin\theta\end{bmatrix} + \mathbf{O} = -\ddot{x}_g\begin{bmatrix}R\cos(\mathrm{sgn}\,\theta\theta_c - \theta) - u\sin\theta\\ \cos\theta\end{bmatrix} \qquad [3.50]$$

### *Uplift criterion*

The foundation uplifts from the supporting rigid soil when the overturning moment (with reference to the foundation centre) due to inertia moments $(mah)$ exceeds the restoring moment $\left[mg(b-u)\right]$. From this moment on, the structural system enters a coupled flexural-rocking oscillation with the corner points O and O' being alternately the rotation pole. From equilibrium of the overturning and the restoring moment the acceleration of the mass at marginal uplift is:

$$a_{uplift} = \frac{b - u_{uplift}}{h} g \qquad [3.51]$$

For an undamped system, the uplifting criterion can be also expressed in the form of the displacement $u_{uplift}$ given that $\omega^2 u_{uplift} = a_{uplift} g$:

$$u_{uplift} = \frac{\tan\theta_c / \omega^2}{\frac{1}{\left(\omega / p\right)^2 \cos\theta_c} + 1} g \qquad [3.52]$$

For $\omega / p \to \infty$ (i.e. for a quite stiff or large structure) the latter equation reduces to the well-known criterion for uplift, originally presented by Meek (1975):

$$u_{uplift} = \frac{\tan\theta_c}{\omega^2} g \qquad [3.53]$$

The normalised displacement $u_{uplift} / b$ calculated with the exact uplift criterion of Eq. 3.52 is plotted in Fig. 3.23 with respect to the natural circular frequency $\omega$ for different values of the frequency parameter $p$ and constant aspect ratio $\left(\theta_c = 0.2 \text{ rad}\right)$. In the same graph the uplifting displacement is compared to that extracted with the simplified approach (Eq. 3.53). It is shown that for sufficiently stiff systems, Meek's criterion may give a close approximation of the uplifting displacement. For more

flexible systems however $(\omega < 2-3 \text{ rad/sec})$, and particularly for quite small structures $(p > 1 \text{ rad/sec})$ the simplified approach fails to accurately predict the displacement $u_{uplift}$.

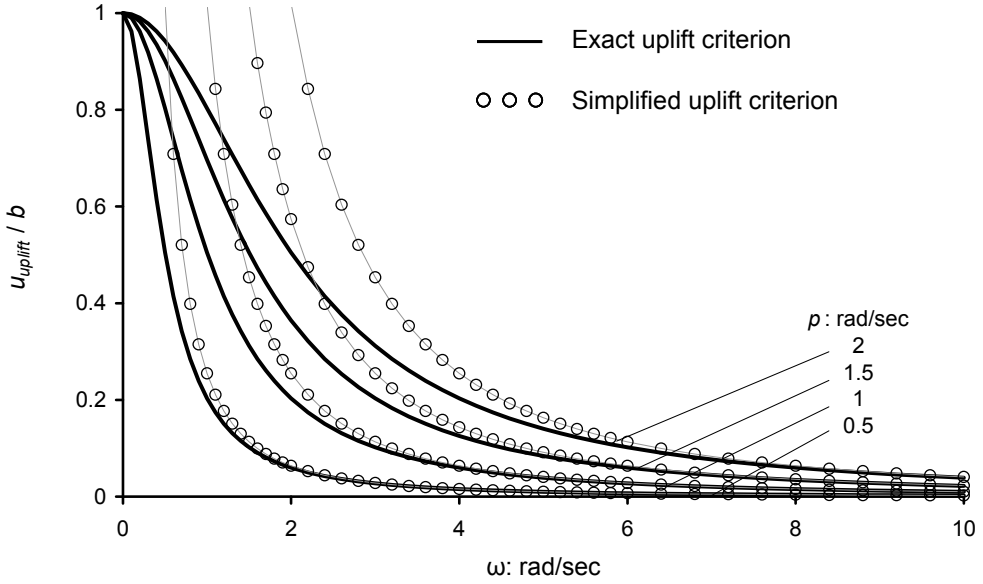


**Figure 3.23** Comparison of the normalised displacement $u_{uplift}/b$ derived from the exact uplift criterion (Eq. 3.52) to that extracted with the simplified approach (Eq. 3.53), for different values of the size parameter $p$. The aspect ratio of the structure is $\theta_c = 0.2$ rad.

### *Re-establishment of full-contact*

After the uplift phase is launched, impacts occur intermittently every time the foundation mat instantaneously rocks back to its initial position. For analysis purposes of this study, the impact is considered elastic, hence conservation of angular momentum exists and the coefficient of restitution is obtained by Eq. 3.7b. Whether the structure continues to rock after an impact by shifting direction or full-contact conditions are re-established, it depends upon the total energy of the uplifting phase $\left(E_{up.phase}\right)$ compared to that of the full contact phase $\left(E_{f.c.phase}\right)$. Hence, if the total energy in the uplifting phase right after impact is smaller than the full contact energy, $\left(E_{up.phase} < E_{f.c.phase}\right)$, the structure will be set on rocking again in the reverse direction. Nevertheless, in the opposite case, $\left(E_{f.c.phase} \le E_{up.phase}\right)$, the structure may still uplift if the overturning moment due to inertial force,

$M_i$, is larger than the available resisting moment due to gravity $M_G$. Consequently, the system returns to full contact conditions if the two following conditions are satisfied simultaneously.

$$E_{f.c.phase} \le E_{up.phase} \quad [3.54a]$$

$$\left|M_G\right| > \left|M_i\right| \quad [3.54b]$$

In contrast to early studies on the uplifting oscillator, the exact formulation for re-establishment of full contact as described above was introduced by Oliveto *et al.*, 2003.

### *Linearisation of the uplifting equations*

**Meek (1991).** In this pioneering work, Meek first studied analytically the undamped uplifting oscillator and extracted the linearised equations of motion in the small-displacement domain. To this extent, he examined dynamic forces equilibrium of the mass and moment equilibrium of the structural system about the foundation toe. Considering only the horizontal component of the mass displacement $\left(h\theta + u\right)$ Meek concluded with the following coupled equations for the uplift regime in matrix notation:

$$\begin{bmatrix} 1/\cos^2\theta_c & 1 \\ 1 & 1 \end{bmatrix} \cdot \begin{bmatrix} h\ddot{\theta} \\ \ddot{u} \end{bmatrix} + \begin{bmatrix} 0 & 0 \\ 0 & \omega^2 \end{bmatrix} \cdot \begin{bmatrix} h\theta \\ u \end{bmatrix} = -\ddot{x}_g \begin{bmatrix} 1 \\ 1 \end{bmatrix} - g\,\mathrm{sgn}\,\theta \tan\theta_c \begin{bmatrix} 1 \\ 0 \end{bmatrix} \quad [3.55]$$

By eliminating the rocking component of the structural acceleration, $h\ddot{\theta}$, and after some algebraic manipulations the uncoupled equations of motion are obtained:

$$h\ddot{\theta} - \frac{\omega^2}{\tan^2\theta_c} u = -\frac{g\,\mathrm{sgn}\,\theta}{\tan\theta_c} \quad [3.56a]$$

$$\ddot{u} + \frac{\omega^2}{\sin^2\theta_c} u = -\ddot{x}_g + \frac{g\,\mathrm{sgn}\,\theta}{\tan\theta_c} \quad [3.56b]$$

In the latter, $\frac{\omega}{\sin\theta_c} \cong \frac{\omega}{\theta_c}$ is the increased natural circular frequency in the uplift regime.

**Chopra and Yim (1985)**. In their study the linearised coupled equations (Eq. 3.55) were re-derived accounting also for the damping terms. In this way, the equations of motion (Eqs 3.56) were written as:

$$h\ddot{\theta} - \frac{2\xi\omega}{\tan^2\theta_c}\dot{u} - \frac{\omega^2}{\tan^2\theta_c}u = -\frac{g\,\mathrm{sgn}\,\theta}{\tan\theta_c} \qquad [3.57a]$$

$$\ddot{u} + \frac{2\xi\omega}{\sin^2\theta_c}\dot{u} + \frac{\omega^2}{\sin^2\theta_c}u = -\ddot{x}_g + \frac{g\,\mathrm{sgn}\,\theta}{\tan\theta_c} \qquad [3.57b]$$

In Eq. 3.57b the quantity $\frac{\xi}{\sin\theta_c} \cong \frac{\xi}{\theta_c}$ corresponds to the increased damping ratio in the uplift regime.

**Psycharis (1991)**. Applying Newton's second law in the horizontal and rocking direction with the assumption of small displacements, Psycharis extracted the equations of motion for the uplift regime, which are identical to those of Eqs 3.57, given that $1+1/\tan^2\theta_c = 1/\sin^2\theta_c$.

**The proposed model**. In the present work, linearised equations of motion are not derived explicitly through a small-displacement configuration but from the exact Lagrange equations (Eqs 3.49) neglecting only the quadratic non-linear terms $(\mathrm{O}_1 \text{ and } \mathrm{O}_2)$. In this way, the coupled equations of motion are written in a matrix form:

$$\begin{bmatrix} R^2 & h \\ h & 1 \end{bmatrix} \cdot \begin{bmatrix} \ddot{\theta} \\ \ddot{u} \end{bmatrix} + \begin{bmatrix} 0 & 0 \\ 0 & 2\xi\omega \end{bmatrix} \cdot \begin{bmatrix} \dot{\theta} \\ \dot{u} \end{bmatrix} + \begin{bmatrix} 0 & -g \\ -g & \omega^2 \end{bmatrix} \cdot \begin{bmatrix} \theta \\ u \end{bmatrix} = -\ddot{x}_g \begin{bmatrix} h \\ 1 \end{bmatrix} - \begin{bmatrix} g\,\mathrm{sgn}\,\theta\, b \\ 0 \end{bmatrix} \qquad [3.57]$$

Eventually, we get for the uplift regime:

$$h\ddot{\theta} + \frac{g}{\tan^2\theta_c}\theta - \frac{2\xi\omega}{\tan^2\theta_c}\dot{u} - \frac{\omega^2 + \left(p^2/\cos\theta_c\right)}{\tan^2\theta_c}u = -\frac{g\,\mathrm{sgn}\,\theta}{\tan\theta_c} \qquad [3.58a]$$

$$\ddot{u}+\frac{2\xi\omega}{\sin^2\theta_c}\dot{u}+\frac{\omega^2+\cos\theta_c\, p^2}{\sin^2\theta_c}u-\frac{g}{\sin^2\theta_c}\theta=-\ddot{x}_g+\frac{g\,\mathrm{sgn}\,\theta}{\tan\theta_c} \qquad [3.58b]$$

### 3.3.2 Earthquake excitation

In a similar way to conventional response spectrum analysis, structural displacement, velocity, or acceleration amplitudes of the uplifting oscillator can be computed as a function of the natural period. In this respect, for a certain geometry (described with the parameters $p$ and $\theta_c$) the time domain analysis (by direct integration of Eqs 3.48 and 3.49) can be repeated each time for a different value of the pier stiffness, $k=3EI/h^3$ (and therefore the natural period). Thus, response spectra can be computed for different levels of damping.

A one-story oscillator of $p=0.909\,\mathrm{rad/sec}$ and $\theta_c=0.388\,\mathrm{rad}$ is first considered to explore the dynamics of the combined uplifting and flexural response. These dynamic parameters correspond to a half-width of the footing, $b=4.5\,\mathrm{m}$ and height of the mass point from base, $h=11\,\mathrm{m}$. A long duration Ricker wavelet $\left(T_E=1.33\,\mathrm{sec}\right)$ is imposed to represent near-fault moderate and strong shaking ($0.4\,\mathrm{g}$ and $0.6\,\mathrm{g}$ respectively). The response spectra of the normalised displacement are plotted in Fig. 3.24. In the same graphs the response spectra of the equivalent fixed base system are also plotted together with the criterion for incipient uplift. It is remarked that for $T=0$, the response of the uplifting oscillator must also be computed with the equivalent rigid system, discussed above. Under a moderate shaking, a very stiff system cannot experience uplift, as the critical acceleration of the rigid system $\left(a_{uplift}=\tan\theta_c\cong 0.41\,\mathrm{g}\right)$ is slightly larger than the imposed $\left(0.4\,\mathrm{g}\right)$. As the flexibility of the pier increases however, the developing structural displacement (equal to that of the fixed base system) exceeds that required for marginal uplift, engaging rocking motion. The amplitude of rocking angle as a function of the natural period is also plotted in Fig. 3.24. Remarkably, within a range of periods around the excitation period $\left(1.33\,\mathrm{sec}\right)$, the displacements of the uplifting system are much

less than those of the equivalent fixed base system. Eventually, for sufficiently flexible systems (i.e. for values of $T$ larger than a critical one), uplift cannot initiate and therefore, the response can be predicted with the fixed base system. As observed in Fig. 3.24, the critical period beyond which uplift does not occur, is larger under strong shaking conditions $(0.6\ \mathrm{g})$. Similar results can be extracted by plotting the acceleration spectra (see also Fig. 3.24)

A flexural-uplifting oscillator with visco-elastic parametres $T_o = 0.5\,\mathrm{sec}$, $\xi = 5\%$ and rocking parametres $p = 1.387\ \mathrm{rad/sec}$, $\theta_c = 0.2\,\mathrm{rad}$ is involved next. The rotation spectrum of the oscillator calculated for different levels of ground shaking is presented in Fig. 3.24. Excitation at the base is a one-sine pulse with a period ranging from 0.01 sec to 2.5 sec. Initially, a weak base excitation $(PGA = 0.10\,\mathrm{g})$ is employed such that a linear resonance curve is obtained with maximum rotation at $f_E \cong f_o = 2\,\mathrm{hz}$. A gradually increasing base acceleration is applied next and the resonance curve is recalculated for each level as plotted in Fig. 3.25. The emerging nonlinearities of the system progressively shift the resonance frequency towards the left side of the spectrum. A large increase of the rotation amplitude is also encountered in this area. Eventually, after a sufficiently strong level of shaking, the resonance curve is distorted such that there is a range of excitation frequencies for which there are more than one possible output amplitudes (*instability area*).

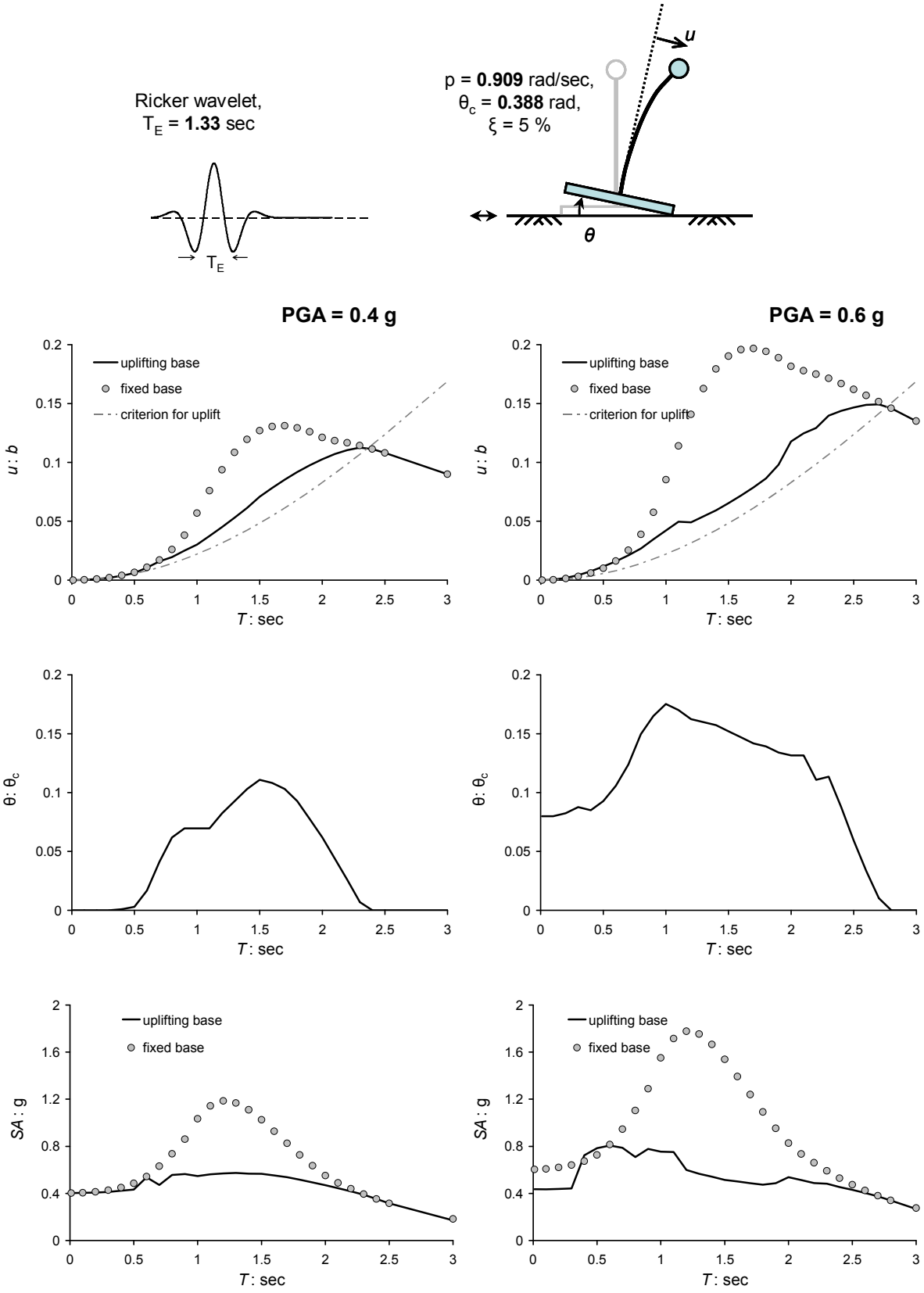


**Figure 3.24** Displacement, rotation, and acceleration spectra of the uplifting oscillator in comparison with the fixed-base system. A long-period (1.33 sec) Ricker pulse is used for moderate (left) and strong shaking (right).

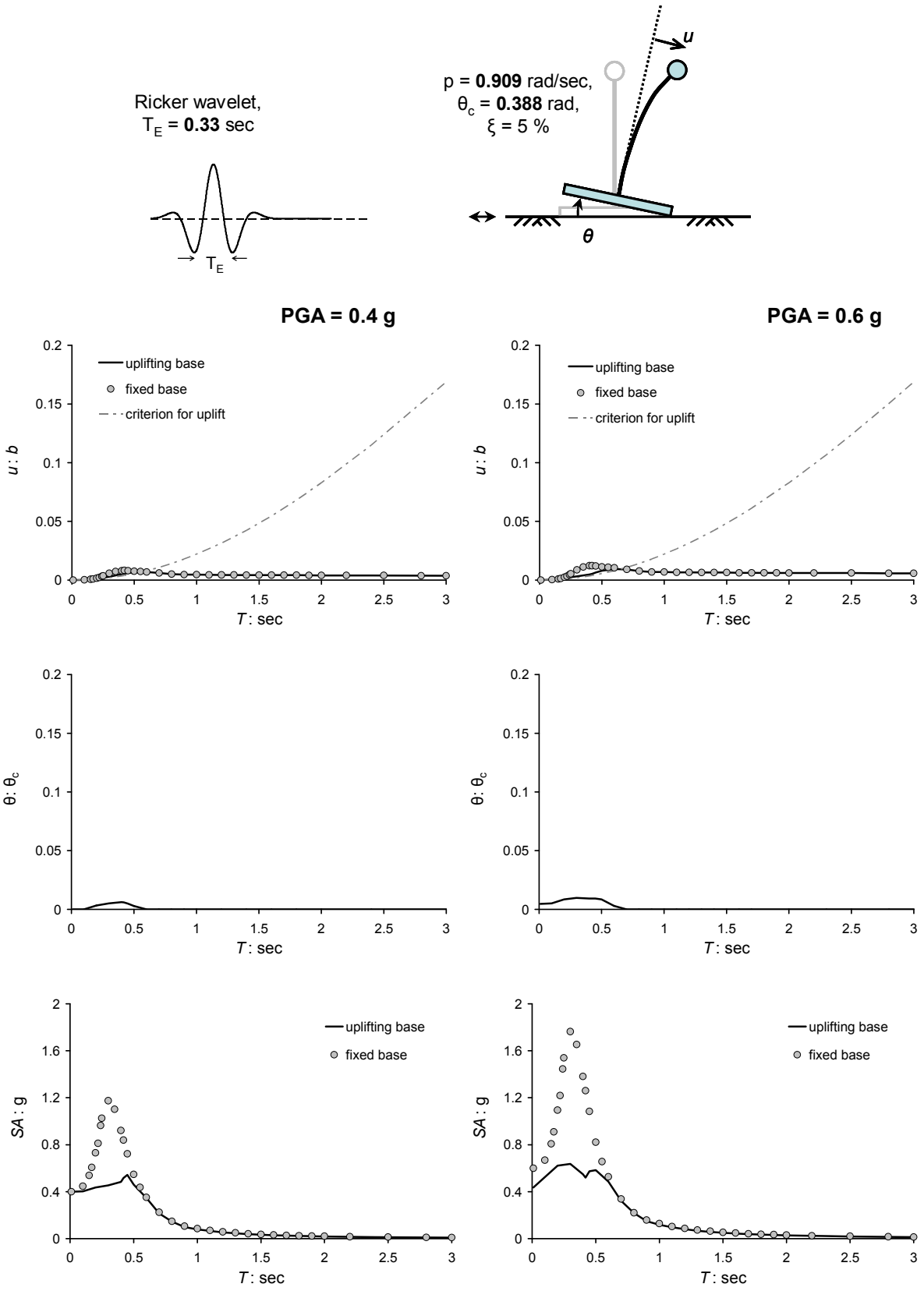


**Figure 3.25** Displacement, rotation, and acceleration spectra of the uplifting oscillator in comparison with the fixed-base system. A short-period (0.33 sec) Ricker pulse is used for moderate (left) and strong shaking (right).

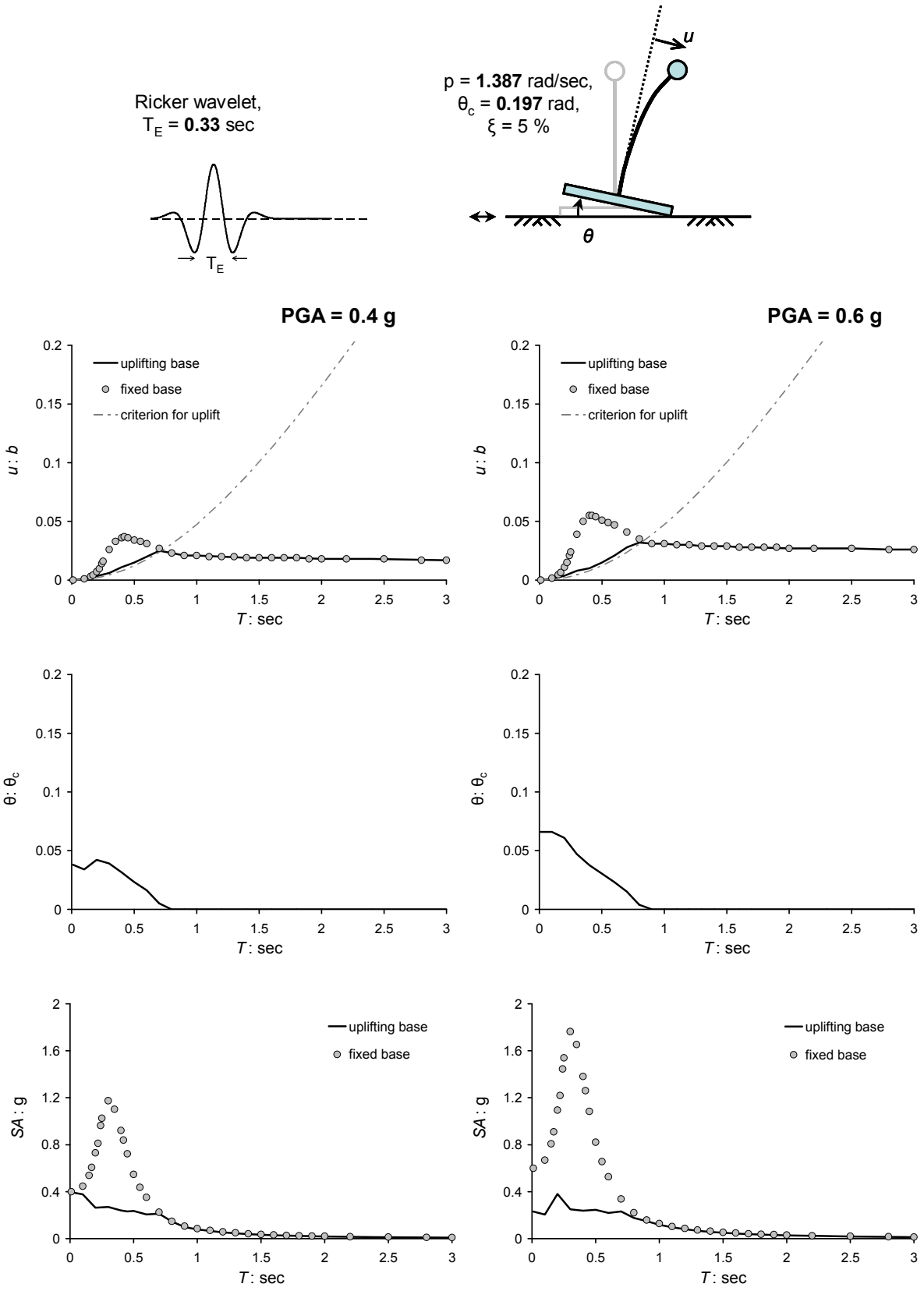


**Figure 3.26** Displacement, rotation, and acceleration spectra of the uplifting oscillator in comparison with the fixed-base system. A short-period (0.33 sec) Ricker pulse is used for moderate (left) and strong shaking (right).

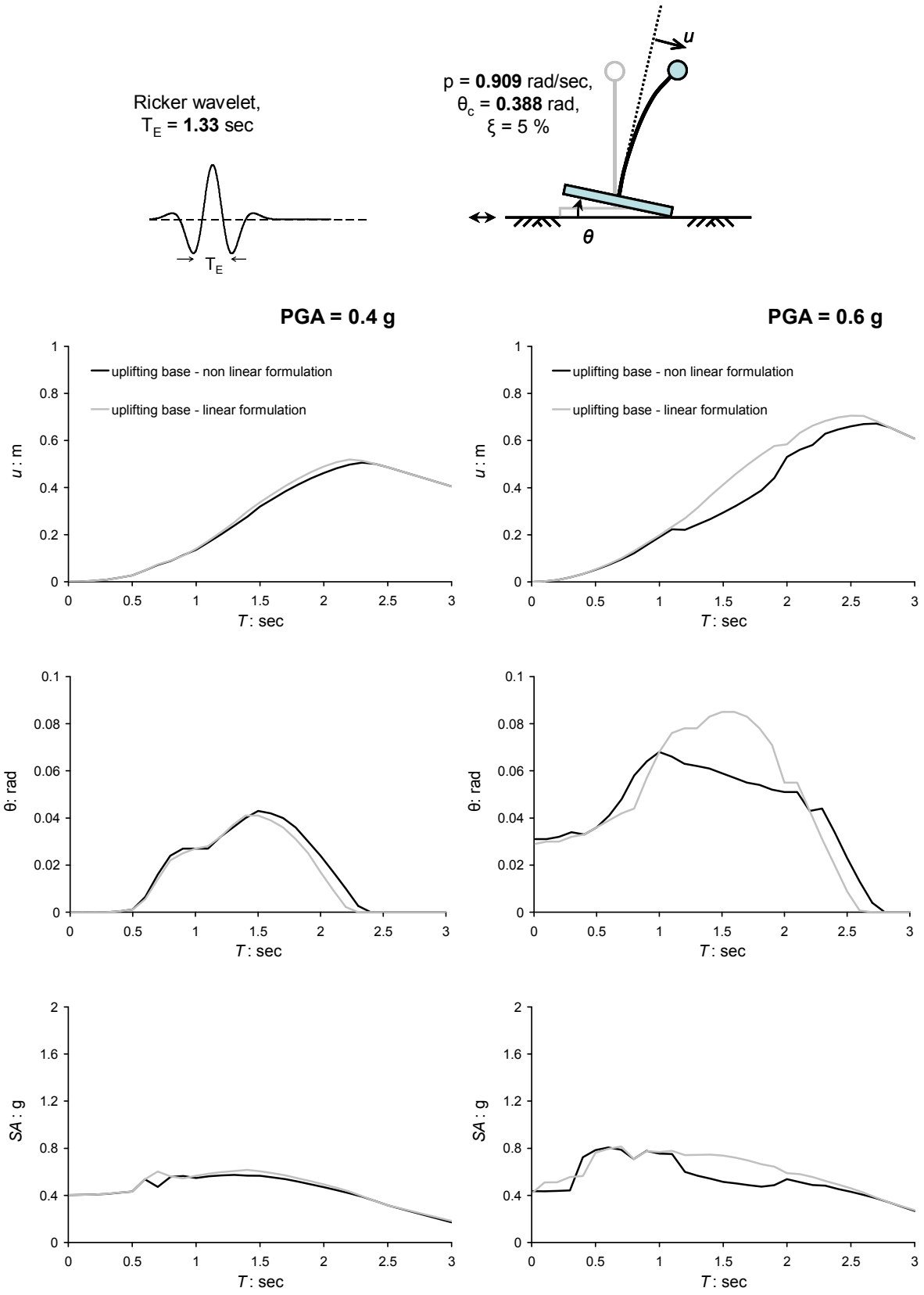


**Figure 3.27** Displacement, rotation, and acceleration spectra of the uplifting oscillator calculated with the linear (grey lines) and the nonlinear formulation (black lines). A long-period (1.33 sec) Ricker pulse is used for moderate (left) and strong shaking (right).

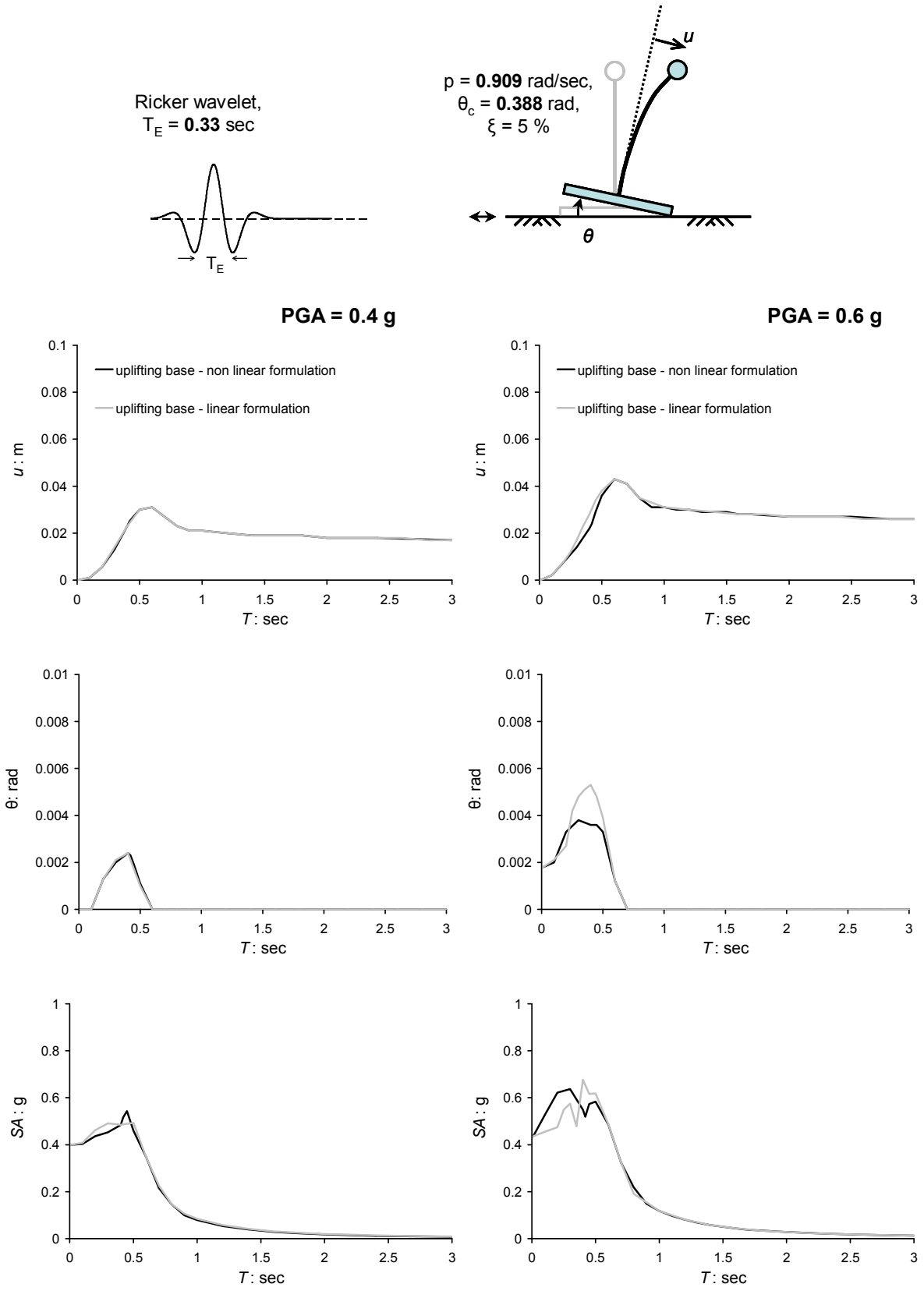


**Figure 3.28** Displacement, rotation, and acceleration spectra of the uplifting oscillator calculated with the linear (grey lines) and the nonlinear formulation (black lines). A short-period (0.33 sec) Ricker pulse is used for moderate (left) and strong shaking (right).

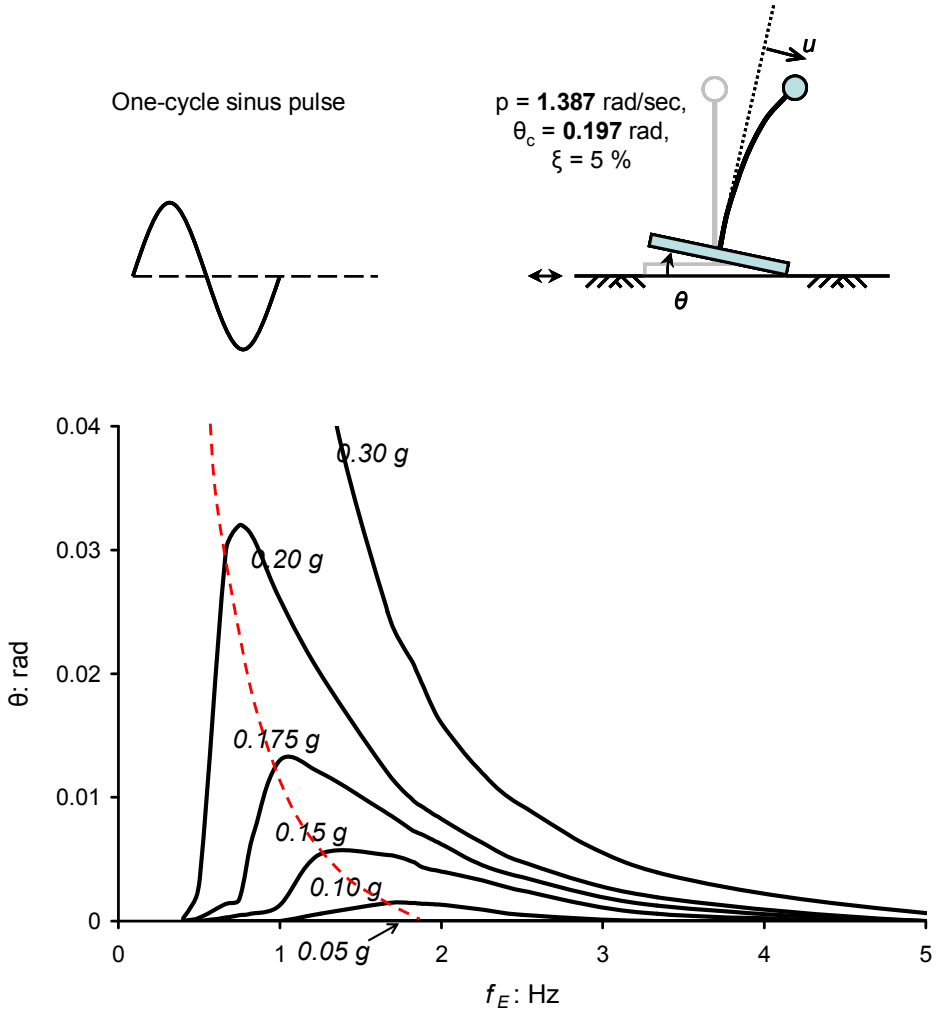


**Figure 3.29** Rotation spectra of the uplifting oscillator with respect to the excitation frequency for different levels of ground shaking. A one-cycle sine pulse is used.

*Chapter 4:*

# Finite element analysis of the uplifting response

## 4.1 INTRODUCTION

In Chapter 3 the dynamic behaviour of a tall structure with a shallow foundation allowed to uplift was explored in depth assuming that the supporting soil is undeformable. Emphasis was given on the (geometrical) nonlinear features of the response, amplified in the large displacement domain due to the gradually developed second order $(P-\delta)$ effects. For some cases such as the analysis of appended equipment, the model of a rocking body on a rigid base may be a reasonable approximation of reality. In civil engineering applications however, the foundation mat is in general supported directly by a soil medium which may experience substantial deformations when undertaking the superstructure loads. Due to soil compliance, a free-standing rigid structure may sustain rocking motion without uplift at low amplitudes of rotation. In this regime, the response can be linear provided that soil material deforms elastically and conventional soil–structure interaction procedures may be applied. For sufficiently large rocking amplitudes though, separation of the footing from the underlying soil occurs and the response alternates between the modes of full contact and uplift. Rocking motion is then nonlinear even under the assumption of elastic soil behaviour. For a very stiff soil, uplifting initiates at a very low rotation and the full contact mode tends to diminish. Hence, rocking is associated with large amplitudes of uplift and the response is similar to the rigid base case. On the contrary, under soft soil conditions, deformations of the supporting soil around the footing edges are significant and impact during the uplifting mode becomes more absorbing. Consequently, dissipation mechanisms (radiation and hysteretic damping) are generated through soil medium, uplift is limited and attenuation of motion is faster. Reasonably, large soil deformations underneath the foundation are accompanied with

generation of plastification zones which further amplifies the dissipative mechanisms and shrinks the uplift mode.

Apart from the size parameter and aspect ratio of the block ($p$ and $\theta_c$ respectively), the main parameters affecting now the dynamics of rocking are:

- the visco-elastic soil properties $G$, $\nu$ and $\xi$ considering homogeneous and isotropic medium,
- the structural weight $N$,
- the presence of bedrock at a shallow depth, and also
- the ultimate load $N_u$, when limited soil strength is implemented in the analysis.

Several analytical studies have been published in the past to elucidate the effect of soil compliance on the uplifting response. In these early studies (Psycharis and Jennings, 1983; Yim and Chopra, 1985; Koh *et al.*, 1986) the underlying soil was represented with distributed tensionless spring-dashpot elements (the *beam-on-winkler-foundation* model). Recently, with the advent of powerful computational resources, some finite element studies have modelled the supporting soil with two-dimensional continuum, either elastic or inelastic (among others Crémer and *et al.*, 2001; Gazetas and Apostolou, 2004). In addition, during the last decade, many experimental studies (primarily centrifuge tests) cast insight on the nonlinear features of the uplifting response (Gajan *et al.*, 2003; Paolucci *et al.*, 2008). Crémer and *et al.*, 2002 also analysed a foundation on inhomogeneous continuum and developed a constitutive law to represent the uplift mechanics in an elastic or elastoplastic soil through a single macro-element. Late studies focused on the macro-element approach aimed at developing simplified yet realistic modelling of soil and foundation (Houlsby and Cassidy, 2002; Gajan and Kutter, 2009; Chatzigogos et al., 2009; Figini et al., 2011). In a parallel path, a new generation of beam-on-winkler-foundation models have been developed to overcome the shortcomings of the early ones (Allotey and El Naggar, 2003, 2008). A detailed review of recently elaborated macro-element models will be discussed in Chapter 5.

In this Chapter, the uplifting response of shallow foundation on compliant soil medium is examined under both monotonic and earthquake loading conditions. The analysis is performed with the finite element method where emphasis is given on the rigorous computation of the response in the domain of large displacements. In this way the results can be utilised to elaborate a sophisticated macro-element model efficient in both static and dynamic analysis.

The system configuration of Fig. 4.1 is considered, comprising a 1-dof structure with shallow foundation supported on deformable soil medium. Compared to the 'rigid soil' problem, the uplifting structure possesses now additional degrees of freedom due to the compliance of the supporting soil. Hence, for such a structural system the independent variables are:

- The horizontal displacement of the footing $u_b$
- The vertical displacement of the footing $w_b$ (upward is positive)
- The rocking rotation of the footing $\theta$
- The contact ratio $\lambda = \beta / b$, where $\beta$ is the half-width of the footing remaining in contact with the soil (from now on *the effective footing*).

For simplicity, in all numerical analyses of this stage the structural system is considered rigid and therefore the superstructure displacements are explicitly derived from the foundation displacements.

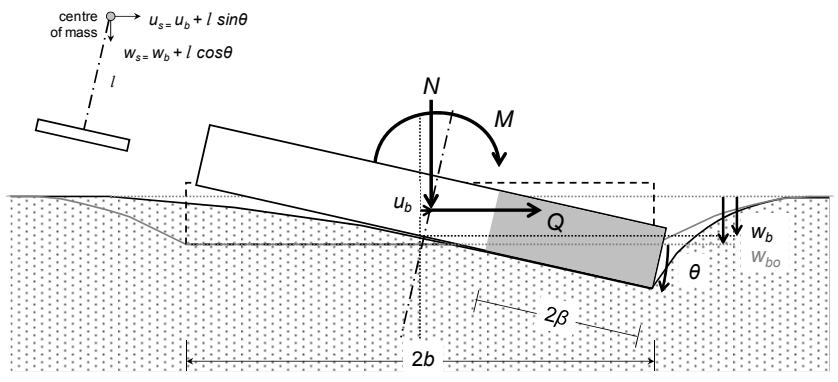


**Figure 4.1** Rocking and uplifting on deformable soil: system configuration.

## 4.2 METHOD of ANALYSIS

### 4.2.1 Finite element modelling

Nonlinear analysis of rocking and uplifting response under static (monotonic) and earthquake loading is implemented numerically with the finite element method. To this extent the sophisticated code *ABAQUS* (Hibbit, Karlsson and Sorensen; 2004) is utilised. In most of the analyses performed in this study the structure and the underlying soil are represented with plane-strain elements. For the purposes of the two- dimensional modelling soil medium is represented with quadrilateral, continuum elements whereas boundary conditions at the far field are described with *infinite* elements. General-section beam elements are utilised to model the superstructure whilst a massless rigid foundation is obtained by a combination of solid and rigid (beam) elements. The structural weight is concentrated at a mass element located at the gravity centre of the superstructure. An advanced contact algorithm has been adopted to incorporate potential slipping or uplifting of the foundation, considering purely elastic impact. To this end soil-foundation interface is modelled with gap elements of zero tensile capacity allowing for a rigorous treatment of finite separation and sliding. The latter is calculated by a Coulomb-type frictional law at the interface. Geometric nonlinearity attributed to $\left(P-\delta\right)$ effects is taken into account through appropriate large displacement formulation. A static step is preceding any static or dynamic analysis to establish geostatic conditions within.

For the analysis of the earthquake response, seismic excitation is imposed to soil medium through the underlying rigid bedrock. In so doing, time histories of recorded earthquake motion or pulse-type *Ricker* wavelets are used. The latter is a very useful tool in numerical wave propagation analysis through soil due to its ability to represent records with distinguishable, long-duration pulses attributed to near-source effects (directivity, fling). An implicit direct-integration algorithm incorporated in the code *ABAQUS* is utilised to compute the nonlinear dynamic response of the system. With this technique the global equations of motion are integrated through time using the implicit Hilber-Hughes-Taylor operator. Equilibrium solution within each time increment is obtained

by an iterative process applying Newton's method. An automatic incrementation scheme is also used with the general implicit dynamic integration method. The scheme uses a half-step residual control to ensure an accurate dynamic solution. The half-step residual is the equilibrium residual error (out-of-balance forces) halfway through a time increment. This half-step residual check is the basis of the adaptive time incrementation scheme. If the half-step residual is small, the accuracy of the solution is high and the time step can be increased safely; conversely, if the half-step residual is large, the time step should be reduced. The automatic incrementation scheme is especially effective in cases where a sudden event is introduced to the dynamic problem e.g. the moment when the foundation impacts the ground during cyclic rocking motion associated with large uplift. In such studies small time increments are required immediately after the sudden event. At later times the response can be modelled accurately with large time increments because most of the high frequency content of the solution has been damped out by the dissipation mechanisms present in the model.

A typical two- dimensional finite element discretisation and the types of elements implemented are portrayed in Fig. 4.2.

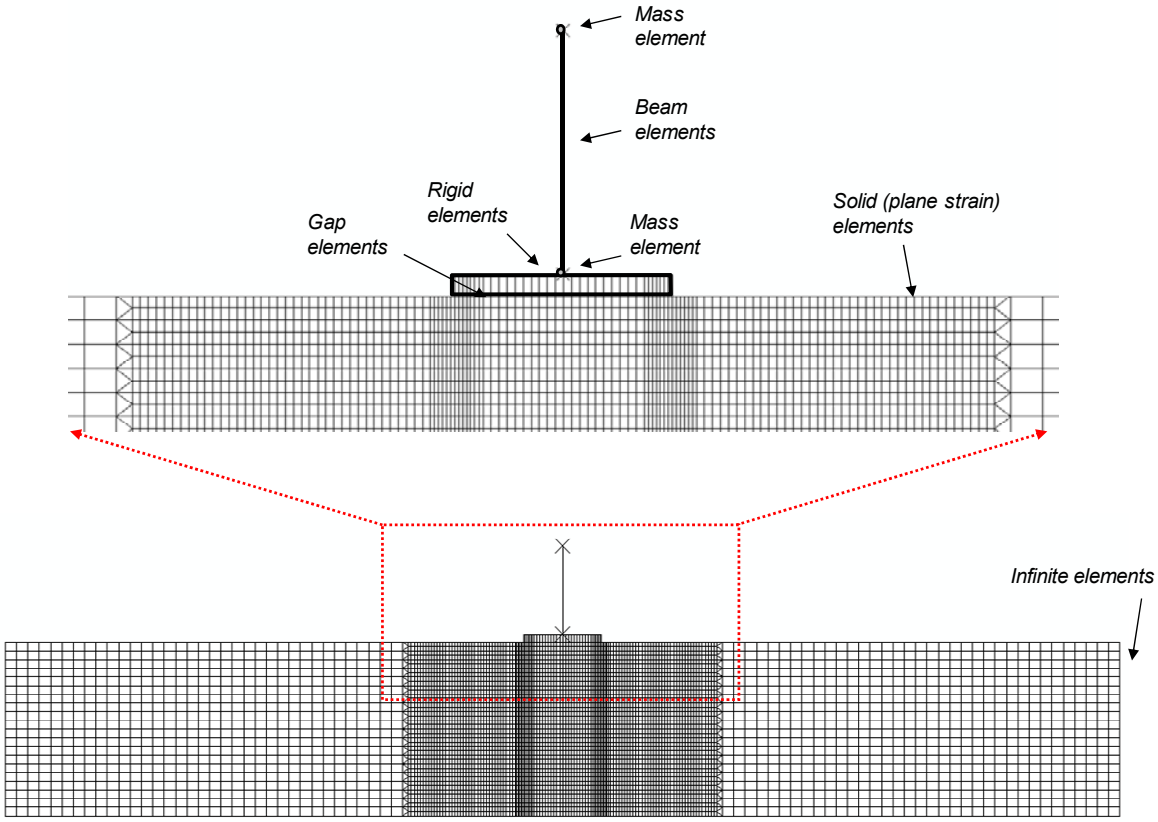


**Figure 4.2** Two- dimensional finite element discretisation and the types of elements applied.

### 4.2.2 Constitutive soil modelling

#### *Mohr-Coulomb model*

Soil yielding is represented with the M-C criterion and the critical parametres $c$ and $\phi$. For stress levels inside the yield surface, soil response is determined by the visco-elastic parametres $E$, $\nu$, and $\xi$. In the post-yield regime, a perfectly plastic behaviour is considered for soil, hence the stress field remains invariant to the development of plastic strains. In the finite element study performed here the Mohr-Coulomb model is confined to static analysis procedures.

#### *Kinematic isotropic/hardening model*

This constitutive soil model is based on the simulation of nonlinear cyclic behaviour of cohesive soils under undrained conditions with the behaviour of ductile metals. It is characterised by an initial,

pressure independent yield surface $\left[p=\left(\sigma_1+\sigma_2+\sigma_3\right)/3\right]$ which is inflated and translated in the stress space through the development of plastic strains. Yield surface is described with Von-Mises criterion $q=\sigma_{ij}$, where $q$ is the *deviatoric* stress: $q=\left[\frac{\left(\sigma_1-\sigma_2\right)^2+\left(\sigma_2-\sigma_3\right)^2+\left(\sigma_3-\sigma_1\right)^2}{2}\right]^{1/2}$ and $\sigma_{ij}$ is the yield stress under uniaxial loading. During two-dimensional (plane-strain) conditions, the yield surface is determined in the principal stress space by the following equation: $\sqrt{\sigma_1^2-\sigma_1\sigma_2+\sigma_2^2}=\sigma_{ij}$. An isotropic/kinematic hardening flow rule is also incorporated in the model to simulate the post-yield behaviour of soil subjected to cyclic loading. This evolution law consists of two components: a nonlinear kinematic hardening component, which describes the translation of the yield surface in stress space and an isotropic hardening component, which describes the change of the equivalent stress defining the size of the yield surface, as a function of plastic deformation. For stress levels inside the yield surface, soil behaviour is determined by the visco-elastic parametres $E$, $\nu$, and $\xi$. One- and three-dimensional representation of the nonlinear isotropic/kinematic hardening flow rule implemented in the numerical analysis for soil behaviour is presented in Fig. 4.3. Nonlinear aspects of the cyclic behaviour predicted by the constitutive model for load- and displacement-controlled loading conditions are illustrated in Fig. 4.4.

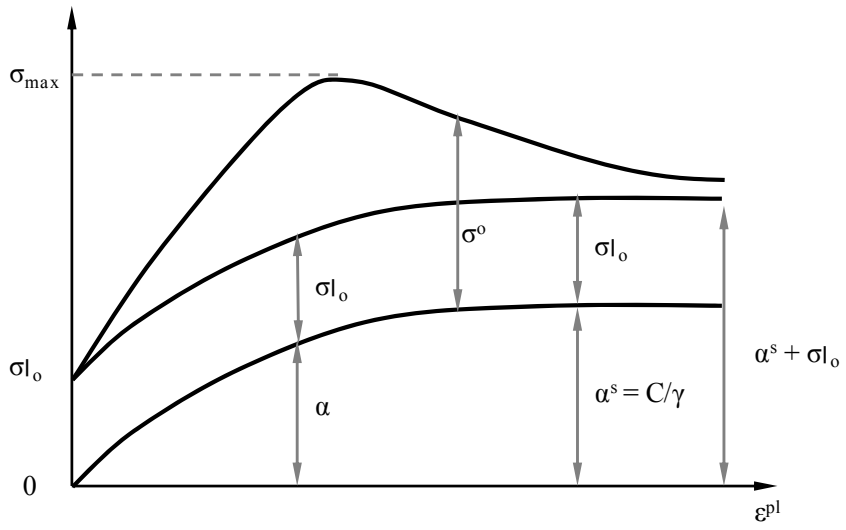


**(a)**

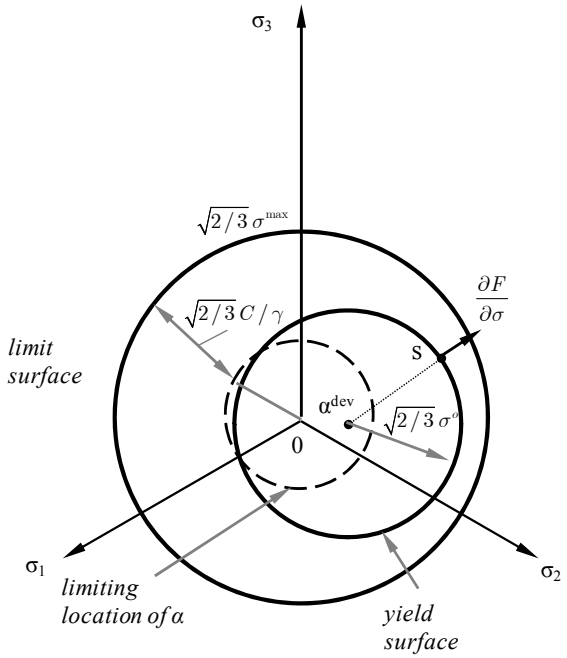


**(b)**

**Figure 4.3** One- and three-dimensional representation of the nonlinear isotropic/kinematic hardening flow rule implemented in the finite element analysis to simulate cyclic soil behaviour.

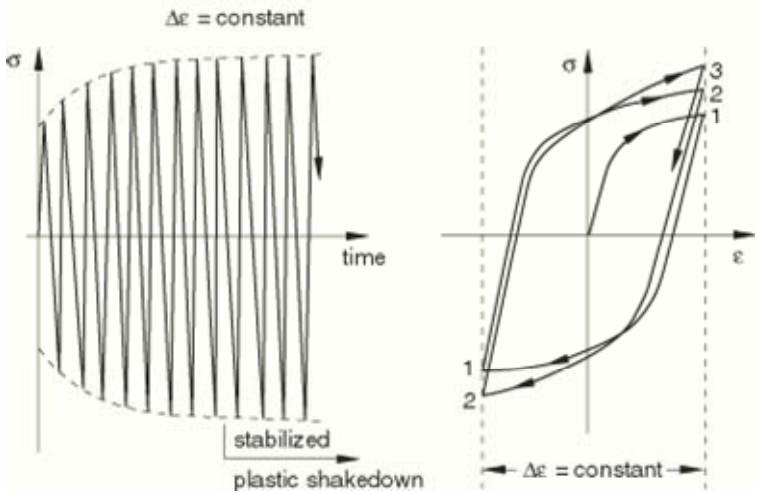


**(α) Displacement-controlled harmonic loading**

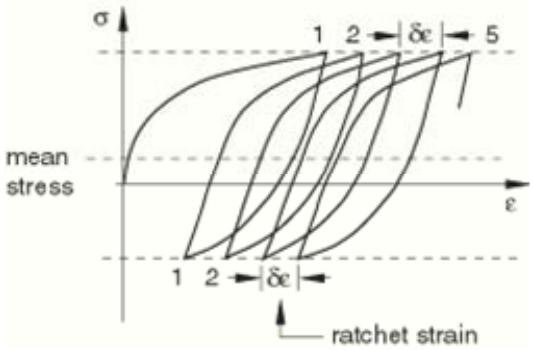


**(b) Stress-controlled harmonic loading**

**Figure 4.4** Cyclic soil behaviour predicted by the isotropic/kinematic hardening model implemented in the finite element analysis.

### 4.2.3 Parameters of the soil-foundation models

The soil-foundation models have been implemented to examine the uplifting response as presented in Table 4.1. These models also portrayed in Fig. 4.5 differ on the aspect ratio and size of the structure, the height of soil stratum over the rigid bedrock, as well as the soil parameters (elastic and strength). It is noted that all soil profiles describe homogeneous soil, apart of one in which increasing stiffness and strength over depth have been implemented.

**Table 4.1** The soil-foundation models implemented in the analyses of the present study

| Parameters | | Numerical model | | | |
|---|---|---|---|---|---|
| | | **Model v.01** | **Model v.02** | **Model v.03** | **Model v.04** |
| **Soil** | $E$ (MPa) | $20-100$ | $3000\,s_u$ | $20-100$ | $20-100$ |
| | $G$ (MPa) | $7-33$ | $1000\,s_u$ | $7-33$ | $7-33$ |
| | $s_u$ (kPa) | $50-100$ | $0.2\sigma'_{vo}+10$ | $50-100$ | $5-200$ |
| | $\sigma_{max}/\sigma_0$ | 0.19 | 0.19 | 0.19 | 0.19 |
| | $H_s$ (m) | 5 | 20 | 20 | 20 |
| | $T_0$ (sec) | $0.30-0.19$ | 0.64 | $1.28-0.59$ | $1.28-0.59$ |
| **Structure** | $2b$ (m) | 2 | 6 | 2 | 11 |
| | $h_{cm}$ (m) | 5 | 12 | 5 | 9 |

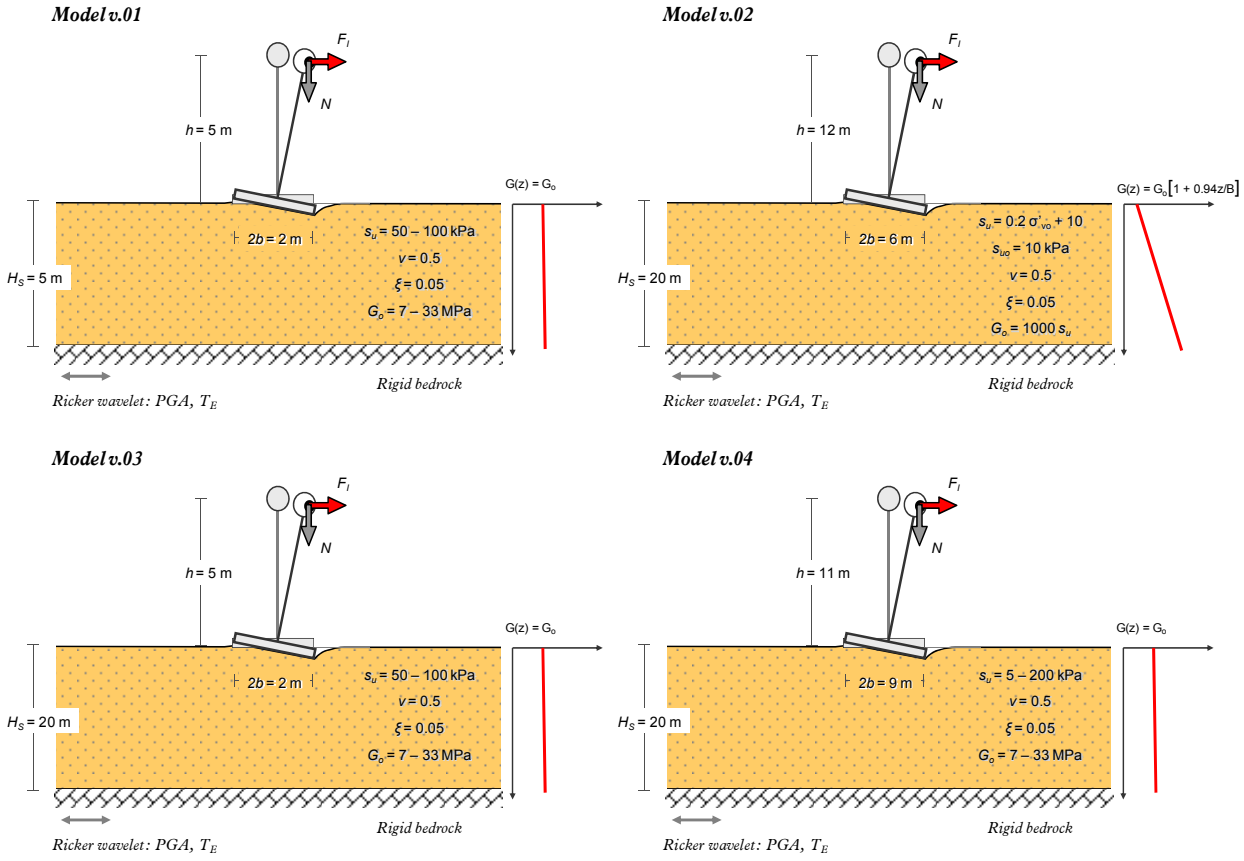


**Figure 4.5** Soil-foundation models utilised in the finite element analysis.

## 4.3 UPLIFT on VISCO-ELASTIC SOIL

The idealised case of an uplifting foundation on elastic soil is directly applicable only to the case of very stiff soil which experiences small deformations limited in the vicinity of the foundation edges. Nevertheless, it serves as a useful tool for highlighting the profoundly nonlinear dynamics of the soil–structure system. The geometrically induced nonlinear behaviour arises primarily from the exceedance of the tensile strength at the soil-foundation interface which engages the uplifting regime. It is amplified though, by the developing second order effects as the mass centre is drifting away from the vertical axis of symmetry during uplift.

### 4.3.1 Monotonic response

The rocking response of a shallow foundation allowed to uplift under static conditions is investigated first. To this extent, the system configuration of Fig. 4.5a is considered (*model v.01*). In the first step the vertical (gravitational) load is applied through the mass centre (symmetric loading). Then a gradually increasing horizontal displacement $\delta$ is applied at the mass centre up to a maximum value of $\delta_{\max} = b$ (antisymmetric loading). For a sufficiently slender structure the horizontal translation of the footing $u_b$ is negligible compared to $\delta$ and therefore, the moment at which $u_{cm} = \delta_{\max} = b$, the footprint of the mass centre has reached the foundation edge. Evidently, critical overturning has already occurred at this loading point. The displacement-controlled loading at the mass centre is restrained by a horizontal shear force $Q$ and an overturning moment $M$ imposed to the foundation by the supporting soil so that static equilibrium is attained. From the vertical displacements of the foundation edges $(w_1, w_3)$ and the mass centre $(w_{cm})$, the rocking rotation $\theta$ and the foundation moment $M$ with respect to the corner point (3) can be computed:

$$\theta = \arcsin\left(\frac{w_1 - w_3}{2}\right) \quad [4.1]$$

$$M = Q_{cm} h\left(w_{cm} - w_3\right) \quad [4.2]$$

in which $Q_{cm} = Q$ is an output of the finite element analysis as well. The foundation moment $M$ can be calculated alternatively by integrating soil pressures over the contact interface:

$$M = M_p = \sum_{i=1}^{n} p_v(x_i) x_i \cos\theta \Delta x_i - Nh\sin\theta \quad [4.3]$$

where $n$ is the total number of nodes on which soil pressures are computed, $x_i$ and $p_v(x_i)$ are respectively the distance of the $i\text{-}th$ node from the footing midpoint and its corresponding soil pressure, and $\Delta x_i = \Delta b_{i-1} + \Delta b_i$ ($\Delta b_{i-1}$, $\Delta b_i$ are the half-lengths of the neighbouring elements). Soil pressure at a node of the foundation is calculated from the axial force of the gap element linking this node to its corresponding soil node.

The half-width of the effective footing $\beta$ is calculated at each increment through the number of the nodes remaining in contact with the supporting soil. Hence for a $m < n$ number of foundation nodes attached to the corresponding soil nodes, upper and lower bounds of uplift can be estimated:

$$\beta_{\min} = \frac{m-1}{n} 2b \quad \text{and} \quad \beta_{\max} = \frac{m}{n} 2b \quad [4.4a]$$

Then the half-width of the effective footing is:

$$\beta = \left(\beta_{\max} + \beta_{\min}\right)/2 \quad [4.4b]$$

It is obvious that for $m = n$ (full-contact regime) it is $\beta_{\min} = \beta_{\max} = b$.

During the linear regime of rocking without uplift, the rotation pole remains fixed at the midpoint of the contact interface and therefore $w_b = w_2 = N/K_v$. After uplift initiates however, the rotation pole shifts towards the pivot point as the area of the effective footing decreases and an upward vertical incremental displacement is developed:

$$\delta w_b = x_p \sin\theta \qquad [4.5]$$

where $x_p$ is the instantaneous position of the rotation pole with reference to the foundation midpoint. In the limiting case of a rigid soil the pole moves from the midpoint to the pivot point right at the uplift onset and $w_b = b\sin\theta$. From kinematic analysis of the rocking foundation the displacement of the pole $x_p$ along the contact interface can be calculated as a function of the incremental vertical displacements of corner points (1) and (3) and the half-width $b$:

$$x_p = \frac{\delta w_1 + \delta w_3}{\delta w_1 - \delta w_3} b \qquad [4.6]$$

***Contact pressures***

A key issue in the analysis of rocking response is to study the constitutive laws that govern the development of soil pressures acting on the foundation. The soil-structure configuration of *model v.01* (Fig. 4.5a) with soil modulus of elasticity $E_o = 20$ MPa $\left(G_o = 7 \text{ MPa}\right)$ is adopted to compute $p-w$ curves along the foundation base. In the graphs of Fig. 4.6 the development of contact pressures is plotted for the interface nodes from the left edge towards the midpoint (red circles) in comparison with their equidistant nodes on the right (solid black lines). Initially, a vertical load is applied to the footing through the mass centre, gradually increasing to reach gravitational load of 500 kN. During this step, the distribution of the contact pressures along the interface is symmetrical to the midpoint and can be validated with the elastic medium solutions available in literature (Sadowsky, 1928) as shown in Fig. 4.7. These soil reactions must be in equilibrium with the external load, and therefore integration along the foundation should lead to the gravitational load $N$. In the $p-w$ curves of Fig.

4.6 this step is represented by the linear branch determined by the points of rest $(p = w = 0)$ and full loading $(w = p/k_v = N/K_v = 0.025 \text{ m})$. As symmetrical nodes are represented on each graph, their load-displacement curves are identical during this phase. Unlike the conventional winkler modelling, the stiffness $k_v$ is not uniform along the foundation, but increases close to the edges. In the succeeding step, a gradually increasing horizontal load is applied at the mass centre. The overturning moment resulted from the imposed displacement generates additional soil pressures and differential settlements. Hence, this antisymmetric loading separates the contact interface to the loading side (on the right of the midpoint) and the unloading side (on the left of the midpoint). Along the loading side soil pressures increase at a steeper rate determined by $k_m$. Likewise, for the unloading side soil pressures gradually reduce at the same rate until they drop down to zero. Interestingly, at this point the vertical displacement has not become zero as well (as the conventional winkler model predicts) but has converged to a residual value. Evidently, uplift is engaged right after the contact pressure of the left corner node becomes zero. As the separation zone is expanding towards the midpoint, the unloading area is shifting rightwards. For the contact pressures on the foundation area remaining in contact with soil, an upperbound exists now beyond which, unloading initiates.

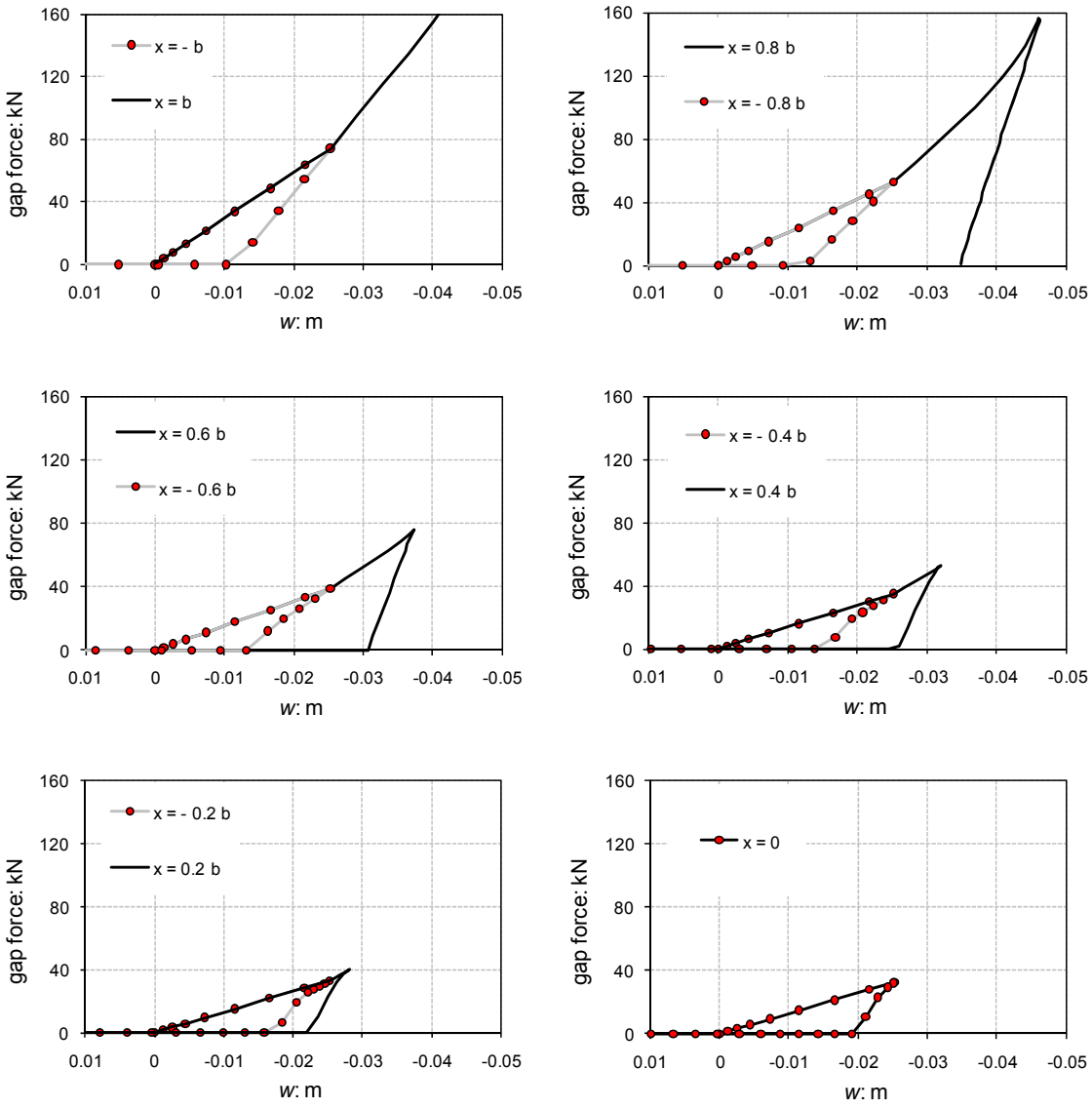


**Figure 4.6** $p-w$ curves of a foundation on elastic soil $\left(E_o = 20 \text{ MPa}\right)$ during: (a) pure vertical load, (b) displacement-controlled horizontal load at the mass centre.

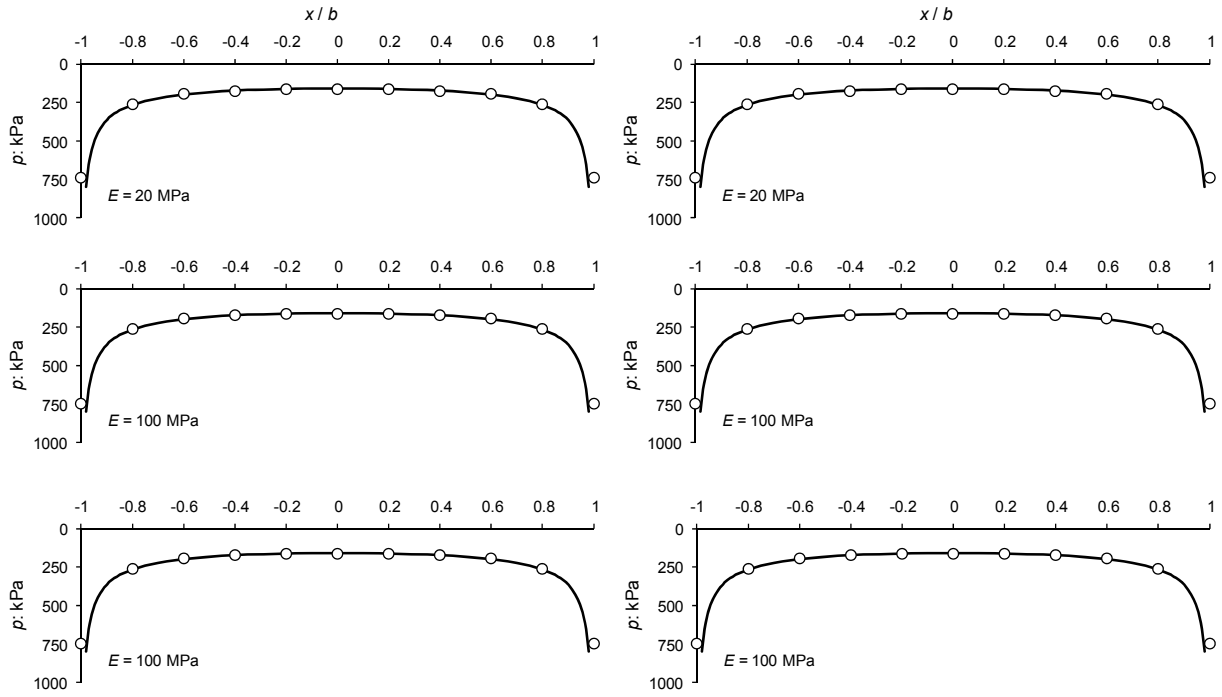


**Figure 4.7** Distribution of contact pressures on the foundation computed with finite element analysis (white circles) and analytical equations (solid lines) for poor or medium soil stiffness: (a) under pure vertical loading, (b) at incipient uplift, and (c) at ultimate moment.

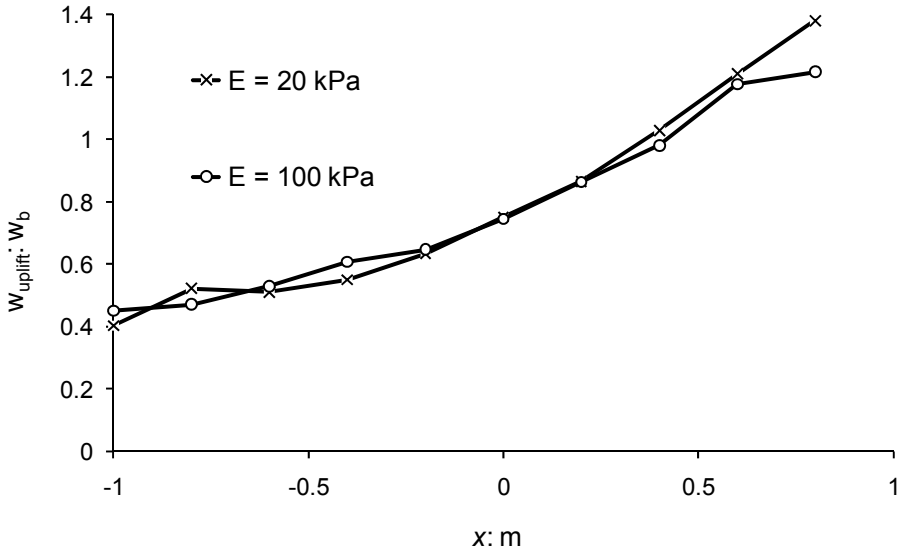


**Figure 4.8** Vertical displacement along the foundation at incipient uplift normalised to the gravitational settlement. Elastic soil of medium or poor stiffness (white circles and black crosses respectively) is considered.

### *Static stiffnesses*

Many researchers have developed analytical solutions for the static stiffness of the soil-foundation system under any type of loading. In this way the static stiffness is expressed as a function of the elastic soil parameters and the width (or diameter) of the footing. Parameters such as the shape of the footing, the embedment, the distribution of soil stiffness with depth, and the possible presence of a shallow bedrock have also been implemented in these equations. Among them, Gazetas (1991) recommendations are the most widely adopted for both analysis and design purposes. For the case of a strip footing on the surface of a homogeneous soil stratum over a rigid bedrock, Gazetas equations for swaying, vertical, and rocking vibrations are simplified as follows:

$$K_h = \frac{2G}{2-\nu}\left(1+2\frac{b}{H}\right) \qquad [4.7a]$$

$$K_v = \frac{1.2G}{1-\nu}\left(1+3.5\frac{b}{H}\right) \qquad [4.7b]$$

$$K_m = \frac{\pi G b^2}{2(1-\nu)}\left(1+0.2\frac{b}{H}\right) \qquad [4.7c]$$

The comparison of these equations with the finite element analysis is summarised in Table 4.2.

**Table 4.2** Static stiffnesses of a rigid strip footing on homogeneous soil over bedrock computed for different values of soil Young's modulus (a) with the finite element method, (b) analytically (Gazetas, 1991).

| | $K_m(\mathrm{MNm/rad})$ | | $K_v(\mathrm{MN/m})$ | | $K_h(\mathrm{MN/m})$ | |
|---|---|---|---|---|---|---|
| $E(\mathrm{MPa})$ | 100 | 20 | 100 | 20 | 100 | 20 |
| Analytical equation (Gazetas, 1991) | 89.7 | 17.9 | 112.1 | 22.4 | 63.3 | 12.7 |
| Finite elements | 92.6 | 16.5 | 98.6 | 19.8 | 45.2 | 8.8 |

An excellent agreement is achieved in the rocking mode for both soft and medium soil conditions, whereas in the vertical mode the analytical solution slightly overestimates the stiffness. In the swaying

mode, the analytical solution is by 1.5 times larger than the numerical values. This difference however, can be attributed to the coupled swaying and rocking motion in the finite element analysis.

### *Load-displacement curves*

A rigorous approach of the static overturning moment about the foundation midpoint as a function of the rocking rotation for a rigid foundation allowed to uplift on elastic soil is depicted in Fig. 4.9. When an undeformable soil is regarded, at incipient uplift the moment instantaneously climbs from zero up to the ultimate value $M_u = Nb$. From this point on, the moment is gradually decreasing due to the amplifying $(P-\delta)$ effects and eventually drops down to zero when the rocking rotation reaches the critical value $\theta_c = b/h$. On the other hand, in the full-contact regime the soil-foundation stiffness is kept constant and therefore the moment is a linear function of the rocking angle. It is concluded that in case of deformable supporting soil and a foundation allowed to uplift, the moment–rotation curve is bounded by the afore-mentioned limiting curves (Apostolou and Gazetas, 2005). This curve comprises: (a) a linear branch from zero up to the point where uplift initiates, (b) a softening branch to the ultimate moment capacity point, in which the soil-foundation rocking stiffness decreases due to the gradually amplifying uplifting mechanism, and (c) a declining branch which is dominated by the $(P-\delta)$ effects and eventually leads to the overturning failure of the foundation at the critical angle $\theta_c$ (Fig. 4.9).

In the full-contact regime the moment is a linear function of rocking rotation and the rocking stiffness is calculated analytically from the afore-described solutions of the literature (e.g. Gazetas, 1991). From all finite element analyses of this study, the moment at incipient uplift is computed equal to half the ultimate value of the 'rigid soil' case, $M_u = Nb$, irrespective of soil stiffness:

$$M_{uplift} = Nb/2 \qquad [4.8]$$

This expression for the uplifting moment has also been extracted from the parametric study of Crémer *et al.* (2002). Regarding the moment capacity of the footing, it reaches a maximum value when a rigid soil is considered. Then, by reducing the stiffness of soil medium, it gradually decreases until eventually drops down to zero for an infinitely compliant soil $(E=0)$.

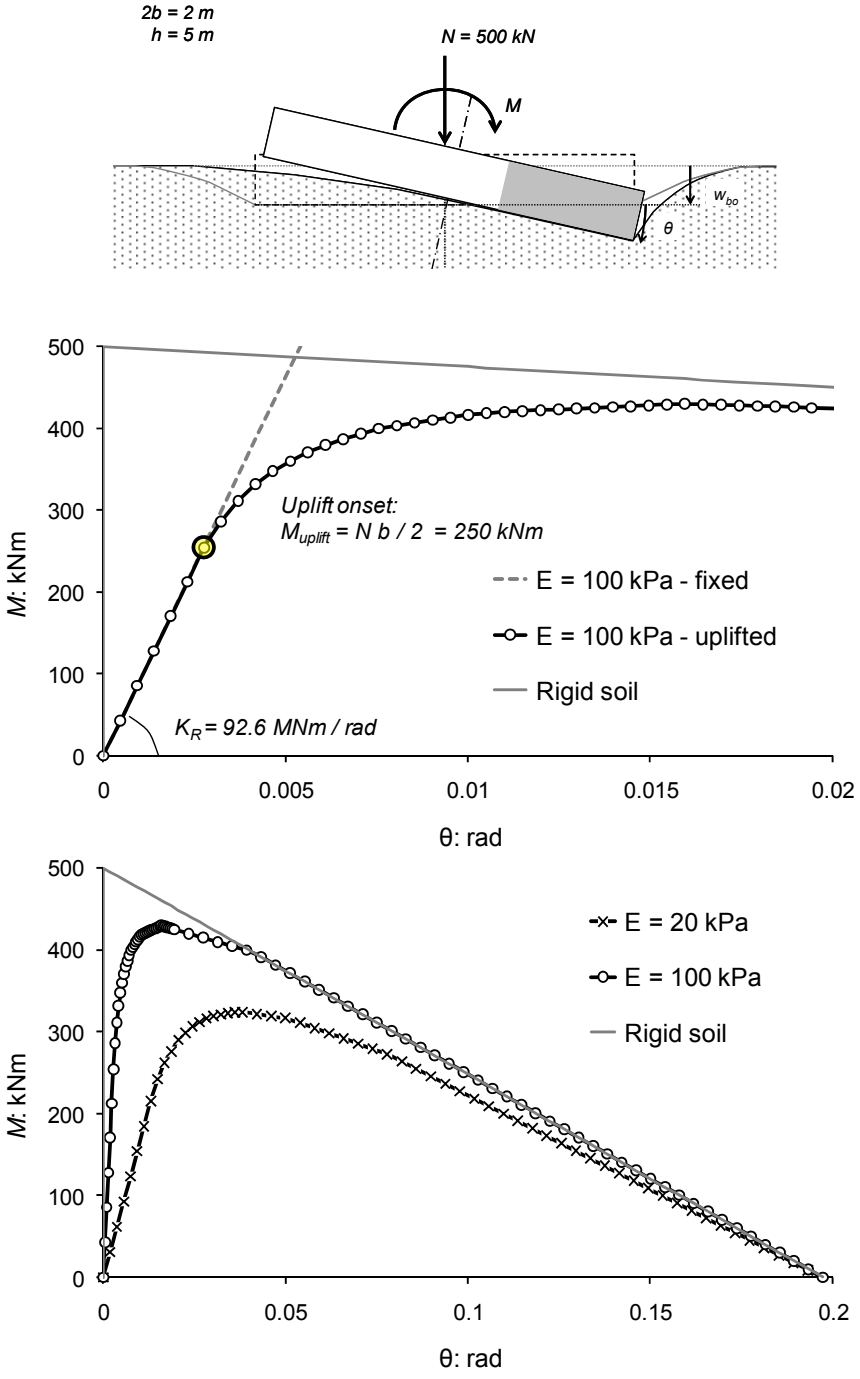


**Figure 4.9** Moment – rotation curves of a rigid strip footing on elastic (soft or medium) or rigid soil.

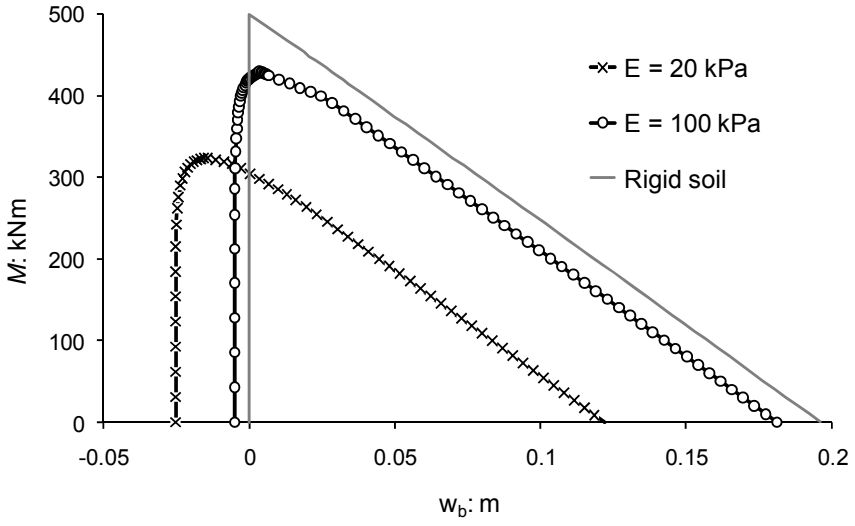


**Figure 4.10** Moment – vertical displacement curves of a rigid strip footing on elastic (soft or medium) or rigid soil.

### *Coupling of foundation displacements with rocking angle*

Apart from force-displacement curves, remarkable conclusions can be drawn from correlating the translational ( $u_b$ and $w_b$ ) with the rotational displacements ( $\theta$ ) of the footing.

The correlation of horizontal displacement, $u_b$ with rocking angle, $\theta$ for the case of soft and medium soil ( $E = 20$ MPa and 100 MPa respectively), is plotted in Fig. 4.11. The $u_b - \theta$ relationship of the 'rigid soil' case is also plotted in the same graph. The latter curve can be computed analytically, from the geometry of the problem $\left[u_b = b\left(1-\cos\theta\right)\right]$. On the other hand, for a footing in full contact with elastic soil, the horizontal displacement $u_b$ can be correlated with rocking rotation by eliminating the moment from its constitutive relationships $M = K_m\theta = K_{mh}u_b$ $\left[\text{then } u_b = \left(K_m / K_{mh}\right)\theta\right]$. Evidently, for a footing prevented to uplift, the trend is linear for any rotation. This linear correlation is followed by the 'elastic soil' curves (Fig. 4.11), at small rotations where uplift has not yet initiated. Nevertheless, after uplift onset, these curves tend to track on the 'rigid soil' curve as the rocking angle approaches the critical value $\theta_c$. The stiffer the soil, the more rapidly the 'elastic soil' curve reaches the limiting

curve. In general the uplifting response weakens coupling between $u_b$ and $\theta$ and sets an upper bound for the horizontal displacement, $u_{b,\max} = b(1-\cos\theta_c)$, as resulted from limit equilibrium. For the slender block examined, it is $u_{b,\max} \cong 0.1 b\theta_c = 0.02$ m. Regarding that $b = \delta_{\max}$ (where $\delta_{\max}$ is the maximum imposed displacement at the mass centre during pushover loading), the following relationship is derived:

$$\frac{u_{b,\max}}{\delta_{\max}} = 1 - \cos\theta_c \qquad [4.9]$$

It is evident that for slender systems, the imposed displacement at the mass centre is transferred to the footing as rocking displacement, the horizontal component of which can be considered negligible.

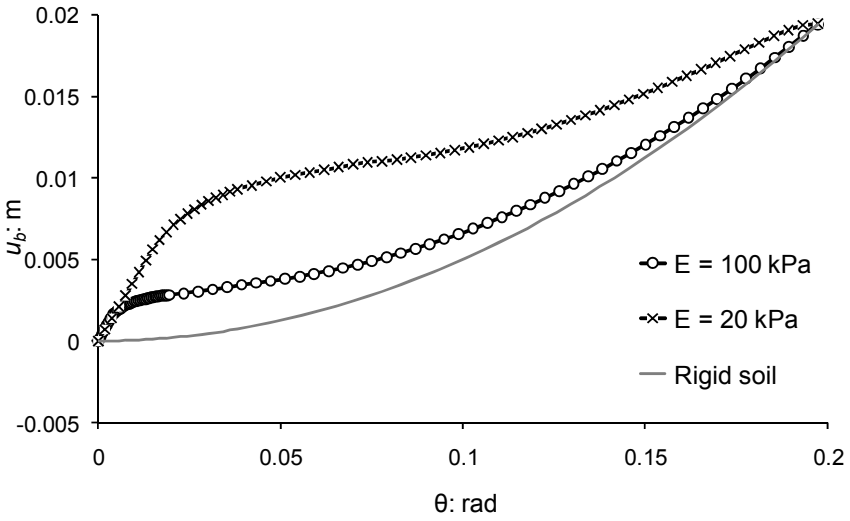


**Figure 4.11** Coupling of horizontal displacement with rotation of a rigid strip footing on elastic (soft or medium) or rigid soil.

The correlation of the vertical displacement with the rocking angle is plotted in Fig. 4.12. The $w_b - \theta$ relationship of the 'rigid soil' case is also plotted in the same graph, computed with the analytical relationship, $w_b = b\sin\theta$. This equation results in a linear curve starting from the point $(0,0)$ and leading to upward displacement, $w_b \cong b\theta_c = b^2/h$ at critical equilibrium. The numerically computed 'elastic soil' curves have an initial vertical displacement at rest (gravitational settlement)

$w_{bo} = -N/K_v$. Like the footing on elastic soil prevented to uplift, this value is kept constant in the full contact regime regardless the rocking angle. Once uplift initiates though, the incremental displacement $\delta w_b$ becomes upward at a rate which depends on the soil stiffness. In general this rate is close to $b$, whereas for a sufficiently stiff soil (in this example $E = 100$ MPa) it can be considered equal to $b$. Under a gross estimate (considering bilinear $w_b - \theta$ curve), the maximum available upward displacement of an uplifting footing on elastic soil is then $w_b = b\left(b/h - Nb/2\right) - N/K_v$.

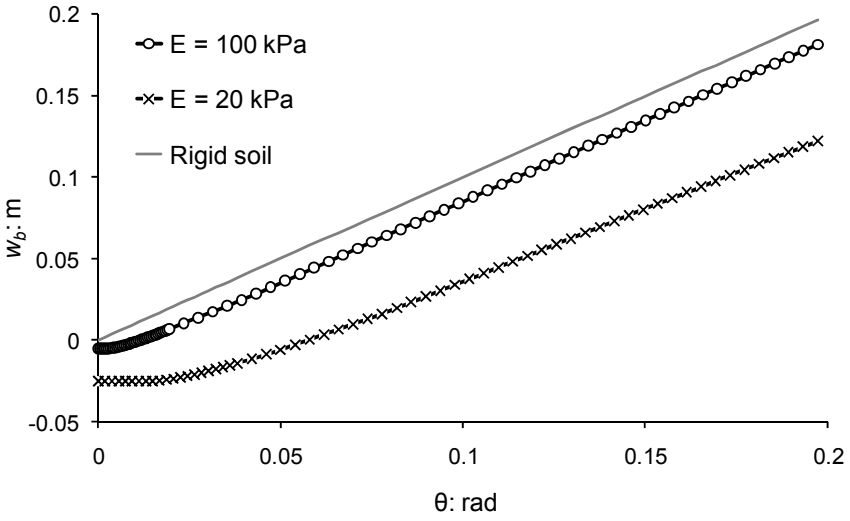


**Figure 4.12** Coupling of vertical displacement with rotation of a rigid strip footing on elastic (soft or medium) or rigid soil.

### *Rotation pole*

The exact positioning of the rotation pole during rocking vibrations is of great importance as it governs the distribution of soil pressures. When a strip footing is rocking in full contact with elastic soil, the pole of rotation lies on the interface midaxis. For a sufficiently slender structure the translational mode can be neglected and the pole is located constantly at the interface midpoint. In any case for the projection of the pole on the footing interface it holds $x_p = 0$. On the other hand, in case of a rigid soil the pole of rotation jumps from the midpoint to the corner of the footing as rocking initiates (Fig. 4.13). In the general case of rocking with uplift on a compliant soil, the pole departs

from the midpoint right after uplift onset moving towards the corner point. The stiffer the supporting soil the more rapid this transition is (Fig. 4.13).

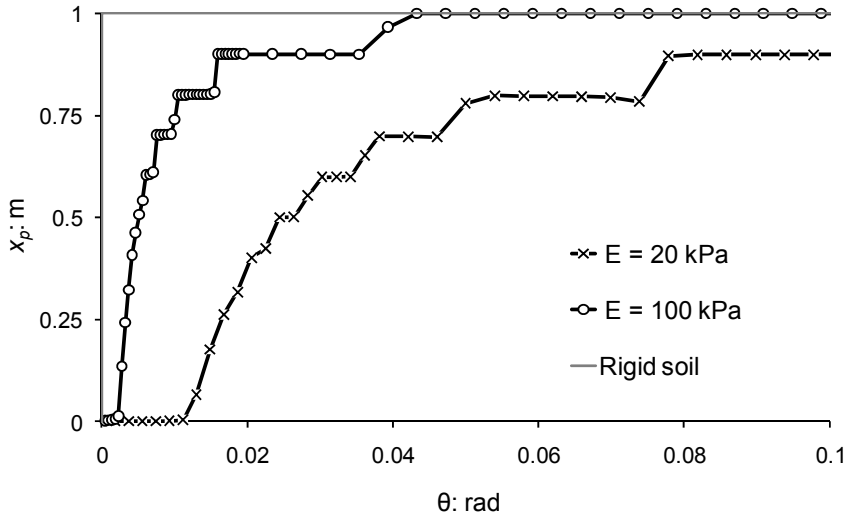


**Figure 4.13** The transition of the rotation pole from the midpoint to the corner of the foundation during rocking.

### *Uplift*

According to Eqs 4.4a, lower and upper bounds of the half-width of the effective footing $\beta$ can be computed from finite element analysis. It is reminded that the effective footing $\beta = \lambda b$ is the part of the footing remaining in full contact with the underlying soil. A mean curve can then be derived according to Eq. 4.4b. The $\beta - \theta$ curves for the medium and stiff soil are plotted in Fig. 4.14. During full contact regime, the effective footing width is equal to $2b$. As uplift initiates, the width $2\beta$ follows an exponential decay and eventually approaches a residual value, $\beta_{res}$ as $\theta \to \theta_c$. The stiffer the soil, the smaller this residual value is. In the limiting case of rigid soil, it yields $\beta_{res} = 0$.

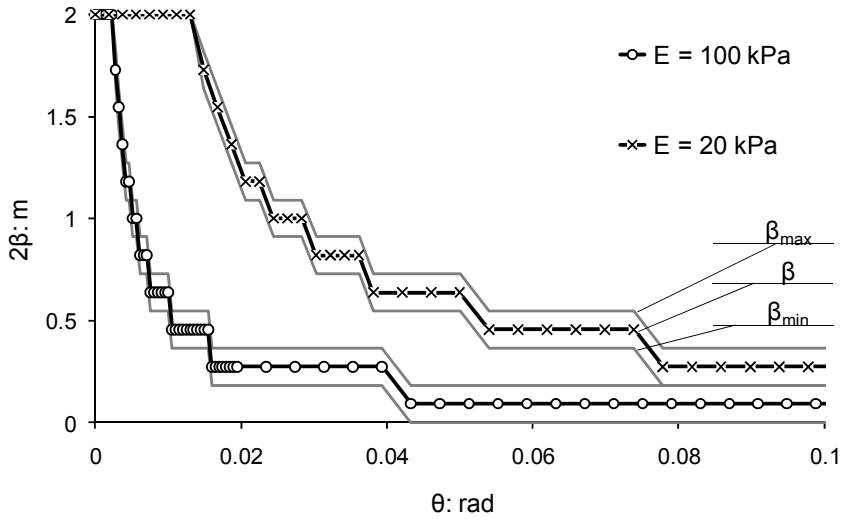


**Figure 4.14** Upper, lower, and average curves of foundation uplift (described with the effective footing) on elastic soil of poor or medium stiffness.

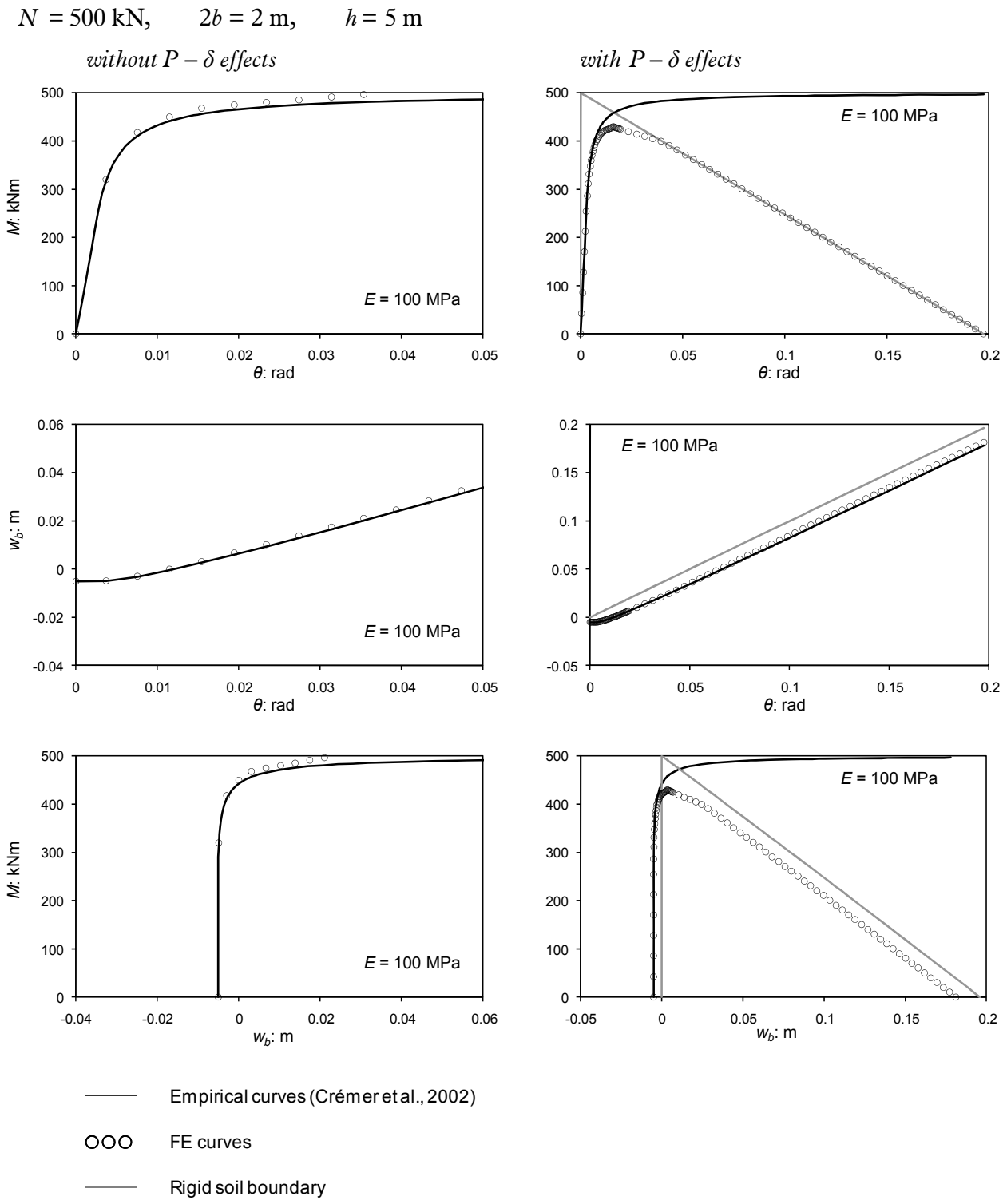


**Figure 4.15** Analytical curves of a rigid strip footing without p – delta effects and comparison with finite element results.

### 4.3.2 Free vibration response

In Chapter 3, the free vibration period of a rigid one-story structure was computed as a function of the rocking amplitude according to linear and nonlinear formulation. It was outlined that the linear formulation as derived by Housner can adequately predict the period. It was also pointed out that in the free vibration regime, the frequency of a rocking structure on a rigid soil is amplitude-dependent even at low levels of rotation, and therefore, the dynamic parameter $p$ is not the eigenfrequency of the system. Contrary to the rigid soil case in which the free vibration period tends to zero under low levels of rocking, postulation of a deformable supporting medium results in linear response before uplifting initiates. In this state the fundamental period of the rigid structure is provided by linear SSI theory for an oscillator with two degrees of freedom (i.e. the horizontal displacement of the base midpoint, $u_b$ and the rotation $\theta$):

$$\tilde{T} = \sqrt{T_h^2 + T_m^2} = 2\pi\sqrt{\frac{J_{cb}}{K_m} + \frac{m}{K_h}} \qquad [4.10]$$

The influence of the vibration in the horizontal direction on the overall response can be estimated by the following period ratio:

$$\frac{\tilde{T}}{T_m} = 1 + \frac{m/K_h}{J_{cb}/K_m} \cong 1 + 0.75\frac{2-\nu}{1-\nu}\tan^2\theta_c \qquad [4.11]$$

in which the mass moment of inertia is $J_{cb} = mh^2$ and the elastic medium is considered as homogeneous halfspace. As demonstrated in Chapter 2, for sufficiently slender structures the fundamental period can eventually yield:

$$\tilde{T} \cong T_m = 2\pi\sqrt{\frac{J_{cb}}{K_m}} \qquad [4.12]$$

Psycharis and Jennings (1983) studied rocking and uplifting of slender structures on a flexible foundation by modelling soil continuum with independent linear springs of zero tensile capacity. In

this study the rocking period was computed as a function of the normalized impulse $\beta = \theta_{\max} / \theta_{uplift}$ where $\theta_{\max}$ is the amplitude of rocking of the equivalent fixed base system and $\theta_{uplift}$ is the critical angle at incipient uplift. For values of $\beta$ smaller than 1.65, a linear correlation was established between the amplitude of rotation and the rocking period:

$$\frac{\tilde{T}}{T_m} = 0.903 + 0.097\beta \qquad [4.13]$$

The influence of soil stiffness to the rocking period of rigid uplifting structures is outlined next through the pattern of a bridge pier with a spread foundation on elastic soil, as represented with *model v.02* of Fig. 4.5. The vertical load of the bridge pier is applied at the mass centre, which is located $12\,\text{m}$ above the ground surface. In the transverse direction the footing of the pier is $6\,\text{m}$ wide, whereas in the longitudinal direction is considered infinite so that plain strain assumption can be adopted. Sliding at the soil-foundation interface is prevented thereby rocking is the dominant mode of the response. Unlike the soil profile associated with the *model v.02*, the supporting medium is now an elastic halfspace of stiffness $E_s = 10$ MPa and 20 MPa (case 1 and 2 respectively) and Poisson ratio $\nu = 0.3$. For these levels of soil stiffness the rocking period prior to uplift is $T_s = 3.1\,\text{sec}$ sec and $2.2\,\text{sec}$. A finite element analysis is performed to compute the rocking response of the pier at the free vibration regime. In Fig. 4.16 the free vibration period is plotted in terms of the rocking amplitude for the two values of soil stiffness (case 1 and 2) and in comparison with the limiting case of a rigid soil medium (case 3). The aspect ratio of the structure is $\tan\theta_c = 0.25$ meaning that when the peak angle is close to $0.25\,\text{rad}$, the period of rocking tends to infinity. The response can be separated in two states depending on whether uplift occurs or not. Initially, for rotation amplitude below the threshold of uplift the rocking system exhibits harmonic oscillations on the flexible base of constant period $T_m$. Once uplifting occurs the period of free vibration converges gradually to the period of the rigid base system even when an extremely soft soil is regarded (case 1). This is a result of the amplifying role of the $P-\delta$ effects on the soil-foundation stiffness (on the expense of soil modulus $E_s$) at large

rotations, as portrayed in Fig. 4.9. Hence, for a peak angle of rotation $\theta_c = 0.1$ rad (40 % of the critical value $\theta_c$), the period of the rigid soil system (case 3) is 5.1 sec , which is merely increased to 5.6 sec and 5.3 sec in cases 1 and 2 respectively. It can therefore be assumed that for high levels of rotation (comparable to the critical angle) a rigid base system can be adequate to compute the free vibration period of an uplifting structure.

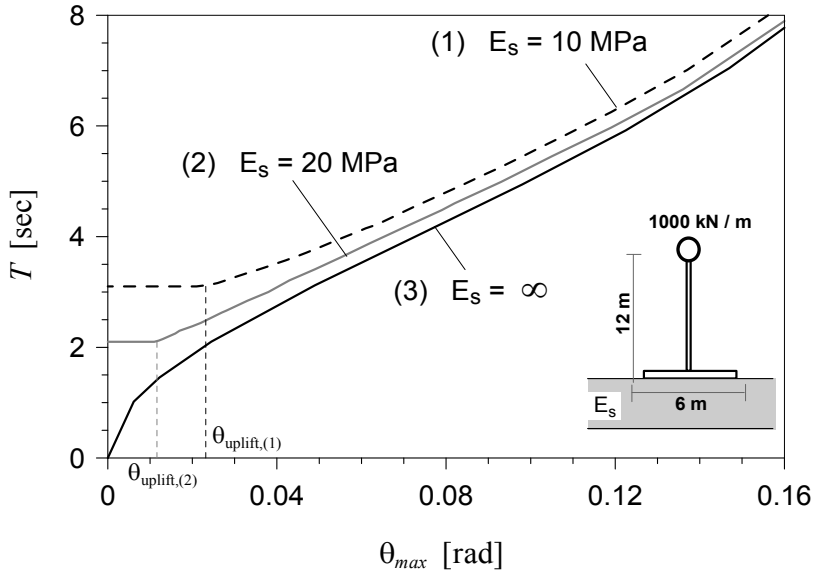


**Figure 4.16** The rocking period of a rigid, one-storey structure supported on, (a) rigid soil, (b) soft soil $(E = 20\,\text{MPa})$, and (c) very soft soil $(E = 10\,\text{MPa})$.

### 4.3.3 Earthquake response

The dynamic response of an uplifting structure subjected to earthquake excitation is next investigating.

At first, rocking of the one-storey structure allowed to uplift is computed for different values of soil stiffness. Each analysis is repeated by preventing uplift. In this way, rocking displacement spectra with respect to the fundamental period, $T_m$ can be computed for both the uplifting and the fixed base system. For the purposes of finite element analysis, the *model v.01* of Fig. 4.5 is considered. A long duration Ricker wavelet of $PGA = 0.3$ g and $T_E = 1.3$ sec is used as excitation at the bedrock.. For

the range of soil stiffness values used in the analysis, the fundamental period of soil layer can be considered adequately small in such a way that no perceptible filtration of the bedrock motion may occur through soil. Time histories of the rocking response are plotted in the upper two graphs of Fig. 4.17, in comparison to that of the fixed base system. For the flexible system of $T_m = 1.66$ sec (left-hand side), the rocking amplitude is not sensitive to whether uplift is prevented or not. A difference in the period of vibration between two systems is also observed. As the pulse-type excitation has ceased after the first three seconds of rocking, this is practically the free vibration period. It turns out that the period of the uplifting system is nearly twice as much as the period of the fixed base, which is attributed to the increase of the amplitude-dependent period due to uplift as predicted in Fig. 4.16. When a stiffer system is regarded by increasing soil modulus ($T_m = 0.74$ sec, right-hand side), uplift results in a fundamentally different response compared to that of the fixed base system. In fact, the amplitude of rocking of the uplifting system is still at high levels much larger than the one of the fixed base system which has significantly reduced. As shown from the rocking displacement spectrum of Fig. 4.16, the rocking amplitude tends to zero as soil becomes infinitely stiff when uplift is prevented, whereas for the uplifting system this amplitude converges to a value of about $0.06$ rad.

| case | $T_m$ [sec] | base |
|---|---|---|
| **1** | 1.66 | uplifting |
| **2** | 1.66 | fixed |
| **3** | 0.74 | uplifting |
| **4** | 0.74 | fixed |
| **5** | 0.37 | uplifting |
| **6** | 0 | uplifting |

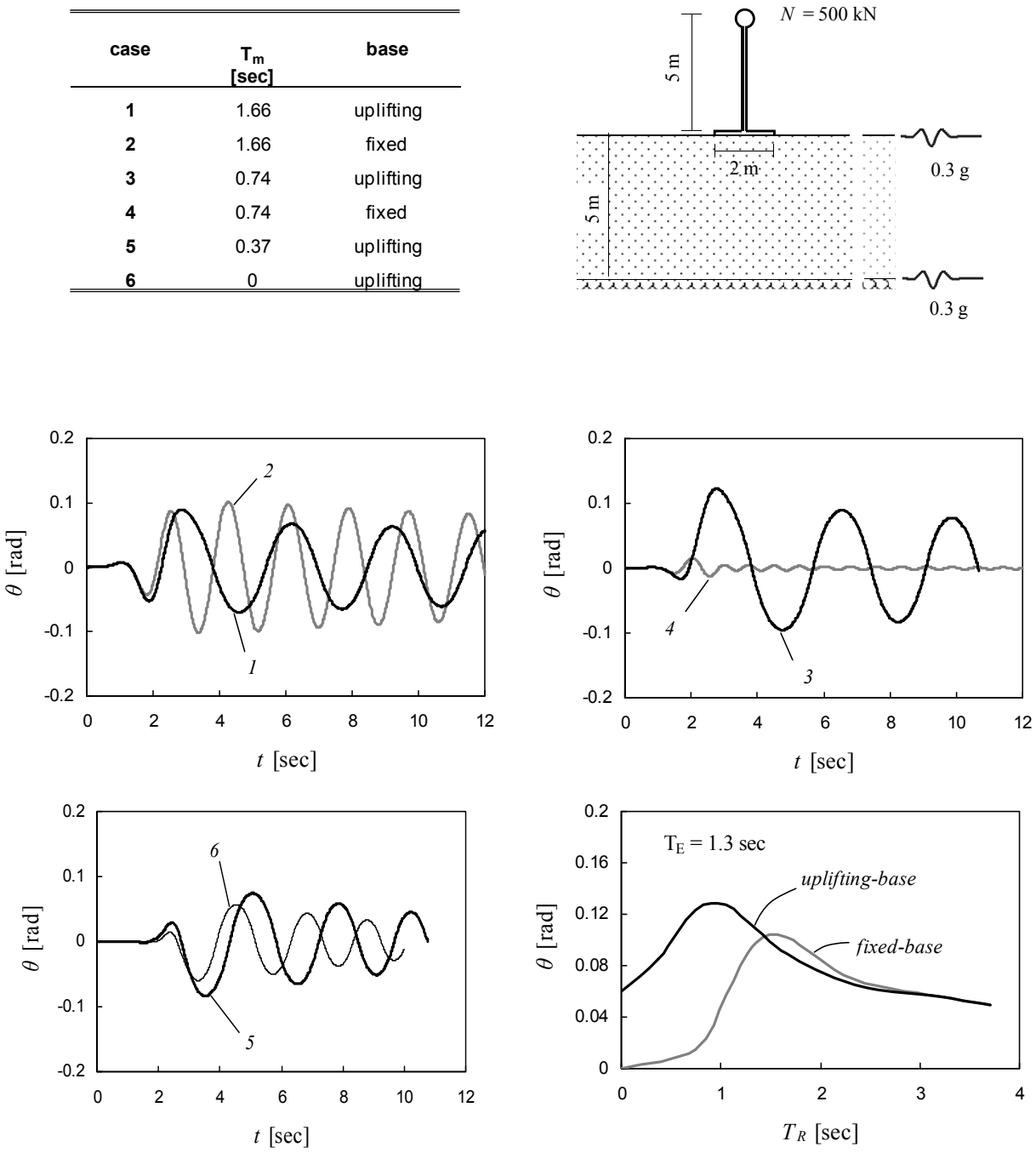


**Figure 4.17** The effect of uplifting on the rocking response of a one-story rigid structure for different values of the rocking period $T_m$.

The structural response of the uplifting structure is examined next, in comparison to that of the rigid soil case, through the pattern of *model v.01*. A soft soil profile of $E = 20$ MPa is first employed to highlight the effect of the compliant supporting medium. The results are plotted in Fig. 4.18 in terms

of normalised time histories of (a) rocking rotation, (b) acceleration of mass point, and (c) foundation moment.

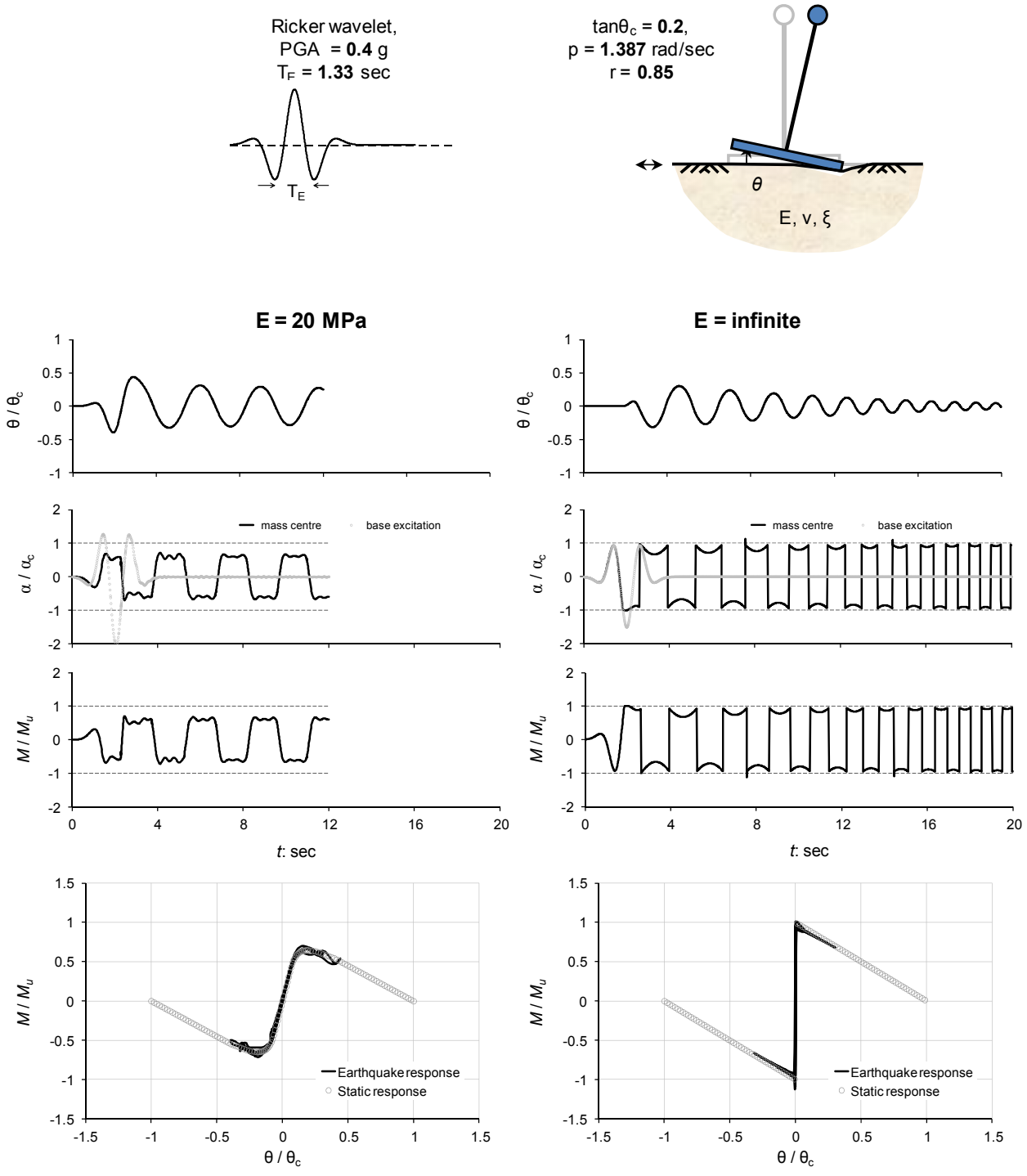


**Figure 4.18** Rocking response of a rigid structure ( $p = 1.387$ rad/sec , $\tan\theta_c = 0.2$ , and $r = 0.85$ ), (a) on elastic soil $\left(E = 20 \text{ MPa}, \ \nu = 0.5\right)$ and (b) on rigid soil. A Ricker pulse excitation of $PGA = 0.4\,\text{g}$ and $T_E = 1.33\,\text{sec}$ is applied at the bedrock.

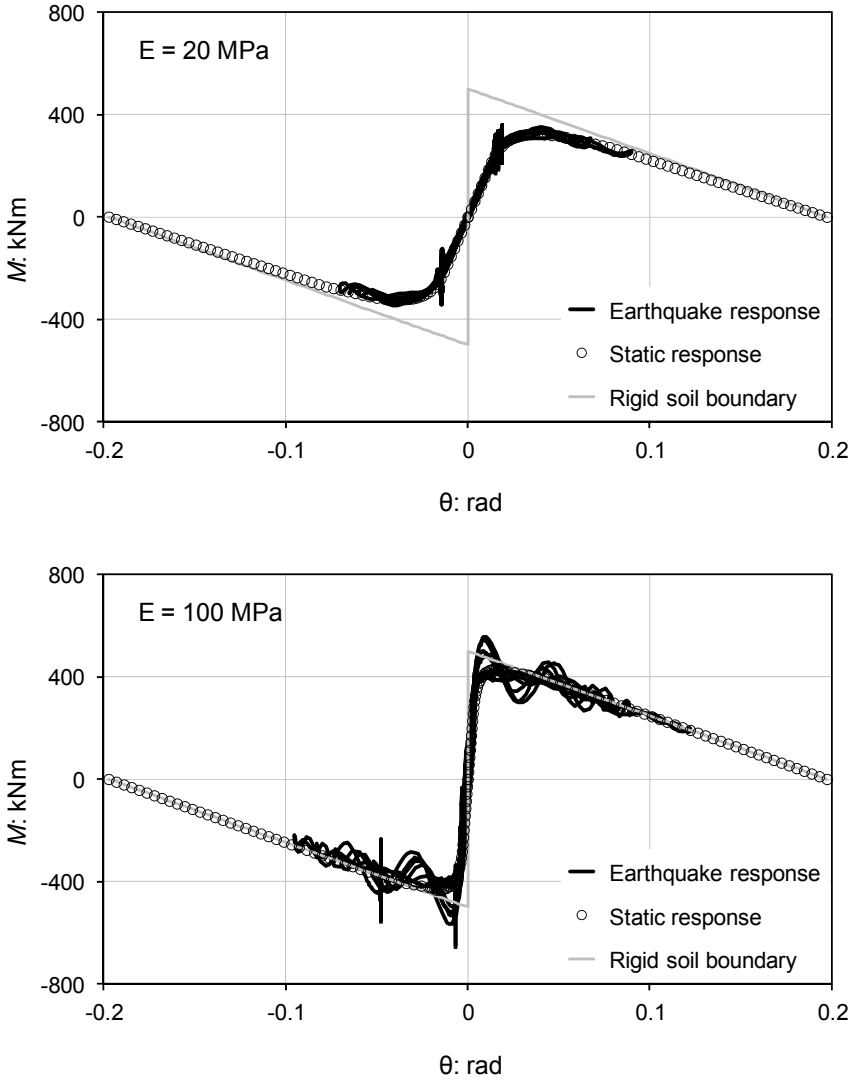


**Figure 4.19** Moment – rotation curves of a rigid footing on elastic soil under earthquake shaking and comparison to the static response. A Ricker wavelet of $PGA = 0.3$ g and $T_E = 1.33$ sec is used as bedrock excitation.

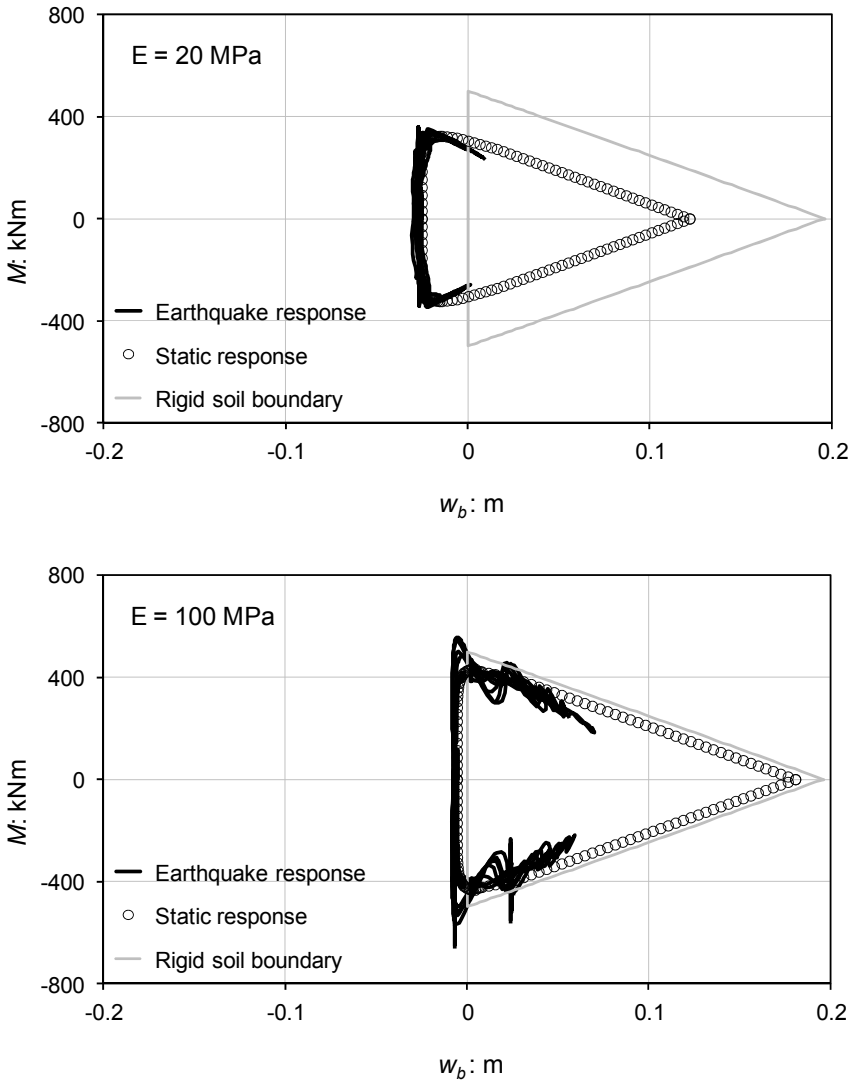


**Figure 4.20** Moment – vertical displacement curves of a rigid footing on elastic soil under earthquake shaking and comparison to the static response. A Ricker wavelet of $PGA = 0.3$ g and $T_E = 1.33$ sec is used as bedrock excitation.

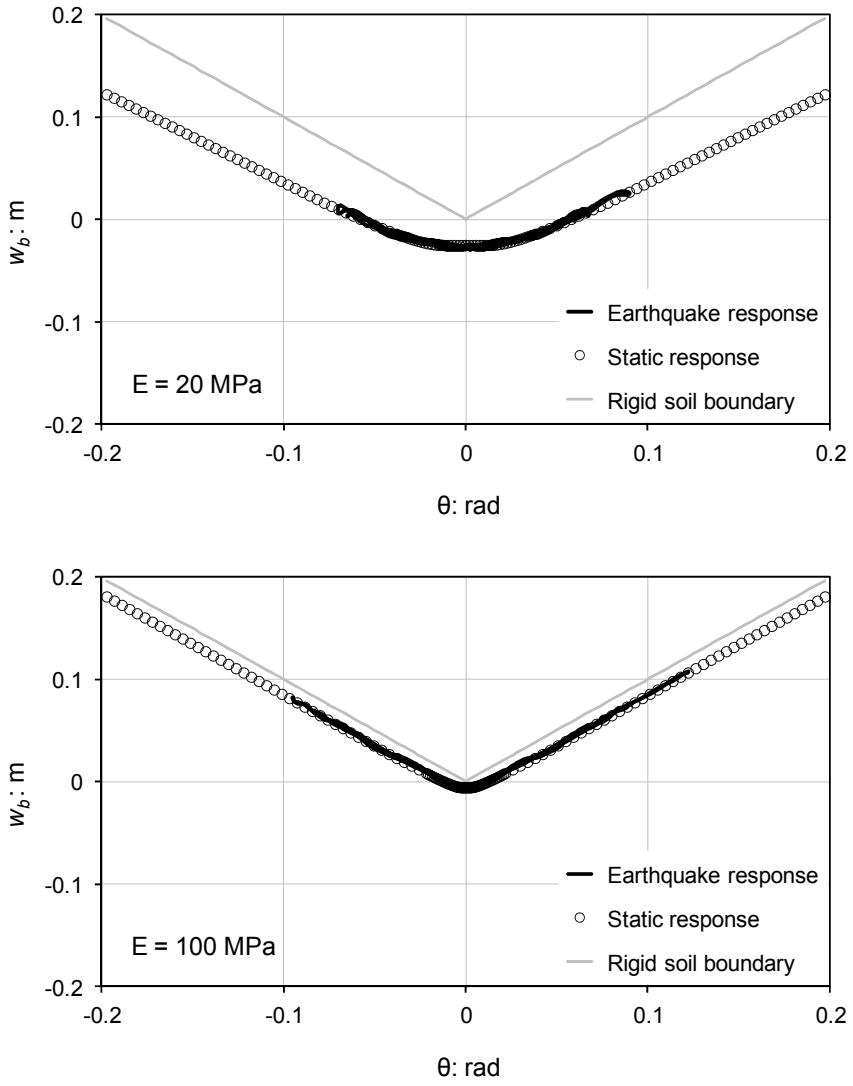


**Figure 4.21** Vertical displacement – rotation curves of a rigid footing on elastic soil under earthquake shaking and comparison to the static response. A Ricker wavelet of $PGA = 0.3$ g and $T_E = 1.33$ sec is used as bedrock excitation.

## 4.4 UPLIFT on INELASTIC SOIL

### 4.4.1 Preliminary analysis – Validation of soil models

The failure mechanism of a rigid strip footing resting on a cohesive soil under central vertical loading is illustrated in Fig. 4.22 (*model v.03*). In the numerical computation of bearing capacity the kinematic/hardening soil model was utilised. A displacement-controlled loading was applied at the centre of the footing and eventually an ultimate load of about 550 kN was computed. As shown in Fig. 4.22, a good approximation to the theoretically predicted slip lines (white dashed line) was obtained. Also, the ultimate load of 550 kN is close to the analytical Prandtl's solution which gives $N_u = (\pi + 2) A s_u = 514$ kPa $(s_u = 50$ kPa$)$.

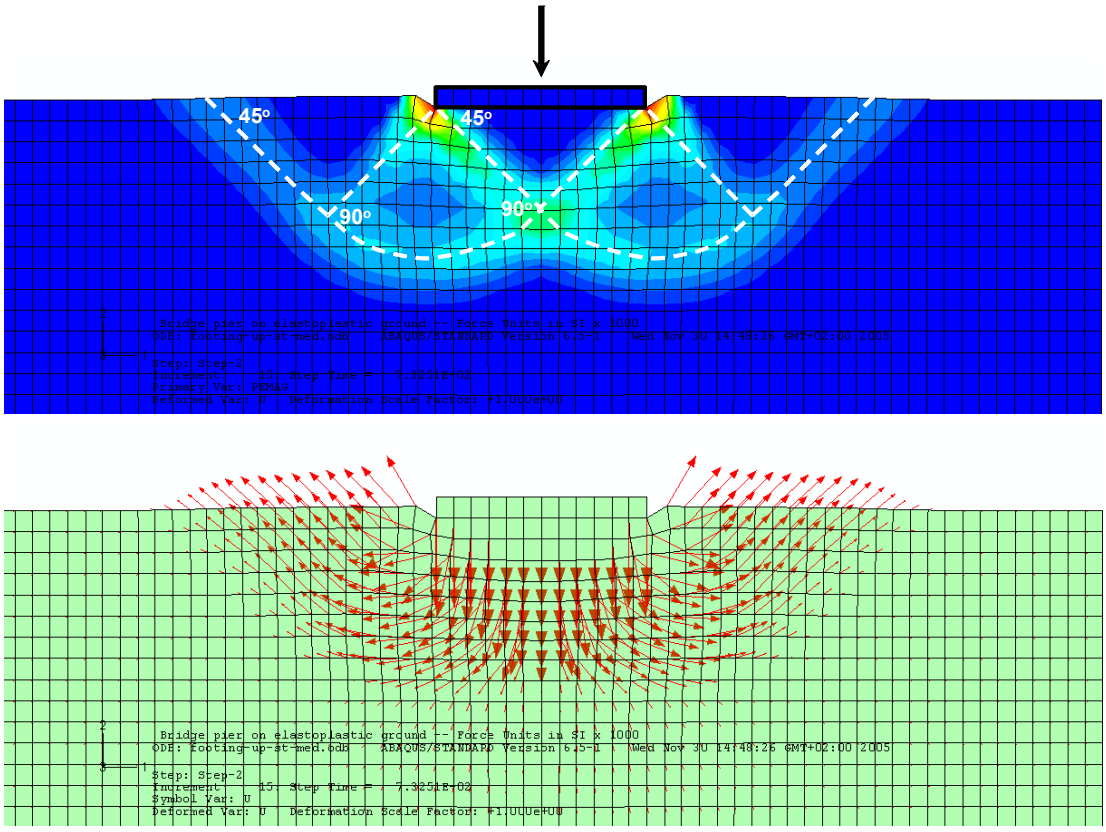


**Figure 4.22** Failure mechanism of a rigid strip footing on a cohesive soil under central vertical loading: Finite element plane strain analysis and comparison to the theoretically predicted slip lines (white dashed line).

The computed failure mechanism of a foundation in the general case of a combined loading $(M-Q-N)$ over cohesive soil is presented in Fig. 4.23. The computed response is in good agreement with the theoretical prediction of Salencon and Pecker (1995).

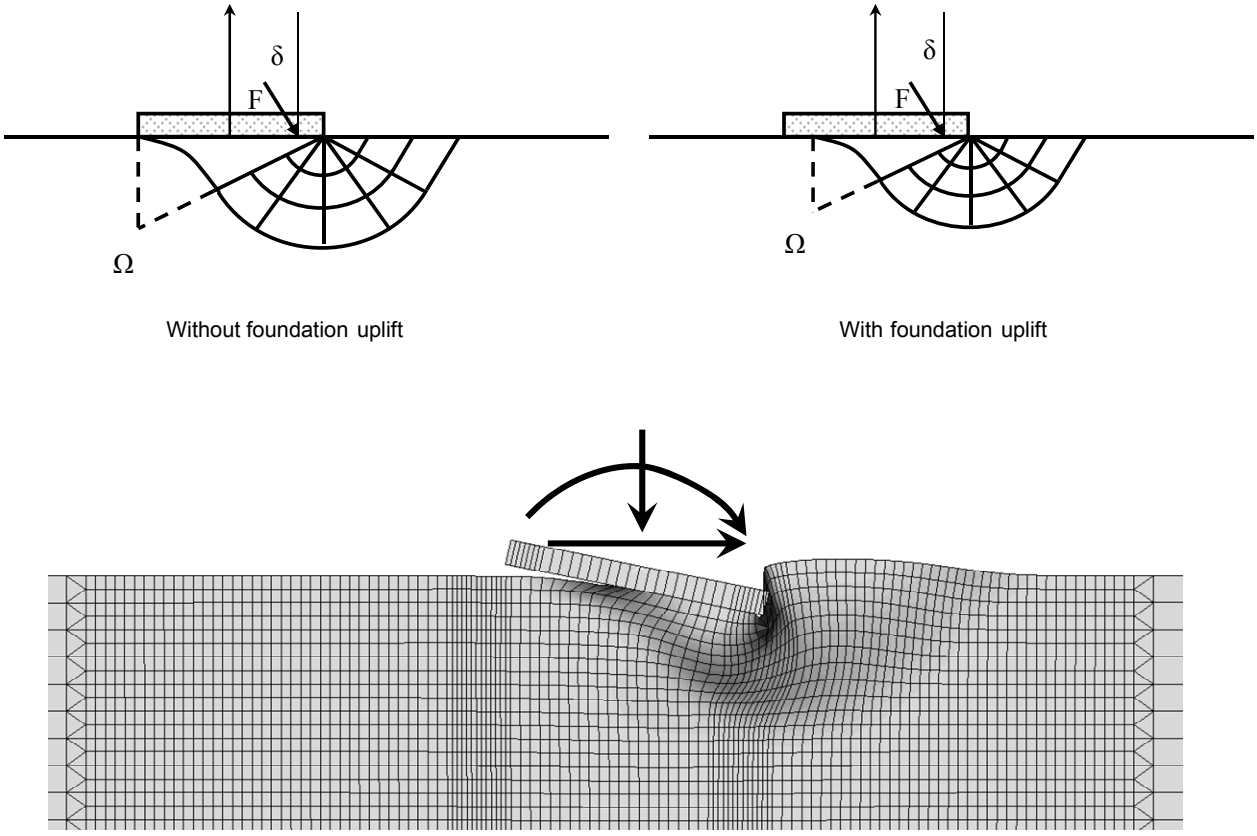


**Figure 4.23** Failure mechanism of a rigid strip footing on a cohesive soil under eccentric inclined loading: Finite element plane strain analysis and comparison to the theoretical mechanism (Salencon & Pecker, 1995).

### *Comparison of the soil constitutive models*

A fundamental comparative study is presented next to highlight the effect of soil constitutive modelling on the foundation response. Nonlinear behaviour of soil is approached by: (a) the elastic – perfectly plastic model, (b) the nonlinear kinematic/isotropic model. In the latter two different values of the yield stress $\sigma|_0$ are employed: (a) $\sigma|_0 = \sigma_{\max}/10$ and (b) $\sigma|_0 = \sigma_{\max}/3$. A uniform distribution of the elastic modulus and the undrained strength ($E = 100$ MPa and $s_u = 50$ kPa respectively) is considered throughout soil medium according to *model v.03* (Fig. 4.5).

Initially, a monotonic displacement-controlled vertical loading is applied at the foundation midpoint, which is gradually increasing up to failure. An ultimate load of $550\ \text{kN}$ is calculated with both methods. This value is consistent to the analytical estimation according to Prandtl's theory $(\pi+2)s_u A = 514\ \text{kPa}$. Nevertheless, Mohr-Coulomb model provides a more stiff backbone curve with an insignificant hardening behaviour after initial yield as shown in Fig. 4.24a. This is a result of perfectly plastic, post-yield behaviour. On the other hand, implementation of the kinematic hardening model leads to a softer behaviour which can be fitted by a log-type curve. From Fig. 4.24a also, it is clear that the yield stress of the kinematic model has a minimal effect on the backbone curve. Similar curves have been computed for a very soft soil profile $(E = 10\ \text{MPa})$ as plotted in Fig. 4.24b.

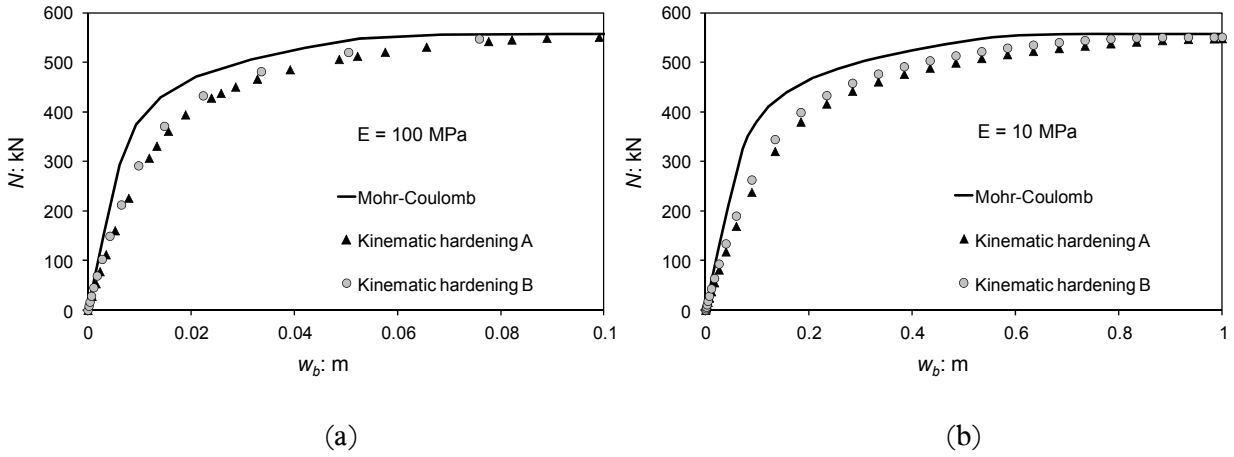


(a) (b)

**Figure 4.24** Monotonic curves for vertical loading extracted from two different models for nonlinear soil behaviour: (1) elastic – perfectly plastic model, and (2) von Mises failure criterion with isotropic/kinematic hardening law.

In Fig. 4.25a the $M-\theta$ curves are plotted for horizontal monotonic loading (displacement-controlled) under a constant vertical load of $100\ \text{kN}$. In Fig. 4.25b the same curves are plotted, zoomed in the small-displacement region. Similar conclusions to those concerning vertical loading can be drawn. It is worthy of note that the computed (from both models) ultimate moment of about $80\ \text{kNm}$ can be approximated by closed-form equation of limit analysis $M = Nb(1-N/N_u) = 100\times 1(1-100/514)$.

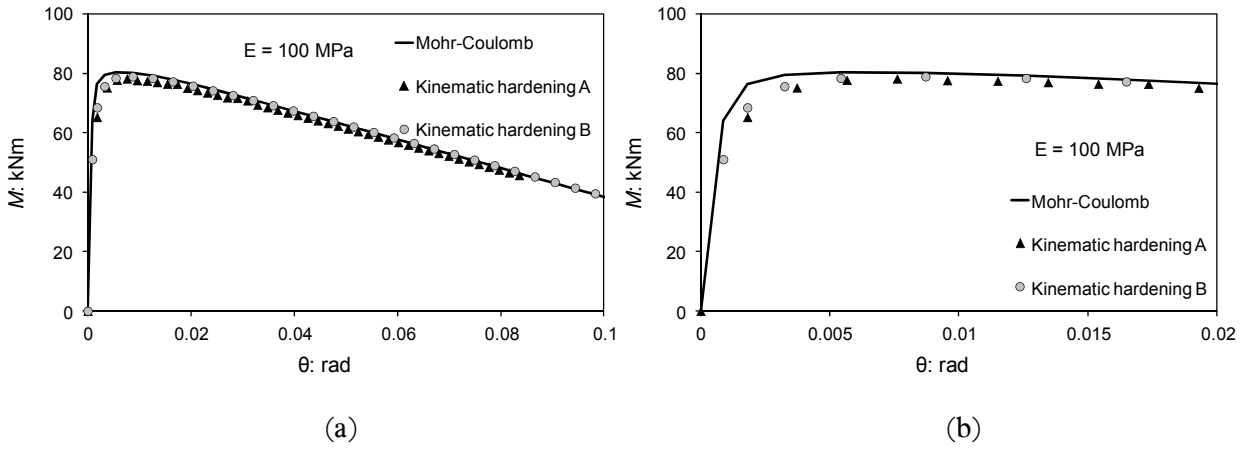


**Figure 4.25** Monotonic curves for moment loading extracted from two different models for nonlinear soil behaviour: (1) elastic – perfectly plastic model, and (2) von Mises failure criterion with isotropic/kinematic hardening law.

Cyclic behaviour of the foundation under a Ricker pulse-type excitation at the seismic bedrock $\left(T_E = 0.33 \text{ sec}, PGA = 0.2 \text{ g}\right)$ is investigated next. The results are plotted in Fig. 4.26 in the form of the foundation moment $M$ and rigid-body displacements $w_b, \theta$ calculated from: (a) the Mohr-Coulomb elastoplastic model, (b) the kinematic hardening model. A good agreement between the two models is obtained in terms of the moment-rotation loops. The elastoplastic model though is not sufficient enough to provide accurate estimates of the cyclic (accumulative) foundation settlement. A harmonic excitation is also employed to compare the two models and the resulting loops are presented in Fig. 4.27. From the results of both analyses it is derived that the M-C elastoplastic model underestimates the additional cyclic settlement of the foundation by a factor of two (see Fig. 4.27).

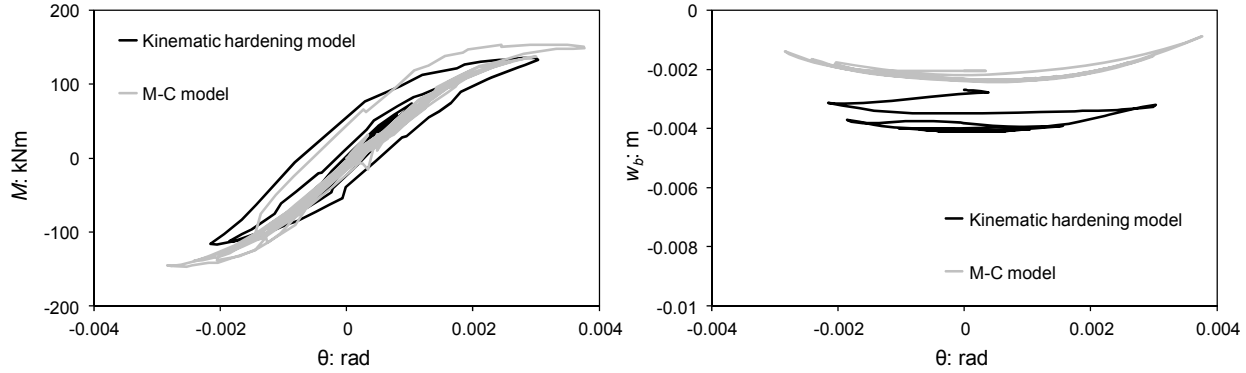


**Figure 4.26** Foundation cyclic behaviour under a Ricker pulse-type excitation $\left(T_E = 0.33 \text{ sec}, PGA = 0.2 \text{ g}\right)$: (1) elastic – perfectly plastic model, and (2) von Mises failure criterion with isotropic/kinematic hardening law.

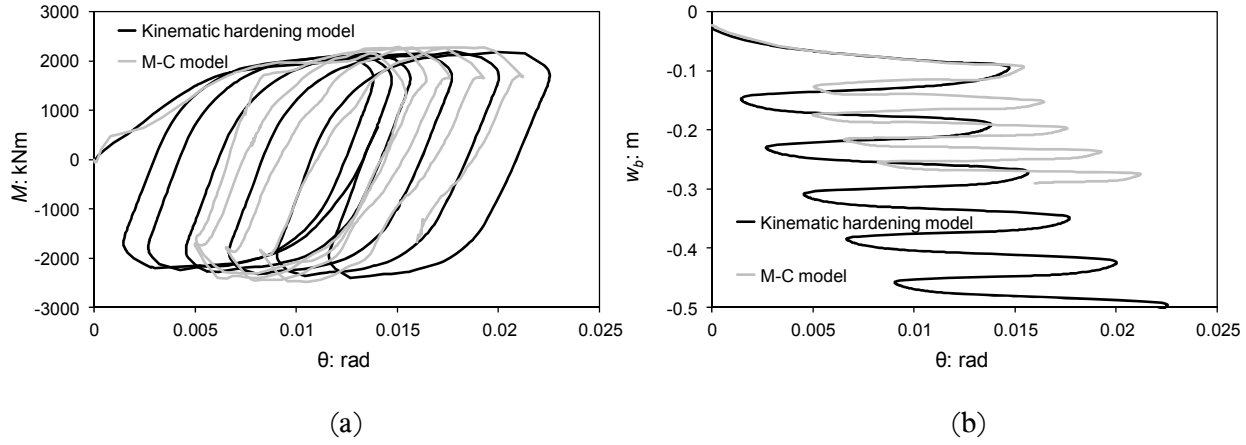


**Figure 4.27** Foundation cyclic behaviour under a long-period harmonic excitation $\left(T_E = 1.00 \text{ sec}, PGA = 0.4 \text{ g}\right)$: (1) elastic – perfectly plastic model, and (2) von Mises failure criterion with isotropic/kinematic hardening law.

### 4.4.2 Monotonic response

As for the study of elastic soil, rocking with uplift under static conditions is investigated first. The system configuration of Fig. 4.5a is revisited (*model v.01*). In addition to the 'elastic soil' problem, the rocking response is also affected by the limited strength of soil material. The soil strength parameter can be implemented to the ultimate load against vertical loading $N_u$ or in a normalised form, to the

load factor $\chi = N / N_u$ (i.e. the inverse of the factor of safety against vertical loading). In the first step the vertical (gravitational) load is applied through the mass centre (symmetric loading). Then a gradually increasing horizontal displacement $\delta$ is applied at the mass centre up to a maximum value of $\delta_{\max} = b$ (antisymmetric loading). For a sufficiently slender structure the horizontal translation of the footing $u_b$ is negligible compared to $\delta$ and accordingly, at the moment that $u_{cm} = \delta_{\max} = b$, the footprint of the mass centre has reached the foundation edge. Evidently, critical overturning has already occurred at this loading point. The displacement-controlled loading at the mass centre is restrained by a horizontal shear force $Q$ and an overturning moment $M$ imposed to the foundation by the supporting soil so that static equilibrium is attained. The rocking rotation $\theta$ and the foundation moment $M$ can be computed again from Eqs 4.1 and 4.2. Alternatively the foundation moment $M$ can be calculated by integrating soil pressures over the contact interface (Eq. 4.3).

The half-width of the effective footing $\beta$ is calculated at each increment through Eqs 4.4.

Unlike the elastic soil case, during rocking without uplift, the rotation pole does not lie along the midpoint axis of the footing. It starts moving towards the unloading corner right after the onset of antisymmetric loading. Depending on the load factor, $\chi$, the rotation pole may shift during uplift either towards the loading or the unloading corner. In any case the incremental vertical displacement $\delta w_b$ can be calculated from Eq. 4.5.

***Contact pressures***

The soil-structure configuration of *model v.01* (Fig. 4.5a) with soil modulus of elasticity $E_o = 20$ MPa $\left(G_o = 7 \text{ MPa}\right)$ is revisited to compute $p - w$ curves along the foundation base. An ultimate shear strength $s_u = 100$ kPa is also introduced leading to an ultimate vertical load $N_u \cong 1000$ kN.

In the graphs of Fig. 4.28 the development of contact pressures is plotted for the interface nodes from the left edge towards the midpoint (red circles) in comparison with their equidistant nodes on the

right (solid black lines). Initially, a vertical load is applied to the footing through the mass centre, gradually increasing to reach gravitational load of $500\,\text{kN}$. During this step, the distribution of the contact pressures along the interface is symmetrical to the midpoint and can be validated with the elastic medium solutions available in literature (Sadowsky, 1928) as shown in Fig. 4.29. These soil reactions must be in equilibrium with the external load, and therefore integration along the foundation should lead to the gravitational load $N$. In the $p-w$ curves of Fig. 4.28 this step is represented by the linear branch determined by the points of rest $(p=w=0)$ and full loading $(w=p/k_v=N/K_v=0.025\,\text{m})$. As symmetrical nodes are represented on each graph, their load-displacement curves are identical during this phase. Unlike the conventional winkler modelling, the stiffness $k_v$ is not uniform along the foundation, but increases close to the edges. In the succeeding step, a gradually increasing horizontal load is applied at the mass centre. The overturning moment resulted from the imposed displacement generates additional soil pressures and differential settlements. Hence, this antisymmetric loading separates the contact interface to the loading side (on the right of the midpoint) and the unloading side (on the left of the midpoint). Along the loading side soil pressures increase at a steeper rate determined by $k_m$. Likewise, for the unloading side soil pressures gradually reduce at the same rate until they drop down to zero. Interestingly, at this point the vertical displacement has not become zero as well (as the conventional winkler model predicts) but has converged to a residual value. Evidently, uplift is engaged right after the contact pressure of the left corner node becomes zero. As the separation zone is expanding towards the midpoint, the unloading area is shifting rightwards. For the contact pressures on the foundation area remaining in contact with soil, an upperbound exists now beyond which, unloading initiates.

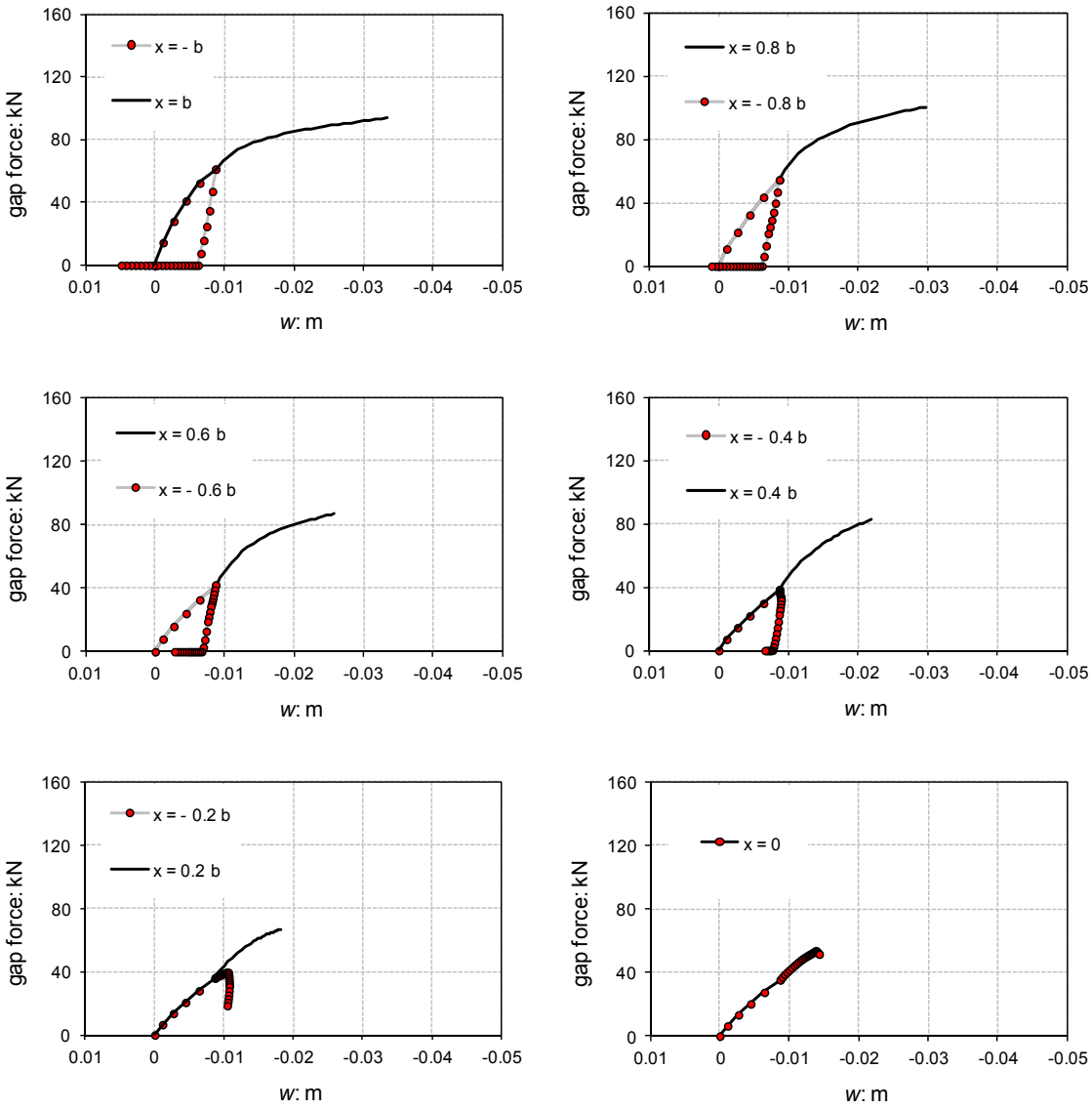


**Figure 4.28** $p-w$ curves of a foundation on elastoplastic soil $\left(E_o = 100 \text{ MPa}, \quad \chi = 0.5\right)$ during: (a) pure vertical load, (b) displacement-controlled horizontal load at the mass centre.

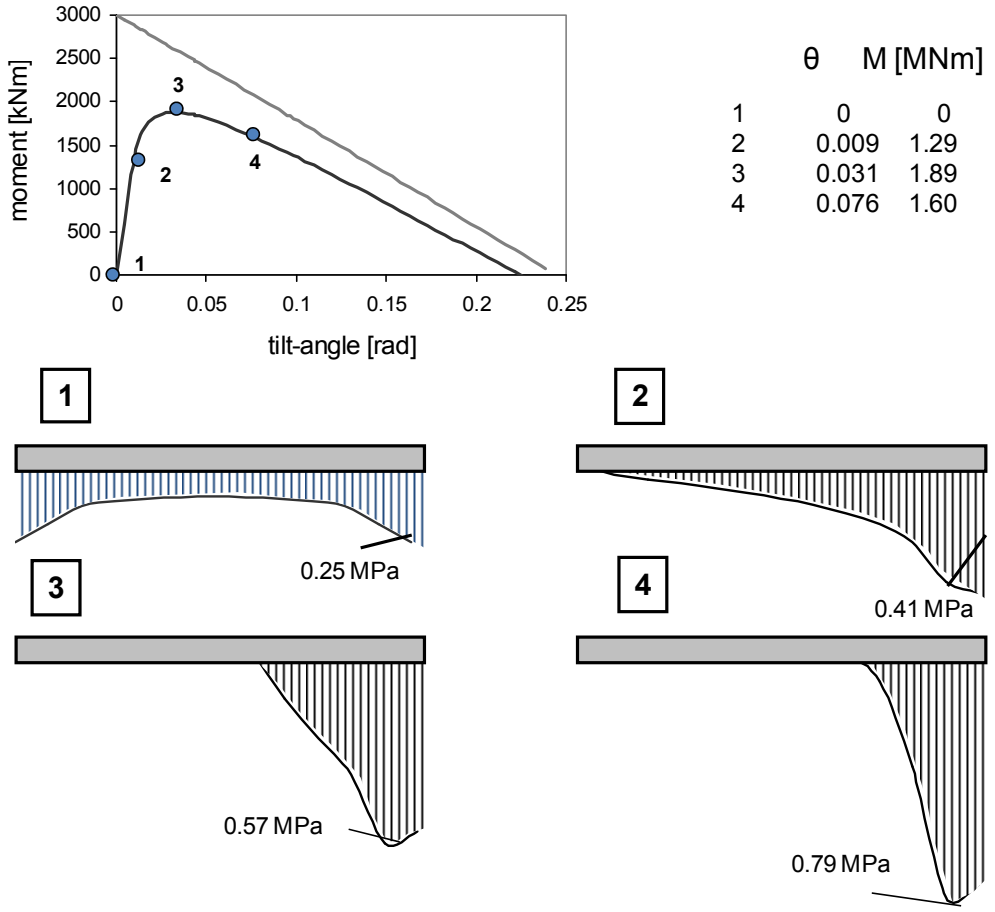


**Figure 4.29** Distribution of contact pressures on the foundation computed with finite element analysis: (1) under pure vertical loading, (2) at incipient uplift, (3) at ultimate moment, and (4) at the declining branch.

### *Load-displacement curves*

A rigorous approach of the static overturning moment about the foundation midpoint as a function of the rocking rotation for a rigid foundation allowed to uplift on elastic soil is depicted in Fig. 4.30. When an undeformable soil is regarded, at incipient uplift the moment instantaneously climbs from zero up to the ultimate value $M_u = Nb$. From this point on, the moment is gradually decreasing due to the amplifying $(P-\delta)$ effects and eventually drops down to zero when the rocking rotation reaches the critical value $\theta_c = b/h$. On the other hand, in the full-contact regime the soil-foundation stiffness is kept constant and therefore the moment is a linear function of the rocking angle. It is concluded that

in case of deformable supporting soil and a foundation allowed to uplift, the moment–rotation curve is bounded by the afore-mentioned limiting curves. This curve comprises: (a) a linear branch from zero up to the point where uplift initiates, (b) a softening branch to the ultimate moment capacity point, where the soil-foundation rocking stiffness decreases due to the gradually amplifying uplifting mechanism, and (c) a declining branch which is dominated by the $\left(P-\delta\right)$ effects and eventually leads to the overturning failure of the foundation at the critical angle $\theta_c$ (Fig. 4.30).

In the full-contact regime the moment is a linear function of rocking rotation and the rocking stiffness is calculated analytically from the afore-described solutions of the literature (e.g. Gazetas, 1991). Uplift initiates for a moment of $Nb/2$. This value for the uplifting moment is also extracted from the parametric study of Crémer *et al.* (2002).

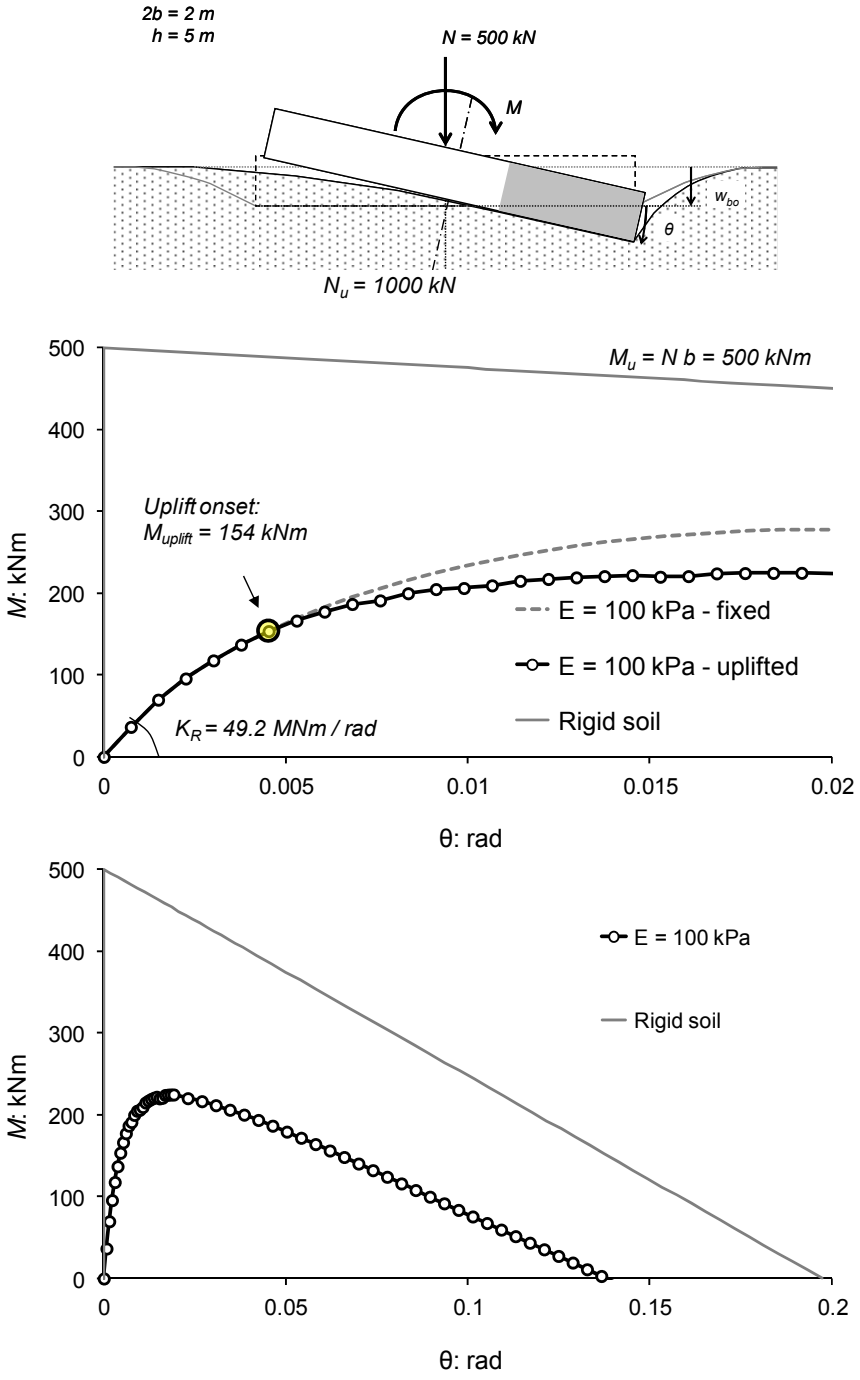


**Figure 4.30** Moment – rotation curves of a rigid strip footing on inelastic (soft and medium) or rigid soil. In the deformable soil the vertical load factor is $\chi = 0.5$.

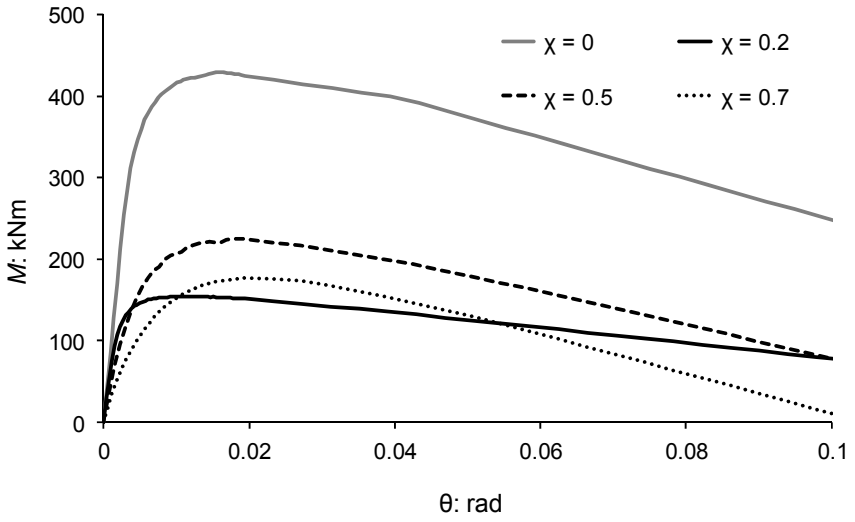


**Figure 4.31** Moment – rotation curves of a rigid strip footing on inelastic soil for different values of $\chi$ and comparison to the rigid soil case.

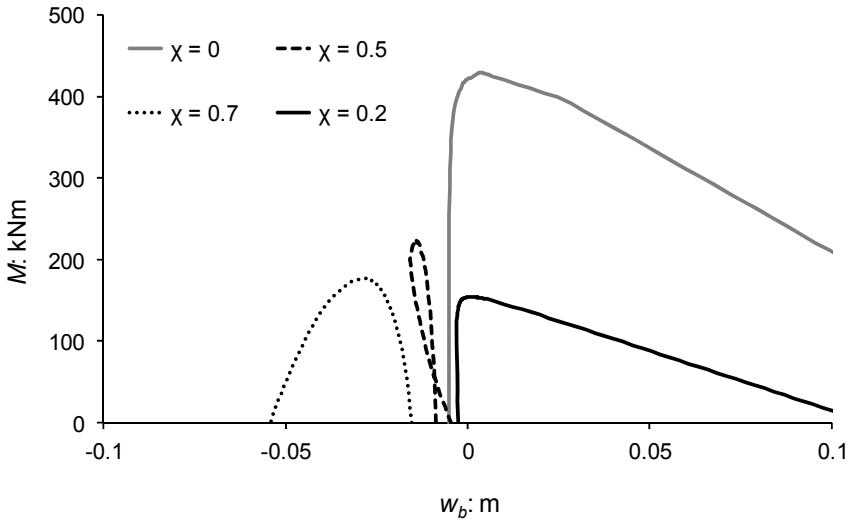


**Figure 4.32** Moment – vertical displacement curves of a rigid strip footing on inelastic soil for different values of $\chi$ and comparison to the rigid soil case.

### *Coupling of foundation displacements and rocking angle*

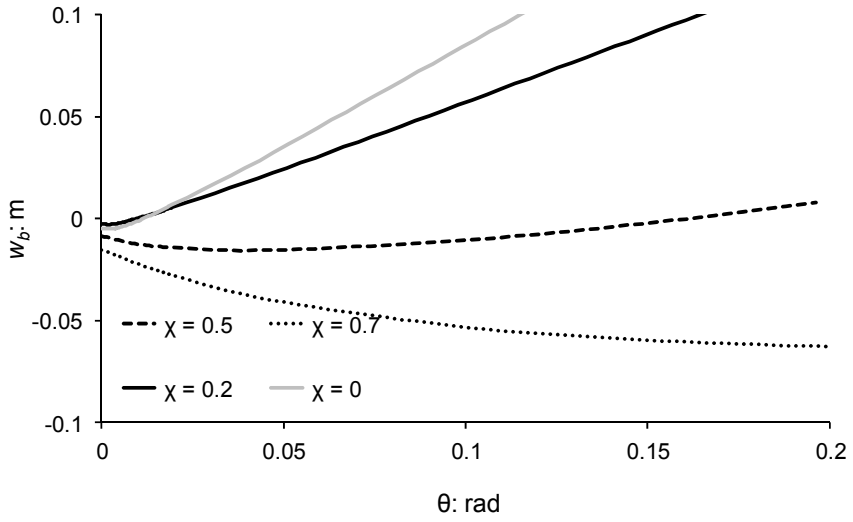


**Figure 4.33** Coupling of vertical displacement – rotation of a rigid strip footing on inelastic soil for different values of $\chi$ and comparison to the rigid soil case.

### *Rotation pole*

The exact positioning of the rotation pole during rocking vibrations is of great importance as it governs the distribution of soil pressures. When a strip footing is rocking in full contact with elastic soil, the pole of rotation lies on the interface midaxis. For a sufficiently slender structure the translational mode can be neglected and the pole is located constantly at the interface midpoint. In any case for the projection of the pole on the footing interface it holds $x_p = 0$. On the other hand, in case of a rigid soil the pole of rotation jumps from the midpoint to the corner of the footing as rocking initiates (Fig. 4.34). In the general case of rocking with uplift on a compliant soil, the pole departs from the midpoint right after uplift onset moving towards the corner point. The stiffer the supporting soil the more rapid this transition is (Fig. 4.34).

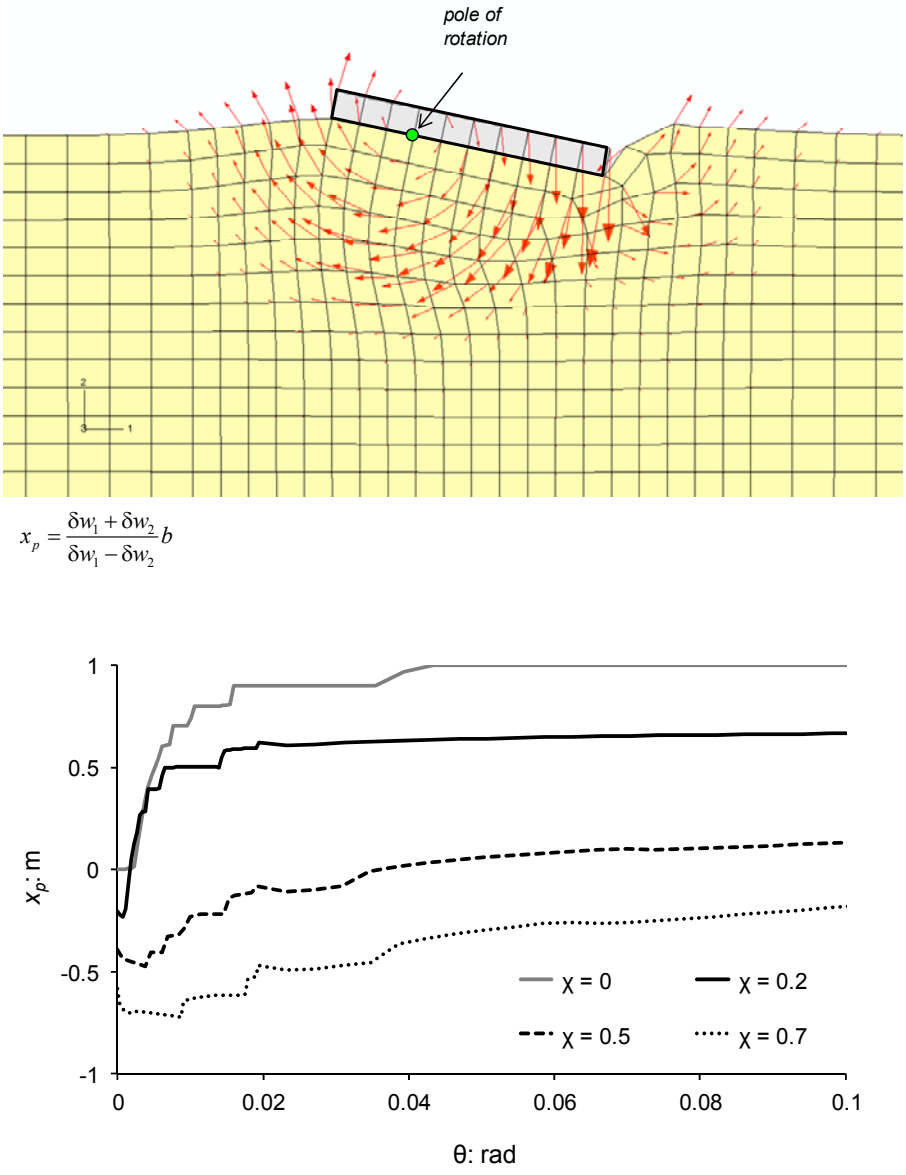


**Figure 4.34** Shift of the rotation pole along the foundation during rocking for different levels of the capacity factor $\chi$.

### *Uplift*

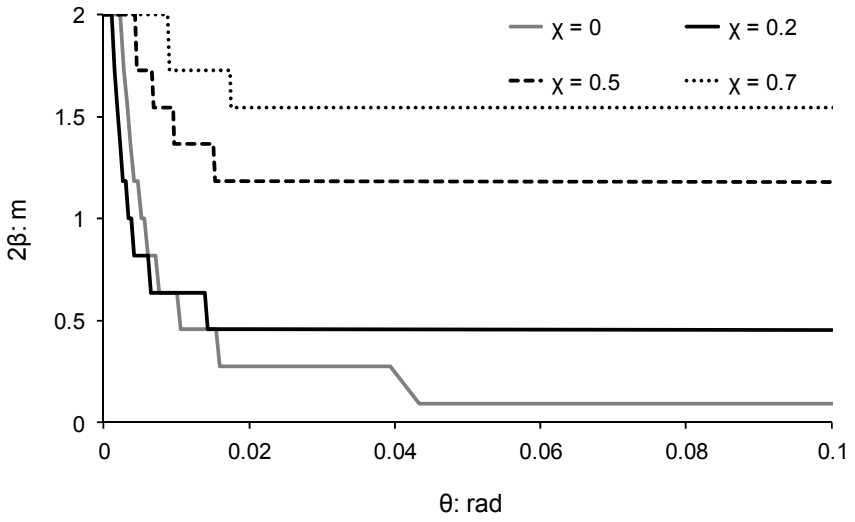


**Figure 4.35** Reduction curves of the contact area (effective footing) during uplift for different levels of the capacity factor $\chi$.

### 4.4.3 Earthquake response

The significance of uplifting and soil inelasticity on the seismic response of the slender structure of Fig. 4.5 is explained in Figs 4.36 and 4.37. Seismic excitation in the form of a long-period Ricker pulse (TE = 2.2 sec, PGA = 0.20 g) is applied at the bedrock and is propagated through soil to produce a free-field "input motion" of a dominant period TE = 1.8 sec and PGA = 0.34 g. Such a Ricker-type excitation represents long-period pulses that are often attributed to near-source rupture-directivity effects.

The response is highlighted in terms of M-θ and M-w hysteresis loops (Fig. 15), as well as time-histories of rotation θ, settlement w, and acceleration Acm at the superstructure (Fig. 16). Two cases are considered :

- a "light" weight structure : N = (1/4) Nu = 1000 kN, corresponding to $\chi = 0.25$
- a "heavy" weight structure : N = (3/4) Nu = 3000kN, corresponding to $\chi = 0.75$

Several conclusions may be drawn from Figs 4.36 and 4.37:

• For the light structure : The initial loading cycle follows the monotonic pushover M–θ curve. Upon unloading after a small excursion in the descending branch of the monotonic curve, the path follows with small deviations the original monotonic curve. This is evidence of reversible behaviour the result of nonlinearly elastic uplifting response. However, after a substantial excursion into the descending branch unloading departs slightly from the virgin curve, as soil inelasticity is "activated" due to the large concentration of the applied normal stress when uplifting reduces substantially the area of contact.

• For the heavy structure: The departure of all branches of loading–unloading–reloading cycles from the monotonic curve is far more substantial apparently the result of strongly inelastic soil behaviour as the bearing capacity failure mechanisms (left and right) are fully "activated" in this case.

• The moment-settlement curves (M–w) reflect the above M–θ response, with the curve of the light-weight case showing the smallest deviation from the monotonic curve, and of the heavy weight the largest.

• From a design perspective, soil-foundation-structure interaction (SFSI) plays a beneficial role in reducing the acceleration ACM at the centre of mass of the superstructure. This reduction is much greater in the heavy-load case, as result of significant soil inelasticity induced by the rocking foundation ("inertial" nonlinearities).

• The "penalty" of the heavily loaded foundation is to sustain substantial additional vertical settlements, ΔW (of about 20 cm) ; by contrast the lightly-loaded foundation ends-up with the same settlement as its original static settlement, w wo 5 cm.

• Particularly significant, although somewhat coincidental, is the very small residual rotation in both cases. This is due to the largely symmetric nature of the excitation, as a result of which the heavily-loaded foundation develops "left" and "right" bearing-capacity failure mechanisms. The

resulting two-sided inelastic deformations lead to a symmetric downward displacement (: Δw) with only a minor residual rotation Δθ.

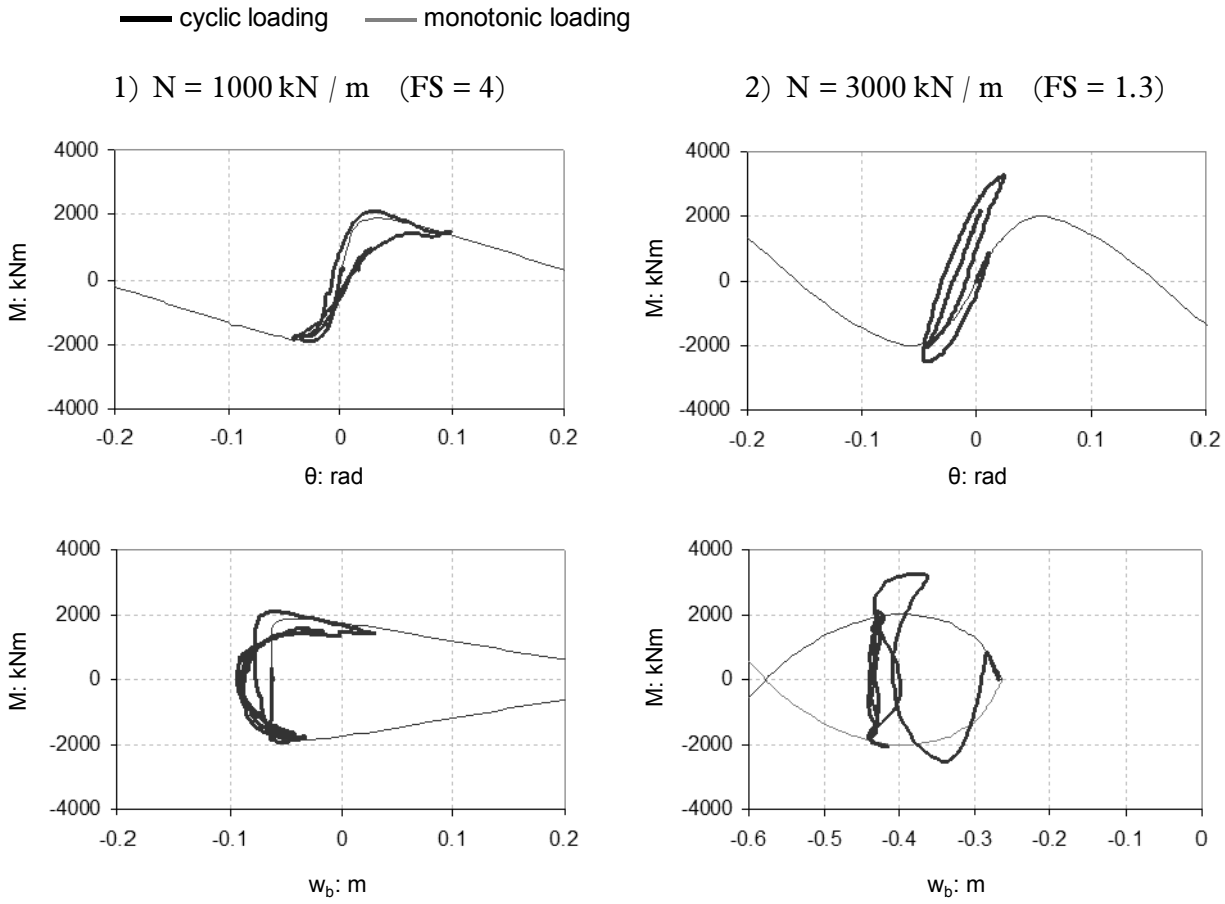


**Figure 4.36** $M-\theta$ and $M-w$ curves for the soil-foundation system of Fig. 4.5.

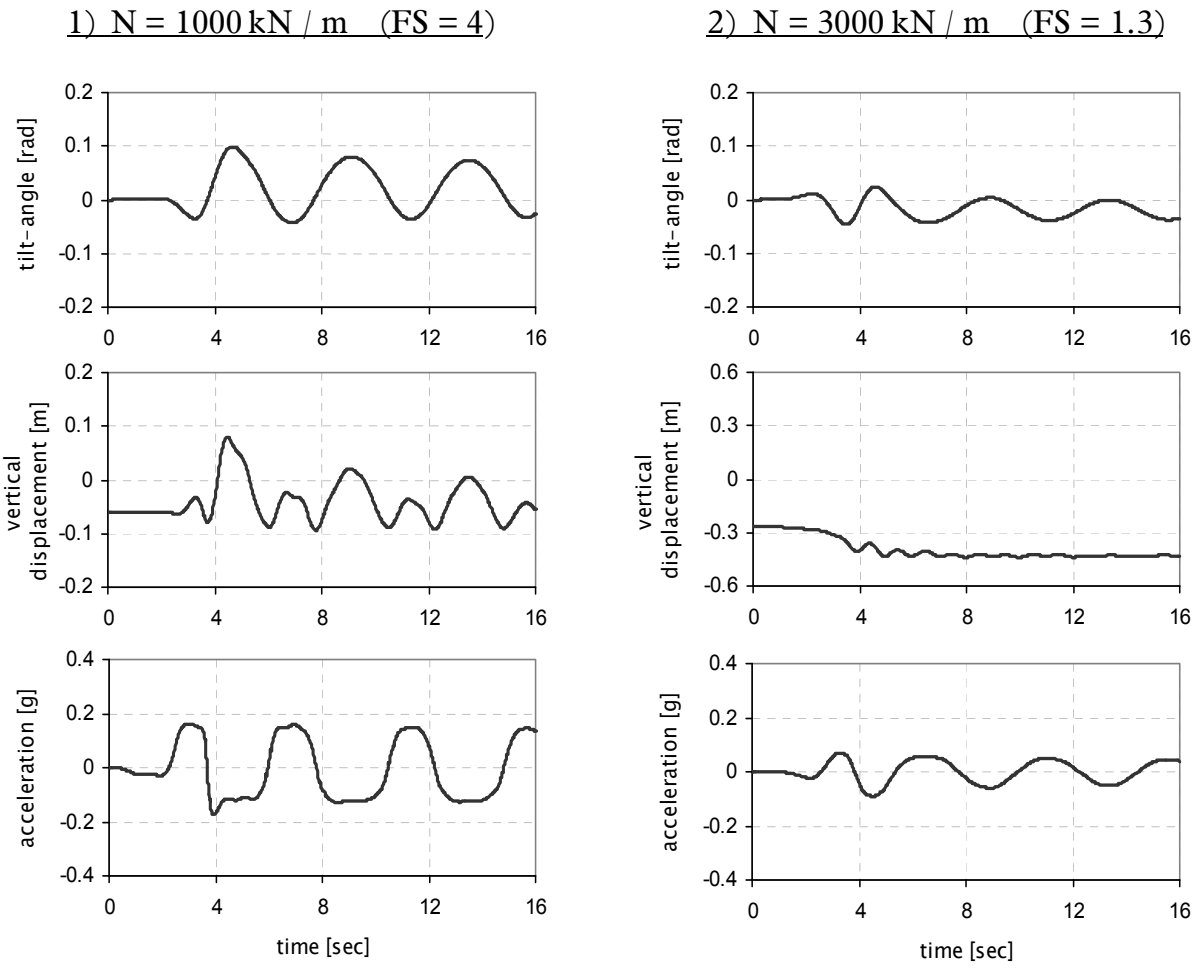


**Figure 4.37** $M-\theta$ and $M-w$ curves for the soil-foundation system of Fig. 4.5.

## 4.5 SIMULATION of CENTRIFUGE EXPERIMENT

In the framework of the 'QUAKER' research project a series of centrifuge tests have been performed at LCPC to investigate a building with a slenderness ratio of two resting on clay under monotonic and cyclic loading. Ultimate capacity and permanent deformation of the foundation have been recorded and discussed. Nonlinear finite element modelling of the experimental tests highlights the effects of the problem parameters on the foundation response. In this series of experiments, a 100x100 mm2 footing (80x80 mm2 in few cases) over soft saturated clay is submitted to (a) purely vertical, (b) monotonic horizontal and (c) cyclic horizontal loading. To this end, a servo-controlled actuator was

used to operate as displacement-controlled for the static tests and force-controlled for cyclic loading. The tests were performed under a centrifugal acceleration of 100 g meaning that a scale of 1/100 should be applied to derive the prototype model. Horizontal loading is applied to the structural centre of gravity at a height of 100 mm above the foundation level leading to a height-to-width ratio of two. Two values of the structural dead weight were chosen to investigate the influence of the vertical load on the rocking response. Principally, a building with a dead weight of 1284 t (for test Tub3 - T07) or 1370 t is implemented, corresponding to a heavily-loaded foundation (M1). A building with a dead weight of 580 t is also used corresponding to a lightly-loaded foundation (M2). The former gives a vertical loading ratio of $\chi = N/Nu = 0.6$ whereas for the latter it is $\chi = N/Nu = 0.26$. Soil material used in the experiments is saturated kaolin Speswhite clay at a water content of about 42 % and density of about 17 kN/m3. The total depth of the soil sample inside the container is 263 mm corresponding to a soil stratum width of 248 mm. Each container has been prepared by consolidation under stress in lab with three or four successive layers of clay. Cone Penetrometer tests were performed at 1 g before consolidation in the centrifuge, and also in-flight after reconsolidation and just before loading the structure. Shear vane tests were also carried out at several points to estimate su. Profiles of su with depth were determined using CPT and well-established correlation between qc and su measured in-flight on Speswhite clay (Garnier, 2001):

$$q_c / s_u = 18.5 \qquad [4.14]$$

Geometry and instrumentation of the model utilised at the centrifuge tests are shown in Fig. 4.38.

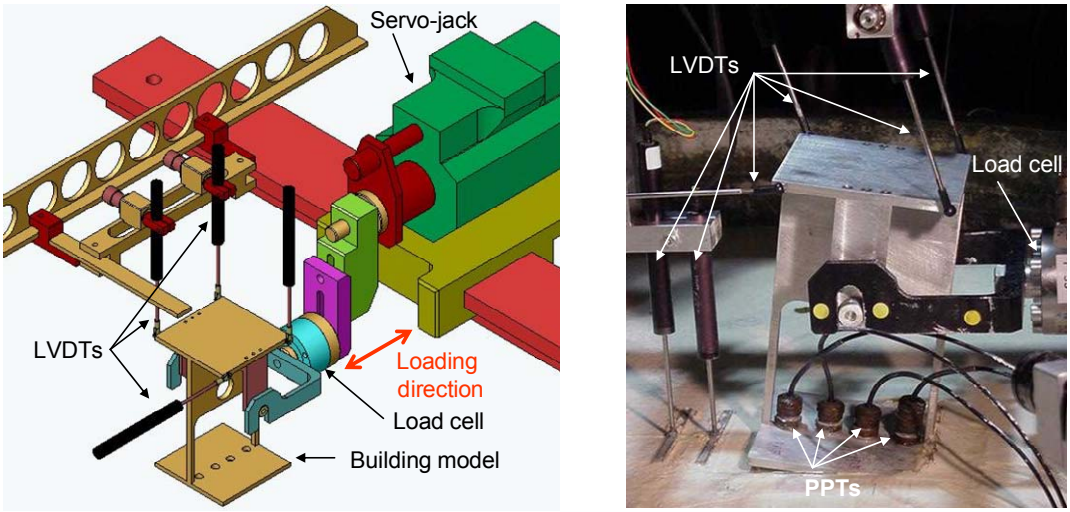


**Figure 4.38** Loading device (left) and deformed position of model M2 after loading (right).

### 4.5.1 Loading program

Within the framework of the Quaker project the following loading conditions have been applied during the centrifuge experiments:

- monotonic, displacement-controlled vertical loading to failure (determination of vertical bearing capacity),
- monotonic horizontal loading to failure (with constant vertical dead weight either M1 or M2). The load is always applied at the centre of gravity, regardless of settlement or rotation,
- cyclic horizontal loading at the gravity centre, under self weight (with and without a sand layer below the footing). The amplitude of the displacement-controlled loading is 0.4 mm (0.4 m in prototype dimensions) and the driving frequency ranges between 0.10 Hz and 0.16 Hz.

The list of the loading tests performed is presented in chronological order in Table 4.3 together with the values of the ultimate capacity.

**Table 4.3** Loading program of the centrifuge tests and ultimate load

| Tub n° | Test | Foundation (mm x mm) | Loading sequences | Ultimate load (MN) |
|---|---|---|---|---|
| Tub 1 | T01 | 8 x 8 | Vertical static (DC) | 10 |
| | T02 | 10 x 10 | Vertical static (DC) (cancelled) | - |
| Tub 2 | T03 | 8 x 8 | Vertical static (DC) | 16.5 |
| | T04 | 10 x 10 | Vertical static (DC) | 24 |
| Tub 3 | T05 | 10 x 10 | Vertical static (DC) | - |
| | T06 | 10 x 10 | Vertical static (LC) | 22 |
| | T07 | 10 x 10 - Building M1 | Horizontal static (DC) | 1.4 |
| Tub 4 | T08 | 10 x 10 - Building M1 | Horizontal static (DC) | 1.2 |
| | T09 | 10 x 10 - Building M1 | Horizontal static (DC)<br>Horizontal cyclic (DC) | 1.3<br>2.0 |
| | T10 | 10 x 10 - Building M1 | Horizontal static (DC)<br>Horizontal cyclic (DC) | - |
| Tub 5 | T10 | 10 x 10 - Building M1 | Horizontal static (DC)<br>Horizontal cyclic (DC)<br>Horizontal cyclic (LC) | - |
| | T11 | 10 x 10 - Building M2 | Horizontal cyclic (LC) | - |
| Tub 6 | T12 | 10 x 10 - Building M2 | Horizontal static (DC) | 0.75 |
| | T13 | 10 x 10 - Building M1 (+sand layer) | Horizontal cyclic (LC) | - |
| Tub 7 | T14 | 10 x 10 - Building M1 | Horizontal static (DC) | - |
| | T15 | 10 x 10 - Building M2 (+sand layer) | Horizontal cyclic (LC) | - |

Prior to lateral loading, preliminary displacement-controlled tests have been performed to estimate the vertical bearing capacity of the foundation for the two structural configurations (tests T01 to T06). Due to the log-type shape of the vertical load-settlement curve no clear failure point could be identified. To overcome this, two 'conventional' failure criteria were established for settlement level of 4.5 mm and 10 mm. On the other hand, horizontal load-displacement monotonic curve after initial yielding tends to a horizontal line determining the lateral load capacity of the foundation. Ultimate loads in horizontal and vertical loading direction are presented in Table 4.3.

### 4.5.2 Finite element simulation

A series of two-dimensional finite element analysis was performed to simulate the centrifuge experiments. The prototype model has been implemented in the numerical study so that all dimensions at the centrifuge model have been properly scaled up. A lumped-mass structure with a

square footing (10x10m2) is considered to represent the building. The mass point located at a height of 10 m above the foundation level is connected to the foundation with a (rigid) beam element so that no flexural deformation of the superstructure is permitted. Horizontal loading is applied at this level. Rigid beam elements have been also utilised to prevent foundation mat deformations. The rigid boundary at the bottom is placed at a depth of 25 m below the foundation level. Nonlinear soil behaviour is described with the above discussed nonlinear constitutive model which incorporates the von Mises yield criterion combined with an isotropic and kinematic hardening model in the post-yield domain. This model is most suitable for the analysis of the dynamic behaviour of cohesive soils under undrained conditions. Some of the analyses were repeated by utilising the elastic–perfectly plastic Mohr-Coulomb model. Linear undrained strength profiles were estimated from in-flight CPT results in association with Eq. 4.14 as presented in Table 4.4. These profiles have been utilised in the two-dimensional finite element analysis. The favourable effect of vertical loading to soil strength underneath the foundation has been taken into account by increasing the values of su at surface, up to su(B/4). Due to lack of experimental data for the soil stiffness, Young's modulus at low deformations is considered as a linear function of the undrained shear strength. Different formulae are implemented to estimate the soil stiffness during horizontal and vertical direction.

**Table 4.4** Linear distributions of the undrained strength with depth based on the CPT results at 100g. These values of su have been implemented in the finite element analysis

| Test | | Undrained shear strength (kPa) | Notes |
|---|---|---|---|
| Tub1 | T01 | $s_u = 12.5 + 3.24z$ | |
| Tub2 | T03/T04 | $s_u = 8.9 + 1.74z$ | |
| Tub3 | T06 | $s_u = 18.5 + 4.24z$ | Profile b |
| | T07 | $s_u = 7.6 + 2.64z$ | Profile c |
| Tub4 | T09 | $s_u = 6.4 + 3.65z$ | |
| Tub6 | T012 | $s_u = 5.6 + 5.87z$ | |

A typical comparison of the numerical and the experimental vertical load-settlement curve (tub3 test) is presented in Fig. 4.39. Upper and lower bound distributions of su from tub3 (profiles b and c respectively) have been utilised in the numerical simulation. Both numerically computed backbone

curves capture the initial stiffness and the hardening behaviour (after the yield onset), of the centrifuge test. The large-displacement response and the ultimate bearing capacity calculated with profile b however are much closer to the centrifuge results. Similar trends for the vertical backbone curve are extracted from the simulation of the other tests. The experimental load-displacement curve under monotonic horizontal loading (tub3 test) is presented in Fig. 4.40. Both profiles b and c of su were used for the numerical interpretation. In this case however, the soil underneath the foundation has been strengthened due to the gravitational preloading (12.6 MN). Hence, an increase of the undrained strength is considered as shown in Fig. 4.40. A correlation of E = 1200su was adopted for the elastic soil modulus. An excellent agreement between the experimental and the numerical results is achieved when the profile b is considered. It is also uncovered from the numerical analysis that the foundation response is marginally influenced by the contact conditions at the interface (rough or smooth). On the contrary, the ultimate horizontal load merely reaches up to 300 kN when the profile c is used; a value which is far less than the centrifuge result.

The foregoing analysis procedure was repeated with profile b, for different values of the initial load N varying from near zero to the ultimate value Nu. The horizontal load was obtained (a) at incipient yield and (b) at u/B = 0.1. The derived failure envelope in the N-Q space (plotted in Fig. 4.41) can be approximated by a parabola with a local maximum at near the half of Nu. This maximum value of the shear force reaches merely 1.7 MN which is significantly lower than Asuo = 2.9 MN. The difference between the two values is attributed to the interaction in Q-M space in the former case. Furthermore, for values of N close to Nu the lateral load at u/B = 0.1 exceeds increasingly the yield load, due to a hardening effect.

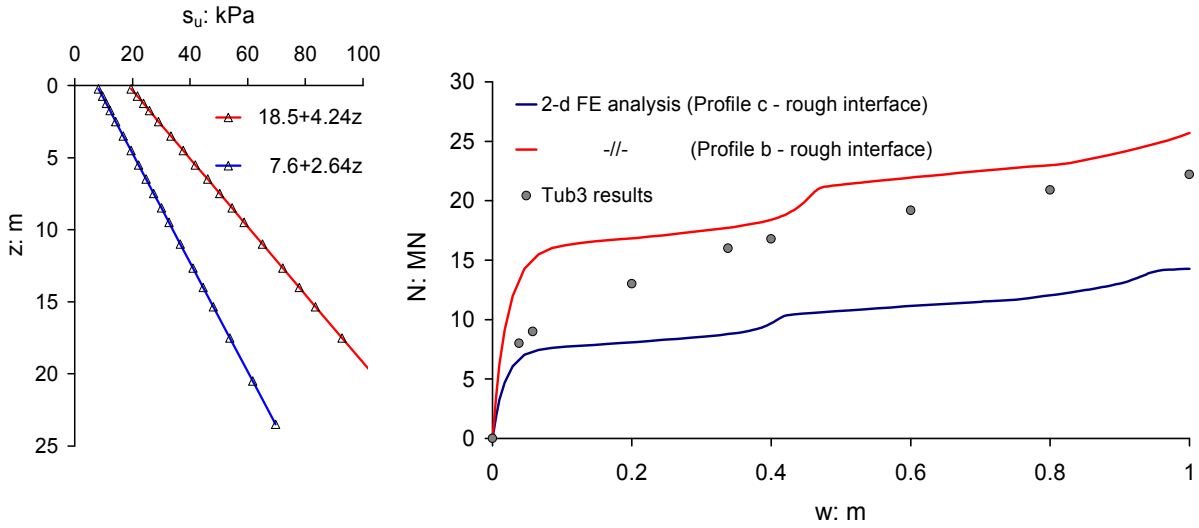


**Figure 4.39** Monotonic vertical load-settlement curve calculated with centrifuge experiment (tub3, testT06) and comparison with the two-dimensional FE analysis.

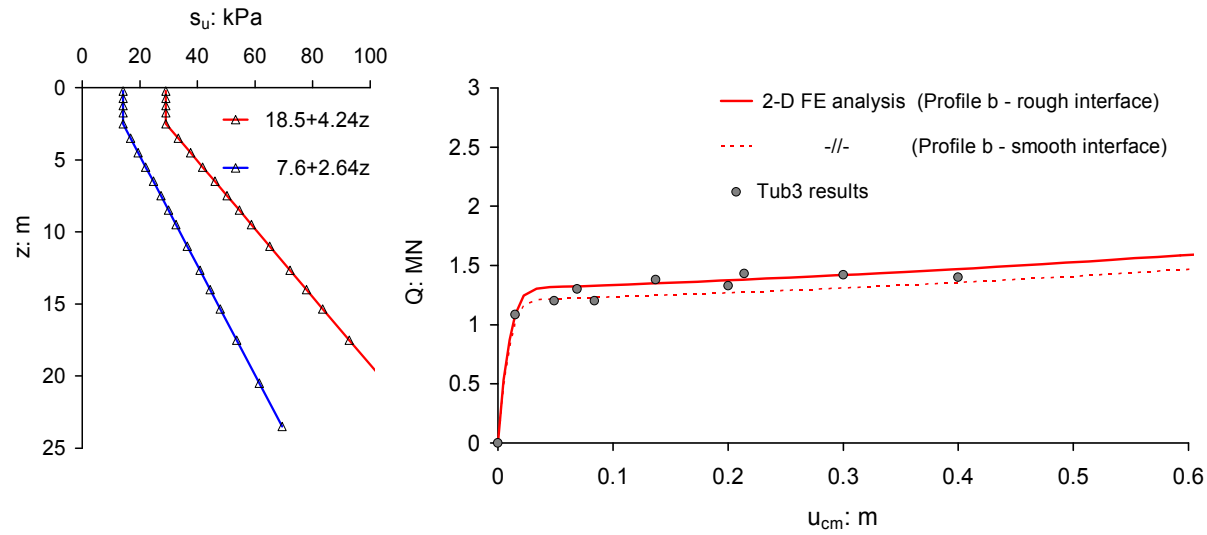


**Figure 4.40** Monotonic lateral load-displacement curve calculated with centrifuge experiment (tub3, testT07) and comparison with the two-dimensional FE analysis

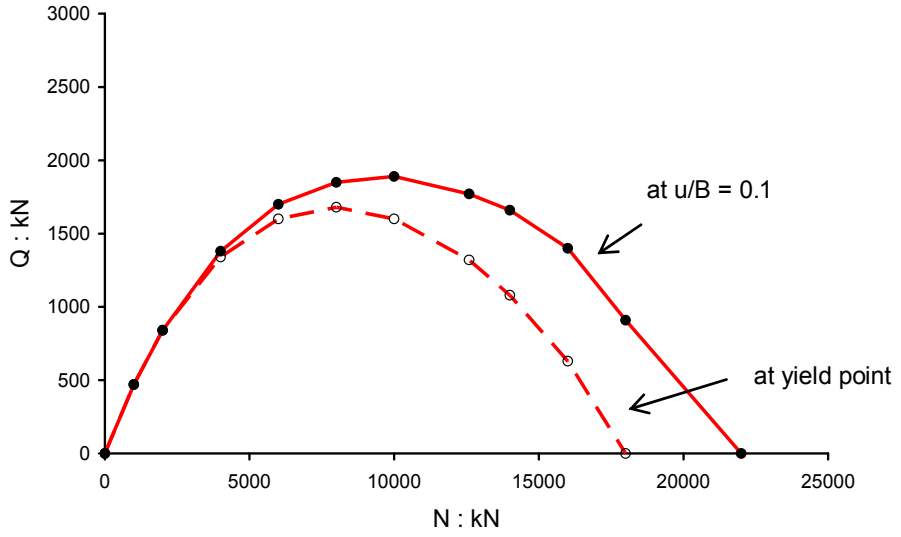


**Figure 4.41** Monotonic failure envelope in the N-Q space calculated with two-dimensional FE analysis (tub3). For each level of vertical load, the ultimate horizontal force is calculated at incipient yield and at u/B = 0.1

Cyclic horizontal loading at the level of the gravity centre, under a constant vertical load was also performed in centrifuge. Typical results of the tub4 test (T09) are presented in Fig. 4.42. Initially, a monotonic loading is applied to the structure until a prototype displacement of 0.2 m is obtained. Then the building is removed automatically to its initial position. The second (dynamic) loading phase is subdivided in three displacement-controlled cyclic sequences: (a) 10 cycles at 0.1 Hz with an amplitude of 0.4 mm (0.04 m in prototype dimensions), (b) 10 cycles at 0.16 Hz with an amplitude of 0.4 mm, and (c) 9 cycles at 0.16 Hz with an amplitude of 0.4 mm. After cyclic loading, a monotonic loading is applied to re-calculate the ultimate horizontal force. In this step the maximum force has increased from 1.2 MN to 2.1 MN which is attributed to the preceding cyclic loading. The interpretation of tub4 cyclic test is also presented in Fig. 4.42. Finite element analysis captures both the initial and the residual (increased) shear force capacity of the foundation. Also dynamic numerical analysis provides the same maximum force with the experimental value (1.8 MN). In the numerical loops however an isotropic behaviour is revealed in the loading and unloading directions.

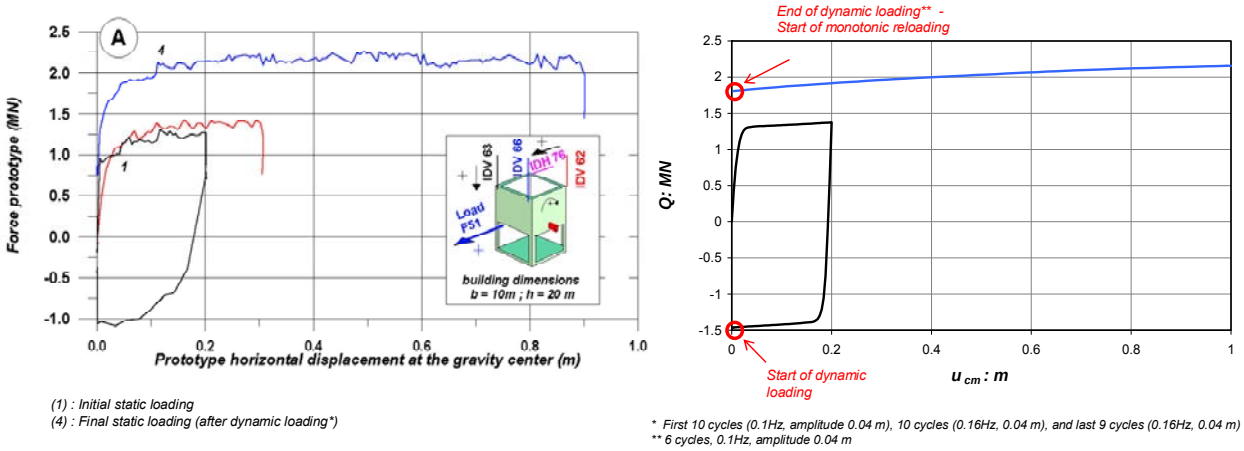


**Figure 4.42** Backbone Q-u curves before and after cyclic loading (tub4) from the centrifuge (left) and numerical simulation (right)

*Chapter 5:*

# Foundation capacity and permanent displacements under earthquake loading

## 5.1 INTRODUCTION – DESCRIPTION of PROBLEM

One of the most important issues in the design of a shallow foundation is to estimate the ultimate capacity under combined vertical, horizontal and moment loading. Under a statically applied central vertical load bearing capacity failure of a shallow foundation occurs when the supporting soil fails in shear. This may involve either a general failure mechanism or punching shear failure. The former is a sudden, catastrophic type of failure and usually occurs in soils that exhibit brittle stress-strain behaviour. The latter develops in soils that exhibit compressible, plastic stress-strain behaviour and is accompanied by progressive downward movement or *punching* of the foundation into the underlying soil (Poulos *et al.*, 2002).

Under a combined vertical, horizontal, and moment loading, foundation failure may also occur by horizontal shear failure of soil (sliding) or excessive rotation (overturning). Slender structural systems are most vulnerable to the latter. There are two distinct types of overturning failure depending on the level of vertical loading, as outlined in Chapter 4. Hence, overturning of a lightly-loaded foundation is associated with large amplitudes of uplift. In this case mobilisation of the moment capacity under dynamic conditions does not necessarily lead to overturning. Depending on the dynamic parameters of the structural system and the kinematic characteristics of ground motion the foundation may safely undergo rocking after the ultimate moment has been exceeded or eventually overturn. It is worthy of note that structural displacements are almost reversible if toppling is prevented. On the contrary, for a heavily-loaded foundation overturning is attributed to a bearing capacity type of failure. Mobilisation

of moment capacity implies permanent displacements which are amplified due to the cyclic nature of loading. In the context of geotechnical design, serviceability issues demand the control of these cumulative foundation displacements.

The bearing capacity problem of a shallow foundation is revisited here with emphasis given on the effect of the dynamic and cyclic characteristics of the (transient) earthquake motion. In this respect a nonlinear finite element method in the time domain is utilised.

## 5.2 AVAILABLE BEARING CAPACITY SOLUTIONS

### 5.2.1 Conventional bearing capacity method

The static bearing capacity of a shallow foundation under central vertical loading was initially calculated by L. Prandtl, back in 1921. In his pioneering work, Prandtl utilised the method of stress characteristics to estimate the ultimate vertical load of a strip footing on weightless soil. Provided that soil medium is described as homogeneous half-space under undrained conditions $\left(c = s_u,\ \phi = 0\right)$ the ultimate vertical soil reaction $p_u$ is:

$$p_u = \left(\pi + 2\right) s_u \qquad [5.1]$$

After Prandtl's work, analytical research on the bearing capacity problem was based on the *upper* and *lower* bound theorems of limit analysis. According to this procedure the ultimate load can be calculated by prescribing either a *statically admissible* stress field (lower bound theorem) or a *kinematically admissible* velocity field (upper bound theorem). It was found that Prandtl's slip line method gives the exact solution for a strip footing on cohesive undrained soil (Drucker, 1952).

Terzaghi (1943) introduced the *general bearing-capacity factors* $N_c$, $N_\gamma$ and $N_q$ to calculate the bearing capacity of a soil described by strength parameters $c$ and $\phi$ with the following formula:

$$p_u = cN_c + \frac{1}{2}B\gamma N_\gamma + qN_q \qquad [5.2]$$

Where $\gamma$ is the unit weight of soil and $q$ is the overburden pressure. This empirically-based method is widely applicable in common foundation engineering practice up to nowadays. Notably, for a cohesive soil under undrained conditions it yields $N_c = \pi + 2$ and $N_\gamma = 0$. If the overburden pressure is neglected, Terzaghi's method leads to Prandtl's analytical solution (Eq. 5.1).

Additional empirical factors have been appended to the Terzaghi formula (Meyerhof, 1953; Vésic, 1975) to account for the effects of (a) the foundation shape and (b) load inclination and eccentricity leading to the following equation:

$$p_u = cN_c i_c R_c s_c + \frac{1}{2}B\gamma N_\gamma i_\gamma R_\gamma s_\gamma + qN_q i_q R_q s_q \qquad [5.3]$$

The factors $i$ and $R$ stand for the inclination and eccentricity of the load whereas $s$ accounts for the foundation shape. Some of the most common empirical correlations of the bearing capacity factors are plotted in the graphs of Figs 5.1 and 5.2.

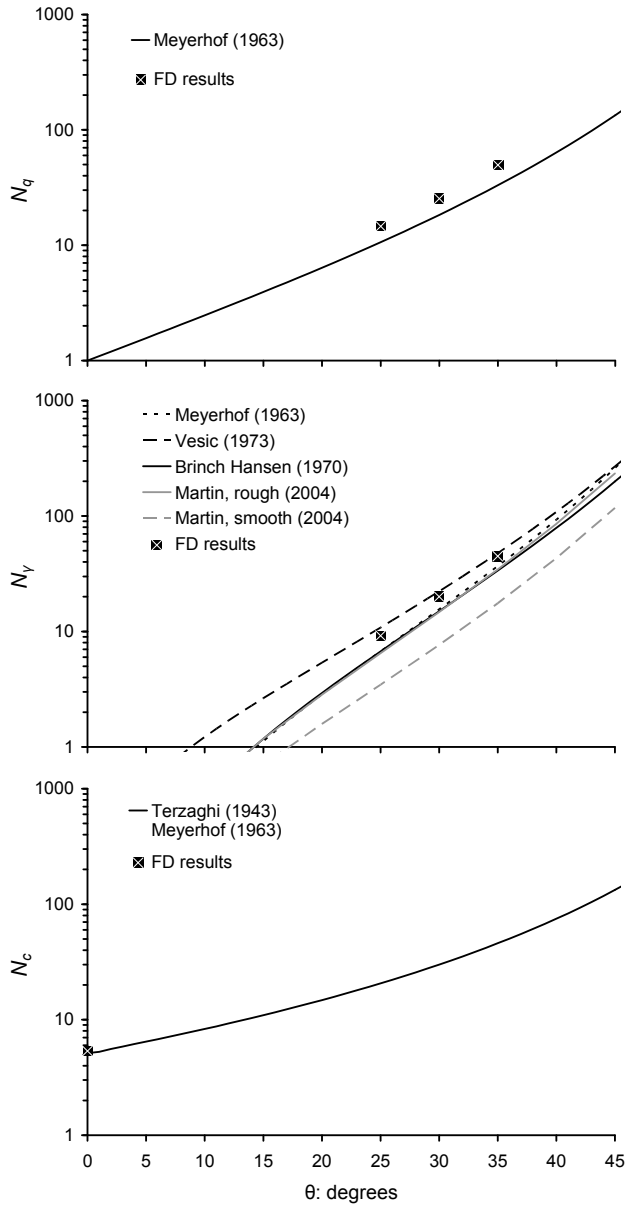


**Figure 5.1** Bearing capacity factors of strip footing for central, vertical load as a function of the friction angle $\phi$. Comparison of classical methods against numerical (finite difference) results (Apostolou *et al.*, 2006).

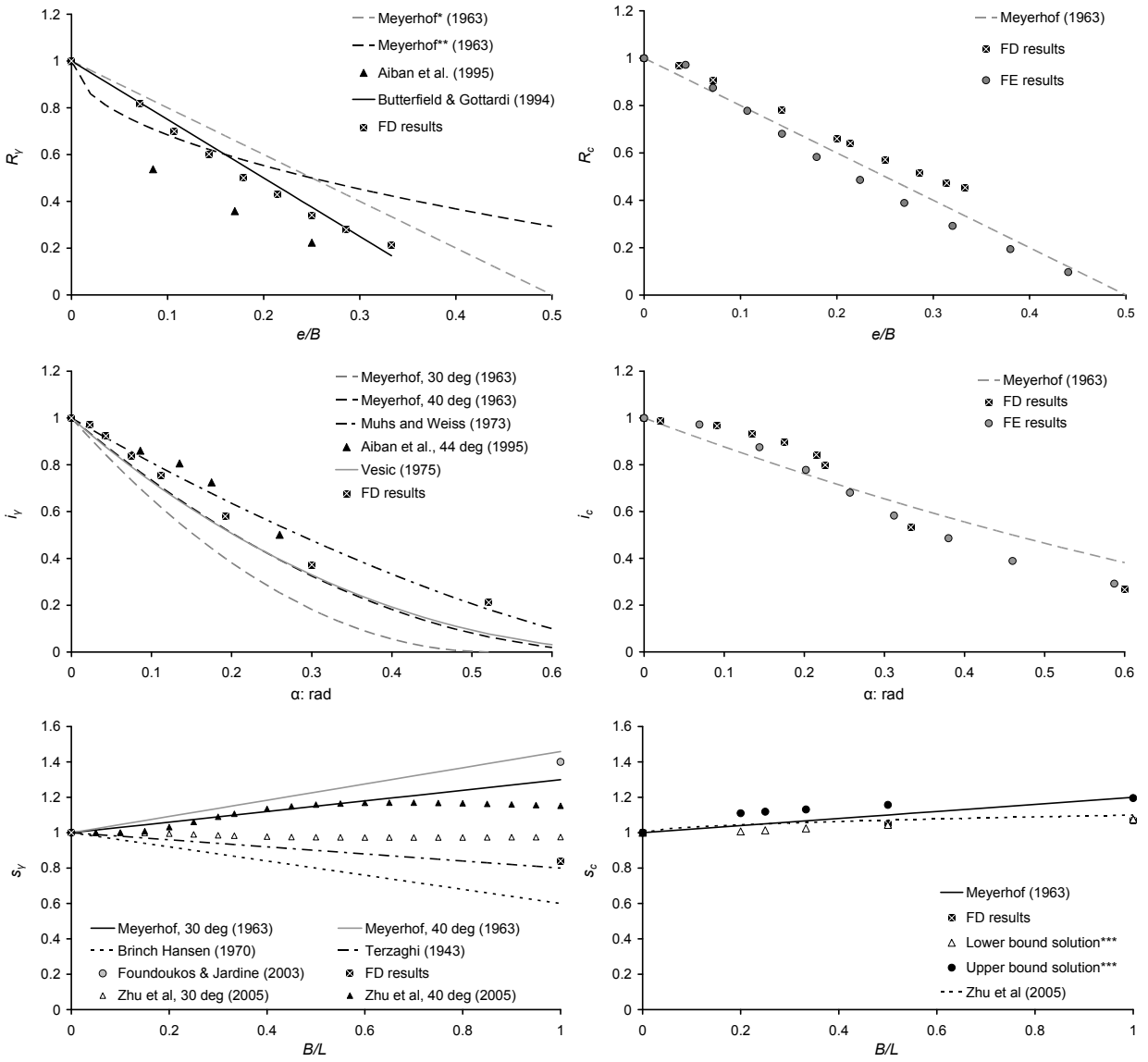


**Figure 5.2** Modification factors for inclination, eccentricity of loading and shape of the footing (Apostolou *et al.*, 2006).

### 5.2.2 Static interaction curves in the *N – Q – M* loading space

Bearing capacity factors have been established in common engineering practice as a simple tool to estimate the ultimate loading of a shallow foundation. It is broadly accepted however, that in some cases such as for foundations subjected to eccentric inclined loads, the existing empirical bearing capacity factors with the proper correction factors attached may not provide reliable failure criteria. For example in case of undrained homogeneous clay the calculated ultimate load may be underestimated by more than 25% compared to the exact collapse solutions. On the other hand for

undrained clay with significant strength gradient with depth these factors may become completely unreliable (Ukritchon *et al.*, 1999).

The accuracy of ultimate load calculations is of great importance particularly for foundations under large lateral and moment loading such as offshore structures (Ukritchon *et al.*, 1999; Bransby and Randolph, 1997). In this respect much of the recent research has been focused on the development of more reliable failure criteria for general planar loading conditions $(N, Q, M)$. It has been found that for any foundation there is a unique closed surface in the generalised loading space $N, Q, M$ containing all possible combinations of loads that would cause failure of the foundation. This surface defines a failure envelope representing the bearing capacity of the foundation under combined loading. It is calculated analytically by a function $f$ of the foundation loads $N, Q, M$ :

$$f(N, Q, M) = 0 \qquad [5.4]$$

In the special case of a purely vertical, horizontal or moment loading Eq. 5.4 must satisfy the ultimate loads $N_u$, $Q_u$ and $M_u$ respectively. The failure envelope is independent of load path and encloses all possible combinations of loads which would cause only elastic deformations. It is also independent of soil characteristics (e.g. cohesion, inhomogeneity) and footing geometry (Butterfield and Gottardi, 1994; Ukritchon *et al.*, 1998; Taiebat and Carter, 2002) and reasonably has prevailed over the conventional Terzaghi method.

Although the hypothesis of a unique failure surface has originally been formulated by Roscoe and Schofield back in 1957, its experimental validation came merely in 1979 by Butterfield and Ticof through small-scale tests with footings on sand. In this study it was uncovered that the combinations of vertical load $N$ and moment $M$ that cause failure to the footing lie on a simple parabolic curve. Additionally it was shown that bearing capacity in the $N-Q$ plane may also be represented by similar parabolic-shaped failure loci. A simple fit of these curves was given by Butterfield and Gottardi (1994):

$$Q = t_h \frac{N}{N_u}\left(N_u - N\right) \qquad [5.5a]$$

$$\frac{M}{B} = t_m \frac{N}{N_u}\left(N_u - N\right) \qquad [5.5b]$$

where $t_h$ $\left(t_m\right)$ is the slope of the $N-Q$ $\left(N-M\right)$ parabola at the intersection points with the horizontal axis (i.e. at the origin and at $N_u$). The failure envelopes of Eqs 5.5 can be rewritten in a non-dimensional formulation:

$$\frac{Q}{N_u} = t_h \frac{N}{N_u}\left(1 - \frac{N}{N_u}\right) \qquad [5.6a]$$

$$\frac{M}{N_u B} = t_m \frac{N}{N_u}\left(1 - \frac{N}{N_u}\right) \qquad [5.6b]$$

Normalised loads $\hat{n} = N/N_u$, $\hat{q} = Q/N_u$, and $\hat{m} = M/N_u B$ can be defined in accordance with Eqs 5.6 leading to the following simplified formulas (Fig. 5.3):

$$\hat{q} = t_h \hat{n}\left(1-\hat{n}\right) \qquad \text{and} \qquad \hat{m} = t_m \hat{n}\left(1-\hat{n}\right) \qquad [5.7]$$

For very small values of vertical load $N$ it yields $t_h \cong N/Q$ and $t_m \cong M/NB = 0.5M/Nb$. Evidently, $t_h$ represents the static coefficient of friction. Also, the coefficient $t_m$ must be always smaller than 0.5 given that the moment capacity of the foundation cannot exceed the rigid soil capacity $\left(M_{u,rigid} = Nb\right)$. Actually, due to elastic soil behaviour at this level of loading $\left(\hat{n} = N/N_u \to 0\right)$ it can be assumed that the moment capacity approaches the rigid soil capacity and eventually $t_m$ is close to 0.5. Furthermore, the maximum horizontal and moment capacity is obtained at $\hat{n} = N/N_u = 0.5$. In combination with Eqs 5.7 this gives the normalised maximum horizontal and moment loads $\hat{q}_{\max} = 0.25 t_h$

and $\hat{m}_{\max} = 0.25 t_m$. Based on experimental results Butterfield and Gottardi (1994) have proposed $\hat{q}_{\max} = 0.125$ and $\hat{m}_{\max} = 0.1$ and correspondingly $t_h = 0.5$ and $t_m = 0.4$.

Houlsby and Puzrin (1999) utilised the lower bound theorem of limit analysis to study the bearing capacity problem for a shallow footing on undrained cohesive soil. They derived a closed-form solution for the failure envelope in the $N-M$ plane:

$$\frac{N}{A} = (\pi + 2) s_u \left(1 - \frac{2M}{NB}\right) \qquad [5.8]$$

Given that the ultimate central vertical load is $N_u = (\pi + 2) s_u A$ and taking $t_m = 0.5$ the failure envelope of Eq. 5.8 reduces to that of Eq. 5.6b. It is also interesting that Eq. 5.8 can be rewritten after introducing the inverse of the safety factor $\chi = N / N_u = N / \left[(\pi + 2) s_u A\right]$ in the following simple form:

$$M = Nb(1 - \chi) \qquad [5.9]$$

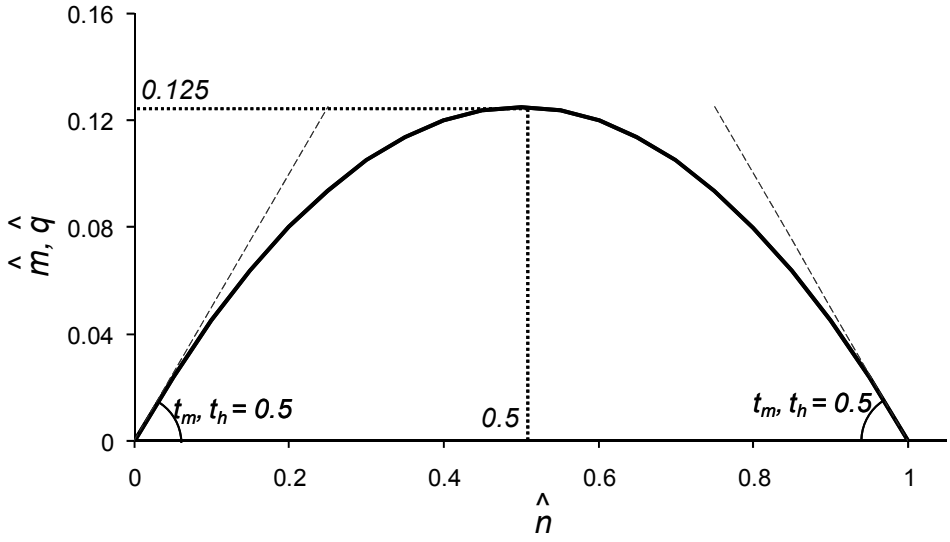


**Figure 5.3** Failure envelope in the non-dimensional $N-M$ and $N-Q$ plane for $t_m = t_h = 0.5$.

In recent years, a plethora of centrifuge tests has led to more systematic work focused on the prediction of the failure envelopes in the three-dimensional space. Based on these experiments together with analytical predictions through advanced plasticity models several analytical expressions

of the function $f$ have been proposed in the literature. For a shallow footing on sand it has been shown that the general form of the three-dimensional failure locus is a rugby-shaped closed surface with its principal axis coinciding with the $N-$ axis. According to Butterfield and Gottardi (1994) the analytical expression of the failure surface in the non-dimensional space $\hat{n}-\hat{q}-\hat{m}$ is:

$$\left(\frac{\hat{q}}{t_h}\right)^2+\left(\frac{\hat{m}}{t_m}\right)^2-2C\frac{\hat{q}\,\hat{m}}{t_h\,t_m}=\left[\hat{n}\left(1-\hat{n}\right)\right]^2 \qquad [5.10]$$

where $C=C\left(t_h,t_m\right)$. The afore-discussed two-dimensional failure envelopes can be obtained from Eq. 5.10. In this way by putting $\hat{m}=0$ it yields $\hat{q}=t_h\left[\hat{n}\left(1-\hat{n}\right)\right]$ which is equivalent to the failure surface in the $N-Q$ plane (Eq. 5.7a). Also, for $\hat{q}=0$ it is derived $\hat{m}=t_m\left[\hat{n}\left(1-\hat{n}\right)\right]$ corresponding to the failure surface in the $N-M$ plane (Eq. 5.7b).

## 5.3 LARGE-DISPLACEMENT ANALYSIS of the FOUNDATION CAPACITY

### 5.3.1 Simplified analytical modelling at limit state

A simplified closed-form expression of the failure locus in the $N-M$ plane can be obtained with the beam-on-winkler-foundation model. In this case a rigid strip footing of width $2b$ is supported by distributed uncoupled springs with no tensile capacity so that uplift is allowed. Compressional load-displacement behaviour of each spring is described with the elastic–perfectly plastic law characterised by the axial stiffness $k_v$ and the ultimate value $p_u$. At first, a small-displacement configuration is adopted as illustrated in Fig. 5.4a. Equation of the overturning and the restoring moment at the state of limit equilibrium provides:

$$M=\left(b-\beta\right)N=\left(b-\beta\right)\left(2\beta p_u\right) \qquad [5.11]$$

where $\beta = \lambda b$ is the half-width of the effective footing. Provided that $N_u = p_u 2b$ it is easy to show through Eq. 5.11 that at limit equilibrium it holds:

$$\lambda = \chi \qquad [5.12]$$

From Eqs 5.11 and 5.12 it yields that:

$$\frac{M}{Nb} = 1 - \lambda = 1 - \chi \qquad [5.13]$$

The latter describes the failure locus in the $N - M$ plane derived by a beam-on-winkler-foundation model. Obviously it is the same with the lower-bound solution for a strip footing on undrained, cohesive soil (Eq. 5.9).

A large-displacement configuration is adopted next (Fig. 5.4b) allowing for $P - \delta$ effects to be incorporated in the analysis. The rotation of the structural system as monotonic loading increases and the accompanying drift of the mass point are taking now into account. In this case equation of the overturning and the restoring moment at the state of limit equilibrium provides:

$$M = N\left[(b-\beta)\cos\theta_u - h\sin\theta_u\right] = (2\beta p_u)\left[(b-\beta)\cos\theta_u - h\sin\theta_u\right] \qquad [5.14]$$

where $\theta_u = \theta(M = M_u)$ is the rocking angle at limit equilibrium. From Eqs 5.12 and 5.14 the failure locus becomes:

$$M = Nb\cos\theta_u\left[(1-\chi) - \frac{\tan\theta_u}{\tan\theta_c}\right] \cong Nb\left(1 - \chi - \frac{\theta_u}{\theta_c}\right) \qquad [5.15]$$

or in non-dimensional variables:

$$\frac{M}{N_u B} = 0.5\frac{N}{N_u}\left(1 - \frac{N}{N_u} - \frac{\theta_u}{\theta_c}\right) \qquad [5.16a]$$

$$\hat{m} = 0.5\hat{n}\left(1 - \hat{n} - \mu_\theta^{-1}\right) \qquad [5.16b]$$

where $\mu_\theta = \theta_c / \theta_u$ is the ductility demand of rocking displacements. It is worthy of note that this term is dependent on the normalised vertical load $\hat{n}$ as the angle $\theta_u$ is a function of $N$. The ultimate rocking response in the large-displacement domain will be further investigated in Chapter 6 in order to derive analytical curves of the moment capacity through macroscopic modelling of the soil-foundation system.

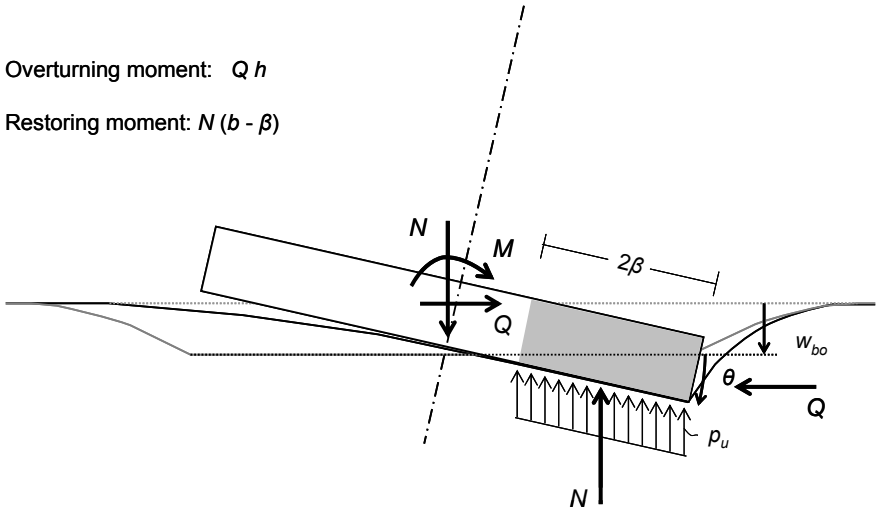


**(a) without P-δ effects**

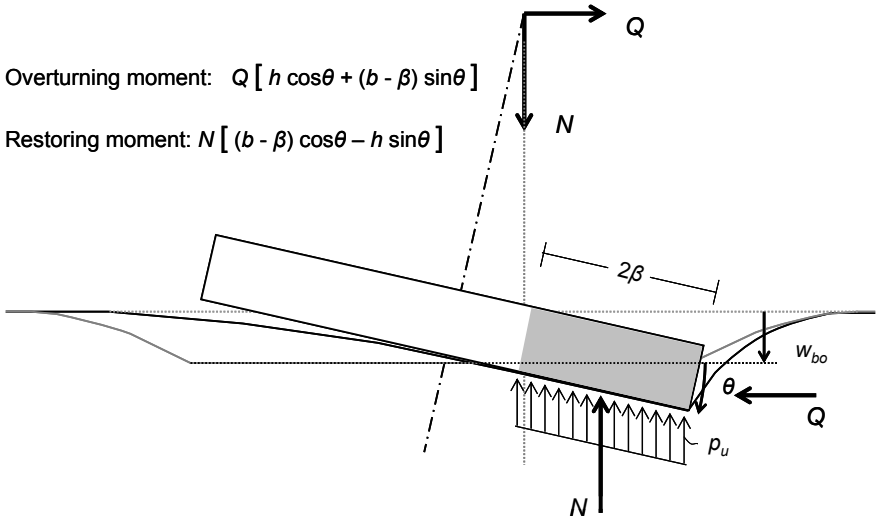


**(b) with P-δ effects**

**Figure 5.4** Schematic of a rigid strip footing at limit equilibrium with and without $P-\delta$ effects.

### 5.3.2 Finite element study

***Small-displacement analysis – Comparison with the analytical solutions***

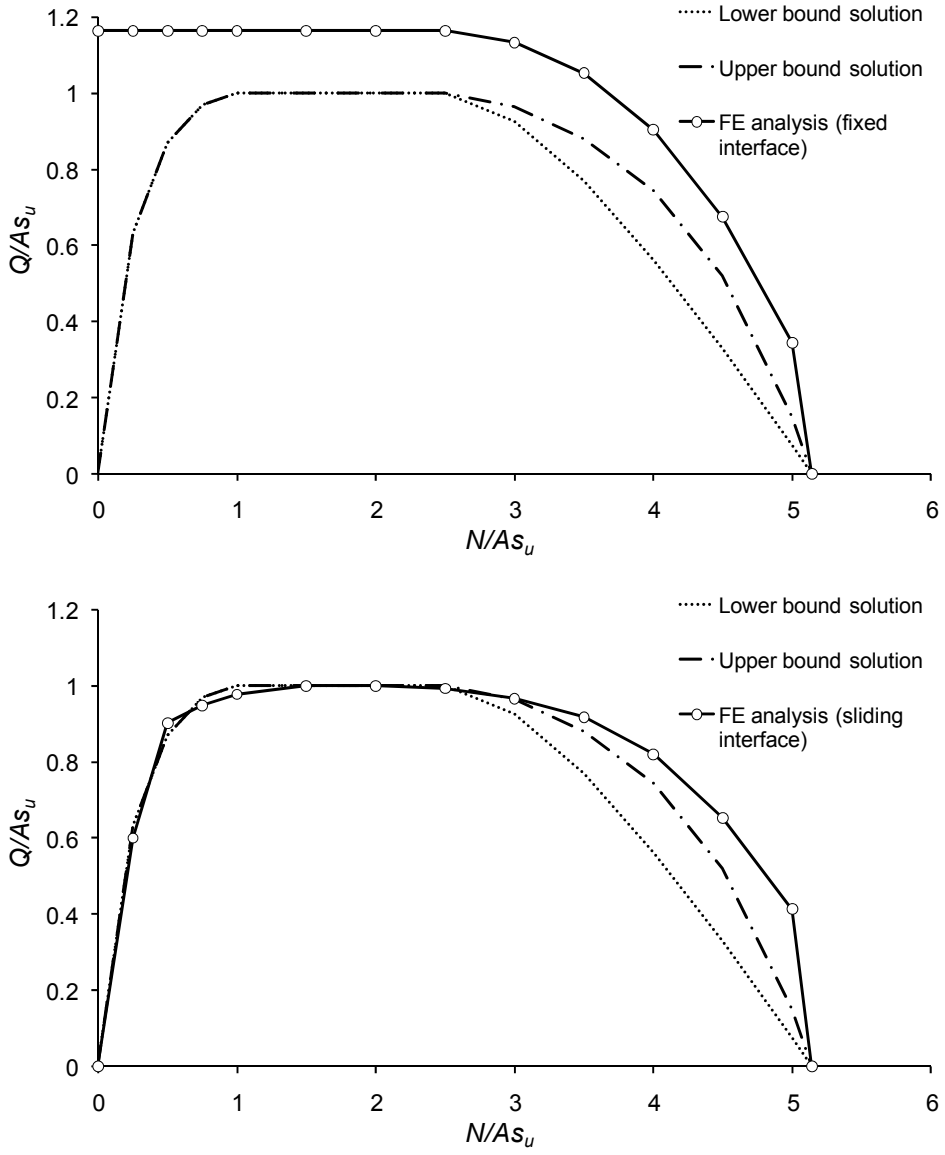


**Figure 5.5** Interaction curves in the Q – N space for cohesive soils computed with finite elements and comparison with analytical solutions.

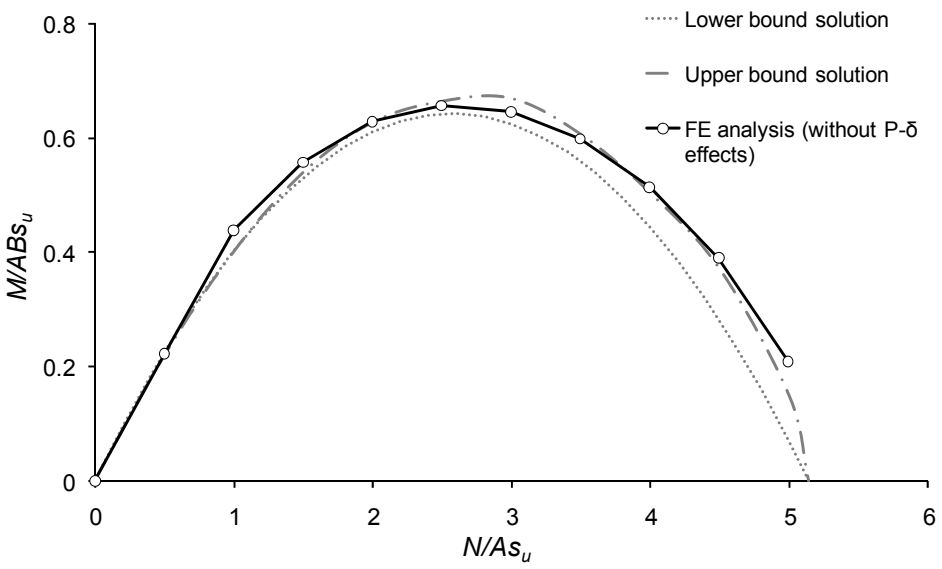


**Figure 5.6** Interaction curves in the M – N space for cohesive soils computed with finite elements and comparison with analytical solutions.

### *Large-displacement analysis*

In principle, a series of static finite element analyses is conducted to derive levels of the moment capacity and compare the calculated failure envelopes to the analytical solutions. Unlike the limit-state theoretical curves, $P-\delta$ effects are now incorporated in the analysis. A homogeneous, cohesive soil medium under undrained conditions is considered. The soil-foundation system described with *model v.01* $\left(B=2b=2 \text{ m},\ h=5 \text{ m},\ E=100 \text{ MPa},\ s_u=100 \text{ kPa}\right)$ is assumed for the analysis. For this configuration, an ultimate vertical load of $N_u=(\pi+2)\times 2\times 100=1028 \text{ kN}$ is predicted. Monotonic $M-theta$ curves are computed for different levels of vertical load by applying a displacement-controlled loading to the mass point. The results are plotted in normalised values $\left(\theta/\theta_c,\ M/ABs_u\right)$ in the graphs of Fig. 5.7. The corresponding failure envelope is also portrayed in Fig. 5.7, in normalised values $N/As_u$, $M/ABs_u$. The upper and lower bound analytical curves (Houlsby and Puzrin, 1999) are plotted in the same graph. As expected, the maximum moment is obtained for the vertical load of 500 kN which is about half the ultimate vertical load (1028 kN). In the normalised form of the derived failure envelope this optimum behaviour occurs at $N/As_u=2.5\cong 2.57\left[=(\pi+2)/2\right]$. However, a

reduction of the ultimate moment occurs when compared to the analytical values, attributed to $P-\delta$ effects. At this point the reduction of the capacity is about 15 %. Taking into account that in common foundation design a value of $\chi \cong 0.5$ is rather typical, it seems that $P-\delta$ effects should not be neglected in analysis of slender structural systems. The reduction of the moment capacity is further amplifying as the vertical loading is heading towards the ultimate value. Remarkably, for values of $N$ close to $N_u$ a small 'bulging' of the numerical curve is also observed, attributed to the passive forces developed behind the footing corner point.

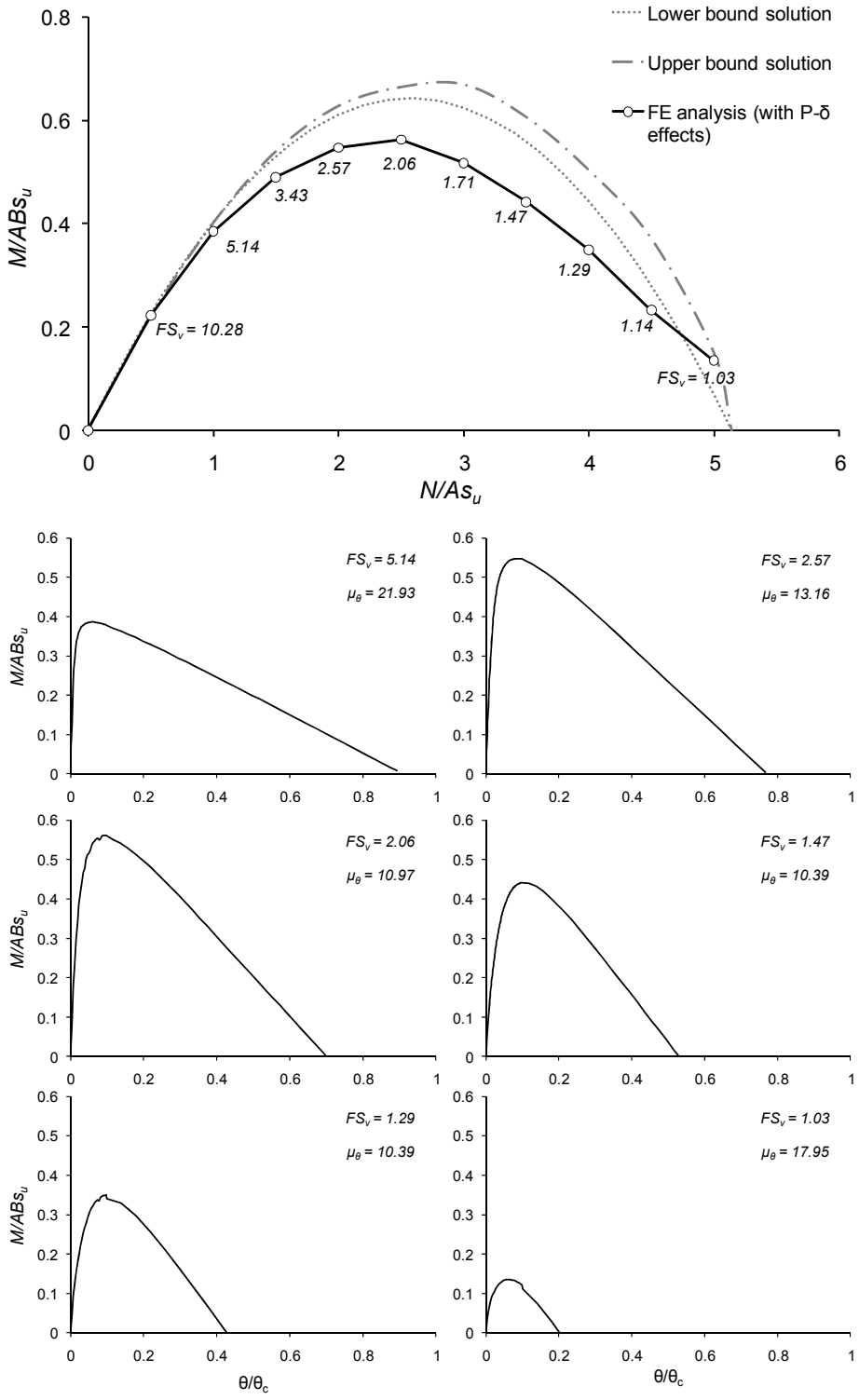


**Figure 5.7** Monotonic $M-theta$ curves for different levels of vertical load and the corresponding failure envelope, computed with finite elements ( $P-\delta$ effects are incorporated). Analytical upper and lower bound failure curves are also plotted. $B=2b=2$ m, $h=5$ m, $E=100$ MPa, $s_u=100$ kPa.

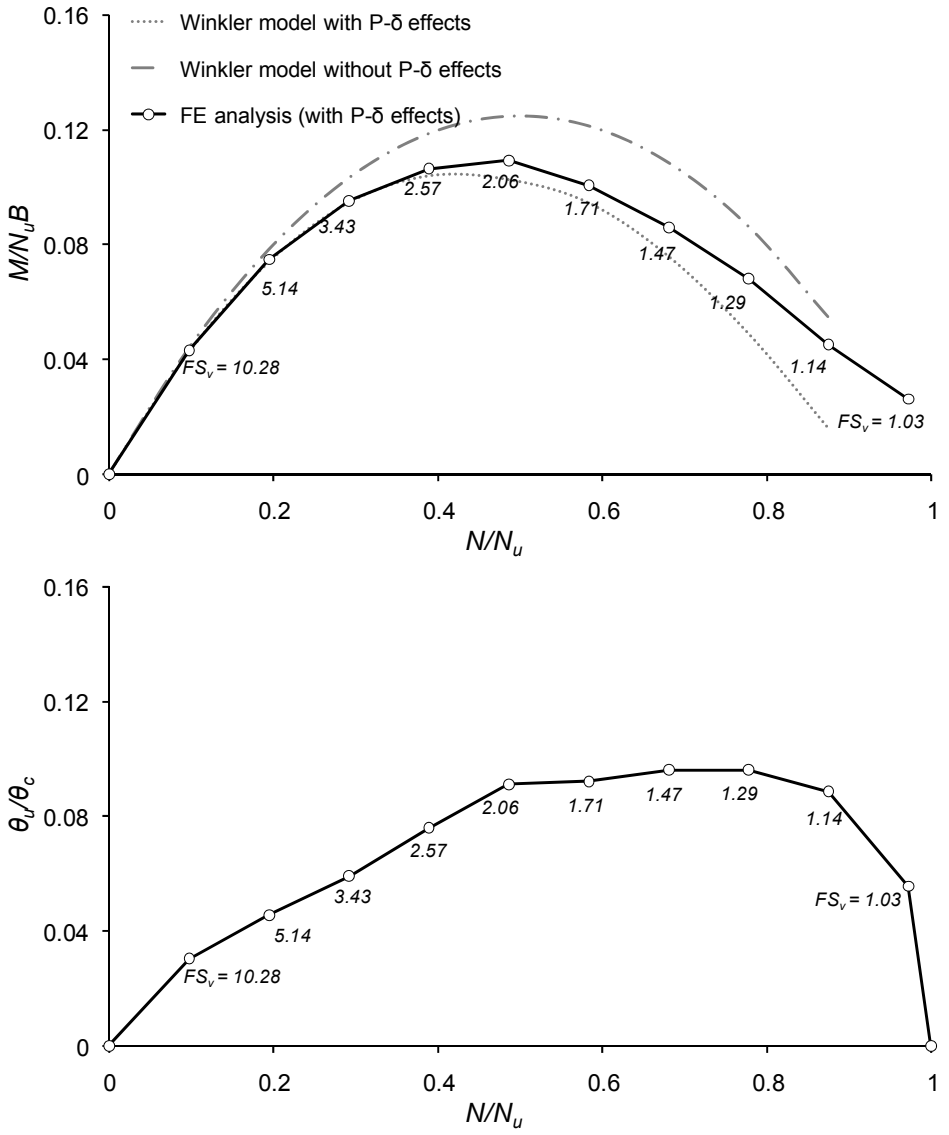


**Figure 5.8** Interaction curves of (i) the moment capacity and (ii) the rocking rotation at the mobilisation of capacity, computed with finite elements ($P-\delta$ effects are incorporated). Winkler-based, analytical failure curves with and without $P-\delta$ effects are also plotted in the $N-M$ plane. $B=2b=2$ m, $h=5$ m, $E=100$ MPa, $s_u=100$ kPa.

## 5.4 DYNAMIC MOMENT CAPACITY CURVES

It is quite often in geotechnical practice to treat the earthquake-induced loading from soil or superstructure upon the foundation with pseudo-static mechanism in order to derive estimates of the ultimate capacity. However, dynamic rocking of a footing with several significant cycles may lead to

substantially higher levels of the moment capacity especially for large values of the vertical load as hinted by recent experimental findings (Fig. 5.9).

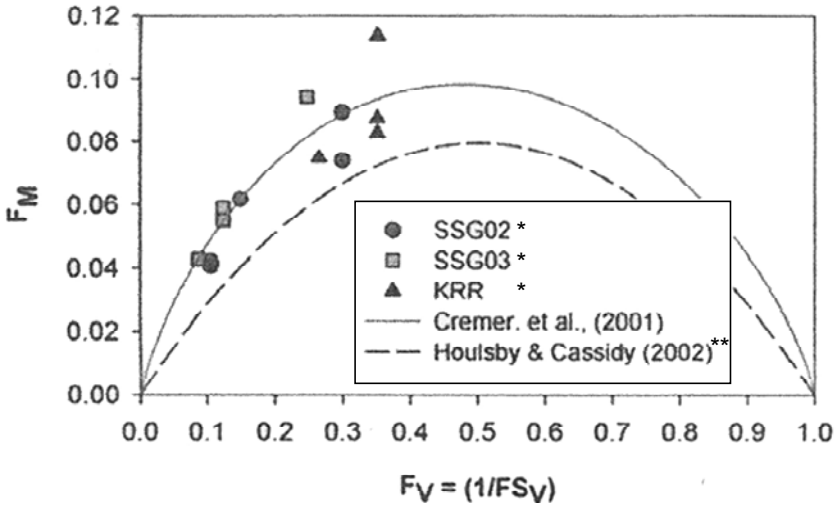


* *Centrifuge experiments (cyclic loading) at Davis, California.*
** *Limit-state pseudostatic analysis.*

**Figure 5.9** Failure envelope and experimental failure points on sands in the normalised $N-M$ plane $F_M=\hat{m},\ F_V=\hat{n}$ for $M/Q=4.9$ m (Gajan *et al.*, 2005).

A series of finite element analyses in the time-domain will try to highlight the effect of the dynamic and cyclic nature of earthquake loading on the foundation moment capacity.

For the analysis purposes the soil-foundation system described by the *model v.01* (Fig. 4.5) is assumed with undrained shear strength of 50 kPa throughout the soil. The seismic bedrock is merely at the depth of 5 m so that any filtration of the excitation frequency components through soil is prevented $\left(T_s=4H_s/V_s<0.1\text{ sec}\right)$. Despite the presence of a shallow bedrock, the footing (2 m in width) can undergo rocking oscillations as if it was supported on a half-space $\left(K_{m,H_s=5\text{m}}\cong 1.04K_{m,half-space}\right)$. A Ricker wavelet excitation is applied in the seismic bedrock with a predominant period of 0.33 sec, 0.67 sec, and 1.33 sec [Ricker nominal frequency $\left(f_R\right)$ of 2.0, 1.0, and 0.5 Hz respectively]. It is considered that these values cover the period range of a typical near–fault pulse–type motion. For a

slender system, rocking is the prevailing mode of response and therefore a simplified calculation of the eigenperiod can be obtained with the following expression:

$$T = 2\pi\sqrt{\frac{J_b}{K_m}} = 2\pi\sqrt{\frac{Nh^2}{K_m g}} \qquad [5.17]$$

Non-linear response is taking into consideration by adopting the secant foundation stiffness, equivalent to the ultimate capacity point, namely $K_{m,\sec} = M_u/\theta_u$. The secant rocking stiffness and the corresponding eigenperiod are depicted in Table 5.1 for different values of vertical load.

**Table 5.1** Equivalent (secant) stiffness and the corresponding eigenperiod in the rocking mode for the soil-foundation system of *model v.01* $(s_u = 50 \text{ kPa})$.

| $N(\text{kN})$ | 100 | 200 | 300 | 400 |
|---|---|---|---|---|
| $K_{m,\sec}(\text{MNm/rad})$ | 14900 | 12300 | 9400 | 6200 |
| $T_{m,\sec}(\text{sec})$ | 0.82 | 1.28 | 1.79 | 2.55 |

Three levels of ground shaking have been implemented in the analysis; a weak, a moderate and a strong shaking level ( $PGA$ : 0.2 g, 0.4 g, and 0.6 g, respectively). For each loading case the 'dynamic' moment capacity of the foundation is calculated for different values of the gravitational load $N$ and failure envelopes in the $N-M$ loading space are derived.

Initially, the moment capacity of the footing is calculated for the short-period (high–frequency) excitation $T_E = 1.33$ sec and plotted in the graph of Fig. 5.10. In the same graph are also presented: (a) the parabolic lower bound solution $\left[M = Nb(1-\chi)\right]$ and (b) the linear 'rigid soil' failure envelope $(M = Nb)$. For the moderate and strong shaking level, a *dynamic over-strength* develops which is enhanced with the increase of the vertical load. Counter-intuitively, this beneficial dynamic behaviour

is highly amplified close to the limiting value of $\chi = N/N_u \cong 1$ where the static ultimate moment is approached. On the other hand, for low levels of vertical load the ultimate dynamic response is similar with the static curve or even with the 'rigid soil' linear curve $(\chi \to 0)$. Only for the weak level of ground shaking, the dynamic failure locus plots below the static curve, over most of the range of $N$.

Two more Ricker wavelets with a long-duration pulse are utilised, under the same shaking levels. The resulting failure envelopes are plotted in the graphs of Fig. 5.10. What is more interesting now is that not only the dynamic over-strength is even higher, but also that the results tend to approach the 'rigid soil' moment capacity, especially for the case of $T_E = 1.33$ sec.

The afore-discussed series of finite element analysis is repeated for the soil-foundation configuration of *model v.02* (see Fig. 4.5). A larger footing $(B = 9\ \text{m})$ and a less slender structure $(\theta_c = 0.388\ \text{rad})$ are now adopted. Moreover soil stiffness and undrained strength are linearly increasing with depth ($E = 4.74z + 30$, $s_u = 15.7z + 10$). Failure loci in the $N - M$ plane are presented in the graphs of Fig. 5.11. It is worthy of note that the short-period excitation of Ricker2.0 demands levels of moment substantially lower than the capacity of the foundation. This can be explained by comparing the period of this pulse $(T_E = 0.33\ \text{sec})$ with the effective eigenperiod of the structural system (Table 5.2). The latter ranges from 1.30 to 4.68 sec, meaning that it is in any case essentially higher than the predominant period of ground motion. On the contrary, for a long-period excitation of Ricker1.0 $(T_E = 0.67\ \text{sec})$ and especially Ricker0.5 $(T_E = 1.33\ \text{sec})$, mobilisation of the foundation capacity is attained even under a weak ground shaking. Interestingly, the dynamic over-strength is limited when compared to the *model v.01* case and only in the Ricker2.0 case is observed over a wide range of vertical load. It is also common in all excitations the minimal effect of the ground shaking intensity on the foundation moment which can be roughly attributed to the high flexibility of the structural system.

**Table 5.2** Equivalent (secant) stiffness and the corresponding eigenperiod in the rocking mode for the soil-foundation system of *model v.01* $\left(s_u = 50 \text{ kPa}\right)$.

| $N\left(\text{kN}\right)$ | 100 | 200 | 300 | 400 |
|---|---|---|---|---|
| $K_{m,\text{sec}}\left(\text{MNm/rad}\right)$ | 34400 | 43900 | 31200 | 10600 |
| $T_{m,\text{sec}}\left(\text{sec}\right)$ | 1.30 | 1.63 | 2.36 | 4.68 |

A preliminary explanation for the favourable nonlinear behaviour during dynamic conditions can be offered by revisiting the *model v.01* case as portrayed in Figs 5.12, 5.13 and 5.14. The maximum moment for five different values of $N$ (from 100 to 500 kN) obtained statically with finite elements and with the lower bound solution (Houlsby and Puzrin, 1999) are depicted in Fig. 5.12. In the same figure, distributions of contact pressures on the footing (at $M = 0$ and $M = M_u$) are presented for each loading case. Interestingly, it is confirmed that the theoretical prediction of the bearing capacity $p_u \left[= (\pi + 2) s_u \cong 255 \text{ kPa}\right]$ is the upper bound of the developed stresses under both vertical and moment loading conditions. In the interaction diagram of Fig. 5.12 a dynamic failure envelope due to a Ricker-type excitation $\left(T_E = 0.67 \text{ sec},\ PGA = 0.40 \text{ g}\right)$ is also plotted. The beneficial role of the dynamic nature of loading can be interpreted through the comparison of the distributions of contact pressures at $M = M_u$. In any loading case and particularly for values of $N$ close to ultimate load, the dynamic distribution of the contact pressures exceeds the static bearing capacity in the vicinity of the pivot point. As the foundation moment is derived from integration of the contact pressures with respect to the midpoint, the exceedance of $p_u$ provides higher levels of dynamic $M_u$ than the statically predicted. Remarkably, for $N = 500$ kN $\left(\chi = 0.97\right)$ the dynamic pressure may reach up to twice the static bearing capacity at the right corner point of the foundation. Time-histories of the contact pressures for this loading case are presented in Fig. 5.14.

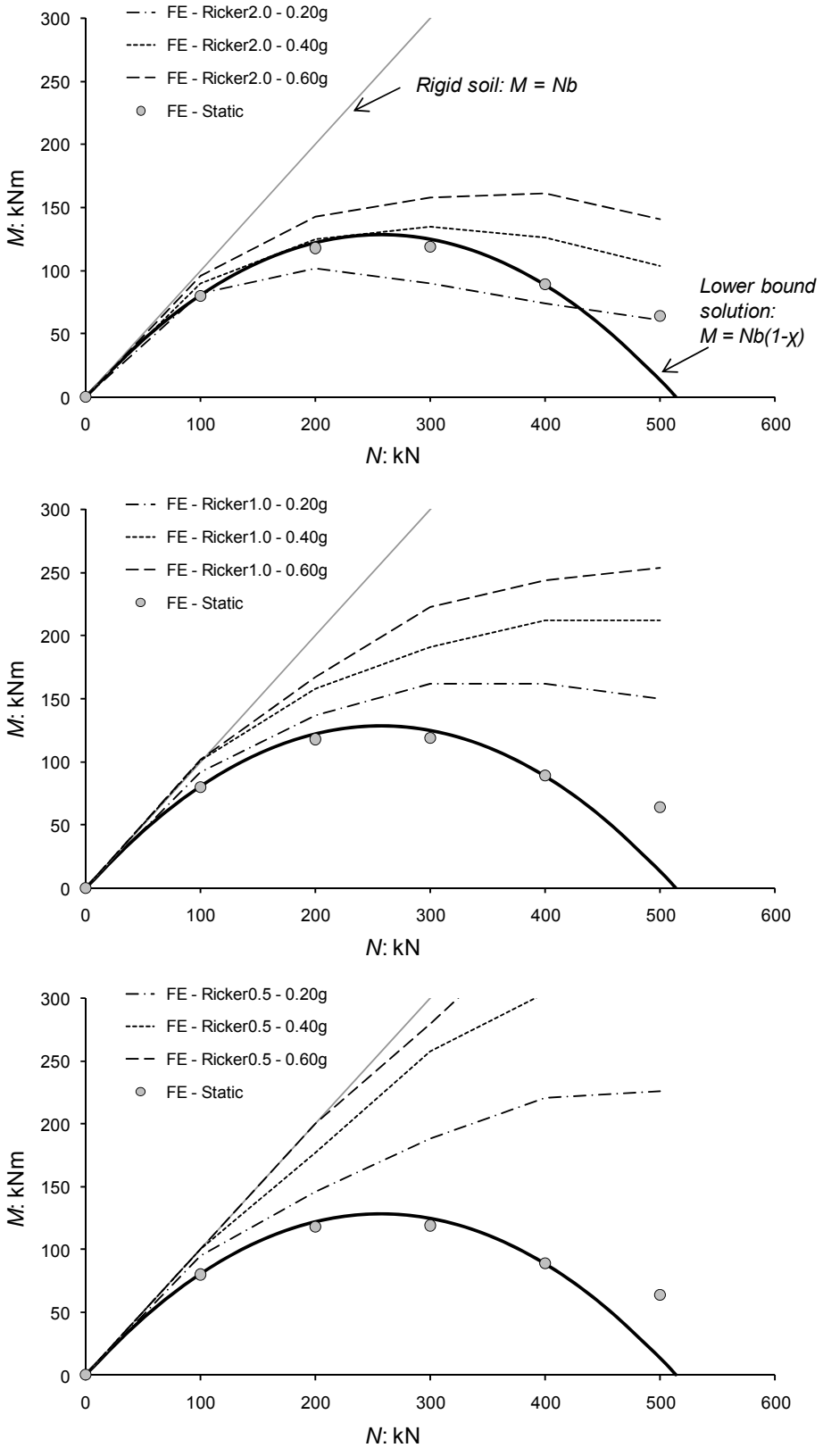


**Figure 5.10** Finite element calculation of $N-M$ interaction curves under earthquake loading and comparison with the static case. The excitation at the seismic bedrock is a Ricker pulse of $pga = 0.2$, 0.4, and 0.6 g and period $T_E = 0.33$, 0.67, and 1.33 sec (Ricker 2.0, 1.0, and 0.5 respectively). $B = 2b = 2$ m, $h = 5$ m, $E = 100$ MPa, $s_u = 50$ kPa (*model v.01*).

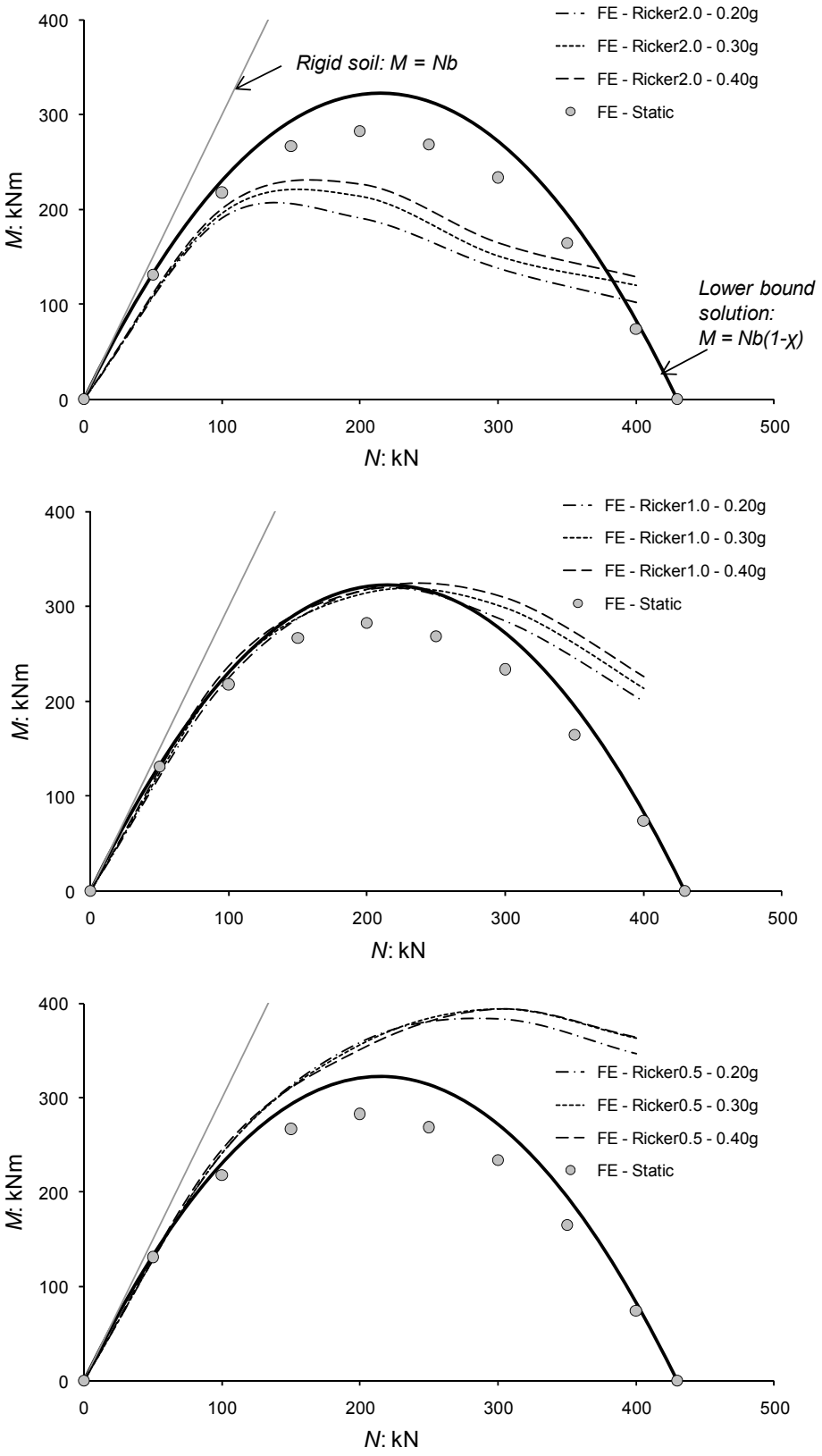


**Figure 5.11** Finite element calculation of $N-M$ interaction curves under earthquake loading and comparison with the static case. The excitation at the seismic bedrock is a Ricker pulse of $pga = 0.2$, 0.3, and 0.4 g and period $T_E = 0.33$, 0.67, and 1.33 sec (Ricker 2.0, 1.0, and 0.5 respectively). $B = 2b = 9$ m, $h = 11$ m, $s_u = 1.57z + 10$ (*model v.02*).

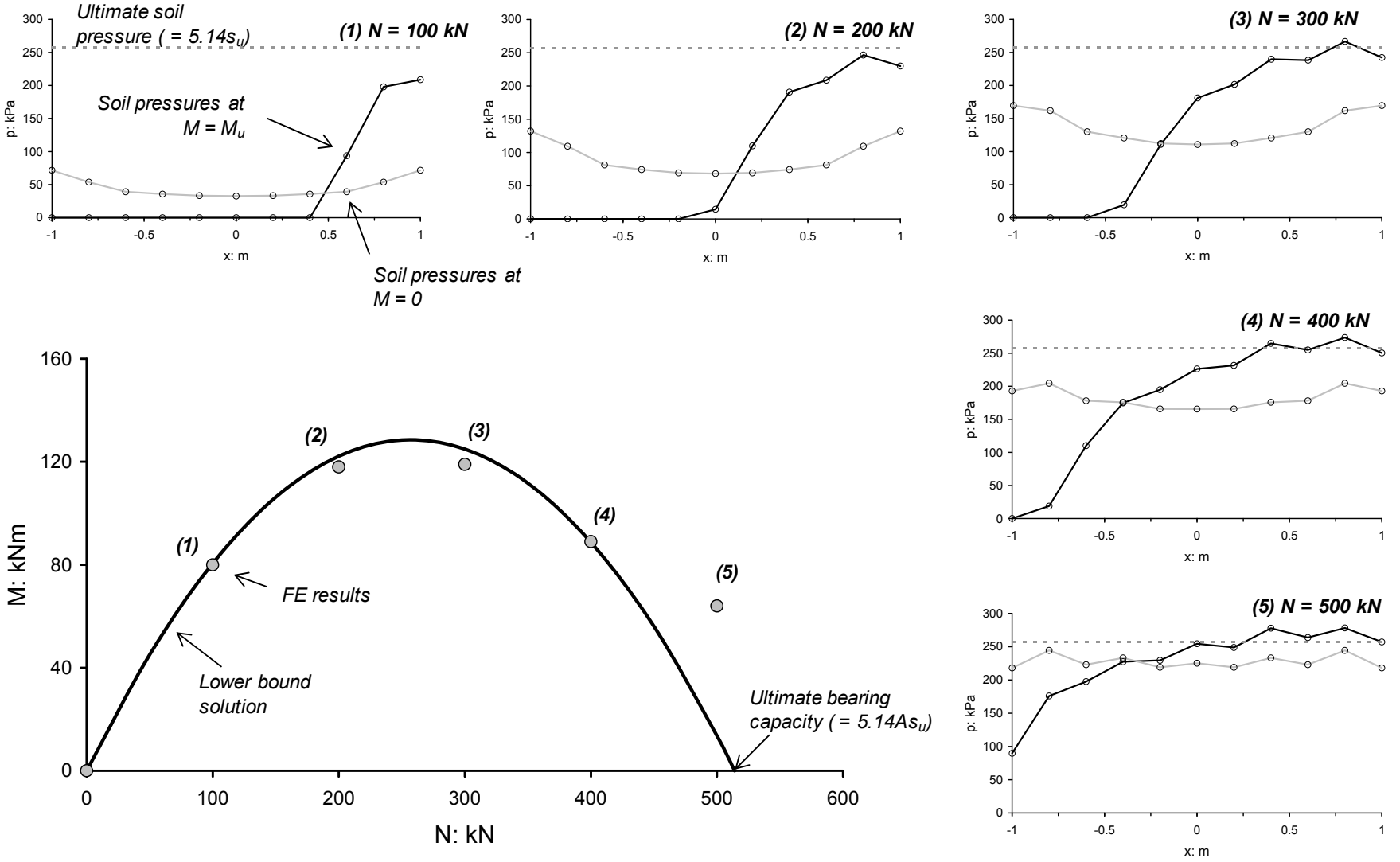


**Figure 5.12** Failure envelope for a strip footing in the $N-M$ space calculated with the finite element model and soil pressure distributions at different points. $B=2b=2$ m, $h=5$ m, $s_u=50$ kPa (*model v.01*).

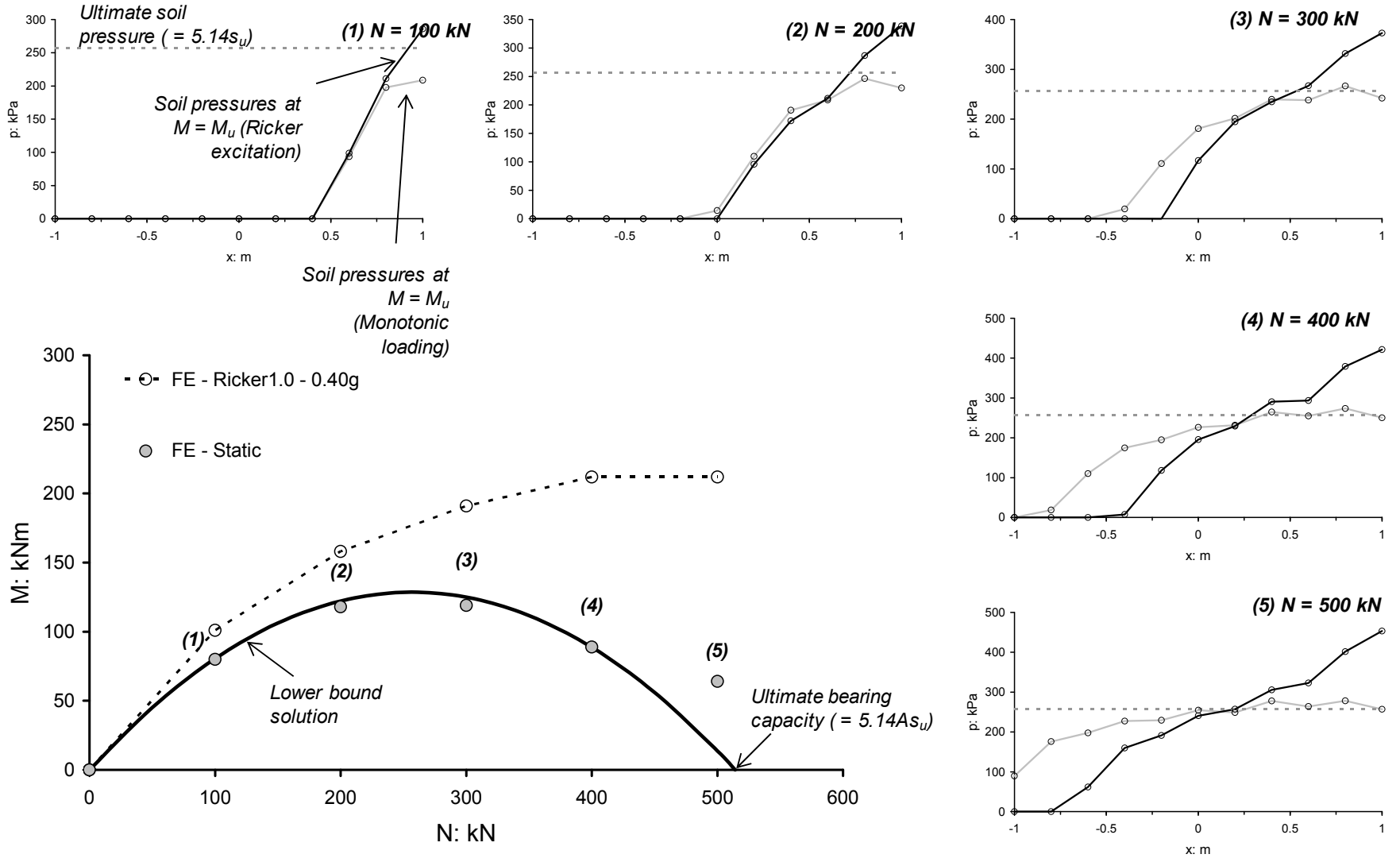


**Figure 5.13** Failure envelope in the $N-M$ space calculated with the finite element model (a) for monotonic loading, (b) for seismic loading with a Ricker-type excitation $\left(T_E = 0.67 \text{ sec},\ PGA = 0.40 \text{ g}\right)$. Contact pressure distributions at different loading points are also presented. $B = 2b = 2$ m, $h = 5$ m, $s_u = 50$ kPa *(model v.01)*.

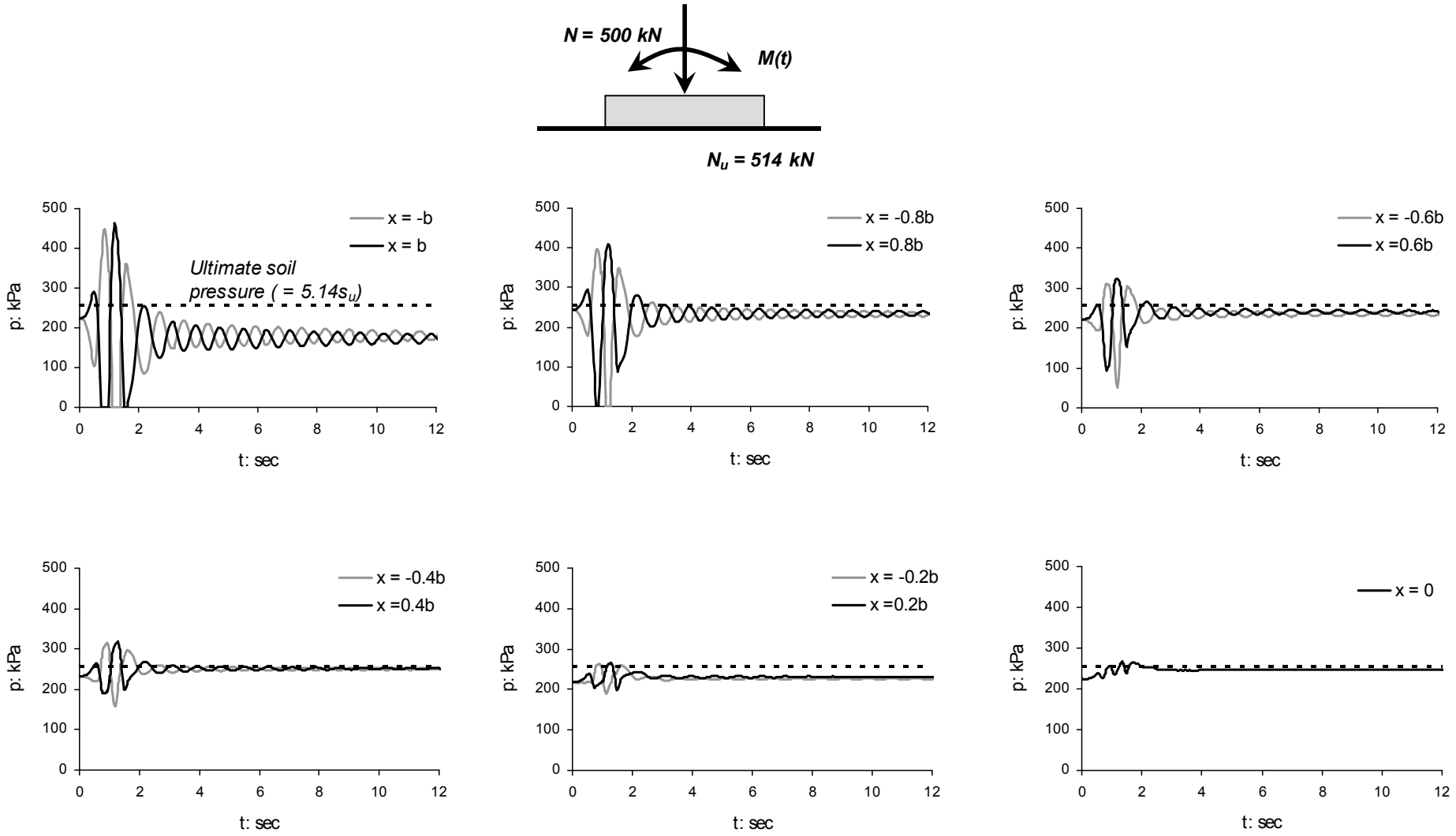


**Figure 5.14** Time-histories of soil pressures at symmetric points underneath the footing. $N = 500$ kN, $B = 2b = 2$ m, $h = 5$ m, $s_u = 50$ kPa (*model v.01*). Excitation at the seismic bedrock is a Ricker pulse $\left(T_E = 0.67 \text{ sec},\ PGA = 0.40 \text{ g}\right)$.

## 5.5 DYNAMIC UPLIFT CURVES

During strong seismic shaking, rocking motion of a shallow footing is often associated with large uplift from the supporting soil. The uplifting level is higher in case of a lightly-loaded foundation or a slender structural system. A simplified estimation for the uplifting level at static overturning conditions can be derived from the schematic of Fig. 5.4 which leads to Eqs 5.13 and 5.14.

A finite element validation of this approximation comes from the static results portrayed in Fig. 5.15, for the soil-foundation configuration of *model v.01* $\left(s_u = 50 \text{ kPa}\right)$.

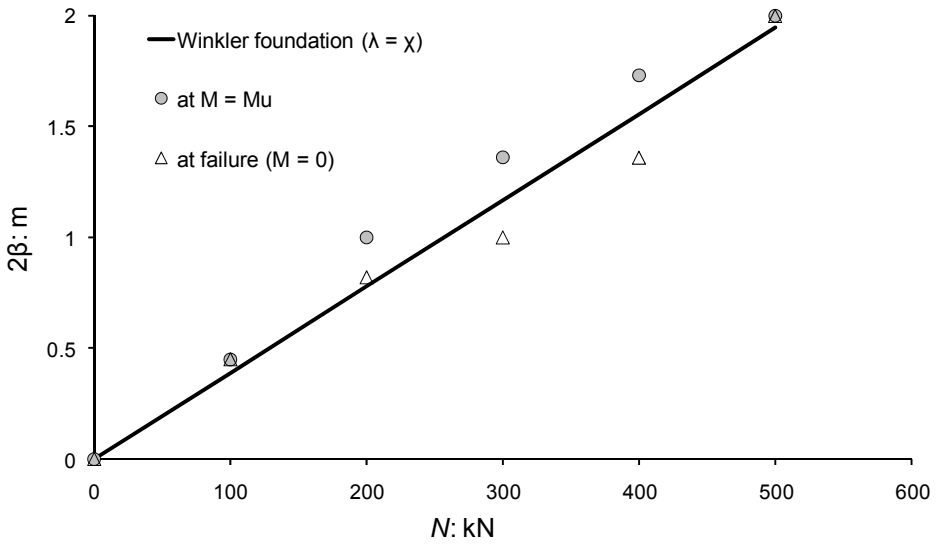


**Figure 5.15** Finite element calculation of the effective width under monotonic loading (a) at the increment of maximum moment $\left(M = M_u\right)$, (b) at failure $\left(M = 0\right)$ and comparison with the elastoplastic Winkler model. $B = 2b = 2$ m, $s_u = 50$ kPa (*model v.01*).

The earthquake-induced uplift of a shallow foundation is investigated for a Ricker-type excitation. In Figs 5.16 and 5.17 the width of the effective footing $\left(2\beta\right)$ at $\left(M = M_u\right)$ is computed from the afore-discussed finite element study of the dynamic moment capacity. Depending on the frequency of ground shaking, the dynamic failure envelope in the $2\beta - N$ plane may be located above or below the static linear trend $\lambda = \chi$. The divergence of the dynamic from the static failure envelope is enlarged

by the intensity of ground shaking. Hence, for a strong shaking $\left(PGA = 0.6\ \text{g}\right)$ the dynamically-induced uplift may be substantially lower $\left(\text{for } T_E = 0.33\ \text{sec}\right)$ or higher $\left(\text{for } T_E = 1.33\ \text{sec}\right)$ than the static prediction. On the other hand, for a weak excitation $\left(PGA = 0.2\ \text{g}\right)$ the expression $\lambda = \chi$ can practically describe the uplifting level.

Slightly different conclusions can be drawn when the soil-foundation system of *model v.02* is considered. Unlike the *model v.01* case, the uplift at ultimate capacity is kept constantly at low levels compared to the static, Winkler-based prediction. Furthermore, when the Ricker1.0 and Ricker0.5 pulses are applied the uplifting response is pretty close to that calculated with pseudostatic finite element analysis. Dynamic uplift is even more limited under the high-frequency excitation of Ricker2.0 and far less than the static predictions, however such a response is expected as the moment capacity is not mobilised in this case.

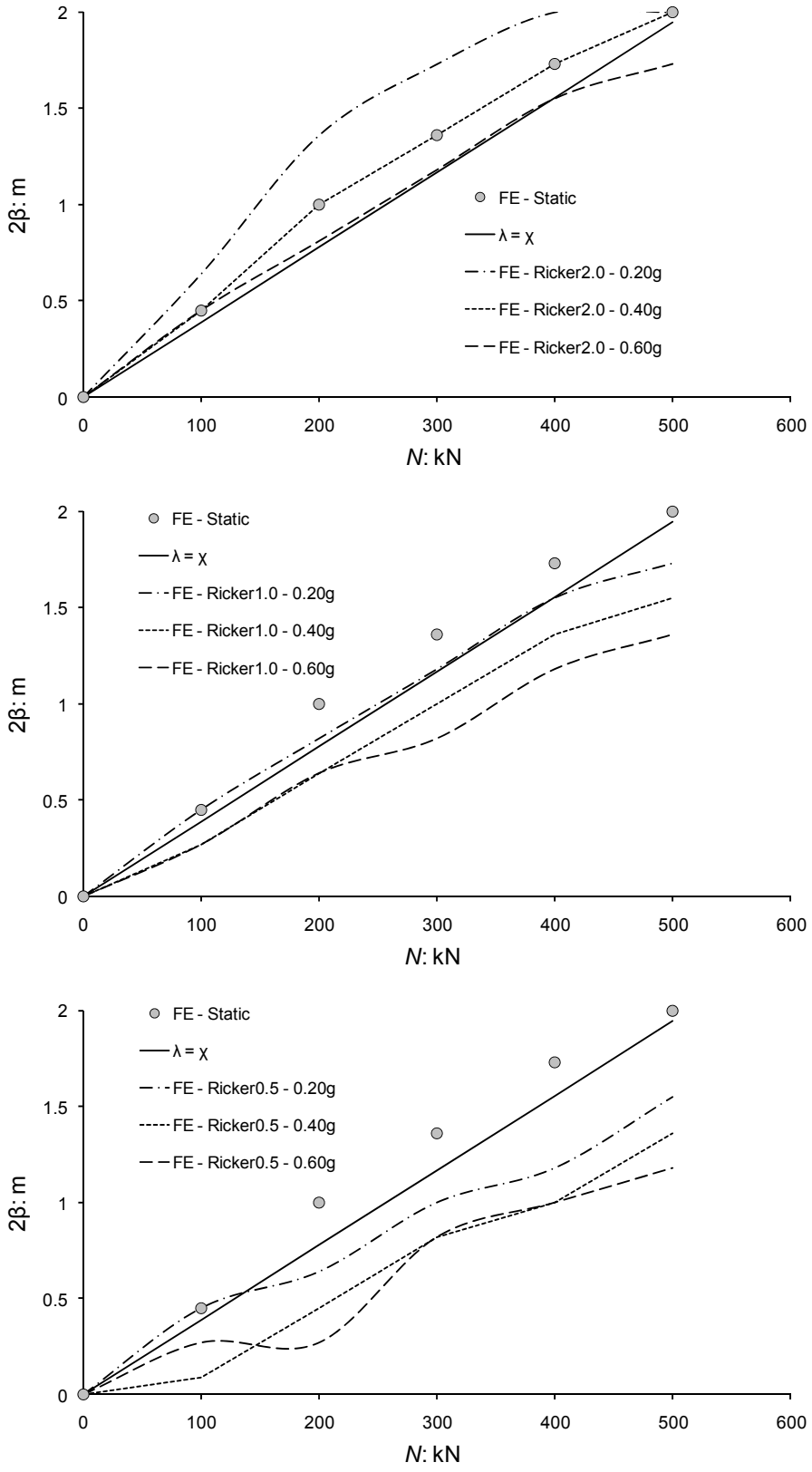


**Figure 5.16** Finite element calculation of $N-2\beta$ interaction curves under earthquake loading and comparison with the static case. The excitation at the seismic bedrock is a Ricker pulse of $pga = 0.2$, 0.4, and 0.6 g and period $T_E = 0.33$, 0.67, and 1.33 sec (Ricker 2.0, 1.0, and 0.5 respectively). $B = 2b = 2$ m, $h = 5$ m, $s_u = 50$ kPa (*model v.01*).

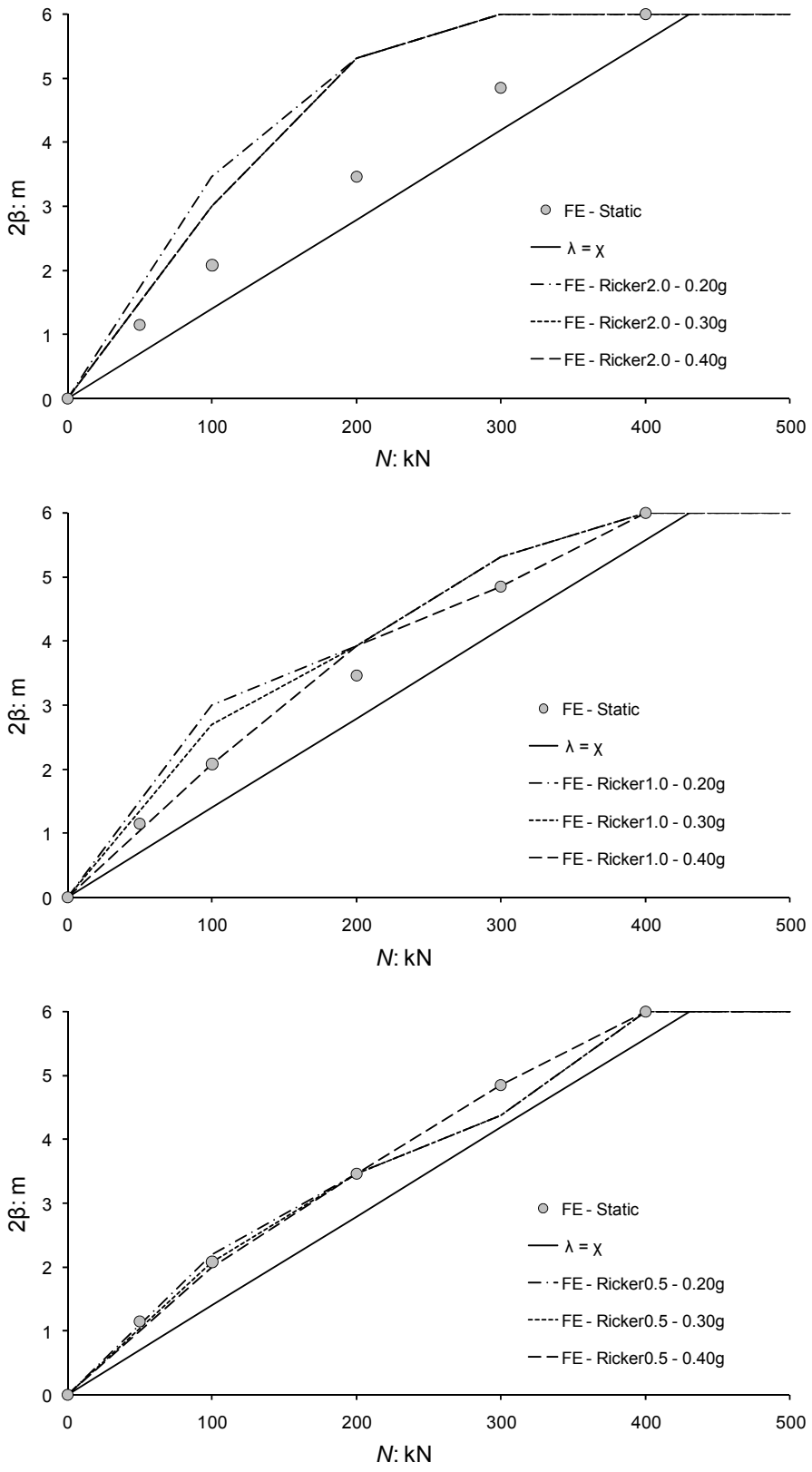


**Figure 5.17** Finite element calculation of $N-2\beta$ interaction curves under earthquake loading and comparison with the static case. The excitation at the seismic bedrock is a Ricker pulse of $pga=0.2$, 0.3, and 0.4 g and period $T_E=0.33$, 0.67, and 1.33 sec (Ricker 2.0, 1.0, and 0.5 respectively). $B=2b=9$ m, $h=11$ m, $s_u=15.7z+10$ (*model v.02*).

## 5.6 DEVELOPMENT of CUMULATIVE DISPLACEMENTS

It has been found in the literature from experimental and numerical studies that cyclic rocking motion of the foundation may lead to significant accumulation of permanent settlement (Gajan *et al.*, 2005 among others). This 'cyclic' vertical displacement $\delta w_{res}$ which is added to the initial (static) settlement $w_o$, is primarily sensitive to the vertical load factor $\chi$, the footing width, the number of cycles, and the frequency content of ground shaking.

The additional (residual) displacements $\delta w_{res}$ (or simply $\delta w$) computed from a series of finite element analyses with the soil-foundation systems of *model v.01* and *v.02* are summarised and plotted as a function of the vertical load in Figs 5.18 and 5.19 respectively. These settlements are also normalised to the initial static settlement $(\delta w / w_o)$ and plotted in Figs 5.20 and 5.21.

It is revealed that the cyclic settlement is very sensitive to the level of vertical loading. Particularly, for a lightly-loaded foundation subjected to rocking vibration $(\chi < 1/3)$, the additional settlement is less than 1% the width of the footing even under strong seismic shaking. This was expected as under such low levels of vertical load uplifting response is prevailing and dynamic displacements $(\theta, w)$ are almost reversible. For higher levels of the vertical load however, the additional settlement increases in an exponential growth and eventually reaches values of about 3% the footing width or even larger. The detrimental effect of the vertical load on the cyclic settlement is amplified when a long-period excitation is applied $(T_E = 1.33 \text{ sec})$.

An interesting way of presenting the cyclic settlement is as a function of the rocking amplitude $\theta_{\max}$. Gajan *et al.* (2005) first published a $\delta w - \theta_{\max}$ correlation extracted from a large database of centrifuge tests as portrayed in Fig. 5.22. The vertical load factor $(\chi = FS_v)$ over all the experiments ranges from 3.4 to 9.6 representative of moderately to lightly loaded foundation. All the results of the

parametric finite element analyses performed in this study are utilised to correlate the cyclic settlement to the rocking amplitude for different levels of $\chi$ as illustrated in the graph of Fig. 5.23.

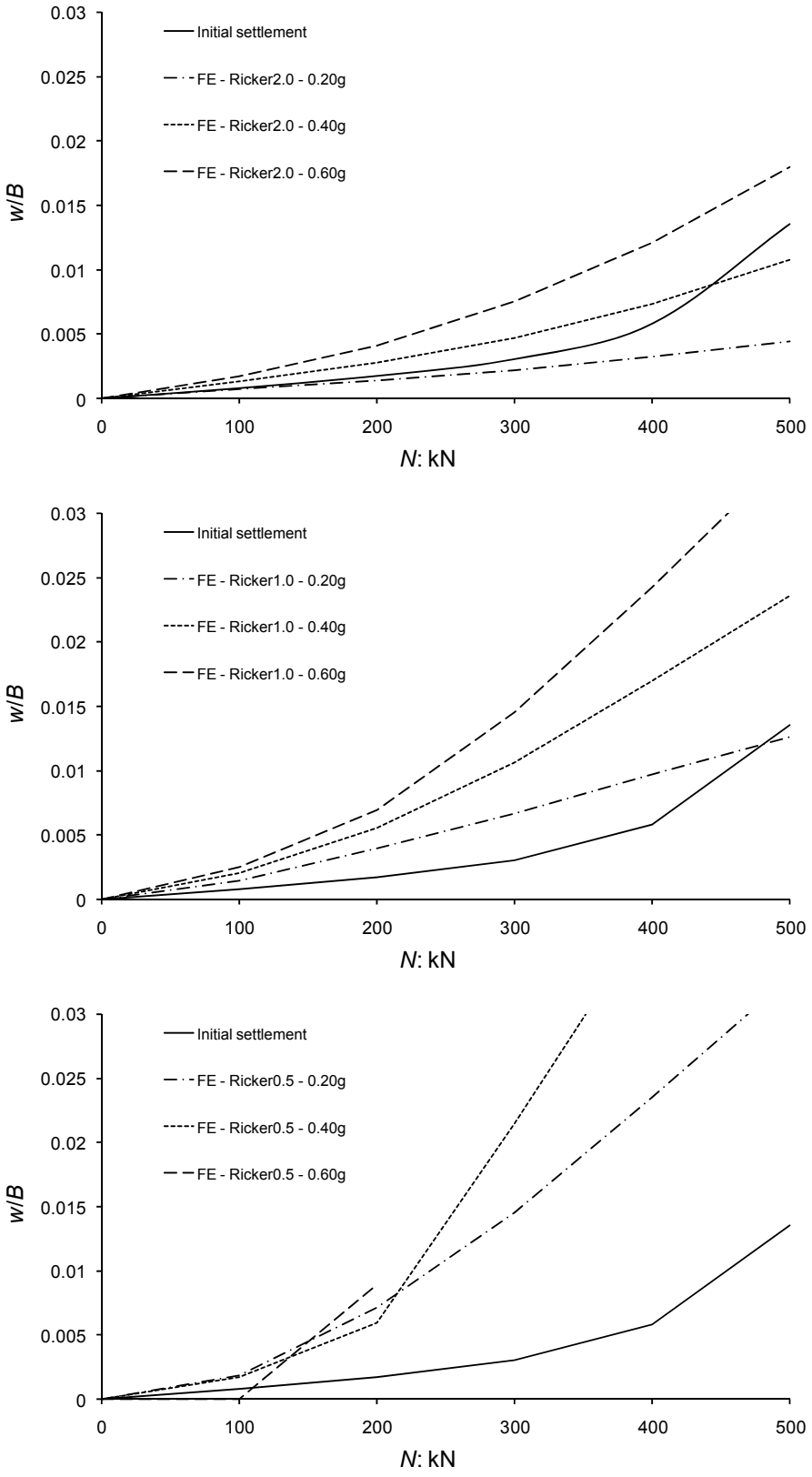


**Figure 5.18** Finite element calculation of $N-\delta w$ interaction curves under earthquake loading. The excitation at the seismic bedrock is a Ricker pulse of $pga = 0.2, 0.4, \text{and } 0.6$ g and period $T_E = 0.33, 0.67, \text{and } 1.33$ sec (Ricker 2.0, 1.0, and 0.5 respectively). $B = 2b = 2$ m, $h = 5$ m, $E = 100$ MPa, $s_u = 50$ kPa (*model v.01*).

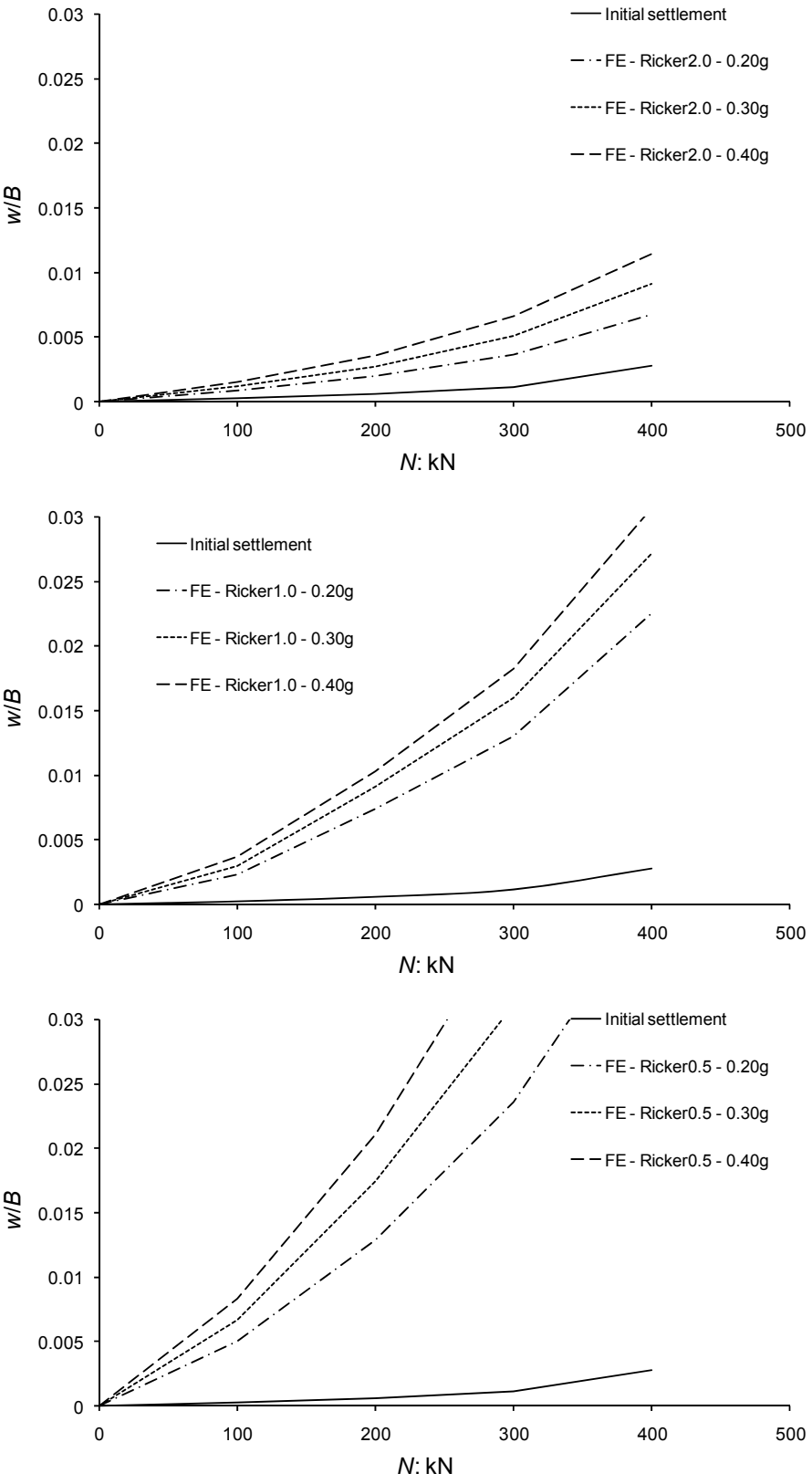


**Figure 5.19** Finite element calculation of $N-\delta w$ interaction curves under earthquake loading. The excitation at the seismic bedrock is a Ricker pulse of $pga = 0.2, 0.3,$ and $0.4$ g and period $T_E = 0.33, 0.67,$ and $1.33$ sec (Ricker 2.0, 1.0, and 0.5 respectively). $B = 2b = 9$ m, $h = 11$ m, $E = 4.74z + 30$, $s_u = 15.7z + 10$ (*model v.02*).

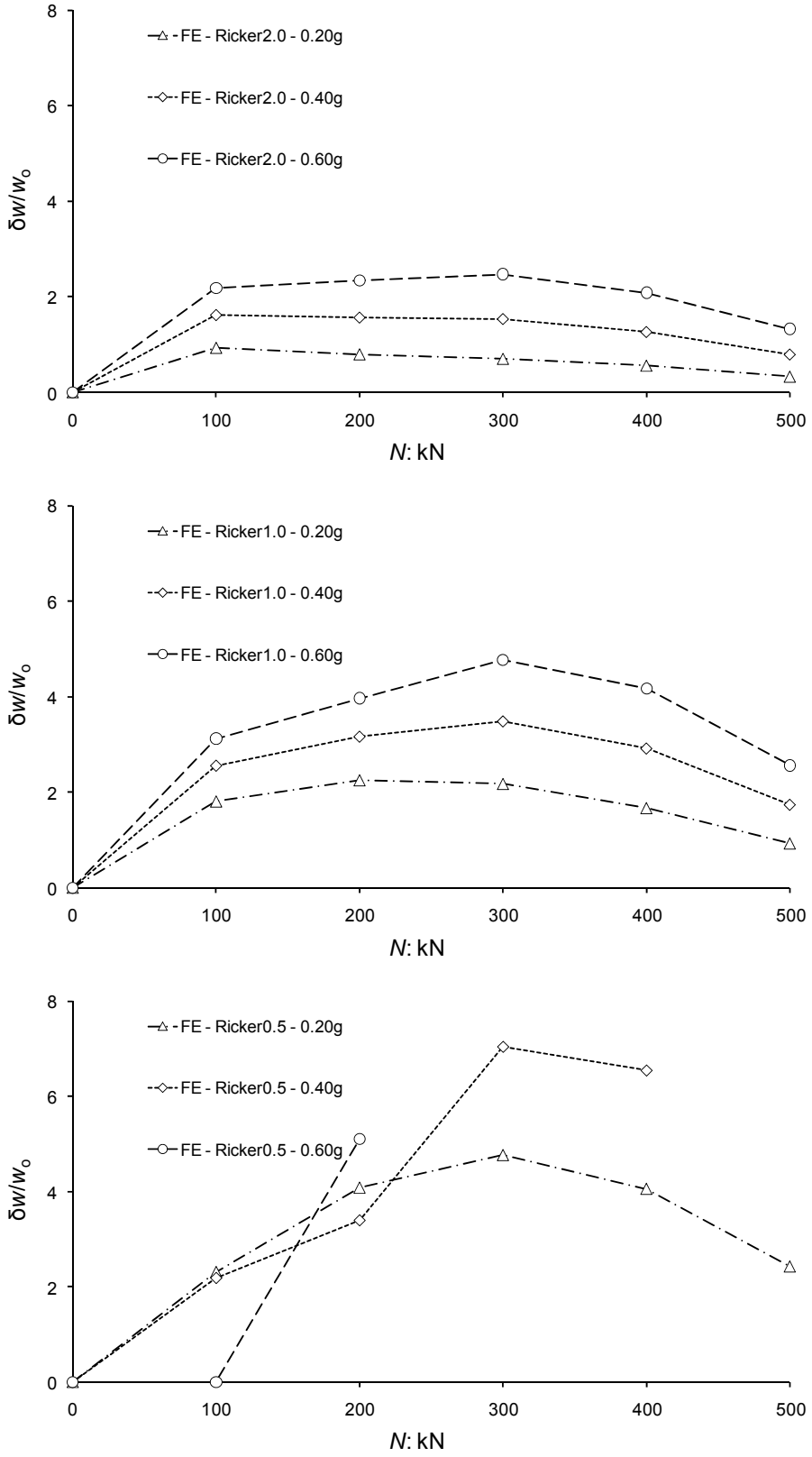


**Figure 5.20** Finite element calculation of $N-\delta w/w_o$ interaction curves under earthquake loading. The excitation at the seismic bedrock is a Ricker pulse of $pga=0.2$, 0.4, and 0.6 g and period $T_E=0.33$, 0.67, and 1.33 sec (Ricker 2.0, 1.0, and 0.5 respectively). $B=2b=2$ m, $h=5$ m, $E=100$ MPa, $s_u=50$ kPa (*model v.01*).

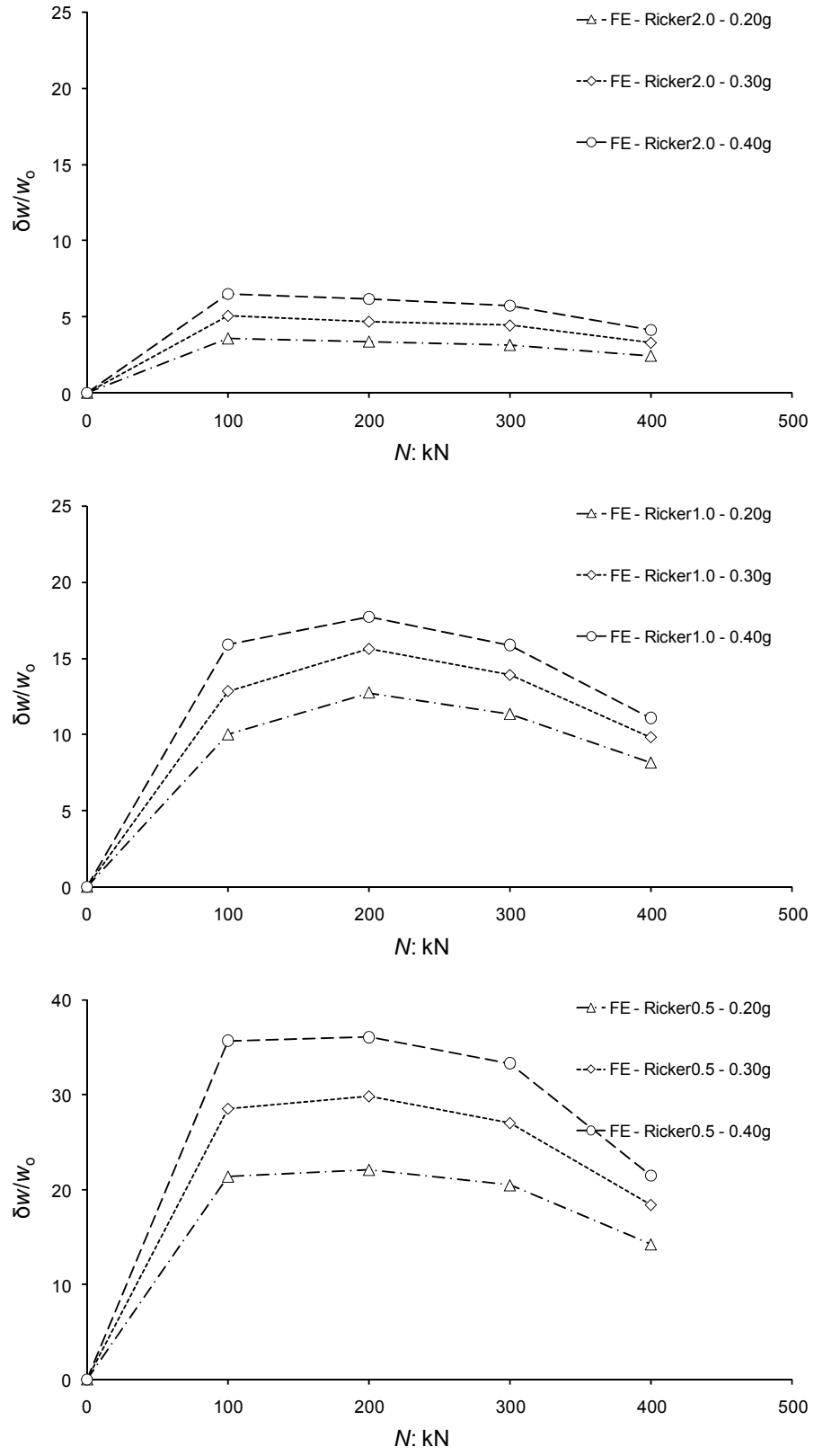


**Figure 5.21** Finite element calculation of $N-\delta w/w_o$ interaction curves under earthquake loading. The excitation at the seismic bedrock is a Ricker pulse of $pga=0.2,\ 0.3,$ and $0.4$ g and period $T_E=0.33,\ 0.67,$ and $1.33$ sec (Ricker 2.0, 1.0, and 0.5 respectively). $B=2b=9$ m, $h=11$ m, $E=4.74z+30$, $s_u=15.7z+10$ (*model v.02*).

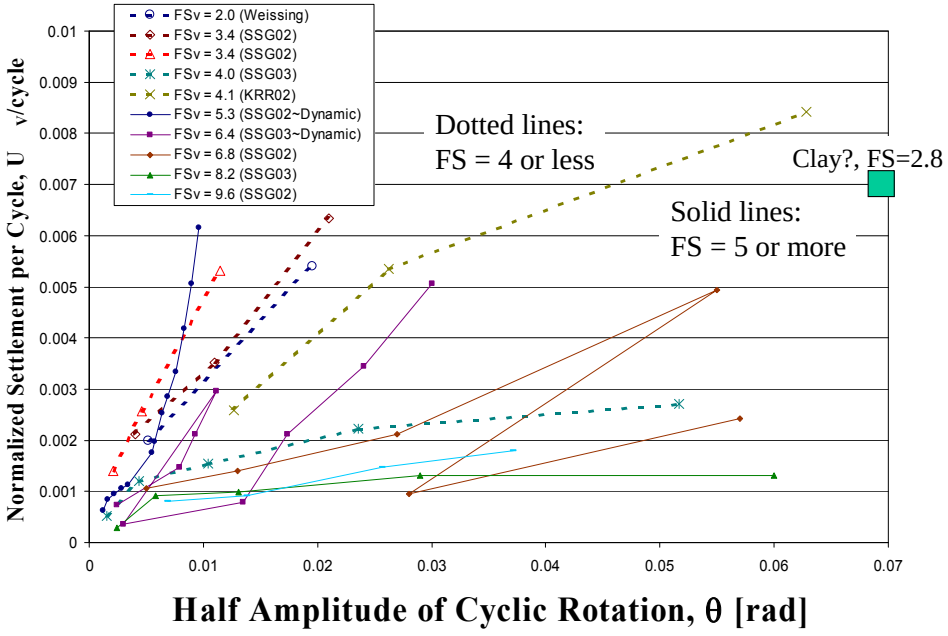


**Figure 5.22** Normalised cyclic (additional) settlements of the foundation from centrifuge experiments (Gajan *et al.*, 2005).

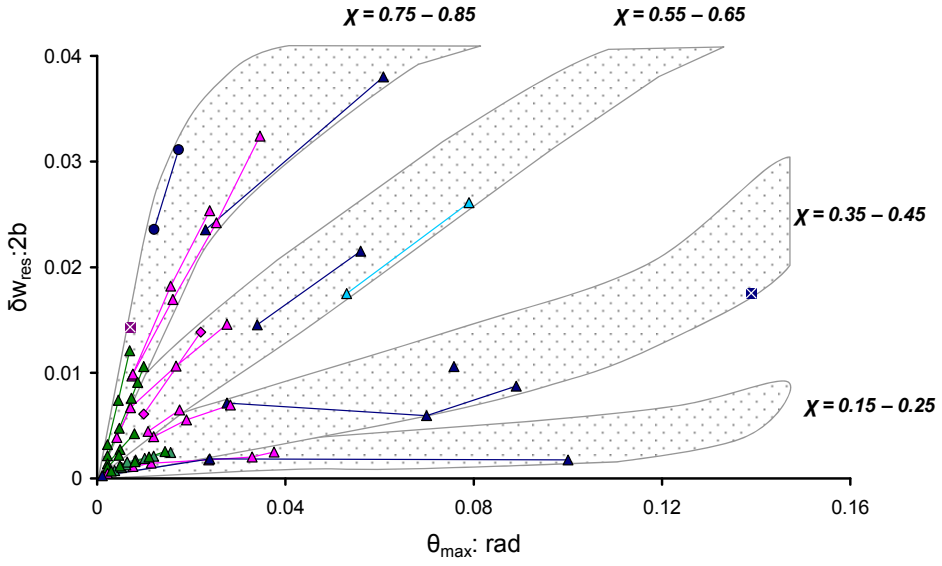


**Figure 5.23** Normalised cyclic (additional) settlements of the foundation from numerical analysis. The excitation at the seismic bedrock is a Ricker wavelet.

*Chapter 6:*

# Macroscopic modelling for large-displacement analysis of uplifting foundation

## 6.1 CONVENTIONAL WINKLER MODELLING

In common SSI analysis procedures, Winkler modelling of soil medium has been found a simple and efficient tool because of its ability to incorporate different nonlinear aspects of the rocking behaviour at relatively low levels of computational cost. For example, no-tension springs can capture uplifting effects at the soil-foundation interface whereas soil yielding can be represented with elastic – perfectly plastic springs. In the context of a conventional Winkler model the following postulations are often encountered:

- A unique spring modulus $k_v$ is adopted for any type of loading (symmetric or antisymmetric) which is independent of the distance from the mid-point $x$. Correspondingly, a purely vertical or moment loading results to a uniform or triangular distribution of contact pressures along the foundation.
- The rotation pole of the structural system remains fixed at the foundation mid-point even after uplift or soil yield initiates.
- During a clockwise (counter-clockwise) rotation, uplift onsets when the vertical displacement at the left edge (right edge) of the foundation becomes zero.
- $P-\delta$ effects are ignored even in the domain of large lateral displacements of the superstructure mass centre.

A schematic of a rigid footing resting on a Winkler foundation is shown in Fig. 6.1. Bartlet (1979) used a conventional soil model of distributed elastic – perfectly plastic springs to study the rocking response of a footing on clay. His considerations on the different states of moment-rotation response have been implemented by FEMA guidelines (273/274 documents) in the modelling of shear walls as portrayed in the graph of Fig. 6.2. The following considerations of the backbone $M-theta$ relationship are presented in this plot: (a) the extreme case of elastic soil conditions represented with the path 1-2-3-5a, (b) the case of a soil with limited strength where uplift occurs before yield (path 1-2-3-4-5b-6), and (c) the case of a soil with limited strength where yield initiates first (path 1-2c-3c-4c-5c-6).

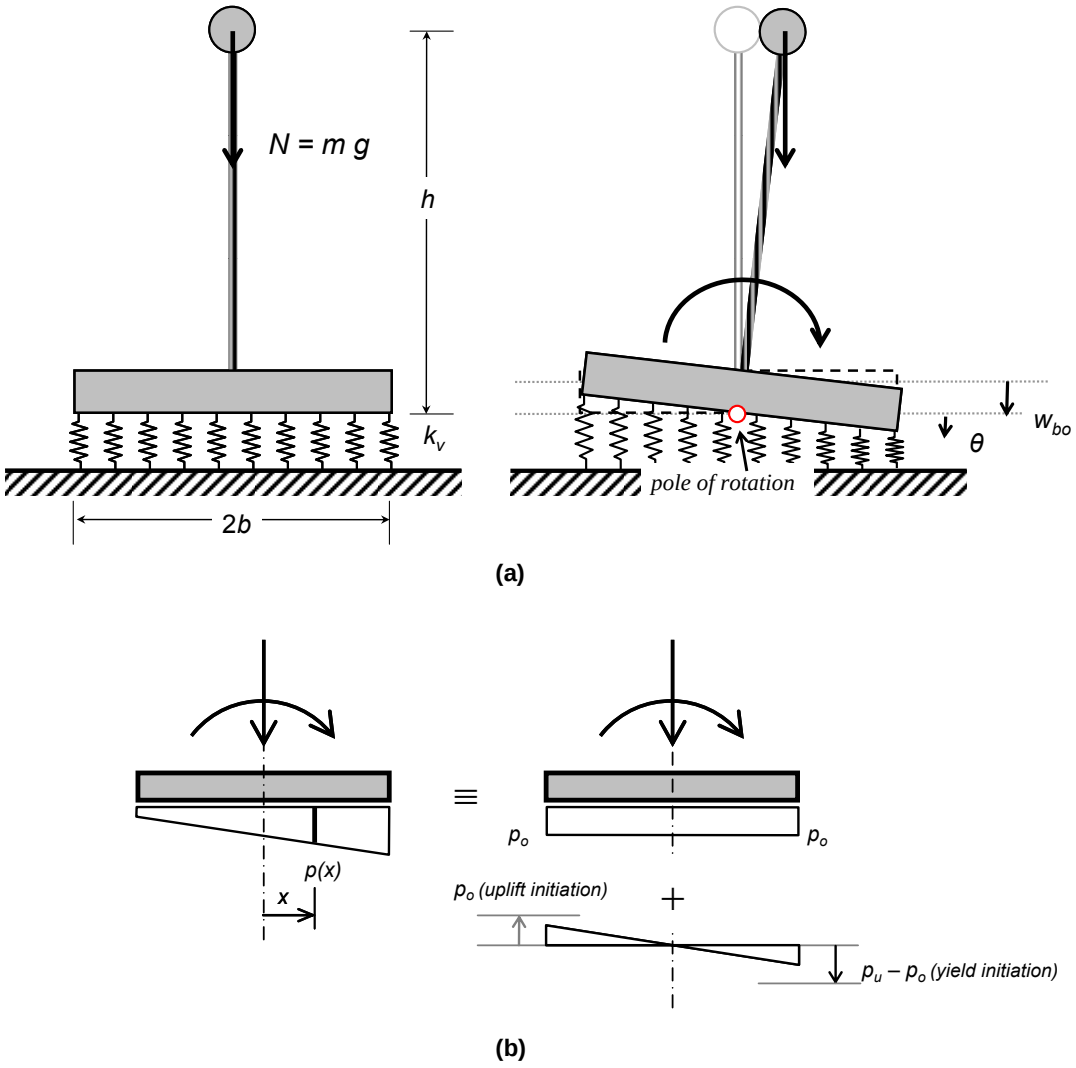


**Figure 6.1** Conventional beam-on-winkler-foundation model: (a) configuration of the model and (b) superposition of soil contact pressures at full-contact state.

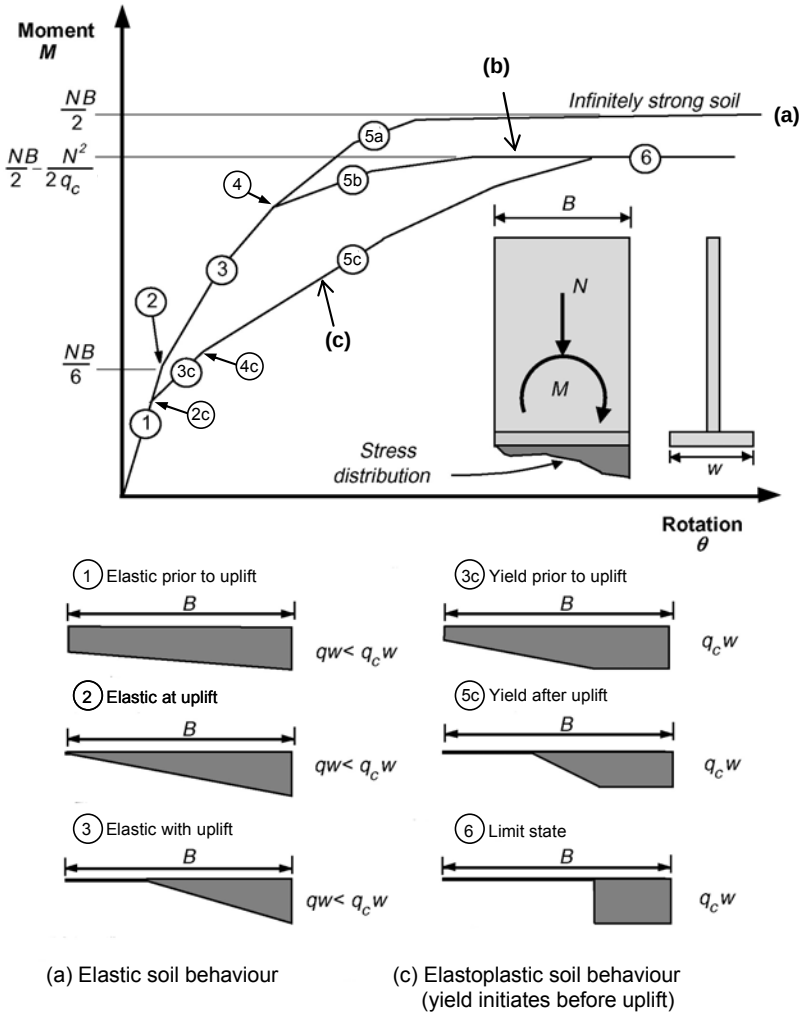


**Figure 6.2** Rocking of a shear wall on strip footing: the different states of the M-theta curve under monotonic loading (Bartlet, 1979, reprinted in FEMA274 document).

### *Elastic soil*:

For purely elastic soil behaviour, nonlinearity of the moment-rotation response emerges once uplifting occurs and leads to an ultimate capacity of $M_u = N\,b$. During full-contact conditions (state 1), the moment with reference to the centre of the footing can be easily extracted by integrating distributed moments over the foundation:

$$M_1 = \int_{-b}^{b} k_v\,\theta\,x^2\,\mathrm{d}\,x \;=\; \frac{2k_v b^3}{3}\theta \qquad [6.1]$$

The rocking rotation and moment at incipient uplift (state 2) can be derived by the uplifting criterion $w(-b)=0$ $\left(=\theta_{uplift}b-N/(2k_vb)\right)$ together with Eq. 6.1:

$$\theta_{uplift}=\frac{N}{2k_vb^2} \quad \text{and} \quad M_{uplift}=\frac{Nb}{3}=M_2 \tag{6.2}$$

After the uplift onset, the moment–rotation curve enters a softening mode (state 3 and 5a). The moment at this level is derived after integration over the remaining in contact part of the footing $2\beta$ as follows (Siddharthan *et al.*, 1992):

$$M_{3,5a}=\int_{b-2\beta}^{b}k_v\,\theta\,x^2\,\mathrm{d}x=Nb\left(1-\frac{1}{3}\sqrt{\frac{2N}{k_vb^2\theta}}\right)=M_{uplift}\left(3-\sqrt{\frac{2N}{k_vb^2\theta}}\right) \tag{6.3}$$

This curve reaches a maximum value of $M_{\max}=Nb$ which represents the ultimate moment capacity of the foundation for elastic soil response when $P-\delta$ effects are ignored.

***Elastoplastic soil*:**

In the general case of soil with limited strength, an ultimate value of the spring reaction $p_u=N_u/2b$ is implemented with $N_u$ being the foundation bearing capacity under central vertical load. It is revealed that the inverse of the safety factor under purely vertical loading $\left(\chi=FS_v^{-1}=N/N_u\right)$ has a significant effect on the rocking behaviour (Allotey *et al.*, 2003). In particular, two separate modes of the moment-rotation curve can be distinguished dependent upon the value of $\chi$: an uplift prevailing state corresponding to a lightly-loaded foundation $\left(\chi<0.5\right)$ and a soil-yield prevailing state in case of a heavily-loaded foundation $\left(\chi>0.5\right)$. The former follows the path 1-2-3-5b-6 in the graph of Fig. 6.2 whereas the latter is represented with the path 1-2c-3c-4c-5c-6. As shown in Fig. 6.1b uplift initiates before soil yield if $p_o<p_u-p_o$ or $p_o<0.5p_u$ $\left(\chi<0.5\right)$. The rocking rotation and moment at

uplift onset are given by Eq. 6.2. Similarly if $p_o > 0.5p_u$ $(\chi > 0.5)$ soil yield occurs first. In this case the yield criterion becomes (Siddharthan *et al.*, 1992):

$$\theta_y = \frac{q_u}{k_v b} - \frac{N}{2k_v b^2} \quad \text{and} \quad M_y = \frac{2q_u b^2}{3} - \frac{Nb}{3} = M_{2c} \tag{6.4}$$

Allotey *et al.*, (2003) derived the analytical $M - theta$ relationship during concurrent uplift and yield (state 5b or 5c):

$$M_{5b,c} = Nb - \frac{N^2}{2p_u} - \frac{{p_u}^3}{24\left(k_v \theta\right)^2} \tag{6.5}$$

Regardless the value of $\chi$ the ultimate moment capacity of the foundation derived from Eq. 6.5 $\left(\text{for } \theta \to \infty\right)$ is:

$$M_6 = Nb - \frac{N^2}{2p_u} \tag{6.6a}$$

The equation of the ultimate moment can be also obtained from moment equilibrium at limit state 6 (see Fig. 6.2). After some algebraic manipulations, Eq. 6.6a yields to the analytical solution of the failure curve in the $N - M$ plane (Eq. 5.9):

$$\frac{M}{N_u B} = \frac{\chi}{2}(1 - \chi) \tag{6.6b}$$

The failure curve in the dimensionless $\hat{n} - \hat{m}$ plane calculated with Eq. 6.6b is plotted in Fig. 6.3 together with the analytical curves for uplift and soil yield onset, as extracted from the foregoing discussion. By plotting these curves, the loading plane bounded by the failure envelope is partitioned in regions of linear and nonlinear response. The nonlinear area is subdivided in smaller parts depending on whether uplift or soil yield or both are encountered. It is worthy of note that a perfectly

symmetric response is achieved about the vertical axis at $\chi = 0.5$. At this point the optimum foundation behaviour in terms of the moment ultimate capacity is attained:

$$\max M \;=\; 0.125\, N_u B \qquad [6.7]$$

In addition, at $\chi = 0.5$ the maximum range of linearly elastic response is achieved before nonlinear conditions due to uplift or soil yield are engaged, with a threshold moment of $0.083\, N_u B = (2/3)\max M$.

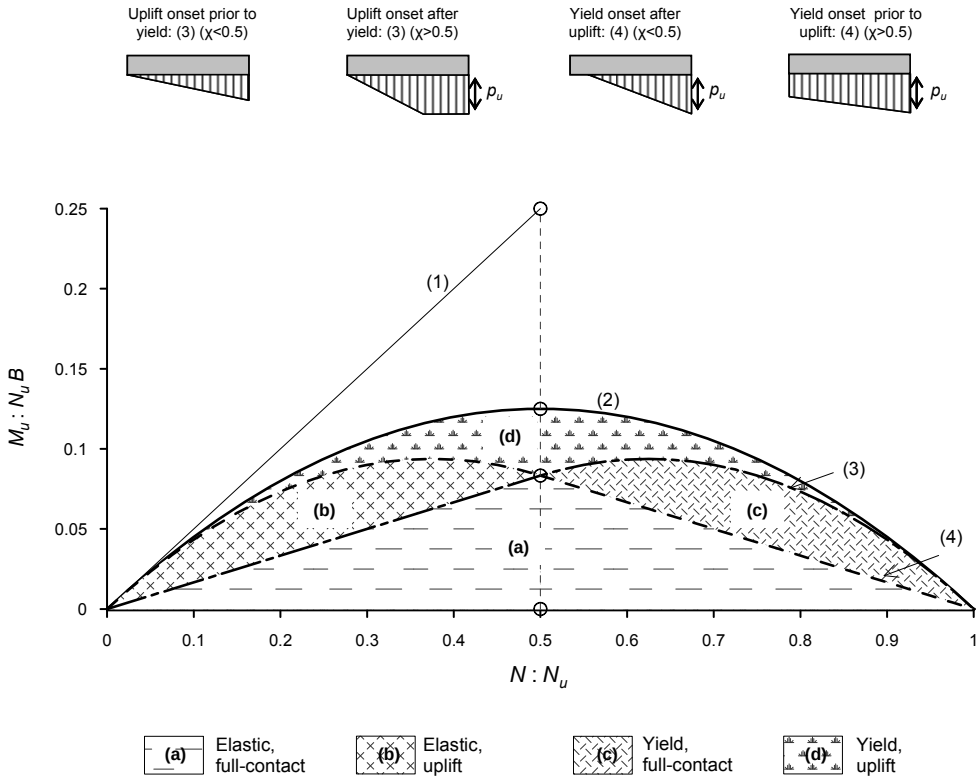


$$(1)\;\therefore\;\frac{M_{u,rigid}}{N_u B} = \frac{\chi}{2} \qquad (2)\;\therefore\;\frac{M_u}{N_u B} = \frac{\chi}{2}(1-\chi)$$

$$(3)\;\therefore\;\frac{M_{uplift}}{N_u B} = \begin{cases} \dfrac{\chi}{6}, & \chi \le 0.5 \\ (1-\chi)\left(\dfrac{2}{3}\chi - \dfrac{1}{6}\right), & \chi \ge 0.5 \end{cases} \qquad (4)\;\therefore\;\frac{M_y}{N_u B} = \begin{cases} \dfrac{\chi}{6}(3-4\chi), & \chi \le 0.5 \\ \dfrac{1}{6}(1-\chi), & \chi \ge 0.5 \end{cases}$$

**Figure 6.3** Interaction curves in the normalised N–M plane for critical *failure* (overturn) on rigid or deformable soil (curves (1) and (2) respectively), *uplift* onset (3), and initiation of *soil yield* (4).

## 6.2 MACROSCOPIC FOUNDATION MODELLING – PREVIOUS STUDIES

Nonlinear numerical modelling of the entire soil-foundation-structure system through realistic representation of the exact geometry and sophisticated tools for inelastic soil behaviour has nowadays become a challenging task given the computational resources and capabilities available nowadays. However such a sophisticated numerical analysis (e.g. with the finite element method) requires also extensive discretisation of soil medium, which may not be feasible to perform in common geotechnical design practice.

An engineering approximation to efficiently evaluate the nonlinear effects of inertial interaction in the domain of large displacements can be obtained if the supporting medium is substructured into two subdomains (Pecker and Pender, 2000):

(a) a *far field* domain which extends a sufficient distance from the foundation, in which soil nonlinearities only governed by the propagation of seismic waves, and

(b) a *near field* domain, in the vicinity of foundation where both geometrical and material nonlinearities associated to SSI are important. The exact boundary between these two domains does not need to be precisely determined.

The far field domain is approached by linear or equivalent linear impedance function in which only radiation damping (viscous type) is implemented. On the other hand, a *macroscopic* approach is adopted for the near field domain which is represented with a nonlinear *macro-element* of six degrees of freedom in the general case (three translational and three rotational). Damping now arises from inelastic soil behaviour underneath the foundation and obeys Masing's law. A schematic of the macroscopic modelling is illustrated in Fig. 2.8.

A dynamic macro-element based on this macroscopic consideration was developed by Cremer *et al.*, 2001 for shallow foundation on cohesive soil. Later studies on macro-element modelling have been presented by Gajan and Kutter, 2009; Chatzigogos *et al.*, 2009; Figini *et al.*, 2011.

## 6.3 FORMULATION of a MACRO-ELEMENT TYPE MODEL

### 6.3.1 Elastic soil

Rigorous finite element analysis of a footing under monotonic loading (Chapter 4) revealed that for a vertical load factor $\chi << 1$ (i.e. for a lightly loaded foundation or for very stiff soil conditions) foundation rocking is associated with large levels of uplift and small soil deformations. Under such circumstances the assumption of elastic soil behaviour is generally a reasonable approximation in analysing the rocking response. Nonlinear behaviour under moment loading is then attributed primarily to the reduction of the footing contact area (geometric nonlinearity). In slender structures geometrical nonlinearity is even more amplified at large rotations due to the accompanying lateral movement of the mass centre ($P-\delta$ effect).

In light of an elastic approach for the soil response, concentration of contact pressures occurs in the vicinity of corner points which cannot be captured by the conventional Winkler modelling. The increase in 'local' soil stiffness with the distance from the footing midpoint is higher under anti-symmetric loading which corresponds to larger values of rocking stiffness $K_m$ compared to the vertical stiffness $K_v$. Table 6.1 shows the ratio of rocking-to-vertical stiffness calculated (a) with the classical 'elastic medium' solutions (e.g. Gazetas, 1991) and (b) with the convectional Winkler modelling. Remarkably the rigorous 'elastic approach' gives a stiffness ratio of about four times higher than the ratio predicted by the simplified Winkler model. It is therefore evident that a more efficient and precise soil model should be incorporated in the non-linear analysis of footings subjected to severe overturning moments. Neglecting the effects of soil nonlinearity, such a rigorous macroscopic modelling of rocking behaviour should be in agreement with: (a) the classical 'elastic medium' solutions of the soil-foundation stiffnesses during full-contact conditions, and (b) the limiting case of an uplifting foundation on a rigid soil discussed in Chapter 3.

**Table 6.1** Rocking and vertical stiffnesses for a strip footing calculated with the analytical approach of the elastic medium (infinite half-space) and the Winkler modelling.

| | $K_m$ | $K_v$ | $K_m / K_v$ | $\frac{(K_m / K_v)_{medium}}{(K_m / K_v)_{winkler}}$ |
|---|---|---|---|---|
| Elastic medium | $\frac{\pi G b^2}{2(1-\nu)}$ | $\frac{1.2G}{1-\nu}$ | $1.3b^2$ | 3.9 |
| Winkler | $\frac{2k_v b^3}{3}$ | $2k_v b$ | $0.33b^2$ | |

To formulate a macroscopic model for the rocking response we consider a rigid strip footing of width $B = 2b$ resting on the surface of a homogeneous half-space. Initially the footing is subjected only to a vertical loading $N$. Then a gradually increasing horizontal force is applied at the mass centre of the superstructure (located at height $h$) leading to an overturning moment $M = Nh\cos\theta$ about the foundation centre. It is postulated that tensile forces cannot be undertaken by the soil-foundation interface. In this way uplift onsets whenever the subgrade reaction due to moment loading at a corner point $p_m$ reaches the initial vertical reaction $p_v$.

The different states rocking response of the foundation in terms of a large-displacement analysis procedure are illustrated in Fig. 6.4.

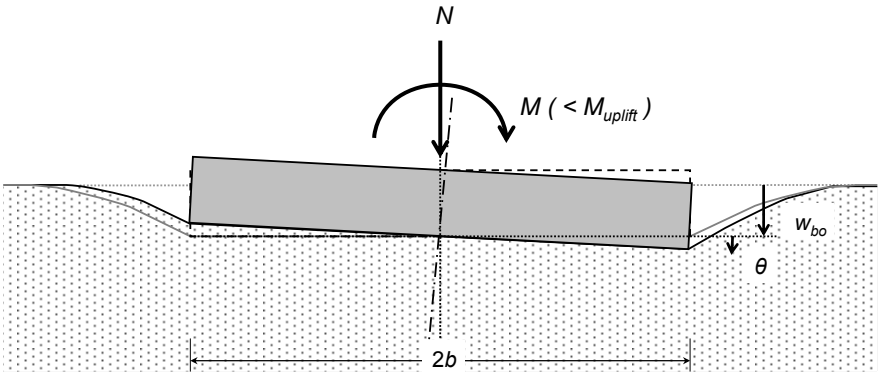


**(a) full-contact phase**

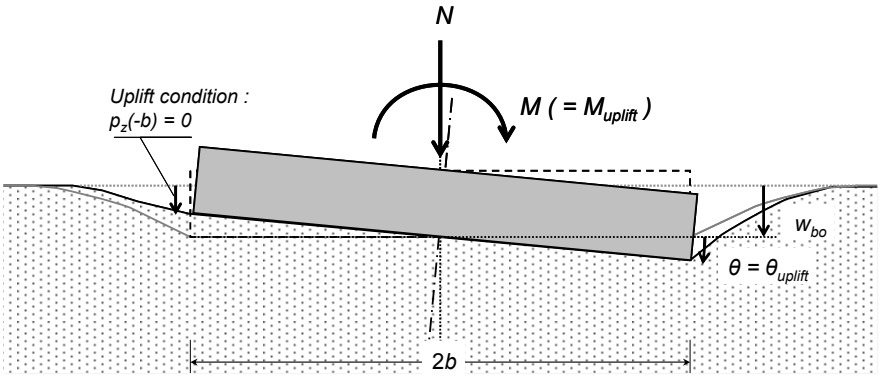


**(b) incipient uplift**

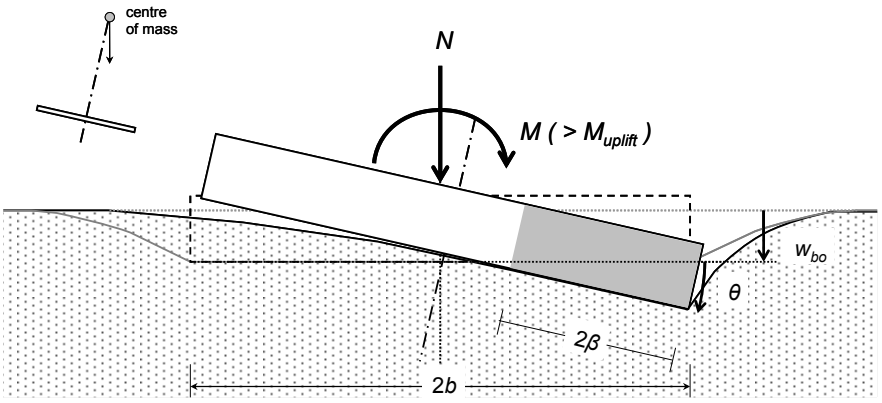


**(c) uplifting phase**

**Figure 6.4** Rocking of a rigid strip footing on elastic soil: different states of response.

***Full-contact phase*:**

For sufficiently low levels of moment, the confinement due to vertical loading ensures a full-contact condition at the interface. At this state, the strip is rocking about its midpoint and therefore any vertical displacement $w$ at a distance $x$ from the centre comprises (a) a *vertical* component $w_{bo}$ and (b) a *rocking* component $x\sin\theta$:

$$w_b(x) = w_{bo} + x\sin\theta \qquad [6.7]$$

Moreover, the contact pressure to the footing at a distance $x$ can be determined with the superposition of the symmetric (vertical) and the anti-symmetric (moment) components of loading:

$$p_z(x,\theta) = p_v(x) + p_m(x,\theta) \qquad [6.8]$$

Where $p_v(x) = k_v(x)w_{bo}$ and $p_m(x,\theta) = k_m(x)x\sin\theta$ are the vertical contact pressures for the case (a) and (b) respectively and $k_v$, $k_m$ are the subgrade moduli for the two loading cases.

It is remarked that in contrast to the conventional beam-on-winkler-foundation modelling, the sensitivity of soil response to the loading conditions is now incorporated by adopting two separate spring constants for vertical and moment loading.

The problem of a rigid strip on a homogeneous isotropic medium can be analysed in a variety of ways. These include Green's function techniques, complex variable methods and integral transform methods. Within the assumption of a smooth interface, closed-form solutions can be derived for simple loading cases. Sadowsky (1928) and Muskhelishvili (1953) developed solutions for the contact pressures in symmetric or anti-symmetric loading:

$$p_v(x) = \frac{N}{\pi b\sqrt{1-x^2/b^2}} \quad \text{and} \quad p_m(x,\theta) = \frac{2Mx}{\pi b^3\sqrt{1-x^2/b^2}} \qquad [6.9]$$

Evidently, the contact pressure for each loading case theoretically approaches infinity at the edges of the footing. In reality the maximum value of the contact pressure is bounded due to the finite soil strength and redistribution of stresses. The *subgrade modulus* for vertical and moment loading at a distance $x$ from the foundation mid-point is derived after dividing Eqs 6.9 by $w_{bo}$ and $x\sin\theta$ respectively:

$$k_v(x)=\frac{K_v}{\pi b\sqrt{1-x^2/b^2}} \quad \text{and} \quad k_m(x)=\frac{2K_m}{\pi b^3\sqrt{1-x^2/b^2}} \qquad [6.10]$$

Where $K_v = N/w_{bo}$ and $K_m = M/\theta$ are the *global* soil-foundation stiffnesses for each loading case. As mentioned above, for a rigid strip on a homogeneous half-space the closed-form solutions for these static stiffnesses are (Gazetas, 1991):

$$K_v = 0.73G/(1-\nu) \quad \text{and} \quad K_m = \pi G b^2/2(1-\nu) \qquad [6.11]$$

Recalling Eqs 6.10 the subgrade moduli ratio at a distance $x$ from the centre is:

$$\frac{k_v(x)}{k_m(x)}=\frac{K_v b^2}{2K_m} \qquad [6.12]$$

Which is independent of the distance $x$ and therefore it is also satisfied for $x=-b$. It is noted that Eq. 6.12 is validated from the findings of the foregoing finite element analysis (Chapter 4), regardless the footing size and the presence of a shallow bedrock.

The sensitivity of the subgrade modulus to the distance from the midpoint and the loading conditions is reflected in the $p-w$ curves, calculated with two-dimensional finite element analysis at the centre and at the edges of the foundation, as plotted in Fig. 6.5. The vertical load which is initially applied to the footing induces a uniform settlement $w_{bo}$. The horizontal (displacement-controlled) loading imposed at the level of the superstructure mass centre invokes an additional loading in the right part of the footing (see curve 3) with stiffer subgrade modulus as well as unloading of the left part (see

curve 1). At this state of response, symmetric points of the footing with respect to the vertical central axis have equal subgrade moduli (i.e. $k_{m1} = k_{m3}$ ).

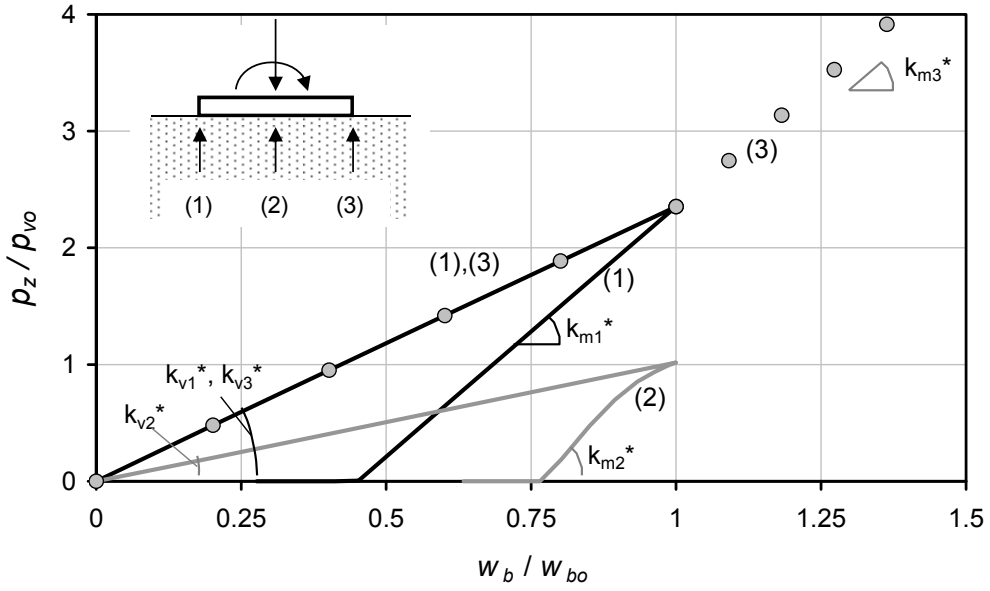


**Figure 6.5** $p-w$ curves underneath the footing at the middle [(2)] and at the corner points [(1) and (3)] for horizontal loading and unloading at the superstructure mass centre.

The resultant moment of the contact pressures with reference to the centre can be computed with integration over the foundation:

$$M = M_{p,v} + M_{p,m} = \int_{-b}^{b} k_v(x) w_{bo} x \cos\theta \, \mathrm{d}x + \int_{-b}^{b} k_m x^2 \cos\theta \sin\theta \, \mathrm{d}x \qquad [6.13]$$

where $M_{p,v}$ and $M_{p,m}$ are the moments associated with the symmetric and anti-symmetric loading respectively. Setting the transformation $x = b\sin\omega$ ( $\mathrm{d}x = b\cos\omega \, \mathrm{d}\omega$ ), these moment components yield:

$$M_{p,v} = \int_{-b}^{b} \frac{Nx}{\pi b\sqrt{1-x^2/b^2}} \cos\theta \, \mathrm{d}x \; = \; \frac{Nb\cos\theta}{\pi} \int_{-\pi/2}^{\pi/2} \sin\omega \, \mathrm{d}\omega \; = \; 0 \qquad [6.14a]$$

and

$$M_{p,m} = \int_{-b}^{b} \frac{K_m x^2 \sin 2\theta}{\pi b^3 \sqrt{1-x^2/b^2}} \mathrm{d}x \;=\; \frac{K_m \sin 2\theta}{\pi} \int_{-\pi/2}^{\pi/2} \frac{1-\cos 2\omega}{2} \mathrm{d}\omega \;\cong\; K_m \theta \qquad [6.14b]$$

Through Eqs. 6.14 it is verified that symmetric loading does not contribute to the resultant moment whereas a linear moment-rotation relationship is established under antisymmetric loading.

***Uplift initiation*:**

For a clockwise rotation, the footing marginally lifts off the supporting soil when the contact pressure at the left edge counter-balances the initial reaction of vertical loading:

$$p_z(-b) = p_v(-b) - p_m(-b) = 0 \qquad [6.15]$$

Unlike the conventional Winkler models, in the proposed model moment loading is associated with stiffer subgrade moduli. This is a result of the two-dimensional geometry of the supporting medium and induces uplift to initiate at a vertical displacement $w(-b)$ larger than zero. This is evident in the numerical analysis results depicted in Fig. 6.5 where uplift onsets before the normalised vertical displacement of the unloading (left) edge $w_{bo}/w_b$ becomes zero. Taking into account that at marginal uplift the vertical displacement of the footing pivot point is $w(-b) = w_{uplift}$ (see Fig. 6.4b) the following expression for the rotation at incipient uplift is derived:

$$\sin\theta_{uplift} = \frac{w_{bo} - w_{uplift}}{b} = \frac{w_{bo}}{b} \frac{k_v(b)}{k_m(b)} \qquad [6.16]$$

Substitution of Eq. 6.12 into Eq. 6.16 derives the following *uplifting criterion* for the angle of rotation:

$$\theta_{uplift} \;\cong\; \frac{N\,b}{2K_m} \;=\; \frac{M_{rigid}}{2K_m} \qquad [6.17a]$$

and therefore:

$$M_{uplift} \cong \frac{N\,b}{2} = \frac{M_{rigid}}{2} \qquad [6.18b]$$

According to the conventional model, the uplifting criterion of Eq. 6.15 is satisfied when $w(-b)=0$ meaning that at the uplift onset the footing edge reaches its initial position. On the contrary, from the proposed model uplifting occurs before the foundation corner point returns to its initial position. For a homogeneous soil profile the arising 'restitution' ratio is depending upon the footing geometry and the presence of shallow bedrock. In fact this ratio is approximately according to Eq. 6.12:

$$\frac{w_{bo}-w_{uplift}}{w_{bo}} = \frac{k_v(b)}{k_m(b)} = \frac{K_v b^2}{2K_m} \cong 0.32 \qquad [6.18]$$

which is non-zero in contrast to that of the conventional model ($w_{uplift}=0$). On the other hand, in terms of the conventional model the critical angle for incipient uplift is $\theta_{uplift}=\sin^{-1}\left(w_{bo}/b\right)$ or $\theta_{uplift}\cong N/K_v b = Nb/3K_m$ and therefore the uplifting moment is $M_{uplift}=N\,b/3=M_{rigid}/3$. Evidently, the conventional model underestimates the moment at incipient uplift by a factor of 1.5 in comparison to the 'exact' two-dimensional solution.

***Uplifting phase*:**

Once uplifting occurs the foundation area remaining in contact with the ground is gradually decreasing (see Fig. 6.4c). As a result the rocking response enters a non-linear regime even under purely elastic soil conditions. During the uplift mode, the moment of the foundation with respect to its midpoint is the sum of (a) the moment due to the contact pressures ($M_{p,v}$ and $M_{p,m}$) and (b) the moment ensued by the lateral movement of the superstructure ($P-\delta$ effects). In this way the foundation moment becomes:

$$M = M_{p,v} + M_{p,m} + M_{P-\delta} = \int_{b-2\beta}^{b} p_v(x)\, x \cos\theta \,\mathrm{d}x \; + \int_{b-2\beta}^{b} p_m(x,\theta)\, x \cos\theta \,\mathrm{d}x \; - \; N\, h \sin\theta \qquad [6.20]$$

It is reminded that $\beta$ is the half-width of the footing remaining in contact with the ground. We define $\xi$ the distance of a point in contact with the ground from the effective footing midpoint. In this case:

$$x = \xi + b - \beta \qquad [6.21]$$

The contact pressures of the effective footing on the basis of elastic soil behaviour are calculated with the *hypothesis of the incipient uplift*:

*The distribution of subgrade reactions along the footing due to combined vertical and moment loading once uplifting occurs is equal to that of a fictitious footing of width $2\beta$, which under the same combined loading is being at incipient uplift.*

A consequence of this hypothesis is that the centre of the effective footing at each step is the instantaneous rotation pole of the footing. This can be expressed by the following incremental equation:

$$\delta w_b = b\left(1-\lambda\right)\delta\theta \qquad [6.22]$$

Where $\lambda$ is the effective-to-initial footing width ratio $\left(\beta / b\right)$.

Now, the vertical displacement of the foundation $w_b$ can be derived by integration:

$$\int_{w_{bo}}^{w_b} \delta w_b = \int_{\theta_{uplift}}^{\theta} b\left(1-\lambda\right)\delta\theta$$

or

$$w_b = w_{bo} + b\left(1-\lambda\right)\theta - \lambda\theta \ln\frac{1}{\lambda} \qquad [6.23]$$

The latter equation provides the analytical relationship between the vertical displacement and the rocking angle of the footing over the elastic soil. The hypothesis of the incipient uplift allows for the superposition principle to be applied for the analytical calculation of the contact pressures developed along the effective footing:

$$p_v(\xi)=\frac{N}{\pi\beta\sqrt{1-\xi^2/\beta^2}} \quad \text{and} \quad p_m(\xi,\theta)=\frac{2M\xi}{\pi\beta^3\sqrt{1-\xi^2/\beta^2}} \tag{6.24}$$

By virtue of Eqs 6.21 and 6.24 the moment due to purely vertical loading for the uplifting footing yields:

$$M_{p,v}=\int_{-\beta}^{\beta}\frac{N(\xi+b-\beta)}{\pi\beta\sqrt{1-\xi^2/\beta^2}}\cos\theta\,\mathrm{d}\xi=\frac{N\cos\theta}{\pi}\int_{-\pi/2}^{\pi/2}(\beta\sin\omega+b-\beta)\,\mathrm{d}\omega=N\cos\theta\big(b-\beta\big) \tag{6.25}$$

This denotes that the moment $M_{p,v}$ is the product of the vertical reaction resultant times the distance from the effective footing centre to the footing midpoint. The moment of the foundation due to purely moment loading is:

$$M_{p,m}=\int_{-\beta}^{\beta}\frac{K_{m,eff}}{\pi\beta^3\sqrt{1-\xi^2/\beta^2}}\sin 2\theta\,\xi\,(\xi+b-\beta)\,\mathrm{d}\xi=\frac{K_{m,eff}\sin 2\theta}{\pi}\int_{-\pi/2}^{\pi/2}\left(\sin^2\omega+\sin\omega\,(\frac{b}{\beta}-1)\right)\mathrm{d}\omega$$

$$=\frac{K_{m,eff}\sin 2\theta}{\pi}\int_{-\pi/2}^{\pi/2}\left(\frac{1-\cos 2\omega}{2}+\sin\omega\left[\frac{b}{\beta}-1\right]\right)\mathrm{d}\omega=\frac{K_{m,eff}\sin 2\theta}{\pi}\frac{\pi}{2}\cong K_{m,eff}\,\theta \tag{6.26}$$

The equation above verifies the expression adopted for the subgrade stiffness due to moment loading. Finally, the total overturning moment of the uplifting foundation yields:

$$M=K_{m,eff}\,\theta+N\big(b-\beta\big)\cos\theta-Nh\sin\theta \tag{6.27}$$

However, the rocking stiffness of the effective footing is:

$$K_{m,eff} = \frac{\pi G \beta^2}{2(1-\nu)} = K_m \frac{\beta^2}{b^2} \quad [6.28]$$

By substituting Eq. 6.28 into Eq. 6.27 we finally get:

$$M = K_m \frac{\beta^2}{b^2} \theta + N(b-\beta)\cos\theta - Nh\sin\theta \quad [6.29a]$$

or

$$M = K_m \lambda^2 \theta + Nb(1-\lambda)\cos\theta - Nh\sin\theta \quad [6.29b]$$

In the finite element study of the uplifting response (Chapter 4) it was shown that the half-width of the effective footing $\beta$ is inversely proportional to the rotation $\theta$ as shown in Fig. 6.6:

$$\lambda = \frac{\beta}{b} = 1 \qquad \theta \le \theta_{uplift} \quad [6.30a]$$

$$\lambda = \frac{\beta}{b} = \frac{\theta_{uplift}}{\theta} \qquad \theta > \theta_{uplift} \quad [6.30b]$$

According to Eqs 6.29 and 6.30 the moment can be determined by a closed-form expression as a non-linear function of rotation. It is worthy of note that the above analytical procedure can be utilised to the computation of the moment: (a) in the *linear* domain where full-contact conditions are established, (b) in the *large-amplitude* region where the gradually amplified $P-\delta$ effects dominate the response, and (c) at *near-overturning* conditions where $\theta \cong \theta_c = \tan^{-1}(b/h)$. In the limiting case that the footing is supported by rigid soil it yields $\lambda = 0$ for any $\theta > 0$ and therefore Eq. 6.29 leads to the well-known moment–rotation relationship:

$$M = Nb\cos\theta - Nh\sin\theta = NR\sin(\theta_c - \theta) \quad [6.31]$$

While the analytical formulation of the foundation moment was based on a strip footing it can also be applied to any rectangular spread foundation where the direction of horizontal loading runs parallel to a normal axis of the foundation cross-section.

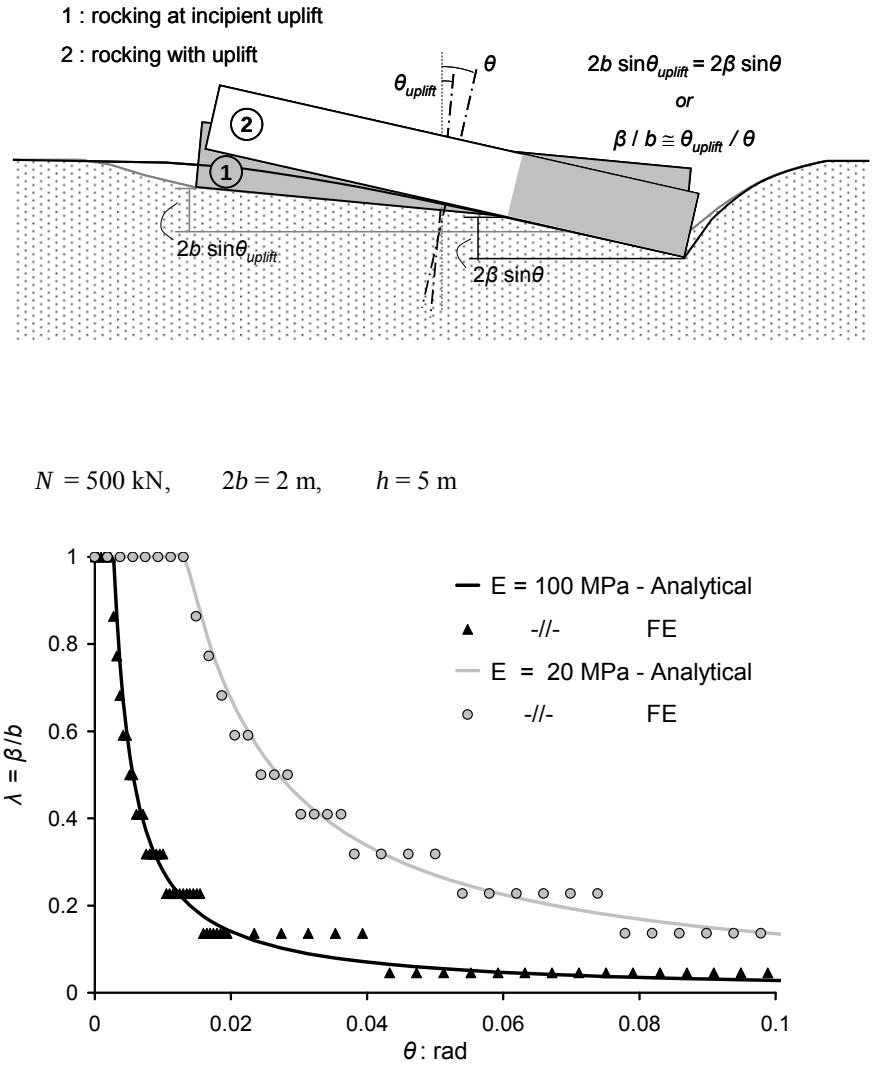


**Figure 6.6** Comparison of the numerical curves of the $\lambda-\theta$ relationship with the analytical prediction.

A comparison of the analytical calculation of the foundation moment and vertical displacement to the results of the finite element analysis is shown in Fig. 6.7 in form of $M-\theta$, $w-\theta$, and $M-w$ curves for a strip footing $(2b=2\text{ m},\ h=5\text{ m},\ N=500\text{ kN})$ on elastic soil layer over rigid bedrock $(E_1=20$ and $E_2$=100 MPa$)$. An excellent agreement between the analytical and the numerical method is achieved throughout the range of the rocking rotation.

$N = 500$ kN, $2b = 2$ m, $h = 5$ m

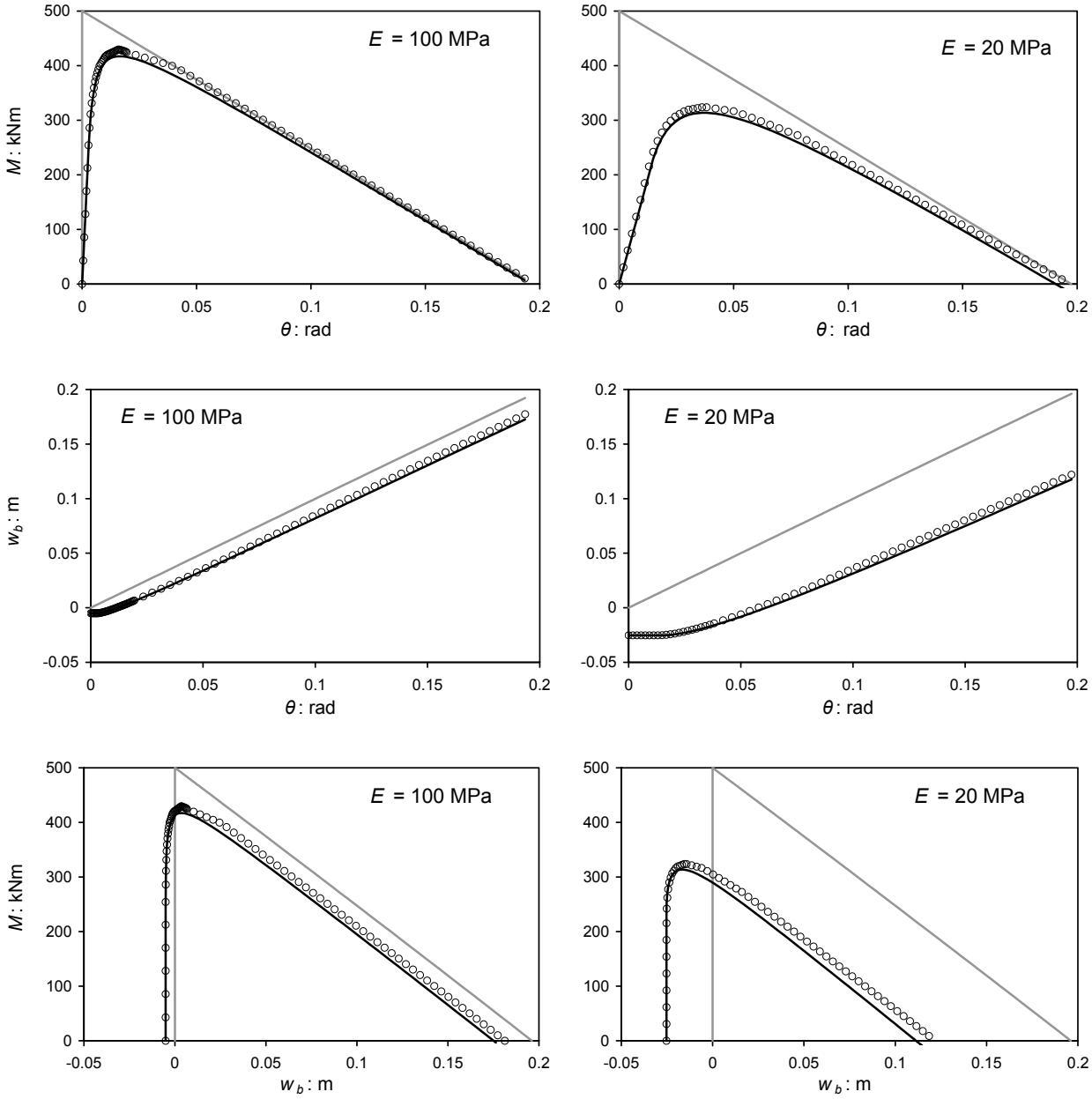


Analytical curves

FE curves

Rigid soil boundary

$$M(\theta) = K_m \lambda^2 \theta + Nb(1-\lambda)\cos\theta - Nh\sin\theta$$

$$w_b(\theta) = w_{bo} + b(1-\lambda)\sin\theta + \lambda\theta\ln(1-\lambda)$$

$$\lambda = \begin{cases} \theta_{uplift}/\theta\ , & \theta > \theta_{uplift} \\ 1\ , & \theta \le \theta_{uplift} \end{cases}$$

**Figure 6.7** Analytical curves of a rigid strip footing on elastic soil and comparison with two-dimensional finite element results.

***Moment capacity of the foundation*:**

During the uplift regime the foundation moment may be expressed explicitly as a function of the effective footing ratio $\lambda$ by substituting the rocking angle given by Eq. 6.30b to Eq. 6.29b:

$$M = M_{uplift}\left(2-\lambda-2\frac{Nh}{K_m\lambda}\right) \qquad [6.32a]$$

or without $P-\delta$ effects

$$M = M_{uplift}\left(2-\lambda\right) \qquad [6.32b]$$

The latter equation has also been presented by Crémer *et al.* (2002) extracted empirically from the results of a parametric numerical study.

In the foregoing it was pointed out that once uplifting initiates the foundation stiffness enters into a softening fashion which bounds the overturning moment to an ultimate value. This upper limit corresponds to the moment capacity of the foundation. It is well known that for the extreme case of an infinitely rigid soil this ultimate moment equals to the vertical load times the half-width of the footing. In reality though, soil deformations in the vicinity of the base edge are inevitable even when dealing with very stiff soils. Thus, soil compliance shifts the axis of the resultant vertical reaction towards the base centre, reducing the moment capacity of the foundation. For elastic soil conditions, the moment $M_u$ is the local maximum of the function $M = M(\theta)$ as defined in Eq. 6.29. Hence it can be calculated by the condition $\mathrm{d}M/\mathrm{d}\theta = 0$. For small angles of rotation (compared to the critical angle $\theta_c$) it is $\sin\theta \cong \theta$ and $\cos\theta \cong 1$. In this case Eq. 6.29 in combination with Eqs. 6.19 and 6.30 can be written:

$$M = K_m\lambda^2\,\theta + N\,b\left(1-\lambda\right) - N\,h\,\theta = -\frac{N^2b^2}{4K_m\,\theta} + N\,b - N\,h\,\theta \qquad [6.33]$$

The rotation at which the ultimate moment of the foundation occurs can be computed with derivation of Eq. 6.33 with respect to $\theta$:

$$\frac{\mathrm{d}M}{\mathrm{d}\theta}=\frac{N^2b^2}{4K_m\theta^2}-N\,h \qquad [6.34]$$

Therefore the angle that satisfies the equality $\frac{\mathrm{d}M}{\mathrm{d}\theta}=0$ is:

$$\theta_u=\sqrt{\frac{Nb^2}{4K_m\,h}}=\tan\theta_c\sqrt{\frac{Nh}{4K_m}} \qquad [6.35a]$$

and the moment at this point:

$$M_u=Nb\left(1-\sqrt{\frac{Nh}{K_m}}\right) \qquad [6.35b]$$

or

$$M_u=Nb\left(1-\frac{2\theta_u}{\tan\theta_c}\right)\cong Nb\left(1-2\frac{\theta_u}{\theta_c}\right) \qquad [6.35c]$$

We notice that when $\theta_u\to 0$ the ultimate moment approaches the rigid soil limiting value ($Nb$), while for $\theta_u\to\theta_c/2$ the moment $M_u$ tends to zero. This means that the locus of points $\left(\theta_u, M_u\right)$ tracks onto the median of the angle defined by the ordinate and the 'rigid' $M-theta$ softening line as portrayed in Fig. 6.8. The exact location of an ultimate point $\left(\theta_u, M_u\right)$ at this locus depends on the vertical load, the height of the mass-point and the soil-foundation rocking stiffness.

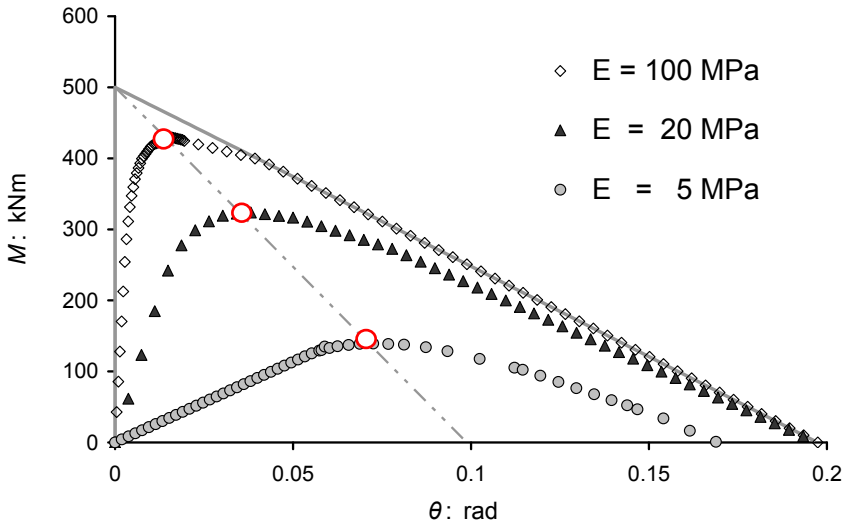


**Figure 6.8** Comparison of the numerical curves of the $\lambda-\theta$ relationship with the analytical prediction.

As shown in Chapter 3 for a one-story uplifting oscillator with a concentrated mass, the period parameter $T_p$ is:

$$T_p = 2\pi\sqrt{\frac{R}{g}} = 2\pi\sqrt{\frac{h}{g\cos\theta_c}} \qquad [6.36]$$

Moreover, when full-contact conditions are considered, the natural period of the rocking structure over elastic soil is:

$$T_m = 2\pi\sqrt{\frac{m\,h^2}{K_m}} = 2\pi\sqrt{\frac{N\,h^2}{g\,K_m}} \qquad [6.37]$$

The period ratio $T_m / T_p$ is then:

$$\frac{T_m}{T_p} = 2\sqrt{\frac{N\,h\cos\theta_c}{4K_m}} \cong 2\frac{\theta_u}{\theta_c} \qquad [6.38]$$

Hence, the ultimate moment of the foundation is rewritten:

$$M_u = Nb\left(1-\frac{1}{\sqrt{\cos\theta_c}}\frac{T_m}{T_p}\right) \cong Nb\left(1-\frac{T_m}{T_p}\right) \quad [6.39a]$$

or

$$M_u \cong Nb\left(1-\frac{p}{\omega_m}\right) \quad [6.39b]$$

The failure locus on the $N-M$ plane determined by Eq. 6.39 can be applied to any strip or rectangular foundation allowed to uplift on elastic soil. Nonetheless, it is very important on the estimate of the ultimate foundation moment as it incorporates the interplay of the two rocking modes of the structural system: (a) the linear component of rocking without uplift on elastic soil which is represented by the rocking period (frequency) and (b) the uplifting (non-linear) component of rocking on a rigid base represented by the period (frequency) parameter. These two simplified rocking systems are illustrated in Fig. 6.??. An interesting way of presenting Eq. 6.39 is portrayed in Fig. 7.??. The ratio of the ultimate to the uplifting moment is plotted as a function of the rocking period for different values of the period parameter.

### 6.3.2 Inelastic soil

The simplification of elastic soil behaviour allows for a tractable analytical calculation of the uplifting response. Excluding some cases of lightly loaded foundations $(\chi<0.2-0.3)$, yielding zones of the supporting soil emanating from the area underneath the foundation edges are often inevitable. This may lead to a 'visible' non-linear fashion of the moment-rotation relationship even under full-contact conditions. Moreover, once uplift initiates, soil material nonlinearity counterbalances the uplifting displacements and contributes to substantially non-linear foundation behaviour.

We consider again a rigid, strip footing of width $B=2b$ resting on the surface of a homogeneous half-space. Initially the footing is subjected to a vertical loading $N$. The vertical displacement of the footing (settlement) $w_{bo}$ is now a non-linear function of the applied load. Two analytical curves are

most suitable to describe the backbone $N-w$ curve according to the exponential and the hyperbolic law (Eqs 6.40a and b respectively):

$$N = K_v \frac{1-e^{-\psi w_b}}{\psi} \qquad [6.40a]$$

$$N = \frac{w_b}{\frac{1}{K_v}+\frac{1}{N_u}w_b} \qquad [6.40b]$$

Where $\psi = K_v / N_u$. In Fig. 6.9 the analytical $N-w$ curves are plotted in comparison with those calculated from finite element analysis of a strip footing $(2b = 2 \text{ m},\ h = 5 \text{ m})$ on homogeneous soil layer over rigid bedrock $(E = 100 \text{ MPa},\ s_u = 100 \text{ kPa})$.

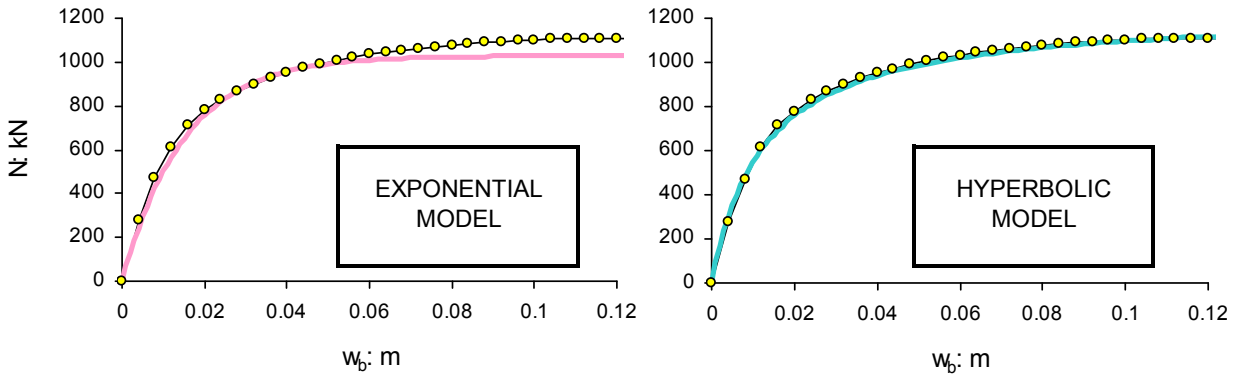


**Figure 6.9** Comparison of the exponential and the hyperbolic model with the finite element analysis in the calculation of the $N-w$ curve.

An excellent agreement is achieved for both models with the numerical results. According to the afore-discussed models the settlement at the end of this loading phase may be calculated as follows:

$$w_b = \frac{\ln(1-N/N_u)}{K_v/N_u} = -\frac{\ln(1-\chi)}{\psi} \qquad [6.41a]$$

$$w_b = -\frac{N_u}{K_v}\frac{1}{1-N_u/N} = -\frac{1}{\psi(1-1/\chi)} \qquad [6.41b]$$

The analytical calculation of the settlement with the exponential model has been successfully evaluated by Nova and Montrasio (1991) through experimental $N-w$ curves on sand.

At the second loading stage, a gradually increasing horizontal force is applied at the level of the superstructure mass (located at height $h$) leading to an overturning moment $M=Nh\cos\theta$ about the foundation centre. As in the elastic case uplift onsets whenever the subgrade reaction due to moment loading at a corner point $p_m$ reaches the initial vertical reaction $p_o$.

***Full-contact phase*:**

For sufficiently low levels of moment the confinement due to vertical loading ensures a full-contact condition at the interface. In contrast to the elastic case the strip is rocking about a point (rotation pole) which is not fixed at the centre of the base but shifts towards the unloading edge. This leftward (for a clockwise rotation) movement of the instantaneous pole is attributed to the plastification of the supporting soil underneath the loading edge of the footing. The larger the structural weight is, the more rapidly the pole moves towards the unloading edge. In the limiting case of $\chi\to 1$ the footing tends immediately to rotate about its unloading edge even under a very small overturning moment. In this case the vertical displacement (settlement) becomes:

$$w_b=-b\sin\theta \qquad [6.42]$$

On the other hand, for elastic soil behaviour $(\chi=0)$ the displacement $w_b$ prior to uplift initiation is zero.

The $M-theta$ curve at the full-contact phase may be calculated with the exponential or the hyperbolic model as follows (Eqs 6.43a and b respectively):

$$M=K_m\frac{1-e^{-\psi\theta}}{\psi} \qquad [6.43a]$$

$$N = \frac{\theta}{\frac{1}{K_m} + \frac{1}{M_u}\theta} \qquad [6.43b]$$

Where $\psi = K_m / M_u$ and $M_u$ is the ultimate moment of the foundation if uplift is prevented. The afore-mentioned analytical models are evaluated in the calculation of the $M-theta$ relationship through finite element analysis for a strip footing $\left(N = 500 \text{ kN},\ 2b = 2 \text{ m},\ h = 5 \text{ m}\right)$ on homogeneous soil layer over rigid bedrock $\left(E = 100 \text{ MPa},\ s_u = 100 \text{ kPa}\right)$ as plotted in Fig. 6.10. Both models seem to capture the basic features of the backbone curve. Nevertheless, a slightly closer fit is achieved with the exponential model throughout the loading sequence.

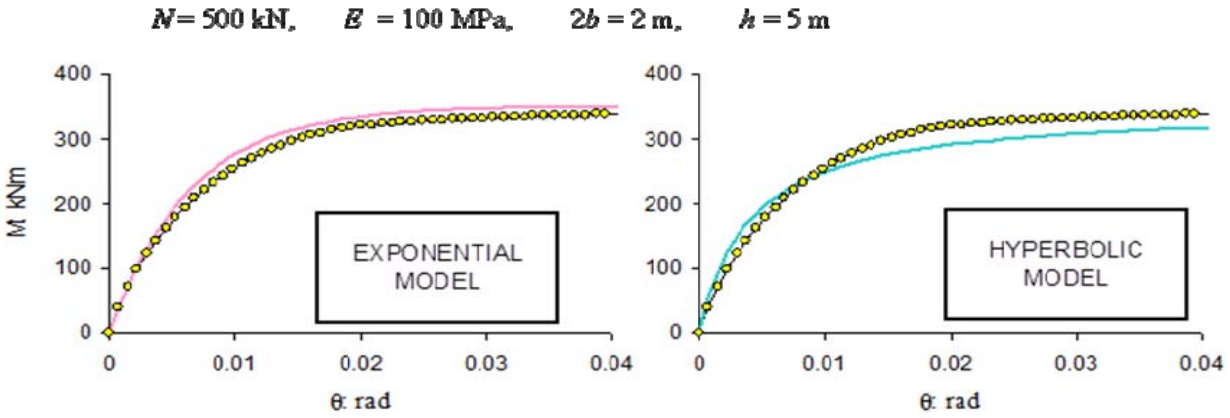


**Figure 6.10** Comparison of the exponential and the hyperbolic model with the finite element analysis in the calculation of the $M-theta$ curve.

### *Uplift initiation*:

As in the elastic case, the footing marginally lifts off the supporting soil when the uplifting criterion described with Eq. 6.15 is satisfied. By applying the exponential law to the $p-w$ curve of the unloading edge, the following uplifting criterion is obtained:

$$p_u\left[1 - e^{-\frac{k_v(-b)}{p_u}w_{vo}}\right] = p_u\left[1 - e^{-\frac{k_m(-b)}{p_u}\left(w_{bo} - w_{uplift}\right)}\right]$$

or $$e^{-\frac{k_v(-b)}{p_u}w_{bo}} = e^{-\frac{k_m(-b)}{p_u}\left(w_{bo}-w_{uplift}\right)}$$

and finally $$\frac{k_v(-b)}{k_m(-b)} = \frac{w_{vo}-w_{uplift}}{w_{vo}} \qquad [6.44]$$

where $k_v$ and $k_m$ are the elastic stiffnesses as determined above.

From the latter equation it is derived that the critical rotation for marginal uplift is equal to the 'elastic' one:

$$\theta_{uplift} \cong \frac{Nb}{2K_m} \qquad [6.45]$$

The moment at incipient uplift is then derived by substituting Eq. 6.45 to the exponential law for the $M-theta$ relationship:

$$M_{uplift} = M_u\left(1-e^{-\frac{K_m}{M_u}\frac{Nb}{2K_m}}\right)$$

or $$M_{uplift} = M_u\left(1-e^{-\frac{Nb}{2M_u}}\right) \qquad [6.46]$$

Equivalently in the dimensionless $N-M$ plane:

$$\frac{M_{uplift}}{M_u} = \left(1-e^{-\frac{1}{2(1-\chi)}}\right) \qquad [6.47]$$

Evidently, the uplifting moment is not anymore a linear function of the vertical load $N$ but exhibits a softening behaviour as $N$ increases. As the failure curve in the $N-M$ plane is described with a parabola, it is expected that a threshold value of $N$ exists where the uplift and failure curves intersect and beyond which no uplifting occurs.

***Uplifting phase*:**

Once uplifting occurs the foundation area remaining in contact with the ground is gradually decreasing. However the magnitude of uplifting (i.e. expressed with the effective footing ratio $\lambda$) is limited with the increase in the structural weight (expressed with the load factor $\chi$).

The vertical displacement $w_b$ in the limiting cases of $\chi = 0$ and $\chi = 1$ is given by Eqs 6.23 and 6.42 respectively. From these two states of response, linear interpolation may provide the vertical displacement $w_b$ of a load factor $\chi$ as follows:

$$w_b \cong w_{bo} + b(1-\lambda)\theta - \lambda\theta \ln\frac{1}{\lambda} - \chi b\theta \qquad [6.48a]$$

or

$$w_b \cong w_{bo} + b(1-\lambda-\chi)\theta - \lambda\theta \ln\frac{1}{\lambda} \qquad [6.48b]$$

During the uplift mode the moment of the foundation with respect to its midpoint is the sum of (a) the moment due to the contact pressures ($M_{p,v}$ and $M_{p,m}$) and (b) the moment ensued by the lateral movement of the superstructure ($P-\delta$ component):

$$M = M_{p,m} + M_{p,v} + M_{P-\delta} \qquad [6.49]$$

The components of the moment associated with the eccentricity of the resultant reaction $N\left(M_{p,v}\right)$ and the $P-\delta$ effects $M_{P-\delta}$ are the same with those of the elastic case.

For the analytical calculation of the moment component associated with the antisymmetric part of the external loading $\left(M_{p,m}\right)$ calculation of soil reactions due to that loading and integration along the effective footing is required. For inelastic soil conditions however, this method leads to complex integral expressions of the resultant moment even when simple analytical $p-w$ curves are employed (for example the exponential law). More than that, the shift of the rotation pole towards the edge of

the footing, further complicates the decoupling of the developed soil reactions into symmetric and antisymmetric components. An alternative approximate method to calculate the moment component $M_{p,m}$ may arise through the extrapolation of the linear $M-\lambda$ correlation extracted for elastic soil conditions.

This linear trend of the $M-\lambda$ correlation is confirmed by the numerical results plotted in Fig. 6.11. In addition, the effective footing ratio $\lambda$ must satisfy: (a) the limiting case of elastic soil $(\chi=0)$ and (b) the limit state condition $\lambda=\chi$. The exponential law of the effective footing ratio $\lambda$ with respect to the rocking angle which satisfies both limitations is given by the following equation:

$$\lambda=\frac{\theta_{uplift}(1-\chi)+\chi\theta}{\theta} \qquad [6.50]$$

Numerical validation of the latter equation through nonlinear finite element analysis of rocking response is presented in Fig. 6.11. Eventually, the moment of the foundation for inelastic soil conditions becomes:

$$M=K_m\left(\frac{\lambda-\chi}{1-\chi}\right)^2\theta+Nb(1-\lambda)\cos\theta-Nh\sin\theta \qquad [6.51]$$

Eqs 6.50 and 6.51 comprise the analytical expression of the foundation moment as a non linear function of the rocking rotation for the general case of inelastic soil.

A comparison of the analytical calculation of the foundation moment and vertical displacement to the results of the finite element analysis is shown in Fig. 6.12 for a strip footing $(N=500\text{ kN},\ 2b=2\text{ m},\ h=5\text{ m})$ on inelastic soil layer over rigid bedrock $(E=100\text{ MPa},\ s_u=100\text{ kPa})$. A close agreement of the analytical results to those obtained from numerical analysis is attained throughout the range of the rocking rotation.

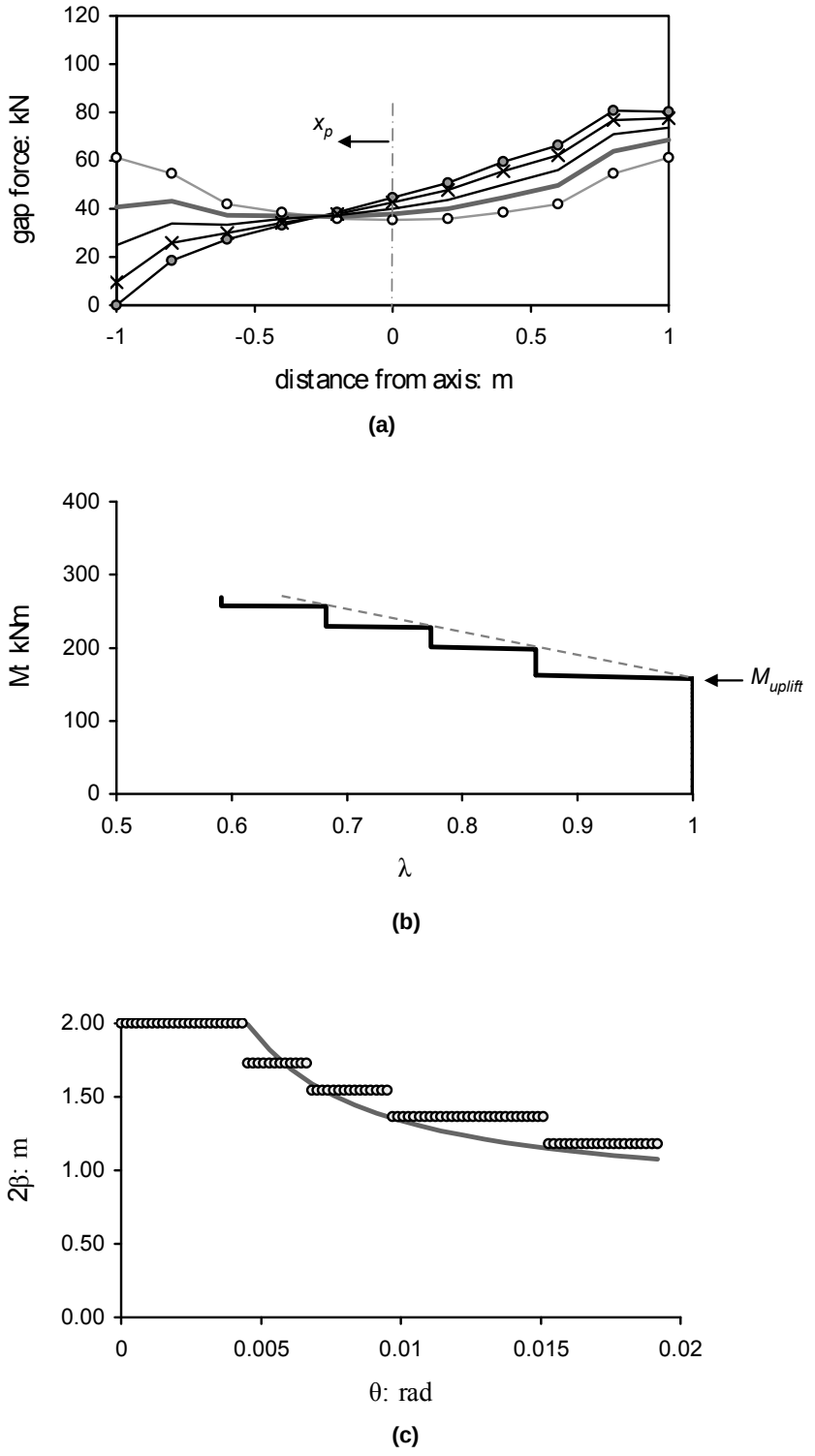


**Figure 6.11** Nonlinear rocking response of a strip footing on inelastic soil, calculated with two-dimensional finite element analysis: (a) distribution of soil reactions in characteristic increments prior to uplift, (b) $M-\lambda$ correlation, and (c) the effective width $2\beta$ with respect to the rocking angle $\theta$ and comparison with the analytical prediction.

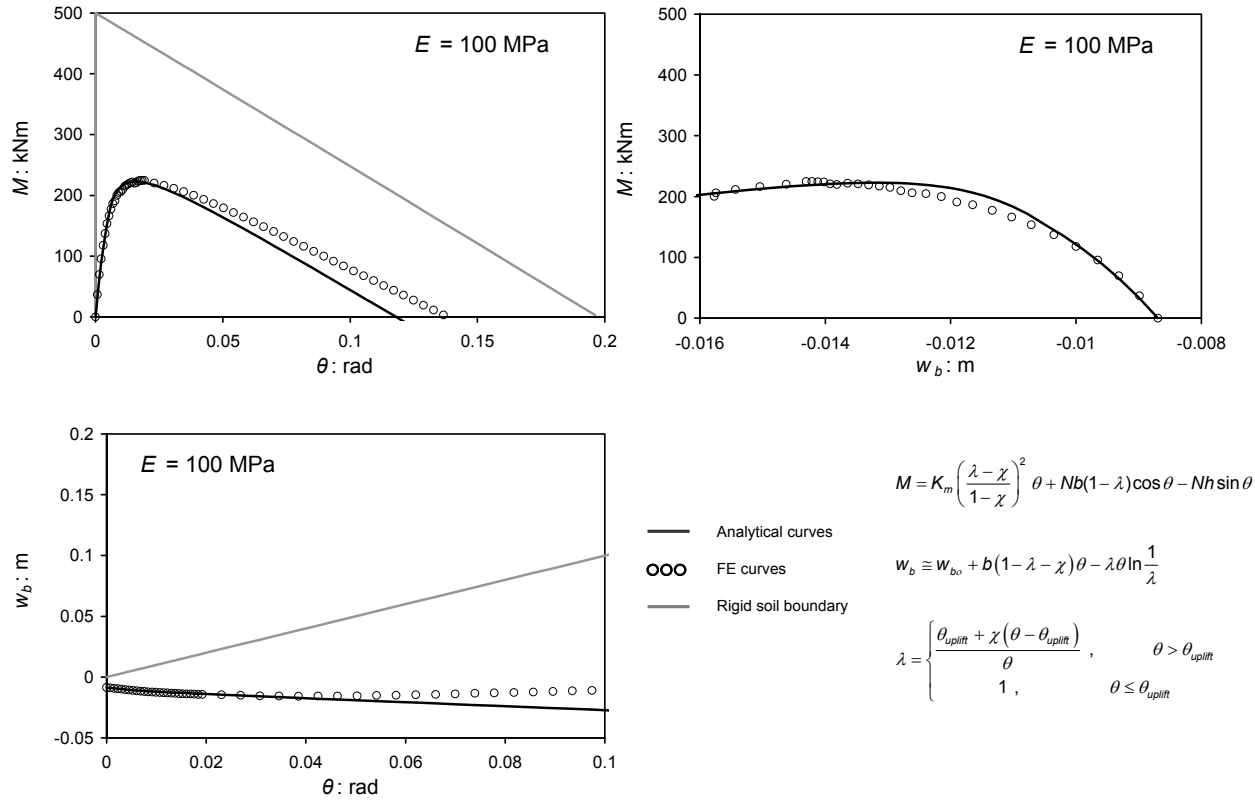


**Figure 6.12** Analytical curves of a rigid strip footing on inelastic soil and comparison with two-dimensional finite element results

## 6.4 ULTIMATE MOMENT CAPACITY

As shown in the foregoing discussion, the $M-\theta$ backbone curve follows a softening fashion due to geometric and soil material nonlinearities. As a result the moment developed by the foundation is bounded by an ultimate value $M_u$. In the optimum case of a rigid supporting soil the foundation undertakes the maximum possible moment which corresponds to the vertical load $N$ times the half-width of the footing $b$. In common geotechnical applications however soil compliance and plastification of the supporting soil result in substantial reduction of the ultimate moment. Moreover, further decrease in $M_u$ is expected in tall structures due to $P-\delta$ effects. In the general case the ultimate moment of the foundation may be derived analytically as the local maximum of Eq. 6.51. To this extent derivation of Eq. 6.51 yields:

$$\frac{dM}{d\theta} = \frac{N^2 b^2}{4K_m \theta^2} - Nh = 0 \qquad [6.52]$$

The rocking angle $\theta_u$ at which the ultimate moment is attained is therefore:

$$\theta_u = \tan\theta_c \sqrt{\frac{Nh}{4K_m}} = 0 \qquad [6.53]$$

Eventually, the ultimate moment is:

$$M_u = Nb\left(1 - \sqrt{\frac{Nh}{K_m}}\right) \qquad [6.54a]$$

or

$$M_u = Nb\left(1 - \frac{2\theta_u}{\tan\theta_c}\right) \cong Nb\left(1 - 2\frac{\theta_u}{\theta_c}\right) \qquad [6.54b]$$

After some algebraic manipulations, the ultimate moment may be expressed as a function of the nonlinear parameters $\eta = \sqrt{\frac{Nh}{K_m}}$ and $\chi$, which represent respectively geometrical and soil material nonlinearities.

$$M_u = Nb(1-\eta)(1-\chi) \qquad [6.55a]$$

In dimensionless form:

$$\frac{M_u}{N_u B} = \frac{\chi}{2}(1-\eta)(1-\chi) \qquad [6.55b]$$

$$\hat{m} = \frac{\hat{n}}{2}(1-\eta)(1-\hat{n}) \qquad [6.55c]$$

Eqs 6.55 provide the analytical expression of the failure curve in the nondimensional $\hat{n}-\hat{m}$ plane when $P-\delta$ effects are considered. Remark that for $\eta=0$ (i.e. no $P-\delta$ effects are considered) the failure curve reduces to that calculated with the conventional Winkler model (Eq. 6.6b).

## 6.6 APPLICABILITY and LIMITATIONS

Non linear features of the rocking response of tall structures founded on shallow foundations are investigated. Principally, based on conventional Winkler modelling, interaction curves in the nondimensional $N-M$ plane were calculated for failure (overturn) as well as incipient uplift and soil yield. A perfectly symmetric response is achieved about the vertical axis at $\chi=0.5$. At this point the optimum foundation behaviour in terms of the moment ultimate capacity is obtained. To highlight the induced nonlinearities in the large-displacement domain, a macroscopic modelling of the soil–foundation system was developed. In this respect analytical equations for the overturning moment and the vertical displacement were extracted as a function of the rocking angle (a) for elastic soil, and (b) for inelastic soil. From the latter case, analytical equation of the failure curve in the nondimensional $N-M$ plane was obtained, incorporating both geometric and material nonlinearities.

*Chapter 7:*

# Analysis of the overturning response of slender structures

## 7.1 INTRODUCTION

The nonlinear features of rocking and uplifting behaviour of a shallow foundation under static and dynamic conditions have been investigated in depth in the preceding chapters. When dealing with slender structural systems subjected to strong seismic excitation however, rocking vibrations may lead to overturning under certain circumstances. In case of rigid or stiff soil conditions toppling of a shallow foundation is attributed to the exceedance of the gravitational (resisting) moment $\left(\cong N\,b\right)$ due to large uplifting. On the other hand, for a foundation on soft soil, overturning failure is usually the result of the loss of strength and the excessive yielding of the supporting soil under large overturning moment. In the former case overturning under a seismic excitation is a sudden and abrupt type of foundation failure associated with the dynamic rocking characteristics of the structural system. In the latter case 'seismic' overturning can be interpreted as a conventional geotechnical failure which is gradually developed and can be described with a 'pseudostatic' mechanism.

The discovery on the ground surface of slender blocks toppled after an earthquake has for many years provided upper-bound and lower-bound estimates of the peak ground acceleration. The fallacy that the acceleration needed to just overturn a block is the one obtained from moment equilibrium between the statically applied inertia force and the weight of the block (see Eq. 3.1), has prevailed for nearly a century and led to the establishment of unrealistically low levels of ground acceleration (of the order of 0.05 g to 0.10 g, even in areas of high seismicity). In fact, much greater acceleration levels are needed for overturning under seismic shaking, especially for large blocks and at high frequencies.

Ironically, this was already known (even if incompletely) as early as 1893 (Milne & Omori), while by 1927 Kirkpatrick had published a simple formula for estimating the 'dynamic' overturning acceleration, which captured the role of the basic problem parameters with sufficient degree of realism. In the subsequent 40 years, the lack or scarcity of accelerographs prompted many researchers and earthquake engineers to study the overturning behaviour of slender bodies. However, the dynamic character of the overturning behaviour was not widely understood by the engineering community until Housner's (1963) publication, in which he derived overturning criteria and showed the importance of both frequency of excitation and size of structure. In recent years the subject of overturning of blocks and structures under seismic excitation has received renewed attention. Makris and Roussos (1998) and Anooshehpoor *et al.* (1999), in particular, focused on the transient response of rigid blocks under near-fault ground shaking. They found that distinguishable long-duration pulses inherent to such shaking may be particularly detrimental to the rocking response of slender structures. Many examples of such pulses have been uncovered in near-fault records of recent Ms 6.5 earthquakes, such as the Imperial Valley 1979, Erzincan 1992, Northridge 1994, Kobe 1995, Kocaeli 1999, and Chi-Chi 1999. These pulses are the result of two effects: the 'forward rupture directivity' effect and 'permanent offset' (or 'fling') effect (Somerville 2003, Hisada & Bielak 2003).

In light of the above we investigate the overturning potential of near-fault ground motion, represented for simplicity and clarity with the following idealised pulses: the Ricker-wavelet, the (truncated) T-Ricker wavelet, the one-cycle sinus, the one-cycle cosinus, and the rectangular half-cycle pulse. Their time histories are plotted in Fig. 7.1. Time histories of recent earthquake records have been also implemented in the analysis. Numerical and analytical solutions of the rocking response are utilised: (a) to derive lower-bound estimates of the overturning amplitude, and (b) to demonstrate how sensitive the overturning behaviour is not only to the intensity and frequency content of the base motion, but also to the presence of strong pulses, to their detailed sequence, and even to their asymmetry. In so doing, *overturning acceleration* and *rotation* spectra are introduced as an efficient tool to quantify the overturning response and to provide criteria for marginal toppling.

Although emphasis is given on the overturning over a rigid soil, the effect of soil compliance is also examined in view of both elastic and inelastic soil behaviour. Rocking and overturning response on a rigid soil is calculated through explicit integration of the governing equation of motion (Eq. 3.2 or 3.50 for a rigid or flexible structure respectively), whereas for a rocking structure on deformable soil, two-dimensional finite element analysis is employed. In any case lower-bound estimates of the overturning amplitude are calculated through a trial-and-error procedure.

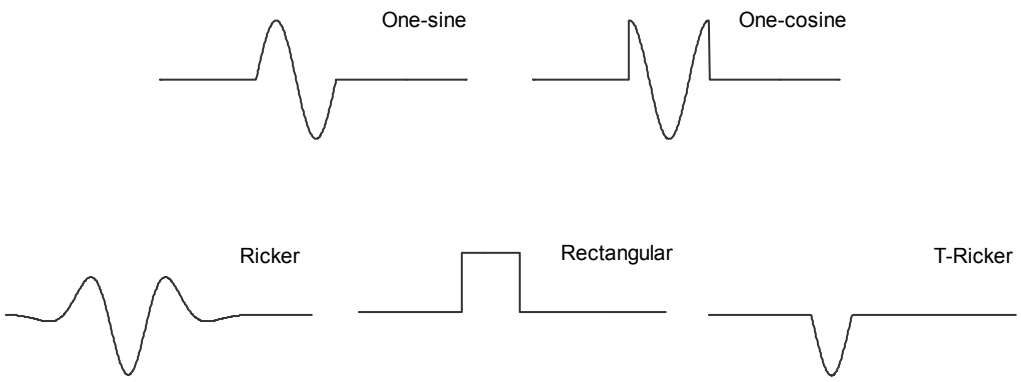


**Figure 7.1** Idealised pulses utilised to represent near-fault ground motion.

## 7.2 OVERTURNING on RIGID SOIL

### 7.2.1 Rigid structure

We consider first the rigid rectangular block shown in Fig. 3.1, which is subjected to horizontal shaking. For small levels of the ground acceleration $a_g = a_g(t)$ the moment of the inertia force with reference to the foundation midpoint ($ma_g h$) does not exceed the restoring, gravitational moment ($mgb$). In this regime, the block remains at rest with respect to the ground. As soon as the ultimate moment $mgb = Nb$ is reached uplifting initiates and the block is set to rocking motion. This peak value of the resisting moment is reached instantaneously at the onset of uplift ($\theta = 0$) and from then

on the moment is gradually decreasing due to $P-\delta$ effects. On the basis of a pseudo-static approach, once uplifting about the corner point initiates, the body will unavoidably overturn. In other words, the critical acceleration for uplifting $a_c$ is identical to the minimum required to *statically* overturn the block ($=b/h$ in units of g). On the contrary, under a dynamic base excitation reaching $a_c$ simply initiates rocking motion. Whether the block will safely undergo rocking or eventually overturn depends on its size and slenderness as well as the kinematic characteristics and intensity of ground shaking.

The state-space formulation of a rocking system driven by a one-cycle sinus pulse is:

$$\dot{\theta}=\phi=f(\theta,\phi,\tau) \qquad [7.1a]$$

$$\dot{\phi}=p^2\sin\left(\operatorname{sgn}\theta\theta_c-\theta\right)+\ddot{x}_{go}\sin\tau=g(\theta,\phi,\tau) \qquad [7.1b]$$

$$\dot{\tau}=\omega_E=h(\theta,\phi,\tau),\quad 0<\tau<2\pi \qquad [7.1c]$$

where $\tau=\omega_E t$ is the dimensionless time. At $\tau_0=2\pi$ the base excitation expires and the nonlinear system enters into the free vibration regime with initial conditions $\left(\theta_0,\phi_0\right)$. For any $\tau<2\pi$ there are no equilibrium points since it is always $\dot{\tau}\neq 0$. Additionally, due to the limited duration of the forced system it cannot be identified an unbounded trajectory representing critical instability. It may be generalised that *for a structure subjected to a transient base motion, critical overturning may occur only in the free vibration regime.* As discussed in Chapter 3, critical overturning in the free vibration regime is associated with a trajectory which is attracted by the heteroclinic orbit and passes through equilibrium point $\left(\theta_c,0\right)$ (see also Fig. 3.6). The phase plane of a slender rocking block $\left(2b=1\text{m},\ \ 2h=5\text{m}\right)$ is revisited in Fig. 7.2 with identified stable and unstable areas separated from the heteroclinic orbit. It is notable that the unstable area may be subdivided into (a) an area where overturning occurs without any impact in the free vibration regime and (b) an area where overturning occurs after an impact (at the instant $t_i$) in the free vibration regime.

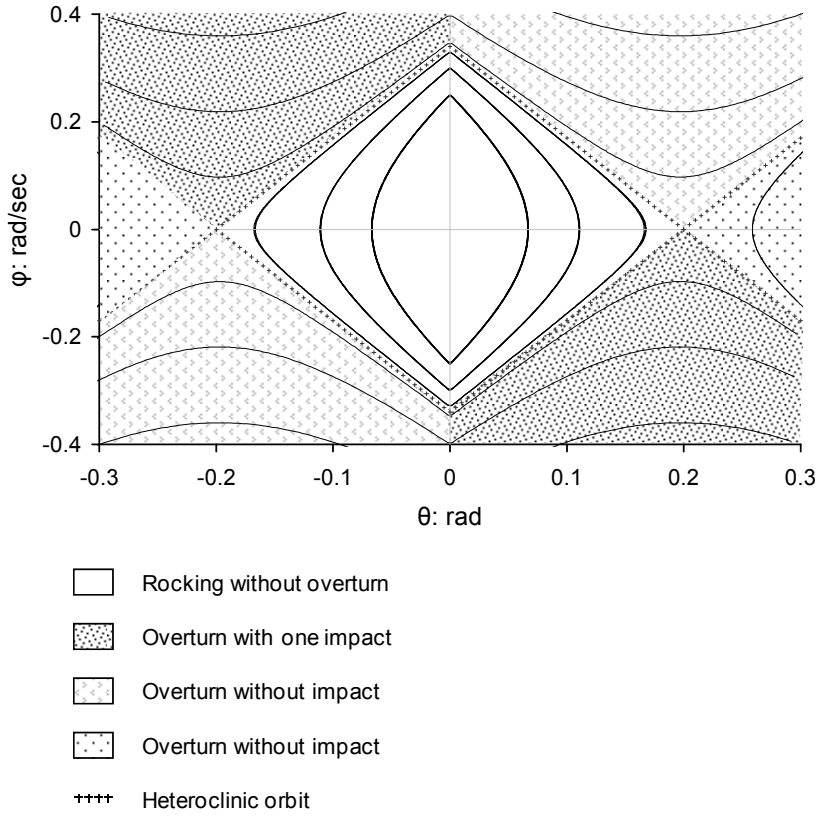


**Figure** 7.2 Phase plane of a rocking block with identified stable and unstable areas $\left(2b = 1 \text{ m},\ 2h = 5 \text{ m}\right)$.

Along the heteroclinic orbit the total energy (i.e. kinetic and potential) is preserved. Hence, for the points of (i) impact $\left(0, \dot{\theta}(t_i)\right)$ $\left[\text{only kinetic energy};\ \frac{1}{2}J_o\dot{\theta}(t_i)^2\right]$ and (ii) saddle equilibrium $\left(\theta_c, 0\right)$ $\left[\text{only potential energy};\ mgR\left(1-\cos\theta_c\right)\right]$ preservation of energy gives:

$$\dot{\theta}(t_i)^2 = 2p^2\left(1-\cos\theta_c\right) \qquad [7.2a]$$

or

$$\dot{\theta}(t_i) = \pm p\sqrt{2\left(1-\cos\theta_c\right)} \qquad [7.2b]$$

The impact points of the heteroclinic orbit can be calculated according to Eq. 7.2b. This equation is also a criterion for marginal overturning when an impact occurs during free vibration.

The potential of the heteroclinic orbit $\left(\mathcal{H} = E/J_o\right)$ is:

$$\mathcal{H} = p^2 = \frac{1}{2}\dot{\theta}^2 + p^2 \cos\left(\operatorname{sgn}\theta\theta_c - \theta\right) \qquad [7.3]$$

It yields that an unstable trajectory will start from the point $\left(\theta_0, \phi_0\right)$ if $\mathcal{H}_0 > p^2$. Accordingly, for a stable trajectory an initial condition $\left(\theta_0, \phi_0\right)$ with $\left(\mathcal{H}_0 < p^2\right)$ is necessary. From Eq. 7.3 the heteroclinic orbit can be determined:

$$\dot{\theta} = \pm p\sqrt{2\left[1 - \cos\left(\operatorname{sgn}\theta\theta_c - \theta\right)\right]} \qquad [7.4]$$

Positive (negative) sign in this equation corresponds to an orbit that approaches (departs from) the equilibrium point.

Linearisation of the response in the neighbourhood of the equilibrium point $(\theta_c, 0)$ denotes that the limit cycle close to this point tracks on the instable manifold $\mathbf{v} = c_2 e^{-pt}\mathbf{v_2}$, and therefore:

$$e^{-pt} = 0 \qquad [7.5]$$

The latter equation indicates that the rocking block approaches the equilibrium point (i.e. critical overturning) asymptotically at a theoretically infinite amount of time: $pt \to \infty$. This conclusion is well established in the qualitative analysis of nonlinear systems (otherwise uniqueness of solutions would be violated) and leads to the following overturning criterion:

$$t \to \infty \quad \text{and} \quad \left(\theta, \phi\right) = \left(\pm\theta_c, 0\right) \qquad [7.6]$$

For sufficiently slender bodies linearisation can be extrapolated along the heteroclinic orbit. In this case Eq. 7.2b and Eq. 7.4 are simplified respectively:

$$\dot{\theta}(t_i) = \pm p\,\theta_c \qquad [7.7]$$

$$\dot{\theta} = \pm p\left(\operatorname{sgn}\theta\theta_c - \theta\right) \qquad [7.8]$$

For critical overturning under a pulse-type motion the state variables $\left(\theta,\dot{\theta}\right)$ must satisfy Eq. 7.8 at the onset of free-vibration regime (i.e. at $t = T_E$) as the point $\left(\theta_{t=T_E},\dot{\theta}_{t=T_E}\right)$ must lie on the heteroclinic orbit. In this way, Eqs 7.6 and 7.8 summarise the conditions of critical overturning. In case of overturning with impact after excitation expires it is evident that Eq. 7.7 can be also implemented instead of Eq. 7.8. These equations together with a closed-form solution of the governing equation of motion allow for analytical estimate of the minimum overturning amplitudes.

The aforediscussed findings are depicted qualitatively in the phase portrait of Fig. 7.3.

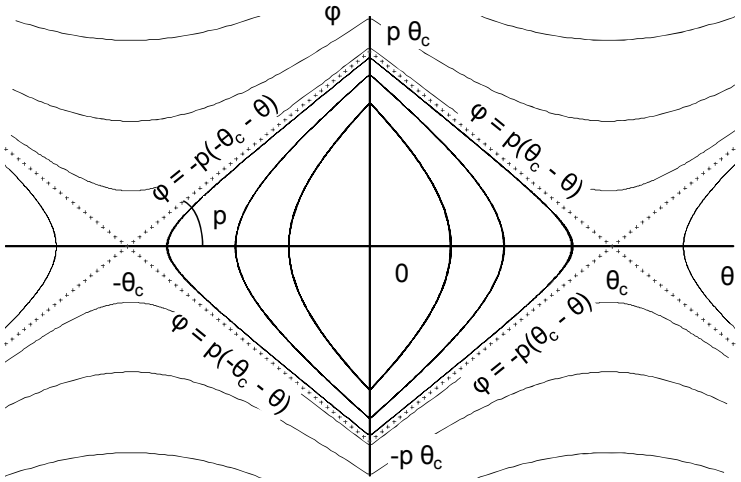


**Figure 7.3** Phase plane of a linearised rocking block; Analytical calculation of heteroclinic orbits, impact, and equilibrium points.

The overturning criterion described with Eq. 7.5 was originally extracted by Anooshehpoor *et al.* (1999). In that study it was correctly stated for the first time that a block at the instant of critical overturning must have zero angular velocity, however it was not considered that this condition should occur at theoretically infinite time. Makris and Zhang (1999) presumed that both Eq. 7.6 (in the form of $\ddot{\theta}\left(t_\infty\right) = 0$) and Eq. 7.8 should exist at critical overturning and showed that a one-cycle trigonometric pulse may overturn a block either after one impact (*mode 1*) or without impact at all

(*mode 2*). A 'safe region' emerges between the two modes, meaning that while the block overturns for a certain level of shaking, it surprisingly remains standing when the amplitude increases. This counter-intuitive conclusion is elucidated graphically through the following numerical example. The rigid block discussed above $\left(2b=1\,\text{m},\ \ 2h=5\,\text{m}\right)$ is set on rocking under a one-sine pulse of $T_E=0.8\,\text{sec}$ for different levels of shaking. The calculated trajectories in the phase plane are presented in Fig. 7.4 together with the time-histories of response (non-linear formulation).

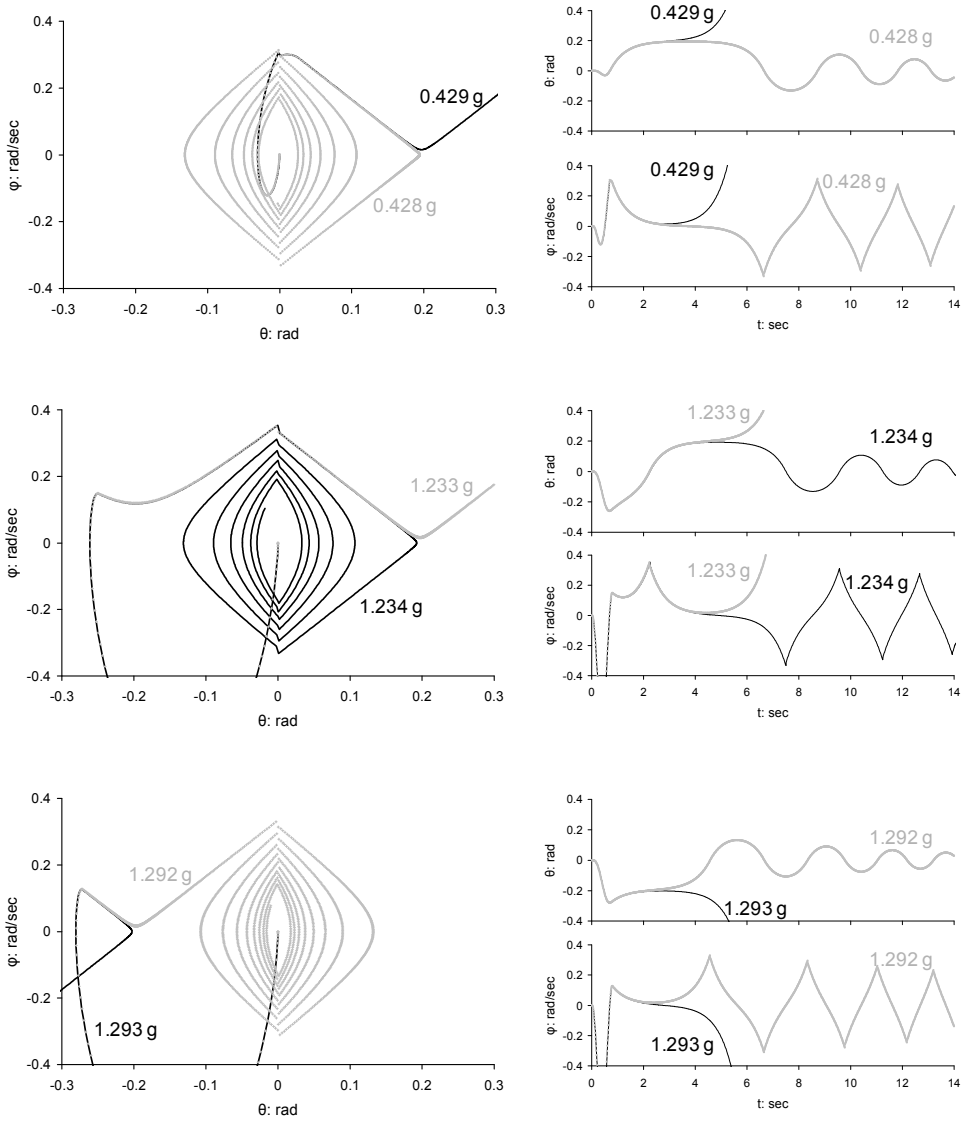


**Figure 7.4** Critical stable and unstable solutions of the rocking block $\left(2b=1\text{ m},\ 2h=5\text{ m}\right)$ under a one-sine pulse of $T_E=0.8\,\text{sec}$.

The block safely experiences rocking motion for acceleration amplitudes lower than 0.428 g whereas it marginally overturns after an impact for a $PGA$ of 0.429 g. The acceleration is further increased gradually up to 1.233 g and the block still overturns after an impact. However for acceleration amplitude of 1.234 g the block undergoes rocking without toppling. Eventually, when the acceleration reaches 1.293 g overturning occurs towards the opposite direction (without impact).

***Block size and excitation frequency*:**

The major outcome of the nonlinear nature of rocking motion is that for a specific type of ground motion, the required acceleration for overturning is a sensitive function of both the block size and the excitation frequency. This has been recognized by many researchers since more than a century (Milne and Omori 1893). Eighty years ago, Kirkpatrick (1927), assuming small rotations of slender structures, was the first to quantify the effects of the two afore mentioned parameters on the overturning response. For a sinusoidal excitation he derived analytically the necessary acceleration for overturning:

$$a_{over} = \frac{b}{h}\sqrt{1+\left(\frac{\omega_E}{p}\right)^2} \qquad [7.9]$$

Housner (1963) studied thoroughly the overturning response under pulse-type and white-noise excitation and re-derived Eq. 7.9 for the case of a half-sine pulse. This simplified formula is a good approximation of the exact solution for steady-state harmonic excitation. However, for the case of a half-sine pulse it was based on a conceptually incorrect overturning criterion [$\theta(t) = \theta_c$ when the pulse expires]. Using trigonometric pulses Makris and Roussos (1998) unveiled the detrimental role of long-duration pulses inherent in near-fault ground shaking. In this study it was shown that Housner's overturning criterion is non-conservative and the overturning amplitude for a sine (half or full cycle) and cosine pulse excitation can be fitted with the following linear trends (Eqs 7.10a, 7.10b, and 7.10c respectively):

half-sine pulse: $$a_{over,half\text{-}sine} = \frac{b}{h}\left(1+\frac{\omega_E}{2p}\right), \qquad \frac{\omega_E}{p} < 3 \qquad [7.10a]$$

one-sine pulse: $$a_{over,sine} = \frac{b}{h}\left(1+\frac{\omega_E}{6p}\right), \qquad \frac{\omega_E}{p} < 3 \qquad [7.10b]$$

one-cosine pulse: $$a_{over,cosine} = \frac{b}{h}\left(1+\frac{\omega_E}{4p}\right), \qquad \frac{\omega_E}{p} < 3 \qquad [7.10c]$$

Revisiting the solution of Spanos and Koh (1984) for the linearised system under harmonic excitation, Makris and Zhang (1999) derived a transcendental equation to calculate analytically the minimum overturning acceleration $a_{over}$ under a *one-sine* pulse for both modes. In the same study, they utilised this equation to calculate minimum acceleration levels for different values of the excitation frequency and derive the *overturning acceleration spectrum*. Within the limits of the linear approximation, the overturning acceleration spectrum can be normalised for a specific value of the coefficient of restitution as plotted in Fig. 7.5 for $r = 0.8$. Overturning accelerations computed numerically in the present study are also portrayed in the same graph.

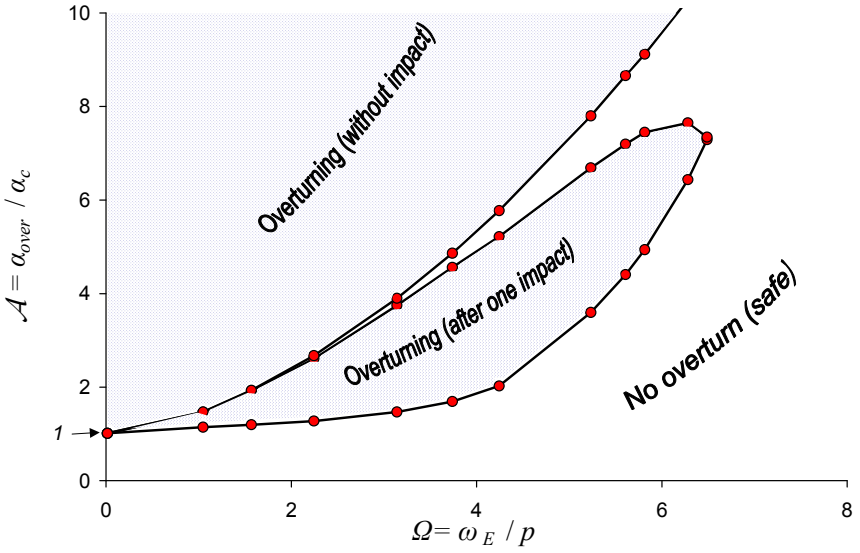


**Figure 7.5** Overturning amplification ratio (i.e. ratio of dynamic overturning acceleration to the pseudostatic overturning acceleration) for slender blocks under a one-sine pulse excitation computed by: (i) numerical integration of equation of motion (circles) and (ii) the analytical formula derived by Makris and Zhang (solid lines). The coefficient of restitution is 0.8.

Evidently, increasing the excitation frequency $\omega_E = 2\pi f_E$ and the size of the block (i.e. decreasing the parameter $p$) affects favourably the overturning response. It is notable that for sufficiently high frequency pulses the required acceleration for toppling can be substantially larger than the critical static value $a_c = b/h$. As an example, for excitation period of $0.3\,\text{sec}$ and block diameter of $0.5\,\text{m}$ the frequency ratio is $\Omega = \omega_E / p \cong 5.45$ which leads to a minimum acceleration about 4 times the static acceleration ($\mathcal{A} \cong 4$). On the other hand, an excitation period of $1\,\text{sec}$ could be regarded as a static loading as for the same block diameter it results to a minimum acceleration that tends to the static value ($\mathcal{A} \cong 1.2$). The profoundly nonlinear-dynamic nature even of the piecewise linear system is not reflected only on the overturning amplitudes. In this respect, the two overturning modes, namely after one impact or without impact at all are also shown together with the 'safe region' emerging between the two modes.

***Asymmetry and detailed sequence of pulses*:**

Sensitivity of the overturning amplitude to the size of the block and the frequency of excitation was previously discussed under a one-sine pulse. In Fig. 7.6 the overturning spectrum for the case of a *one-cosine* pulse is presented as calculated by (a) the analytical solution of Makris and Zhang (1999) and (b) numerical integration (trial-and-error approach). The two distinct overturning modes (i.e. overturn after one impact or without impact at all) and the 'safe region' between the two modes are encountered again. However, the difference of the overturning amplitude levels in comparison to those computed under a one-sine pulse is remarkable. For all frequency ratios $\Omega$ larger values of acceleration are now required to overturn the block (compared with the one-sine case). Also, the critical value of the frequency ratio beyond which only overturning without impact can occur has dropped down to about 4. The beneficial effect of the cosine pulse with respect to the sine pulse is attributed merely to the phase shift of $\pi/2$.

Cycloidal pulses are reasonable idealisations of near-fault ground motions, nevertheless, they cannot fully capture the effect of a slight asymmetry inherent to near- fault pulses. The Ricker wavelet has a distinct advantage in this respect as will be discussed later. It is thus employed here to excite the rectangular block of $2b = 1\,\text{m}$ and $2h = 5\,\text{m}$ in rocking vibrations (with $r = 0.89$). As portrayed in the overturning spectrum plotted in Fig. 7.7, more failure loops 'appear' in this case. It is also remarkable that there is no distinction between overturning with one or no impact as derived from the time-histories of Fig. 7.8. The difference between two 'neighbouring' loops is now in the direction of toppling.

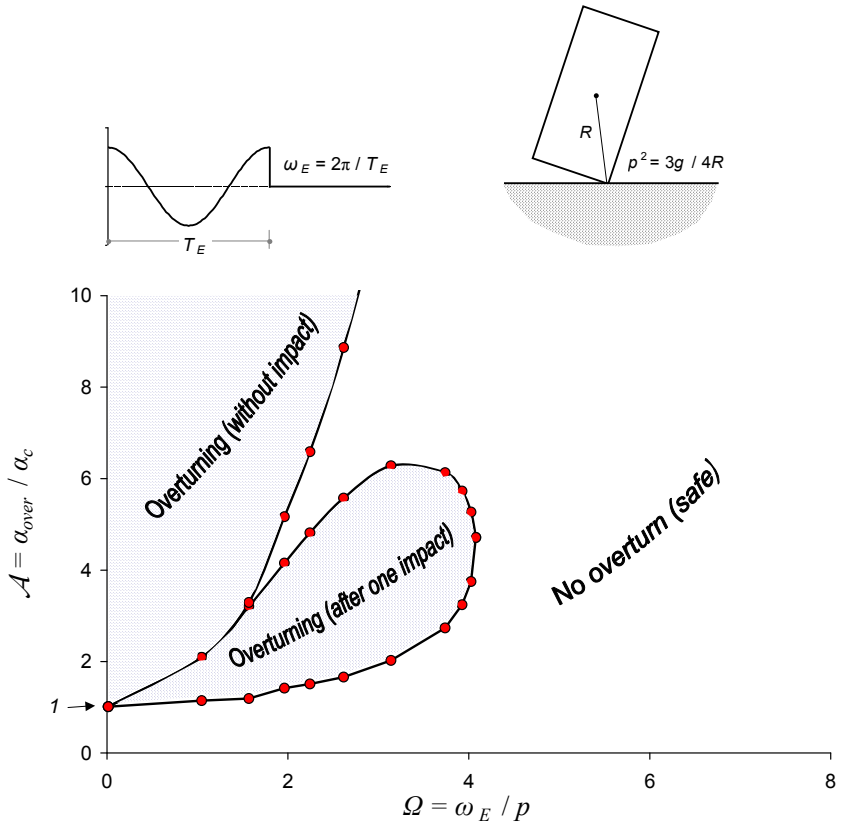


**Figure 7.6** Overturning amplification ratio under a one-cosine pulse excitation computed by: (i) numerical integration of equation of motion (circles) and (ii) the analytical formula derived by Makris and Zhang (solid lines). The coefficient of restitution is 0.8.

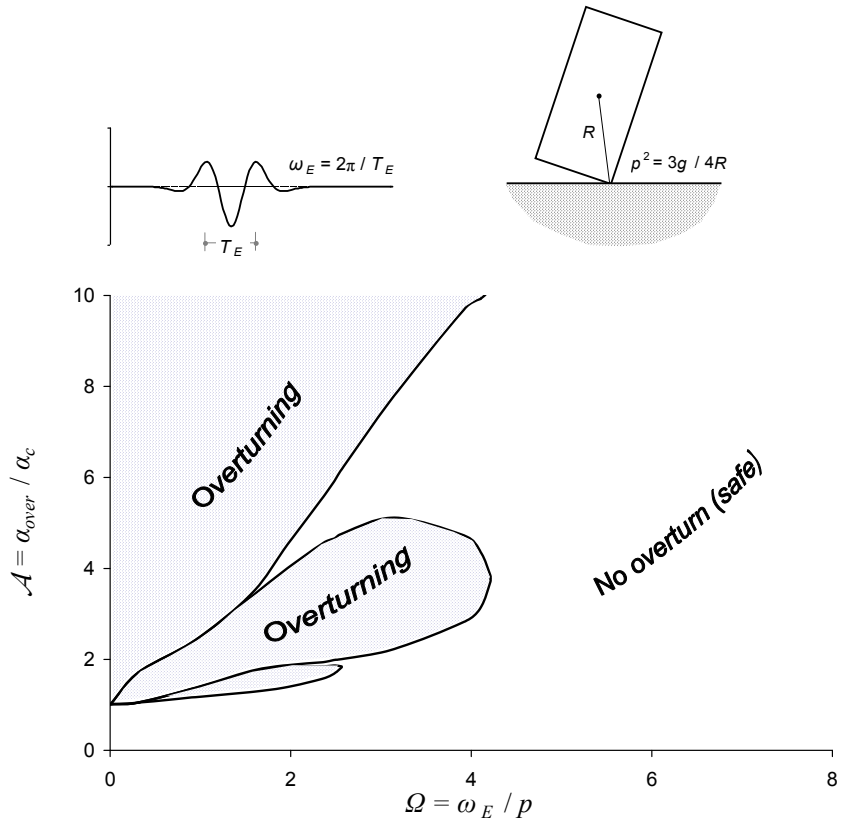


**Figure** 7.7 Overturning amplification ratio under a Ricker pulse excitation computed by numerical integration of equation of motion. The coefficient of restitution is 0.8.

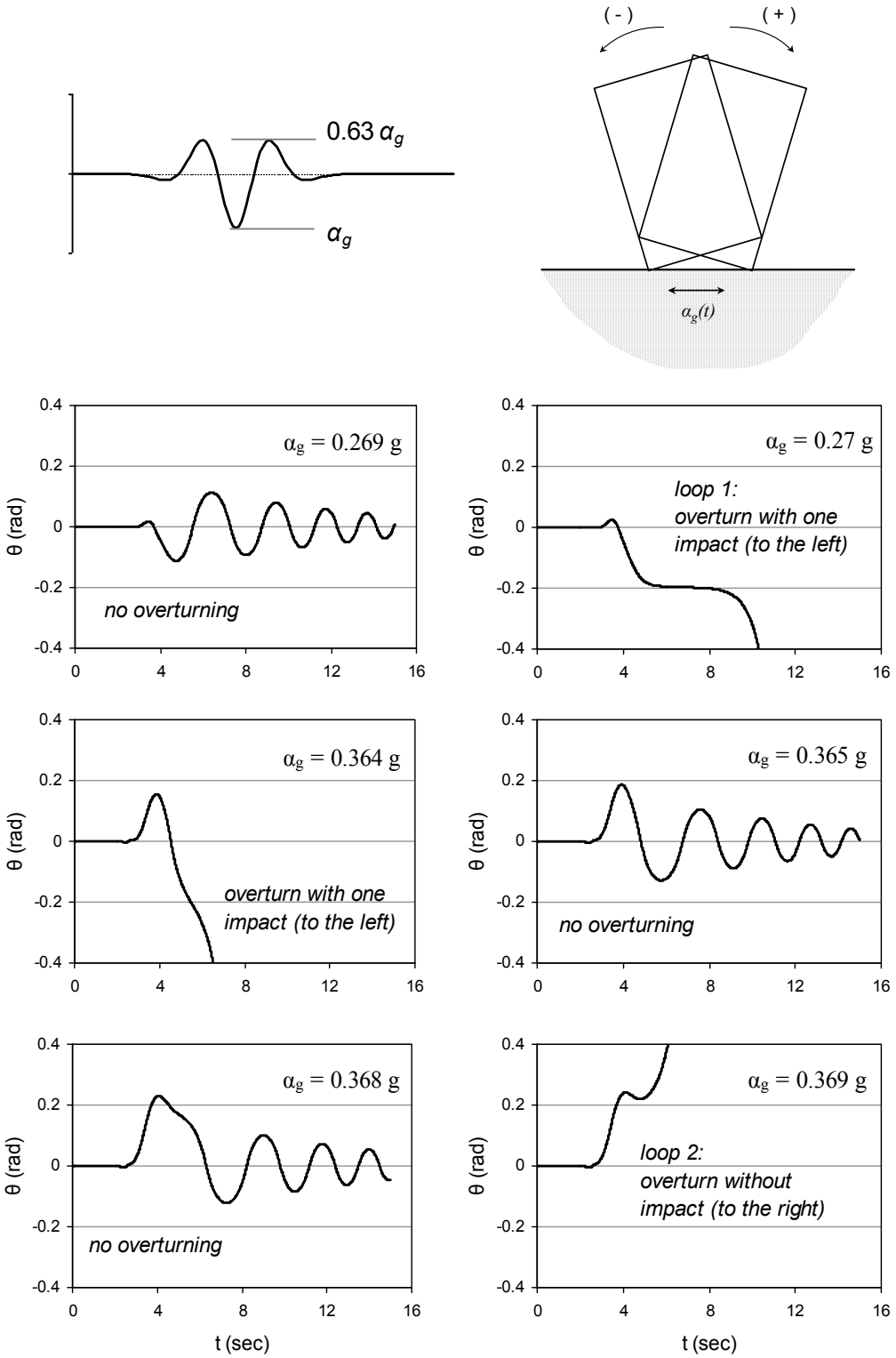


**Figure 7.8** Time-histories of the rocking response for a rectangular block with $2b = 1\text{m}$ and $2h = 5\text{m}$ subjected to a Ricker-wavelet excitation of $f_E = 0.53$ hz . The coefficient of restitution is 0.89 (elastic impact).

***Overturning potential of large structures*:**

An important question arises as to whether or not large structures such as high-rise buildings or tall bridge piers may safely uplift from their foundation during strong shaking. Although such tall structures are unlikely to behave as rigid blocks, and their (unavoidable) flexibility is a favourable factor, the rigid block assumption may give a conservative glimpse on the threat of overturning. The beneficial effect of increased block size to overturning response is already known. However, with very tall and slender buildings, the slenderness ratio $h/b$ is also large. The interplay between slenderness and size regarding overturning is clarified with the help of a rectangular block of a constant half-width $b$. In the plots of Fig. 7.9 the height of the block is gradually increased so that both its slenderness ( $h/b$ ) and its frequency parameter ( $p$ ) keep rising.

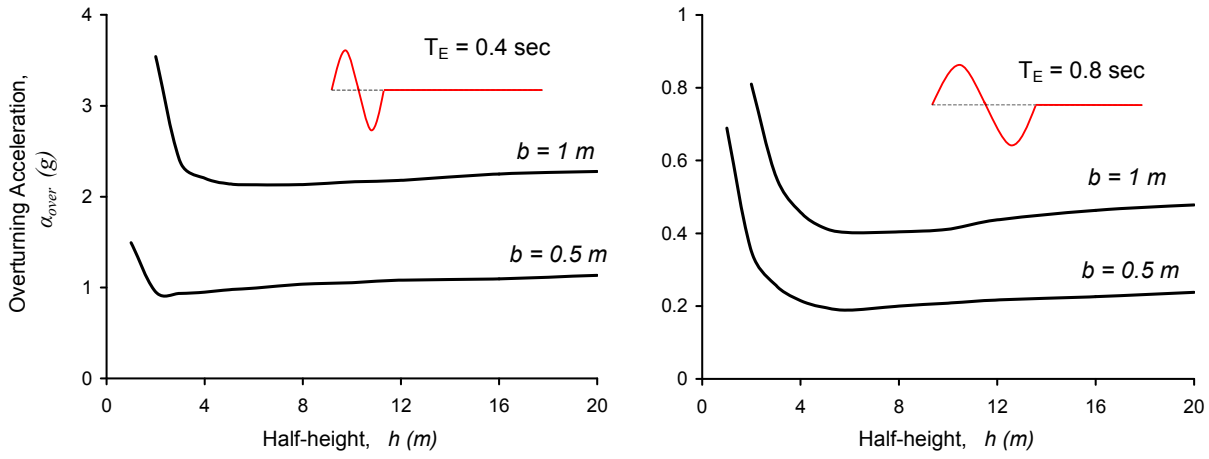


**Figure 7.9** Overturning spectra with respect to the half-height h for blocks with half-width 0.5 m and 1 m subjected to a one-cycle sinus pulse of period 0.4 sec (left) and 0.8 sec (right).

Initially, a block of $b = 0.5\,\text{m}$ and $h = 1\,\text{m}$ is set on rocking under a long-duration one-cycle sinus pulse of $T_E = 0.8\,\text{sec}$; to topple it, a peak ground acceleration of $0.7\,\text{g}$ is needed. By increasing $h$ by a mere $1\,\text{m}$, the overturning acceleration drops to $0.35\,\text{g}$ -- an example of detrimental influence of slenderness. However, as the height of the structure is further increased, the decrease of the overturning acceleration diminishes and the beneficial effect of the size parameter gradually takes over. Paradoxically, after reaching a minimum about $0.18\,\text{g}$ the overturning acceleration tends to

increase, not decrease, with increasing height and slenderness! All that happens is that the size effect overshadows the influence of the slenderness and becomes the prevailing parameter on the overturning response. Hence for a sufficiently tall structure of a certain width, the more slender is made the less vulnerable to overturning it will be! This can explain why large slender structures survive toppling even under severe seismic shaking. In the experimental work of Huckelbridge & Clough (1976) it was made clear that for a practical building, transient uplifting response would in no way imply imminent toppling.

***Resemblance of near-fault ground motions with idealised pulses*:**

The resemblance of near-fault ground motion with cycloidal symmetric pulses has been demonstrated by Anooshehpoor *et al.* (1999), Makris *et al.* (1998, 1999), Mavroeidis & Papageorgiou (2003). Asymmetric pulses can be represented with a Ricker or a T-Ricker wavelet. For example the directivity affected *Düzce* record (in the *Kocaeli* 1999 earthquake) is compared with a Ricker wavelet ($PGA = 0.28\,\text{g}$ and $T_E = 1.3\,\text{sec}$) in Fig. 7.10. The two time histories excite in rocking a slender block ($\theta_c = 0.2\,\text{rad}$) for different values of the *period parameter* $T_P = 2\pi / p$.

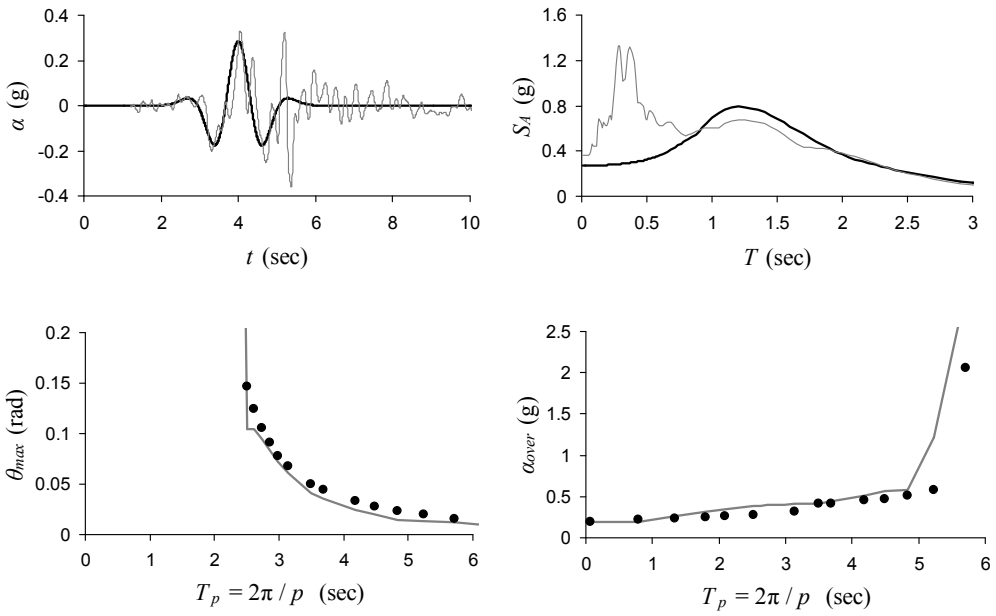


**Figure 7.10** Rocking and overturning spectra for blocks with $h/b = 5$ ($\theta_c = 0.2\,\text{rad}$) subjected to the time-histories of: (a) Düzce, in the Kocaeli Earthquake (plotted with gray solid lines) and (b) a Ricker wavelet (plotted with black solid lines and circular dots).

The resulting spectra of peak rotational angle $\theta_{\max}$ and minimum acceleration level for overturning (derived by scaling up and down each motion). Evidently the simple Ricker pulse can simulate the long-duration pulse inherent in the Düzce record for all values of $T_P$. This almost excellent agreement (with respect to rocking) of the Düzce record with a simply fitted Ricker wavelet indicates that the rocking and overturning is practically unaffected by the high-frequency acceleration peaks that are ever present in every strong accelerogram.

***The case study of the toppled tombstones (Athens earthquake, 1999)*:**

While the overturning hazard may not be the key issue in the seismic response of slender structures (at least if stiff soils support them), it is usually addressed in engineering practice for two different reasons: (a) toppling of non-structural elements are in many cases of special interest in seismic design procedures (for example appended equipment, electrical transformers and so on and (b) for nearly a century the engineering community analysed overturning failures observed after an earthquake to obtain rough estimates of the true intensity of (unrecorded) seismic shaking. To demonstrate how difficult it is to obtain reliably such estimates, toppling of a typical cemetery tombstone in the Athens earthquake of 1999 is studied (Fig. 7.11). It was expected that back analysis of the overturning would reveal the intensity of the unknown ground motion at this location, 2 km away from the causative fault (Apostolou *et al.*, 2007). Two different earthquake records are used as the basis of the analyses:

- The accelerogram of Sepolia station, recorded in the Athens 1999 earthquake, as a typical stiff-soil record of a moderate ($M_s$ 5.9) magnitude event, at a distance of about 9 km from the ruptured normal fault zone. The record has a peak ground acceleration of 0.35 g and dominant periods in the range of 0.15-0.25 seconds.
- The accelerogram of Düzce in the Kocaeli 1999 earthquake, which is typical of a large ($M_s$ 7.4) magnitude event whose strike-slip rupture is directed towards the recording soil site, and stops a few kilometres before it. The strong forward-directivity effect has given the Düzce

record a characteristic long duration acceleration pulse. Its $PGA = 0.37$ g is similar to the one of the Sepolia record, but its significant periods range from about 0.40 to at least 1.50 seconds.

Minimum acceleration levels required to topple the tomb are computed after scaling up or down each record. Elastic impact conditions are considered throughout the analysis leading to a coefficient $r = 0.928$. In the case of the Sepolia-type excitation the block can sustain rocking motion without overturning until the accelerogram is increased so that it acquires a $PGA$ of 0.85 g (about 2.5 times the recorded value). By contrast, the Düzce excitation must be scaled down to a $PGA$ of 0.27 g for overturning to occur (about 0.73 times the recorded value). Ground acceleration and rotation time histories for marginal overturning for the two records are plotted in Fig. 7.11. Evidently, the long-duration pulse in the Düzce record tends to reduce the overturning acceleration towards its static value (0.20/1.27 g ≅ 0.16 g).

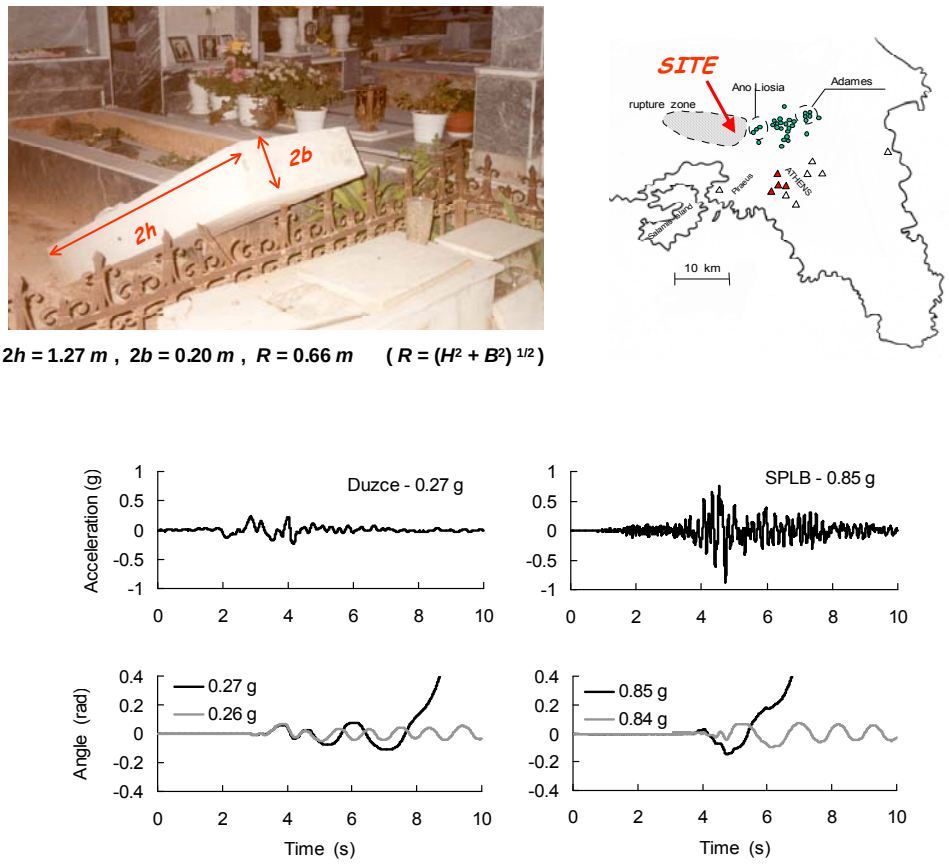


**Figure 7.11** (a) A typical free-standing tombstone that toppled after the Athens earthquake, (b) the up-and-down-scaled accelerograms SPLB/Athens and Düzce/Kocaeli with the corresponding time histories of induced rotation just leading to overturning of the tombstone.

The rocking response of the tomb under the Sepolia–type motion is revisited next. Now the time increment of this accelerogram is artificially increased by 10% and by 20%. This leads to an increase of the predominant period of motion from 0.26 sec to 0.29 sec and to 0.31 sec, respectively. The slight modification of the excitation period has a dramatic effect on its rocking response: the overturning acceleration is reduced from 0.85 g down to 0.61 g and to 0.58 g for the two modified records! A 2–sec detail of each modified time-history along with the original time–history (each one scaled to the critical acceleration) is plotted in Fig. 7.12.

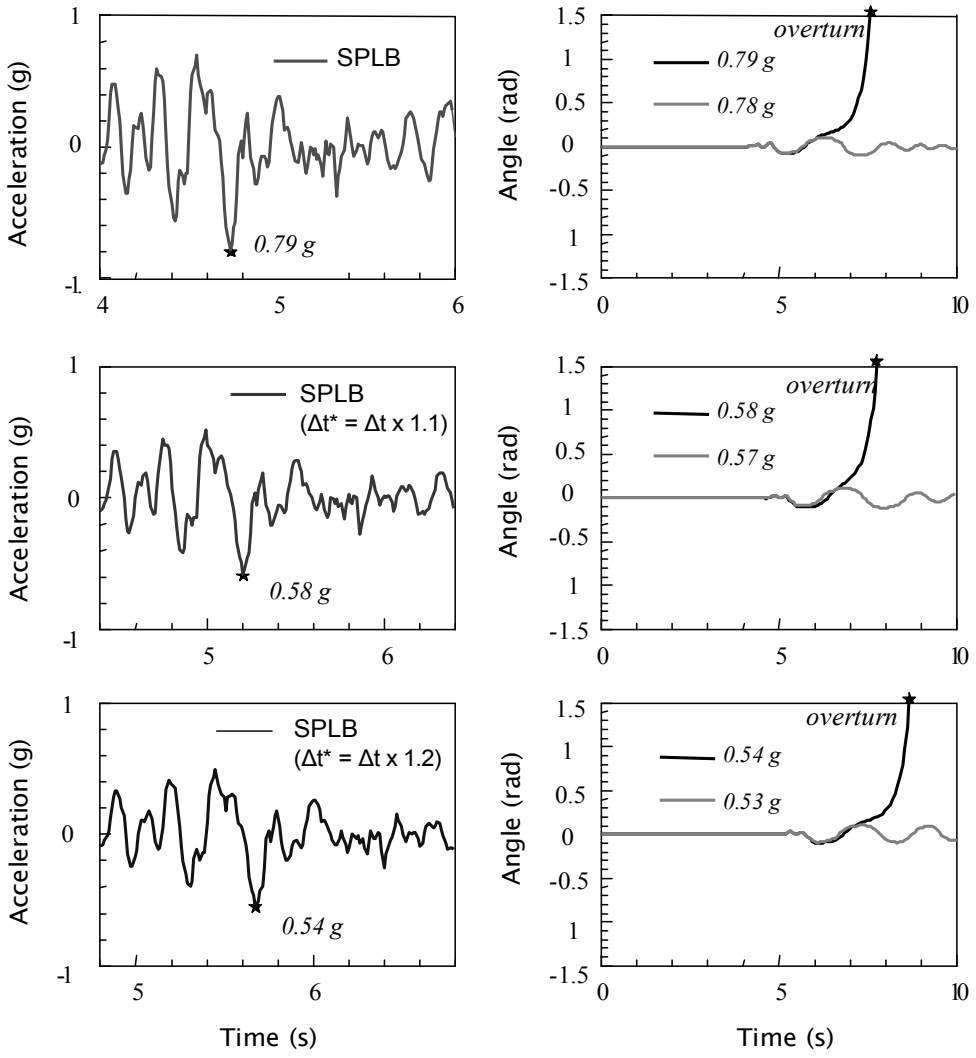


**Figure 9.12** The up-and-down-scaled accelerograms SPLB/Athens (original and time-extended) with the corresponding time histories of induced rotation just leading to overturning of the tombstone of Fig. 7.11.

The two distinct modes of overturning for trigonometric pulses as discussed by Makris and Zhang (1999) are now extracted for the tombstone and plotted in the overturning spectrum of Fig. 7.13. For

relatively low values of the excitation period, a rocking block such as the tomb of Fig. 7.10 will not overturn even for peak ground acceleration 4 or 5 times the pseudo-static critical acceleration (0.16 g). For values of $T_E$ exceeding about 0.3 sec the minimum $PGA$ to overturn the block is rapidly decreasing. Eventually for sufficiently large periods ($T_E > 0.7\,\text{sec}$) the minimum overturning acceleration approaches the pseudo-static value. As seen in Fig. 7.13 the real records and the sinusoidal pulses give fairly similar results for the overturning response.

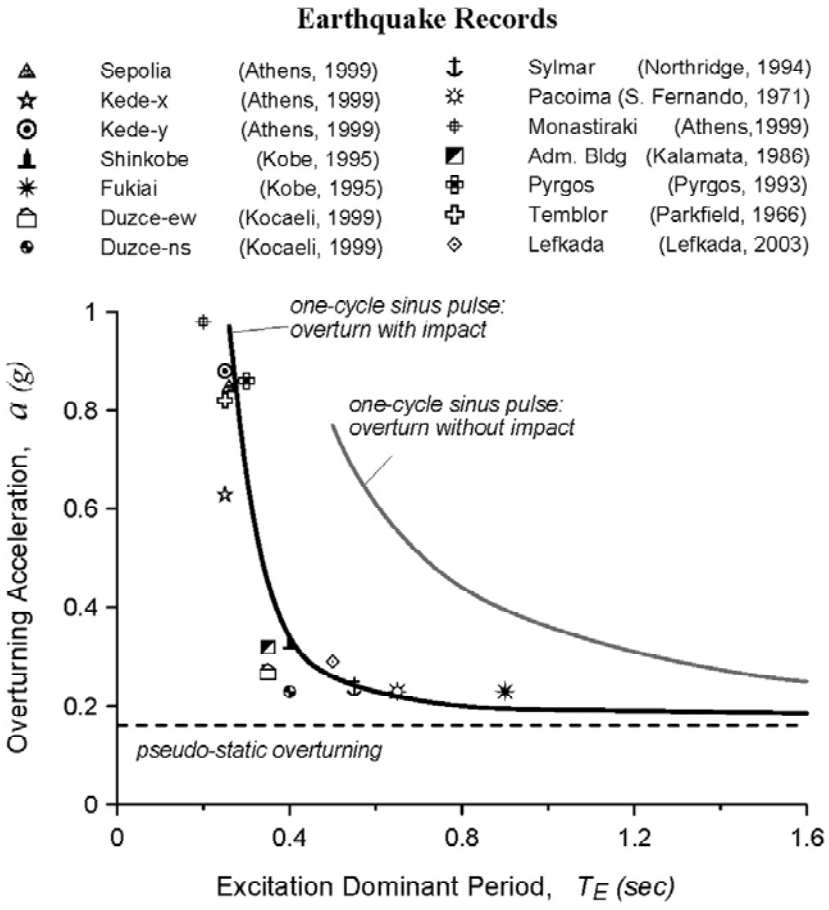


**Figure 7.13** Overturning spectra of the cemetery tomb ($h/b = 6.35$) for one-cycle sinus-type and for numerous ground motions used as earthquake excitation.

Concluding, the peak ground acceleration that toppled the cemetery block could vary from about 0.20 g to 0.80 g within a period range 0.25 sec – 0.5 sec. The former period is closer to the records of the Athens 1999 earthquake, which however being far–field. However, it is evident that the practice of estimating ground acceleration from observations of toppled and untoppled slender blocks, which has

for a century been utilised to assign levels of design acceleration in many parts of the world, is meaningless in view of the strong frequency-and detail-dependence and the profoundly nonlinear nature of rocking behaviour.

### 7.2.2 Flexible 1-dof structure

While the rigid block is a convenient approximation of a rocking structure in view of estimating the overturning potential, for slender systems the structural flexibility may affect the overturning response. To this extent, the rocking response of a flexural 1-dof oscillator with a foundation mat (see Fig. 3.10) is now revisited. The structural dimensions of the oscillator are chosen in such a way that the rocking parametres be the same to those of the afore-discussed rigid block $\left(p=1.699\,\text{rad}/\text{sec},\ \theta_c=0.2\,\text{rad}\right)$. A one-cycle sinus pulse is imposed to the base with a period range from 0.35 sec to 2 sec. Initially, a quite stiff visco-elastic oscillator is employed $\left(T_o=0.1\text{sec},\ \ \xi=5\%\right)$ so that flexural deformations cannot affect the rocking vibrations. The minimum overturning amplitudes are calculated from Eqs 3.48 and 3.50 for elastic impact conditions $\left(r=0.89\right)$ as portrayed in the overturning spectrum of Fig. 7.14. In the same graph, the minimum acceleration estimates of the equivalent rigid block $\left(p=1.699\,\text{rad}/\text{sec},\ \theta_c=0.2\,\text{rad}\right)$ are also plotted. It is evident that the sdof oscillator can be considered as a rigid rocking system. The overturning analysis is repeated next for two more flexible oscillators of eigen-period 0.3 sec and 0.5 sec respectively. The calculated overturning spectra are presented in Fig. 7.15 in comparison with the spectrum of the stiff system. It turns out that structural flexibility affects favourable the overturning response in such a way that the minimum acceleration amplitude after an impact ('loop 1') may be significantly increased especially at high-frequency pulses whereas the safe area between the two modes expanses. On the other hand no prominent effect on the overturning mode 2 (without impact) is revealed. The progressive shrinkage of the overturning 'loop 1' is further illustrated in the overturning spectrum of Fig. 7.16. In this spectrum the overturning amplitudes are calculated for

different values of the structural eigen-period under a base excitation of period 0.6 sec (a vertical section at $f_E = 1.67\,\text{hz}$ in the spectrum of Fig. 7.15). It is shown that the increase of the structural period results into (a) a slight decrease of the overturning acceleration without impact, and (b) the shrinkage of the failure loop with an impact at an accelerating pace, which eventually vanishes at a period of 0.6 sec. For even more flexible systems only overturning without impact is possible.

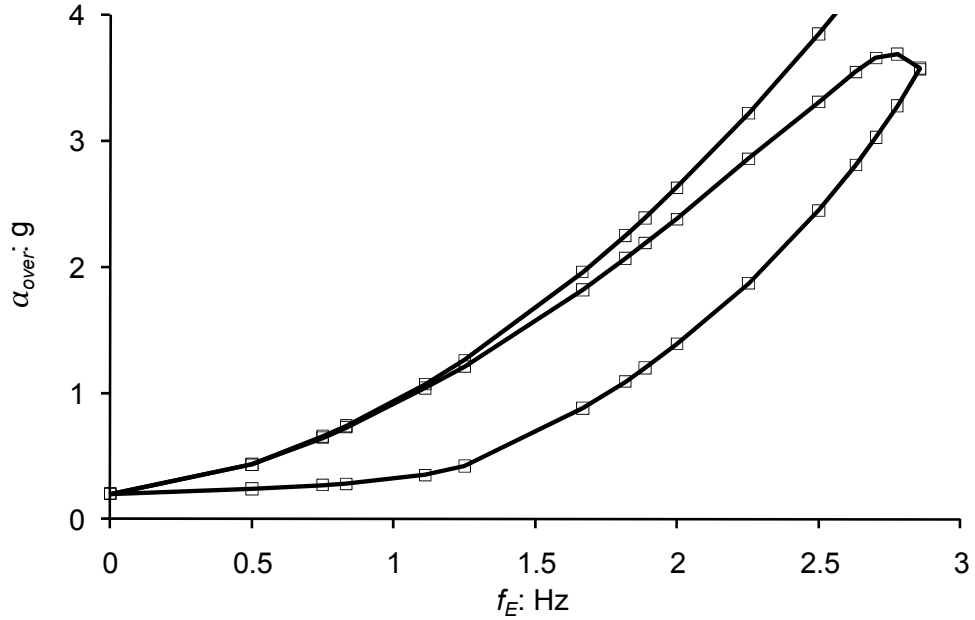


**Figure 7.14** Overturning acceleration spectra of a one-storey structure $\left(p = 1.699\,\text{rad/sec},\ \theta_c = 0.2\,\text{rad}\right)$ of eigenperiod $T_o = 0.1\,\text{sec}$ and a rigid block $\left(p = 1.699\,\text{rad/sec},\ \theta_c = 0.2\,\text{rad}\right)$ under a one-cycle sinus pulse of frequency $f_E$. The coefficient of restitution is 0.89.

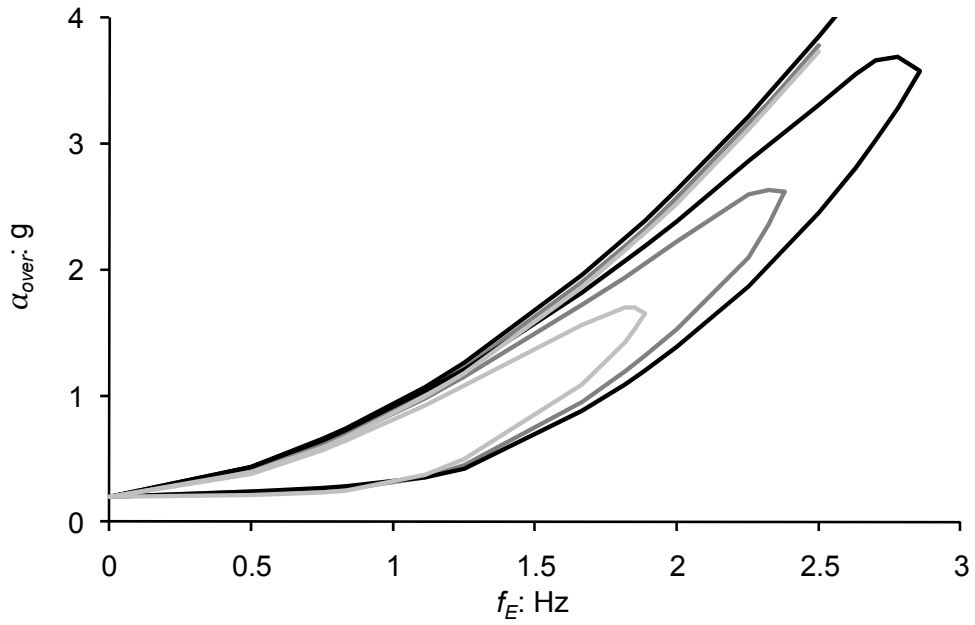


**Figure 7.15** Overturning acceleration spectra of a one-storey rocking structure $\left(p=1.699\,\text{rad/sec},\ \theta_c=0.2\,\text{rad}\right)$ of eigenperiod $T_o=0.1,\ 0.3,$ and $0.5$ sec (black, grey, and light grey lines respectively) under a one-cycle sinus pulse of frequency $f_E$. The coefficient of restitution is 0.89.

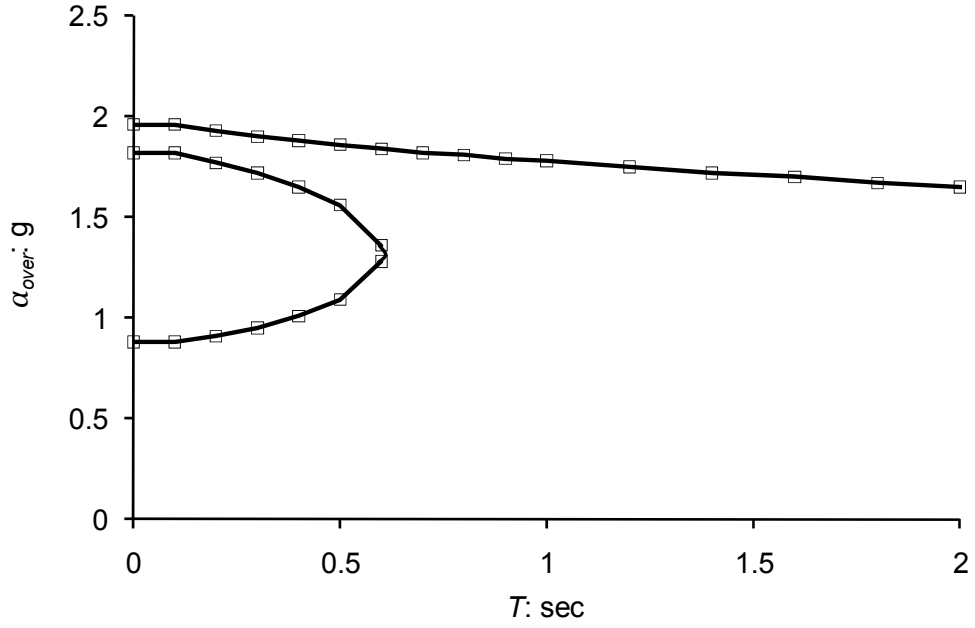


**Figure 7.16** Overturning acceleration spectra of a one-storey rocking structure $\left(p=1.699\,\text{rad/sec},\ \theta_c=0.2\,\text{rad}\right)$ for different values of the eigenperiod $T_o$ under a one-sine pulse excitation of $T_E=0.60\,\text{sec}$ (a vertical section of the spectrum of Fig. 7.15 at $f_E=1.67\,\text{hz}$). The coefficient of restitution is 0.89.

## 7.3 OVERTURNING on COMPLIANT SOIL

The profoundly non-linear behaviour that a rocking structure experiences can be even more complicated when a flexible base is considered. In order to gain an insight to the dynamic phenomena related to the rocking motion on a flexible base we investigate the response of two rectangular blocks on an accelerating base. The dimensions of the two blocks are ( 1 x 5 m ) and ( 2 x 10 m ) so that the critical angle be 0.2 rad for both cases and the frequency parameter be 1.7 rad/sec and 1.2 rad/sec respectively. A one-cycle sine pulse (TE = 0.8 sec and 1.2 sec) is applied as an excitation so that the results can be comparable to the findings that Makris *et al.*, outlined for the rigid base case. The supporting soil medium is assumed to be a homogeneous, elastic halfspace with Poisson ratio 0.3. Moreover when the rocking structure impacts the ground, elastic conditions are considered, hence the coefficient of restitution is given by Eq. 3.4.

Minimum acceleration levels for toppling are computed in terms of the rocking period of the fixed-based system $T_m$, for two different values of the effective density, namely 0.25 t/m3 and 2.5 t/m3. The overturning spectra are plotted in Figs 7.17 and 7.18 along with the rigid base case ($T_m = 0$).

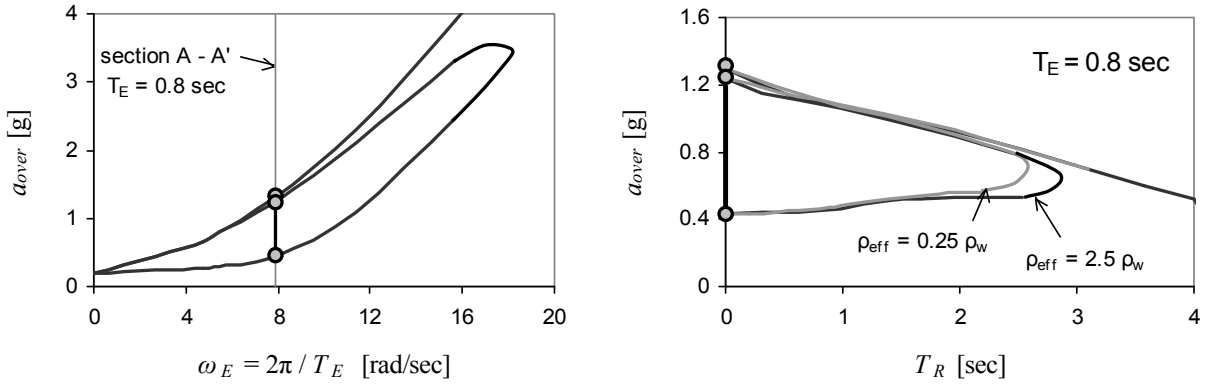


**Figure 7.17** Overturning acceleration spectra of a rectangular block (2b = 1m, 2h = 5m) on a rigid (a) or deformable (b) base. The structure is subjected to rocking by a one-cycle sinus excitation at the base.

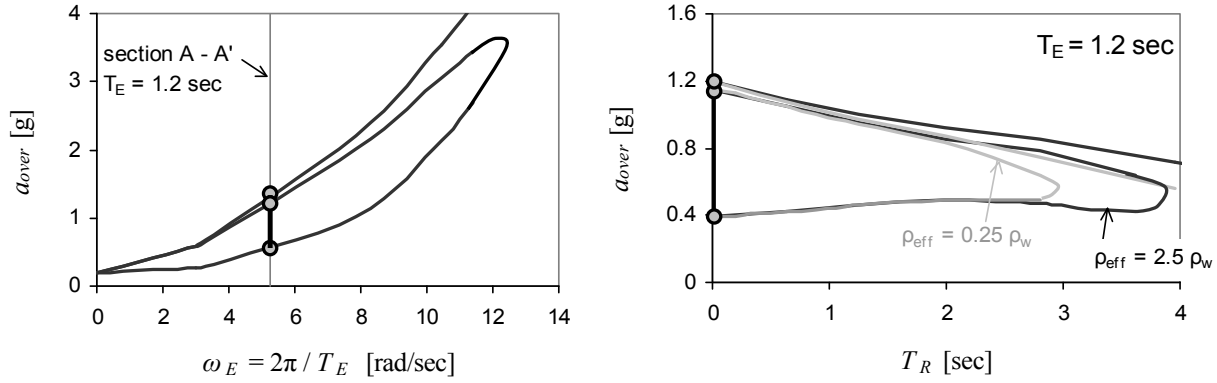


**Figure 7.18** Overturning acceleration spectra of a rectangular block (2b = 2m, 2h = 10m) on a rigid (a) or deformable (b) base. The structure is subjected to rocking by a one-cycle sinus excitation at the base.

*Chapter 8:*

# Conclusions

## 8.1 SUMMARY of CONCLUSIONS

This thesis studies the dynamic response of simple rigid structures with foundation uplift under strong seismic shaking.

Some of the key conclusions of the thesis are as follows:

- Foundation uplifting has a multiply beneficial role on the dynamic response of the structure.
- The available rotation ductility of the foundation is substantially higher comparing to a fixed base system. Given that uplifting restrains plastification of the supporting soil, the maximum rotation that a rocking system with significant uplift can experience tends to the critical angle $\theta_c \cong b/h$ which is in any case much higher than the angle a fixed base system can tolerate without toppling due to soil yielding.
- The ultimate moment of an uplifting foundation is significantly reduced compared to the fixed-base moment resulting to a beneficial effect for the seismic design of structural foundations.
- Overturning of a rigid free-standing structure is a very sensitive function of the nature and dominant period of the horizontal excitation, as well as of the aspect ratio and the absolute size of the block. Under static conditions, or for an extremely long-period motion, the overturning acceleration is equal to the aspect ratio $(b/h)$ of the block times the acceleration of gravity. However, under strongly dynamic (short-period) excitation the block can sustain rocking

motion without toppling even if peak ground acceleration increases three or four times the static critical value. Moreover, increasing the size of the block affects rocking response in a similar way to decreasing the dominant period of ground motion. Thus, large blocks can safely undergo rocking motion while smaller ones exhibit rocking vibration with higher magnitudes of uplifting, and are thus much more vulnerable to toppling.

- Dynamic failure envelopes in the $N-M$ plane may reach considerably higher levels than the corresponding static curves. This is an outcome of larger dynamic bearing capacity $p_{u,dyn}$ than the static value (e.g. $p_u=(\pi+2)s_u$).

- Under monotonic loading the part of the footing remaining in contact with soil (effective width: $2\beta$) when the moment capacity of the foundation is mobilised $\left(M=M_u\right)$ can be estimated by the simple relationship: $\lambda=\chi$ (or $2\beta=N/p_u$). This formula can be easily drawn by the elastic-perfectly plastic footing-on-Winkler springs model. Even under dynamic-cyclic loading conditions the effective width can be approximately calculated through this equation; however the frequency and the amplitude of the seismic excitation may be significantly different from the linear trend under certain circumstances.

- A simplified 'dynamic' failure envelope in the $N-M$ space can be derived by adopting at the increment of $M=M_u$ a distribution of contact pressures that is: (a) different from the rectangular (as in the conventional static approach), and (b) not bounded by the static ultimate capacity $p_u$. Considering the linear expression $\lambda=\chi$ for the effective width, the distance of the vertical reaction axis to the footing midpoint becomes $\zeta=b-2\beta+4\beta/3=b-2\beta/3$. In this way the ultimate moment becomes (see also Fig. 8.1):

$$M=N\zeta=Nb\left(1-\frac{2}{3}\chi\right) \qquad [8.1]$$

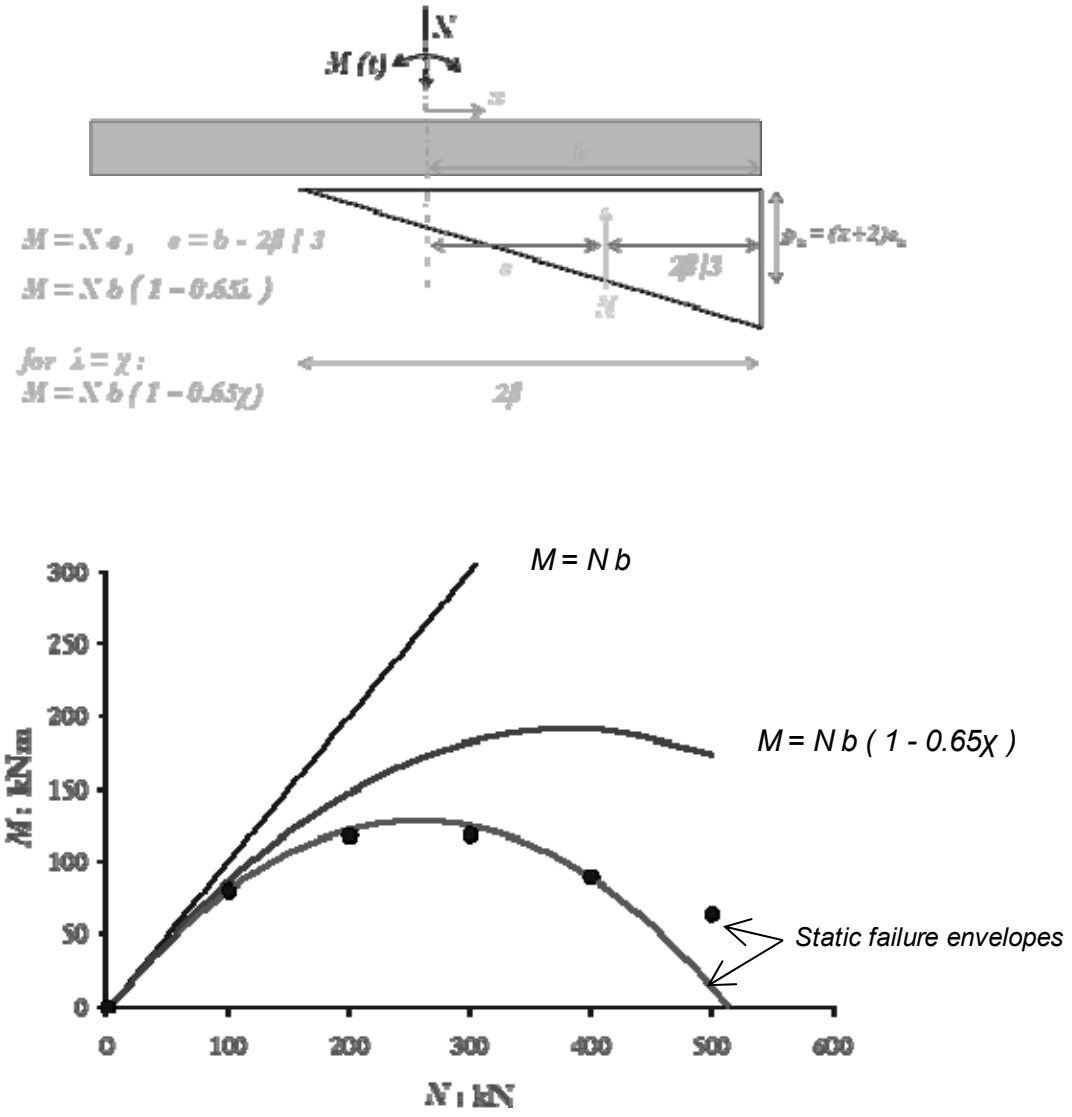


**Figure 8.1** Dynamic failure envelope in the N-M plane for a triangular distribution of contact pressures

According to the findings of the present study, a simplified methodology for the design of footings on soft soil against large seismic moment can be proposed, based on the interaction curves of the generalised loads:

(a) The bearing capacity of the supporting soil is first computed. For example, for linearly increasing strength with depth $\left(s_u = s_{uo} + \kappa z\right)$, the ultimate vertical load is (Davies and Booker, 1974): $p_u = F\left[(\pi+2)s_u + \kappa(b/2)\right]$, in which $F$ is a inhomogeneity factor

dependent on the coefficient $\kappa$, the footing width, and the interface conditions. For a smooth strip it ranges between 1 and 1.5.

(b) Based on the vertical design superstructure load, the vertical load factor $\chi = N/N_u$ is computed.

(c) The vertical load – moment interaction curve is computed according to the equation: $\frac{M}{N_u B} = \frac{\chi}{2}(1-\eta)(1-\chi)$, in which $\eta = \sqrt{\frac{N h}{K_m}}$ is a factor describing P – delta effects.

(d) The moment for incipient uplift is then calculated: $M_{uplift} = M_u \left(1 - e^{-\frac{Nb}{2M_u}}\right)$, in which $M_u$ is the moment capacity considering full contact conditions.

(e) For vertical load factor smaller than 0.3, and in particular for $M_d < M_{uplift}$, the permanent displacement can be neglected.

(f) For vertical load factor larger than 0.3 and given that limited permanent rotation is developed, the cumulative settlement can be estimated from the following conservative formula: $\delta w = 4 n b \bar{\theta}_{\max}$, in which $n$ is the number of significant cycles of inertial vibration ($n_{\max} = 3$, given that foundation soil is gradually hardening due to cyclic rocking), and $\bar{\theta}_{\max}$ the effective rocking amplitude. This angle can be estimated from the effective period of the system $T \cong 2\pi\sqrt{J_b / K_m}$ in combination with the rocking displacement spectrum.

Alternatively, for a time domain analysis of earthquake response through macroscopic modelling, the foundation moment can be estimated analytically as follows: $M = K_m \left(\frac{\lambda - \chi}{1-\chi}\right)^2 \theta + Nb(1-\lambda)\cos\theta - Nh\sin\theta$, in which $\lambda = \frac{\theta_{uplift}(1-\chi) + \chi\theta}{\theta}$ is the dimensionless effective half-width of the footing. The cumulative settlement can be predicted

as before, given that the effective rocking amplitude and the number of significant cycles will be estimated from the nonlinear analysis.

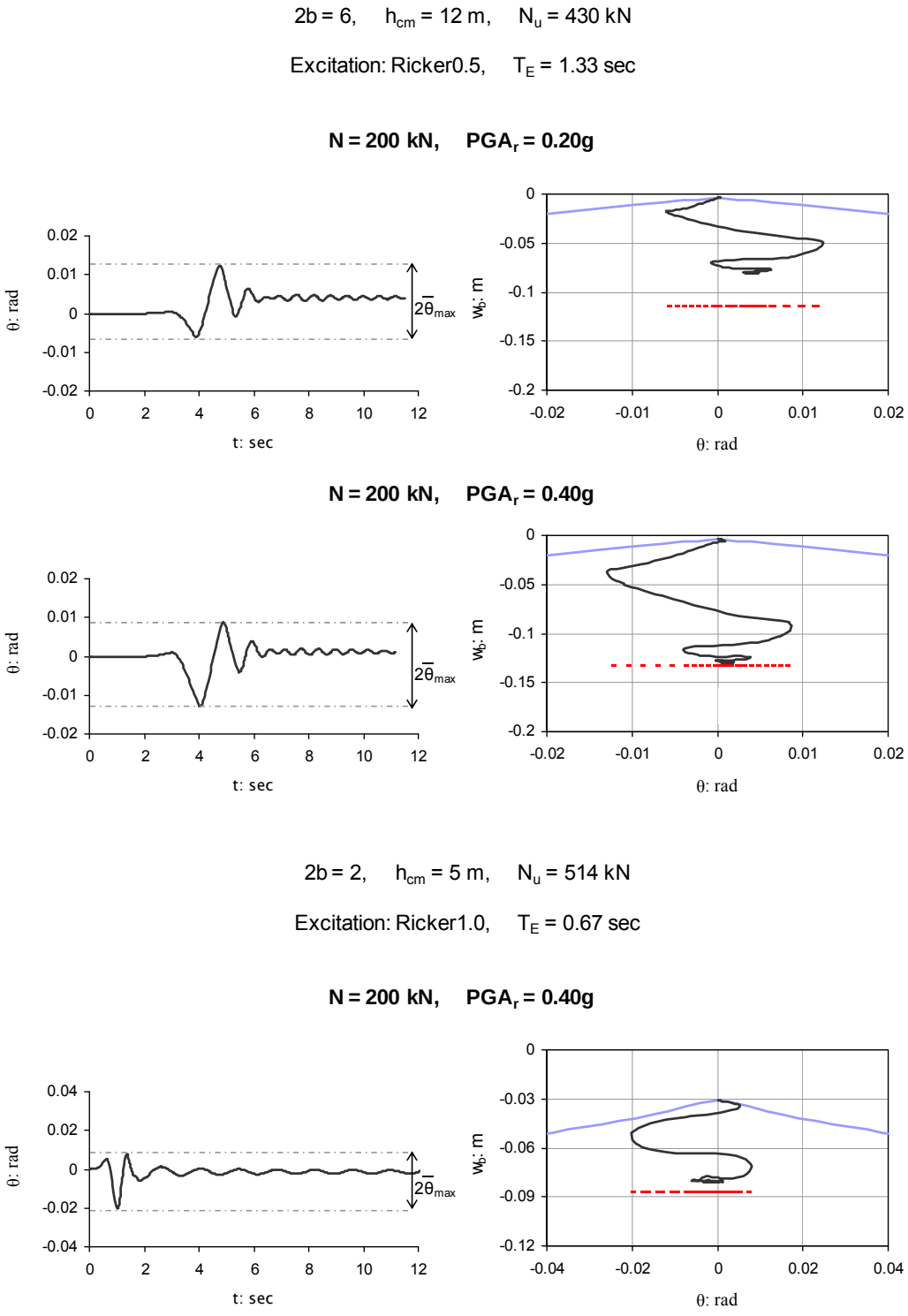


**Figure 8.2** A proposed methodology for assessment of cumulative displacements during rocking on inelastic soil.

# Bibliography


1. ABAQUS 6.3. (2004). Standard user's manual. Rhode Island: Hibbit, Karlsson and Sorensen Inc.

2. Allotey, N. and El Naggar, M. H. (2003). Analytical moment-rotation curves for rigid foundations based on a Winkler model. *Soil Dyn. and Earth. Engng* **23**, No. 5, 367-381.

3. Allotey, N. and El Naggar, M. H. (2008). An investigation into the Winkler modeling of the cyclic response of rigid footings. *Soil Dyn. and Earth. Engng* **28**, No. 1, 44-57.

4. American Society of Civil Engineers (2000). FEMA356, Prestandard and commentary for the seismic rehabilitation of buildings. FEMA, Washington, DC.

5. Anastasopoulos, I., Gazetas, G., Loli, M., Apostolou, M., Gerolymos, N. (2009). Soil failure can be used for seismic protection of structures. *Bull Earthquake Eng* **8**, No. 2, 309-326.

6. Anooshehpoor, A., Heaton, T., Shi, B. and Brune, J. (1999). Estimates of the ground acceleration Point Reyes station during the 1906 San Francisco earthquake. *Bull. Seismol. Soc. Amer.* **89**, No. 4, 843-853.

7. Apostolou, M., Gazetas, G. and Garini, E. (2007). Seismic response of slender rigid structures with foundation uplifting. *Soil Dyn. and Earth. Engng* **27**, No. 7, 642-654.

8. Apostolou, M., Gerolymos, N., Rizos, D. and Gazetas, G. (2006). Bearing capacity of rectangular foundation under inclined eccentric loading. *Proc. 6th Greek Conf. on Geotech. Engng*, Xanthi, Greece (in Greek).

9. Apostolou, M. and Gazetas, G. (2004). Seismic response of simple structures with foundation uplift. *Proc. 11th ICSDEE and 3rd ICEGE*, Berkeley, Ca.

10. Apostolou, M. and Gazetas, G. (2005). Rocking of foundations under strong shaking: Mobilisation of bearing capacity and displacement demands. *1st joint Greece-Japan Workshop on Seismic design, observation, and retrofit of foundations*, Athens.

11. Applied Technology Council (1984). ATC-3-06 amended: Tentative provisions for the

development of seismic regulations for buildings. ATC, Redwood city, Ca.

12. Applied Technology Council (1994). ATC-40: Seismic evaluation and retrofit of concrete buildings. ATC, Redwood city, Ca.

13. Aslam, M., Godden, W. G. and Scalise, D. T. (1980). Earthquake rocking response of rigid bodies. *J. Struct. Div., ASCE* **106**, No. 2, 377-392.

14. Bartlett, P. E. (1979). Foundation rocking on a clay soil. *M.E. Thesis, Report* No. 154, School of Eng., Univ. of Auckland, 144 pp.

15. Beck, J. L. and Skinner, R. I. (1972). The seismic response of a proposed reinforced concrete railway viaduct. *DSIR Rept* No. 369.

16. Beck, J. L. and Skinner, R. I. (1974). The seismic response of a reinforced concrete bridge pier designed to step. *Earth. Engng and Struct. Dynamics* **2**, No. 4, 343-358.

17. Bransby, F. and Randolph, M. (1997). Shallow foundations subjected to combined loadings. *Proc. ISOPE.*

18. Building Seismic Safety Council (1997). FEMA273/274, NEHRP guidelines for the seismic rehabilitation of buildings; I– guidelines, II–commentary. FEMA, Washington, DC.

19. Building Seismic Safety Council (2000). FEMA368/369, NEHRP recommended provisions for seismic regulations for new buildings and other structures; I– provisions, II–commentary. FEMA, Washington, DC.

20. Building Seismic Safety Council (2004). FEMA450, NEHRP recommended provisions for seismic regulations for new buildings and other structures; I– provisions, II–commentary. FEMA, Washington, DC.

21. Butterfield, R. and Gottardi, G. (1994). A complete three-dimensional failure envelope for shallow footings on sand. *Géotechnique* **44**, No. 1, 181-184.

22. Butterfield, R. and Ticof, J. (1979). The use of physical models in design. Discussion. *Proc. 7th Eur. Conference Soil Mechanics*, Brighton, 4, 259-261.

23. Chatzigogos, C. T., Pecker, A. and Salencon, J. (2009). Macroelement modelling of shallow foundations. *Soil Dyn. and Earth. Engng* **29**, No. 5, 765-781.

24. Chopra, A. K. and Yim, S. C-S. (1985). Simplified earthquake analysis of structures with foundation uplift. *J. Struct. Engng, ASCE* **111**, No. 4, 906-930.

25. Cloud, W. K. (1963). Period measurements of structures in Chile. *Bull. Seismol. Soc. Amer.* **53** No. 2, 359-379.

26. Crémer, C., Pecker, A. and Davenne, L. (2001). Cyclic macro-element for soil-structure interaction: material and geometrical non-linearities. *Int. J. Numer. Anal. Meth. Geomech.* **25**, No. 13, 1257-1284.

27. Crémer, C., Pecker, A. and Davenne, L. (2002). Modeling of nonlinear dynamic behaviour of a shallow strip foundation with macro-element. *J. Earth. Engng* **6**, No. 2, 175-211.

28. Drucker, D., Greenberg, H. and Prager, W. (1952). Extended limit design theorems for continuous media. *Q. Appl. Math.* 9, 381-389.

29. Dunkerley, S. (1894). On the whirling and vibration of shafts. *Phil. Trans. R. Soc. Lond. A* **185**, 279-360.

30. Eurocode 8-Part 5. Foundations, retaining structures and geotechnical aspects. Ref. No prEN 1998-5:1999

31. Figini, R., Paolucci, R. and Chatzigogos, C. T. (2011). A macro-element model for non-linear soil-shallow foundation-structure interaction under seismic loads: theoretical development and experimental validation on large scale tests. *Earth. Engng and Struct. Dynamics* (to be published, available online).

32. Gajan, S., Kutter, B. L., Phalen, J. D., Hutchinson, T. C., Martin, G. R. (2005). Centrifuge modeling of load-deformation behavior of rocking shallow foundations. *Soil Dyn. and Earth. Engng* **25**, No. 7-10, 773-783.

33. Gajan, S. and Kutter, B. L. (2008). Capacity, settlement, and energy dissipation of shallow footings subjected to rocking. *J. Geotech. Engng, ASCE* **134**, No. 8, 1129-1141.

34. Gajan, S. and Kutter, B. L. (2009). Contact interface model for shallow foundations subjected to combined cyclic loading. *J. Geotech. Engng, ASCE* **135**, No. 3, 407-419.

35. Gazetas, G. and Apostolou, M. (2004). Nonlinear soil-structure interaction: Foundation uplifting and soil yielding. *3rd joint US-Japan Workshop on SSI*, Menlo Park, Ca.

36. Gazetas, G., Apostolou, M., and Anastasopoulos, I. (2003). Seismic uplifting of foundations on soft soil with examples from Adapazari (Izmit 1999 earthquake). *Proc. BGA Int. Conf. on Foundations*, Dundee.

37. Gazetas, G. (2001). Foundation failures in Adapazari during the 17-8-99 Izmit (Kocaeli) Earthquake. *Proc. 4th Nat. Greek Conference Geotech. Engng*, Athens, 3 (*in Greek*).

38. Gazetas, G. (1991). Foundation vibrations. *Foundation engineering handbook*, H. F. Winterkorn and H. Y. Fang, eds. Van Nostrand Reinhold, New York, N.Y., 553-593.

39. Gazetas, G. (1983). Analysis of machine foundation vibrations: state of the art. *Soil Dyn. and Earth. Engng* **2**, No. 1, 2-42.

40. Gazetas, G. and Mylonakis, G. (1998). Seismic soil-structure interaction: new evidence and emerging issues. *Proc. Geotech. Earth. Engng and Soil Dynamics, Geo-Institute ASCE Conference*, Seattle, Wa.

41. Gazetas, G. and Roesset, J. M. (1976) *Forced vibrations of strip footings on layered soils. Meth. Str. Anal. ASCE* **1**, 115-131.

42. Gerolymos, N., Apostolou, M., and Gazetas, G. (2005). Neural network analysis of overturning response under near-fault type excitation. *Earth. Engng and Engng Vibr.* **4**, No. 2, 213-228.

43. Hill, R. (1950). The mathematical theory of plasticity. Oxford classic texts in the physical sciences, Oxford University Press.

44. Hisada, Y. and Bielak, J. (2003). A theoretical method for computing near-fault ground motions in layered half-spaces considering static offset due to surface faulting, with a physical interpretation of fling step and rupture directivity. *Bull. Seismol. Soc. Amer.* **93**, No. 3, 1154-1168.

45. Houlsby, G. T. and Cassidy, M. J. (2002). A plasticity model for the behaviour of footings on sand under combined loading. *Géotechnique* **52**, No. 2, 117-129.

46. Houlsby, G. T. and Puzrin, A. M. (1999). The bearing capacity of strip footing on clay under combined loading. *Proc. Royal Society* **455A**, 893-916.

47. Housner, G. W. (1963). The behaviour of inverted pendulum structures during earthquakes.

*Bull. Seismol. Soc. Amer.* **53**, No. 2, 403-417.

48. Hsieh, T. K. (1962). Foundation vibrations. *Proc. Inst. Civil Engrs*, **22**, 211.

49. Hsiung, C. M. (1988). Base isolation benefits of rocking and uplift. PhD thesis, Texas Tech. Univ. at Lubbock.

50. Huckelbridge, A., Clough, R. (1978). Seismic response of uplifting building frame. *J. Struct. Engng, ASCE* **104**, No. 8, 1211-1229.

51. Idriss, I. M. and Seed, H. B. (1968). Seismic response of horizontal soil layers. *J. Soil Mech. Found. Div., ASCE* **94**, No. 4, 1003-1031.

52. Ishiyama, Y. (1982). Motions of rigid bodies and criteria for overturning by earthquake excitations. *Earth. Engng and Struct. Dynamics* **10**, No. 5, 635-650.

53. Jeffcott, H. H. (1918). The periods of lateral vibration of loaded shafts. The rational derivation of Dunkerley's empirical rule for determining whirling speeds. *Proc. Royal Society* **95A**, 106-115.

54. Kagawa, T., Sato, M., Minowa, A. Abe and Tazoh, T. (2004). Centrifuge simulations of large-scale shaking table tests. *J. Geotech. Engng, ASCE* **130**, No. 7, 663-672.

55. Kausel, E., Roesset, J. M., and Christian, J. T. (1976). Nonlinear behaviour in soil-structure interaction. *J. Geotech. Engng, ASCE* **102**, No. 12, 1159-1178.

56. Kausel, E. and Roesset, J. (1974). Soil structure interaction for nuclear containment structures. *Proc. ASCE, Power Division Specialty Conference*, Boulder, Co.

57. Kirkpatrick, P. (1927). Seismic measurements by the overthrow of columns. *Bull. Seismol. Soc. Amer.* **17**, No. 2, 95-109.

58. Koh, A-S. and Mustafa, G. (1990). Free rocking of cylindrical structures. *J. Engng. Mech., ASCE* **116**, No. 1, 35-54.

59. Koh, A-S., Spanos, P. D. and Roesset, J. M. (1986). Harmonic rocking of rigid block on flexible foundation. *J. Engng. Mech., ASCE* **112**, No. 11, 1165-1180.

60. Kumar, J. and Mohan Rao, V. B. K. (2002). Seismic bearing capacity factors for spread foundations. *Géotechnique* **52**, No. 2, 79-88.

61. Lamb, H. (1904). On the propagation of tremors over the surface of an elastic solid. *Phil. Trans. R. Soc. Lond. A* **203**, 1-42.

62. Lysmer, J. (1965). Vertical motions of rigid footings. *Ph.D. thesis*, Univ. Michigan, Ann Arbor.

63. Makris, N. and Roussos, Y. (1998): Rocking response and overturning of equipment under horizontal pulse-type motions. Pacific Earthquake Engineering Research Center, Technical Report No. 5.

64. Makris, N. and Zhang, J. (1999): Rocking response and overturning of anchored equipment under seismic excitations. Pacific Earthquake Engineering Research Center, Technical Report No. 6.

65. Makris, N. and Konstantinidis, D. (2003). The rocking spectrum and the limitations of practical design methodologies. *Earth. Engng and Struct. Dynamics* **32**, No. 2, 265–289.

66. Makris, N. and Black, C. (2001). Rocking response of equipment anchored to a base foundation. Pacific Earthquake Engineering Research Center, Technical Report No. 14.

67. Martin, G. and Lam, I. (2000). Earthquake resistant design of foundations – Retrofit of existing foundations. *Proc. GeoEng Conference*, Melbourne.

68. Mavroeidis, G. and Papageorgiou, A. (2003). A mathematical representation of near-fault ground motions. *Bull. Seismol. Soc. Amer.* **93**, No. 3, 1099-1131.

69. Meek, J. (1975). Effect of foundation tipping on dynamic response. *J. Struct. Div., ASCE* **101**, No. 7, 1297-1311.

70. Meek, J. W. and Veletsos, A. S. (1973). Simple models for foundations in lateral and rocking motions. *Proc.5$^{th}$ World Conference on Earthquake Engng*, Rome.

71. Mergos, P. E. and Kawashima, K. (2005). Rocking isolation of a typical bridge pier on spread foundation. *J. Earth. Engng* **9**, No. 2, 395-414.

72. Meyerhof, G. G. (1953). The bearing capacity of foundations under eccentric and inclined loads. *Proc. 3rd Int. Conference Soil Mechanics and Foundation Engng*, Zurich, 1, 440-445.

73. Milne, J. and Omori, F. (1893). On the overturning and fracturing of brick and other

columns by horizontally applied motion. *The Seismological Journal of Japan*, 1, 59-86.

74. Muskhelishvili, N. (1953). Some basic problems of the mathematical theory of elasticity. Groningen, P. Noordhoff (a monograph).

75. Muto, K., Umemura, H., Sonobe, Y. (1960). Study of the overturning vibrations of slender structures. *Proc. 2nd World Conference on Earth. Engng*, Tokyo.

76. Mylonakis, G., Nikolaou, S., Gazetas, G. (2006). Footings under seismic loading: Analysis and design issues with emphasis on bridge foundations. *Soil Dyn. and Earth. Engng* **26**, No. 9, 824-853.

77. Oliveto, G., Calio, I. and Greco, A. (2003). Large displacement behaviour of a structural model with foundation uplift under impulsive and earthquake excitations. *Earth. Engng and Struct. Dynamics* **32**, No. 3, 369-393.

78. Paolucci, R., Shirato, M. and Yilmaz, M. T. (2008). Seismic behaviour of shallow foundations: Shaking table experiments vs numerical modelling. *Earth. Engng and Struct. Dynamics* **37**, No. 4, 577-595.

79. Pecker, A. and Teyssandier, J. P. (1998). Seismic design for the foundation of the Rion-Antirion Bridge. *Proc. Instn Civ. Engrs Geotech. Engng* **131**, No. 1, 4-11.

80. Pecker, A. and Pender, M. (2000). Earthquake resistant design of foundations: New construction. *Proc. Geoeng Conference* **1,** Melbourne, 313-332.

81. Poulos, H., Carter, J. and Small, J. (2002). Foundations and retaining structures – Research and practice. *Proc. 15th Int. Conference Soil Mechanics and Foundation Engng*, Instanbul, 1-80.

82. Prager, W. (1959). An introduction to plasticity. Addision–Wesley, London.

83. Prandtl, L. (1921). On the penetrating strengths of plastic construction materials and the strength of cutting edges (in German). *Zeit. Angew. Math. Mech.* **1**, No. 1, 15-20.

84. Priestley, M., Evison, R., and Carr, A. (1978). Seismic response of structures free to rock on their foundations. *Bulletin of the New Zealand National Society for Earth. Engng* **11**, No. 3, 141–150.

85. Prieto, F., Lourenco, P., and Oliveira, C. (2004). Impulsive Dirac-delta forces in the rocking motion. *Earth. Engng and Struct. Dynamics* **33**, No. 7, 839-857.

86. Psycharis, J. and Jennings, P. (1983). Rocking of slender rigid bodies allowed to uplift. *Earth. Engng and Struct. Dynamics* **11**, No. 1, 57-76.

87. Psycharis, J. (1991). Effect of base uplift on dynamic response of sdof structures. *J. Struct. Engng, ASCE* **117**, 733-754.

88. Reissner, E. (1936). Stationare, axialsymmetrische, durch eine scht-telnde masse erregte schwingungen eines homogenen elastischen halbraumes. *Arch. Applied Mech.*, **7**, No. 6, 381-396.

89. Richart, F. E., Woods, R. D. and Hall, J. R. (1970). Vibrations of soils and foundations. Prentice-Hall, Englewood Cliffs, N.J.

90. Richart, F. E. And Whitman, R. V. (1967). Comparison of footing vibration tests with theory. *J. Soil Mech. Found. Div., ASCE* **83**, No. 6, 143-167.

91. Roscoe, K. H. and Schofield, A. N. (1957). The stability of short pier foundations in sand. Discussion. *British Welding Journal*, 12-18.

92. Sadowsky, M. (1928). Zweidimensionale probleme der Elastizitätstheorie. *Zeit. Angew. Math. Mech.* **8**, No. 2, 107-121.

93. Salencon, J. and Pecker, A. (1995a). Ultimate bearing capacity of shallow foundations under inclined and eccentric loads. Part I: Purely cohesive soil. *Eur. J. Mech. A/Solids* **14**, No. 3, 349-375.

94. Salencon, J. and Pecker, A. (1995b). Ultimate bearing capacity of shallow foundations under inclined and eccentric loads. Part II: Purely cohesive soil without tensile strength. *Eur. J. Mech. A/Solids* **14**, No. 3, 377-396.

95. Salgado, R., Lyamin, A. V., Sloan, S. W. and Yu, H. S. (2004). Two- and three-dimensional bearing capacity of foundations in clay. *Géotechnique* **54**, No. 5, 297-306.

96. Selvadurai, A. P. S. (1979). Elastic analysis of soil-foundation interaction. *Developments in Geotechnical Engineering* **17**, Elsevier Scientific Publishing Company, Amsterdam.

97. Sexton, H. J. (1976). Discussion of ref 6. *J. Struct. Div., ASCE* **102** No. 6, 1262.

98. Siddharthan, RV., Ara, S., Norris, GM. (1992). Simple rigid plastic model for seismic tilting

of rigid walls. *J. Struct. Engng, ASCE* **118** No. 2, 469-487.

99. Somerville, P. (2003). Characterization of near fault ground motions for design. *American Concrete Institute Conference*, San Diego.

100. Spanos, P. and Koh, A-S. (1984). Rocking of rigid blocks due to harmonic shaking. *J. Engng Mech., ASCE* **110** No. 11, 1627-1642.

101. Taylor, P., Bartlett, P. and Wiessing, P. (1981). Foundation rocking under earthquake loading. *Proc. 10th Int. Conference Soil Mechanics and Foundation Engng*, **3**, 33-322.

102. Taiebat, H. (1999). Three dimensional liquefaction analysis of offshore foundations. PhD thesis, Univ. of Sydney.

103. Taiebat, H. and Carter, J. (2002). Bearing capacity of strip and circular foundations on undrained clay subjected to eccentric loads. *Géotechnique* **52**, No. 1, 61-64.

104. Terzaghi, K. (1943). *Theoretical soil mechanics.* John Wiley and Sons, Inc. N.Y.

105. Ticof, J. (1978). Surface footings on sand under general planar loads. PhD thesis, Univ. of Southampton.

106. Uematsu, T., Miyagi, M. and Ishiyama, Y. (2000). Rocking motion and criteria for overturning of bodies on a floor – comparison between analysis and experiment. *Proc. 12th World Conference on Earth. Engng*, Auckland.

107. Ukritchon, B., Whittle, A. and Sloan, S. (1998). Undrained limit analyses for combined loading of strip footings on clay. *J. Geotech. Engng, ASCE* **124**, No. 3, 265-276.

108. Veletsos, A. S. and Meek, J. W. (1974). Dynamic behavior of building foundation systems. *Earth. Engng and Struct. Dynamics* **3**, No. 2, 121-138.

109. Vésic, A. S. (1975). Bearing capacity of shallow foundations. *Foundation engineering handbook*, H. F. Winterkorn and H. Y. Fang, eds. Van Nostrand Reinhold, New York, N.Y., 121-145.

110. Whitman, R. (1972). Analysis of soil–structure interaction: State-of-the-art review. *Experimental and Structural Dynamics*, Inst. of Sound and Vibration, Southampton.

111. Wolf, J. P. (1988). *Soil-structure interaction analysis in time domain.* Prentice-Hall, Englewood Cliffs, N.J.

112. Wolf, J. P. (1985). *Dynamic soil-structure interaction*. Prentice-Hall, Englewood Cliffs, N.J.

113. Wolf, J. P. (1977). Seismic response due to traveling shear wave including soil-structure interaction with base-mat uplift. *Earth. Engng and Struct. Dynamics* **5**, No. 4, 337-363.

114. Yasumi, M. and Akao, S. (1951). Overturning of prismatic columns due to earthquake. Technology reports, Osaka Univ. **1**, Nos 10-24, 192-200.

115. Yim, S. C-S. and Chopra, A. (1984). Earthquake response of structures with partial uplift on Winkler foundation. *Earth. Engng and Struct. Dynamics* **12**, No. 2, 263-281.

116. Yim, S. C-S. and Lin, H. (1991a). Nonlinear impact and chaotic response of slender rocking objects. *J. Engng. Mech., ASCE* **117**, 2079-2100.

117. Yim, S. C-S. and Lin, H. (1991b). Chaotic behavior and stability of free-standing offshore equipment. *Oc. Engng* **18**, 225-250.